DISSERTATION

BEAM-DRIVEN CO-LINEAR X-BAND ENERGY BOOSTER (CXEB) FOR A COMPACT FEL

Submitted by

Taylan Sipahi

Department of Electrical and Computer Engineering

In partial fulfillment of the requirements

For the Degree of Doctor of Philosophy

Colorado State University

Fort Collins, Colorado

Fall 2017

Doctoral Committee:

Advisor: Stephen V. Milton
Co-advisor: Sandra G. Biedron

Carmen S. Menoni
Alexander Brandl

ABSTRACT

BEAM-DRIVEN CO-LINEAR X-BAND ENERGY BOOSTER (CXEB) FOR A COMPACT FEL

Achieving compact, efficient and cost-effective particle accelerators is overall major goal of the community to help propel future projects forward. In the realm of particle accelerators that enable both the high-energy physics and light-source communities, achieving the highest energy with the brightest beams in the shortest distance is most important and it is here where a paradigm shift is needed. Achieving high energies in a shorter distance (higher gradients) than presently achievable is important for even small laboratory settings, i.e. universities or industries desiring light sources, as it would permit an affordable cost. While there are several methods being considered for compact, efficient particle accelerators, it was chosen to pursue a unique application of X-band (11.7 GHz) RF cavities as they are capable, due to their intrinsic high shunt impedance, of generating high gradients with relatively low input power. A novel idea that can push the Colorado State University's (CSU) Advanced Beam Laboratory's beam energy up from the present 6 MeV to over 32.6 MeV, without the need of additional, expensive X-band power sources was conceived. The concept is called the co-linear X-band energy booster (CXEB) and it relies on the use of X-band structures powered by the beam that is already available from the facility's existing L-band (1.3 GHz) linear accelerator system. Also, this proposed system can provide electron beam to a compact free-electron laser (FEL) at CSU. The overall FEL system is quite compact and comparatively cost-effective given the fact that the existing L-band infrastructure already exists.

ACKNOWLEDGEMENT

I would like to thank to my advisor and my committee members for their contributions to my Ph.D. studies.

My sincere thanks goes to Cho-Kuen Ng and Oleksiy Kononenko from Computer Division at SLAC National Laboratory, Stanford University for their continued support, technical guidance and valuable discussions about the ACE3P simulations during my Ph.D. studies.

I also would like to thank Universities Research Association Inc. (URA) to support me as a URA Visiting Scholar and Robert Zwaska as my URA advisor at Fermilab. I would like to especially thank to Jim Hylen for his guidance, contributions and friendship during my research at Fermilab.

I would like to thank all of my friends for their valuable friendship during my Ph.D. studies and in my life.

More importantly, my grateful thanks to my parents for their endless support that brings me to the point I am standing right now and to Kandemir family for believing in me all the time and their endless support in every point of my life. Moreover, my special thanks are to Uygar for always being there to encourage me and to Mehmet for being my brother and un-ending support. You are the best brothers in the world.

My other grateful thanks are to Özdemir family for encouraging me all the time and to Güngör family for their valuable support.

Finally, my hearty and greatest thank is for my love, my wife and my colleague Nihan. I could not do this work without your endless love and continuous support. Thank you for believing in me and supporting my work all the time in my life.

LIST OF TABLES

LIST OF FIGURES

TABLE OF CONTENTS

1. INTRODUCTION

One of the future desires for many users of particle accelerators, including the high-energy physics (HEP) and light source communities, is to achieve higher energies in a more compact, efficient and cost-effective way [1, 2]. This can help make their research projects more attainable, mostly because of cost. For this reason, there are several research efforts to achieve compact particle accelerators.

1.1. Typical Radio Frequency (RF) Configurations

The typical features of a radio frequency (RF) particle accelerator system are shown in Figure 1.1. An electron source provides the initial beam to the accelerator system, in this case a linear accelerator (linac). Power for the RF accelerating fields in the linac are provided by a high-power RF amplifier system, for instance the klystron indicated in Figure 1.1. And the beam is guided and focused with a series of magnets such as the solenoids and quadrupole magnets indicate in the figure. A control system is used to set and control and readback all conditions. Ancillary systems, such as electrical, power and vacuum systems are also employed.

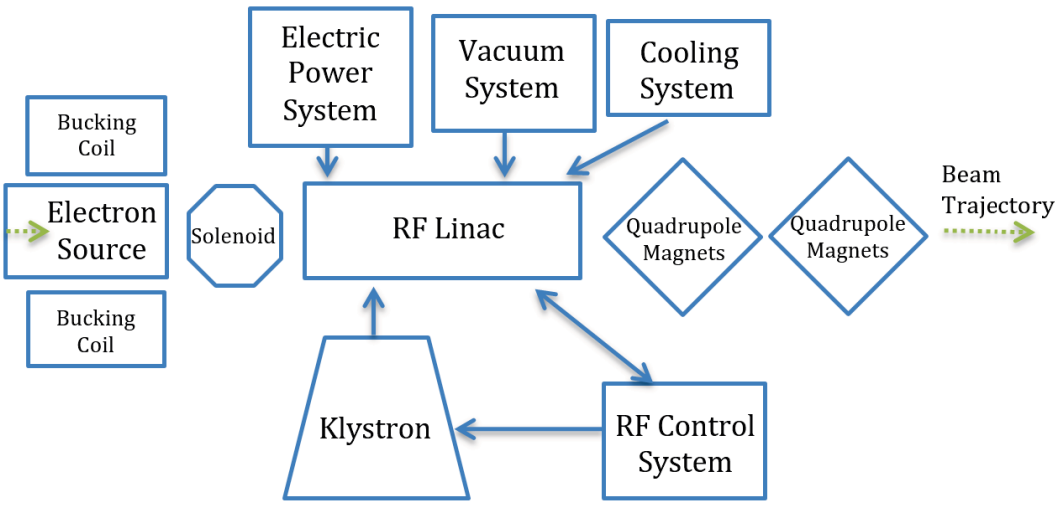

Figure 1.1 Generic block diagram of a linear accelerator (linac) and its subsystems

In the system shown a klystron, provides RF power. The frequency is chosen to be resonant with fundamental mode of the linac structures. As such the electromagnetic fields build up in the structure to very high levels. Properly designed the electric fields in the structure can add net energy to a charge particle passing along the length of the structure. In an RF linac, the beam is accelerated by RF electromagnetic fields with a harmonic time-dependence. Because the linac uses a sinusoidal varying electric field for acceleration, particles can either gain or lose energy depending on the beam phase relative to the crest of the wave. To provide efficient acceleration for all the particles, the beam must be bunched as shown in Figure 1.2, and the phase velocity of the electromagnetic wave must equal that of the electrons. Bunches can be separated longitudinally by one or more RF periods according to the desired application.

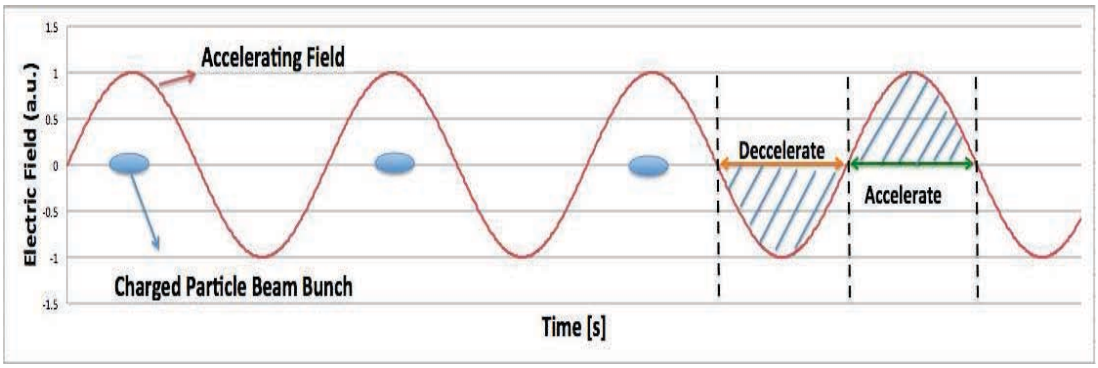

Figure 1. 2 Beam bunch in an RF linac

While there are many details and limitations [Appendix A] related to the explanation above it is correct almost for all RF-based particle accelerator systems.

First the RF power source is considered. Many of the sources still in use today were a product of radar research and development (R&D) for military and outer space related research efforts. Higher powers were always desired to improve range and resolution, but material properties and system efficiencies limit single device powers to 1 to 2 megawatts (MW) for a continuously operated device and to 10s of megawatts to nearly 100 megawatts for single pulsed devices. These are very significant numbers, but they do impose a limit on the maximum achievable fields that can be generated and used to accelerate a charged particle beam. Next in line are the resonant structures used to accelerate the particle beams. When RF power enters the structure the fields build up over time until equilibrium is reached where the power in equals the power dissipated. Assuming most losses are resistive, the higher the conductivity of the structure material the higher the obtained fields for a given input power. For that reason most of the structures are made of copper. (The superconducting materials are not discussed in this dissertation.) RF frequencies tend to lie in the few hundred megahertz (MHz) to 10 plus

gigahertz (GHz) range, which implies RF wavelengths in the range of tens of centimeters (cm) to less than a centimeter. A structure typically consists of multiple resonant cavities and so overall structure lengths tend to be in the tens of centimeter to single digit meter (m) range. Depositing the megawatt level power continuously into such a structure requires extraordinary measures to cool the device. This limits the peak achievable accelerating fields. The work around for this has been to use pulsed-power sources with limited duty factors to temporarily achieve very large accelerating potentials at a much lower average power, however this still runs into a limitation. At very high gradients field emission occurs on the surfaces of the structure and leads to electrical breakdown thus limiting the maximum achievable gradient. This limit increases with the RF frequency. A phenomenological equation known as the Kilpatrick criterion quantifies this

$$f[MHz] = 1.64E_k^2 e^{-8.8/E_k} \tag{1.1}$$

where E_k is the maximum cavity field in MV/m. This relationship is shown in Figure 1.3.

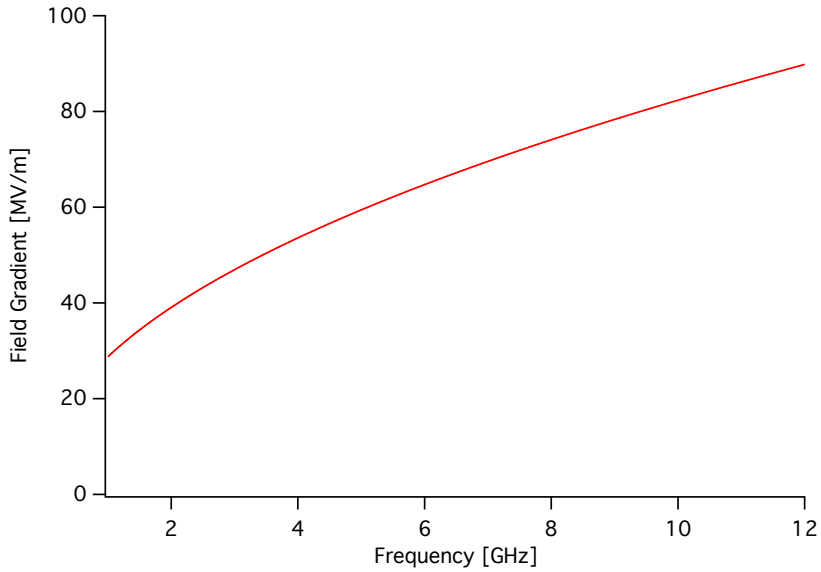

Figure 1.3 Kilpatrick plot

At high frequencies the maximum obtainable field scales as $f^{1/2}$. It is clear that to reach high gradients it is needed to go to increasingly higher frequencies [3-5].

Without going into details another quantity that represents a useful measure of the ability of an RF structure to convert power into net accelerating voltage can be introduced here. This quantity is referred to as the shunt impedance per unit length r_{sh}, and is given by

$$P = \frac{V^2}{r_{sh}L} \tag{1.2}$$

where L is the length of the structure, V is the net accelerating potential, and P is the power applied to the structure. For a chosen voltage V, one requires less power for structures with higher shunt impedance.

For completeness, the scaling with frequency for the parameters commonly used to describe accelerator cavity design are summarized in Table 1.1.

Table 1.1 Frequency dependence of room- temperature radio frequency accelerating cavity parameters

Parameter	**Symbol**	**Frequency Dependence**
Shunt Impedance per Unit Length [Ω/m]	(r_{sh})	$f^{1/2}$
Unloaded Quality Factor	(Q_0)	$f^{-1/2}$
Power Dissipation Capability of Accelerator Structure [kW]		$f^{-1/2}$
Maximum Permissible Electric Field Gradient [MV]		$f^{1/2}$

As indicated in Table 1.1, there are some significant trade-offs to be considered when designing structures. While one might wish to achieve a maximum field gradient one needs to balance this

with other issues. For instance these include the lower unloaded quality factor (to be described later) and lower power dissipation capability of the accelerating structure. In addition, to achieve the calculated performance, the surface finish and tolerances scale inversely with the frequency and place significant demands on machining and construction [6-8].

In our concept, presented in this dissertation, some of the scaling listed in Table 1.1, will be exploited and our focus will be kept on more conventional types of accelerating structures, although in a new configuration. However, before moving on to the details of our concept it is necessary to touch upon the topic of advanced acceleration techniques (AAT) due to some of their features indeed show up in our concept.

1.2. Advanced Acceleration Techniques (AAT)

The classical method of particle acceleration as described above is very mature, and further progress without new concepts and ideas is slow to come. There are several methods being considered for compact, efficient particle accelerators, and there is an entire sub-community dedicated to Advanced Accelerator Techniques.

There are several techniques that aim to achieve gradients higher than those produced by conventional linacs. The main categories are: two-beam acceleration (TBA) [9], wakefield acceleration (WFA) [10], plasma acceleration [11] and dielectric direct laser acceleration (DLA) [12]. As our concept has features of both TBA and WFA acceleration, the details of these two techniques and ongoing research efforts are discussed here.

1.2.1. Two-Beam Acceleration (TBA)

In two-beam acceleration (TBA) a high power beam (high current, but modest beam voltage) is passed through an RF cavity structure where it losses it energy to the structure fields. This energy is fed into a second RF cavity structure whose frequency is tuned to the frequency coming out of the first structure. The gradients in the second RF structure are much higher than those in the first. A second beam is then passed through the second structure, but at a much lower current, and is accelerated to very high energies. This system is very analogous to a power transformer where one "exchanges" current for voltage. Thus the high-current, low voltage drive beam serves as an RF power source for the low-current, high voltage main beam. The Compact Linear Collider (CLIC) [13,14] at CERN, a high-gradient multi-mode two-beam accelerating structure, is based on the two-beam scheme and aims to provide an acceleration gradient of greater than 100 megaelectronvolt per meter (MeV/m) for a next generation multi-teraelectronvolt (TeV) linear collider.

1.2.2. Wakefield Acceleration (WFA)

Similarly, in WFA two beams are used, but this time in the same beam tube. In a general sense the wakefield mechanism can be described as a speedboat rushing over the water. Each drive bunch leaves an electromagnetic wake behind itself that creates an electric gradient that is then used to accelerate the main beam. This electric wakefield gradient can be achieved in a number of different ways, the most popular well studied of which are with dielectric structures as in the Argonne Wakefield Accelerator (AWA) at Argonne National Laboratory (ANL) [15, 16], or in a plasma such as that used in the Facility for Advanced Accelerator Experimental Tests (FACET)

program at SLAC National Accelerator Laboratory, [17, 18] and the Proton Driven Plasma Wakefield Acceleration Experiment (AWAKE) program at the European Organization for Nuclear Research (CERN) [19,20].

1.2.3. Plasma Acceleration

While the FACET program uses an electron and positron beams to excite the plasma, others are exploring the use of a high power laser system to excite the plasma in a manner that generates very high gradients, i.e. greater than 10s and perhaps even 100s of gigavolts per meter (GV/m). AWAKE is also proposed to use plasma wakefields driven by a proton beam could accelerate charged particles. The most successful of these is the basic laser plasma wakefield acceleration techniques as practice by the group on the Berkeley Lab Laser Accelerator (BELLA) project at Lawrence Berkeley National Laboratory [21, 22], where they it has been shown an acceleration of a bunch to a few gigaelectronvolts (GeV) with relatively small energy spread. There are also other potentially exciting paths. For instance the beat frequency of two lasers of different frequency can be used to excite the plasma oscillations, the so-called laser beat-wave acceleration (LBWA) method [23]. Another example is a laser pulse modulated by the stimulated Raman forward scattering instability (self-modulated laser wakefield acceleration-SMLWFA) [24].

1.3. CSU Linear Accelerator

Colorado State University (CSU) has constructed an Advanced Beam Laboratory (ABL) as shown in Figure 1.4 for use in the study of both accelerator and laser systems. The goal of the

ABL is to have a purpose-built facility that co-locates accelerator and laser technologies. This will allow for the merging of the two fields to perform novel science and engineering that would not necessarily be accomplished independently. In addition, the ABL serves as a training facility in accelerator science for engineers and physicists over the broad span of education from high school through post-doctoral researchers.

Figure 1.4 Advanced Beam Laboratory (ABL)

One side of the ABL is planned to be the CSU Accelerator Laboratory (CSUAL) [25, 26]. The floor plan with the planned radiation shielding walls, laser room and control room is shown in Figure 1.5.

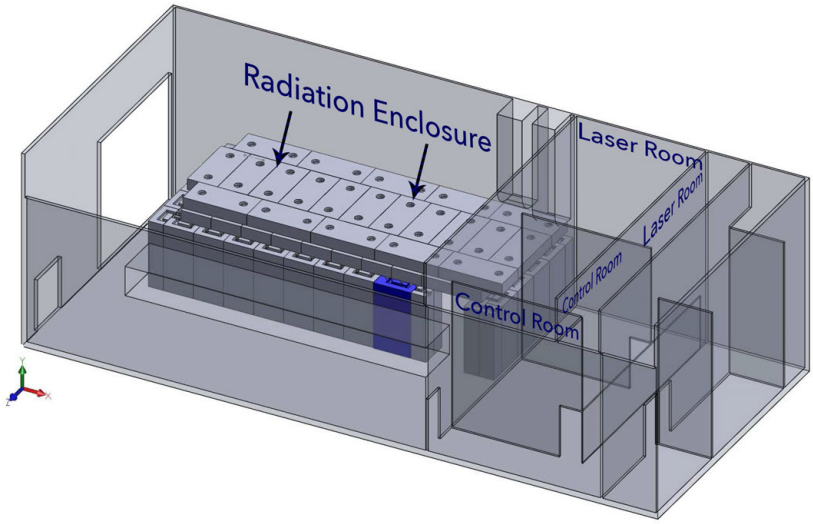

Figure 1.5 The floor plan of the CSUAL with shielding

1.3.1. L-band (1.3 GHz) Photo Injector

One of the main components is an L-band (1.3-GHz), photocathode-based 6-MeV normal-conducting electron linac donated by University of Twente [27, 28] shown in Figure 1.6 (a) and (b).

(a)

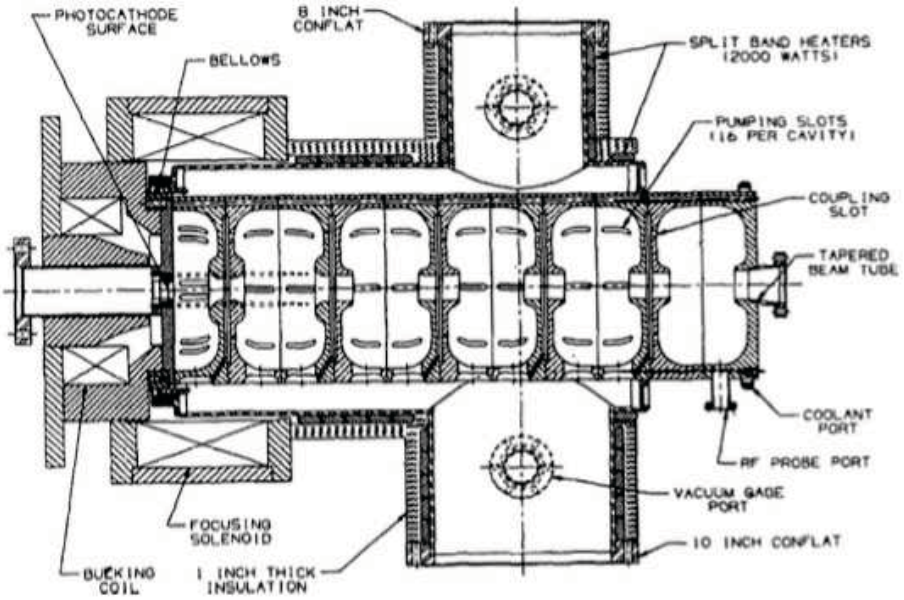

(b)

Figure 1.6 (a) The 5+1/2 cell photocathode 6-MeV Linear Accelerator (linac) originally built by Los Alamos National Laboratory (LANL) (b) Schematic (side-view-half symmetry) of 6-MeV linac including solenoid and bucking coils [29]

1.3.2. High Power Klystron and Pulsed Power System

Figure 1.7 shows one of our existing L-band (1.3 GHz) klystrons, a 20 MW Thomson TV2022 tube (left) and pulsed power modulator system (right) [30]. This system can be capable of generating 20 MW RF bursts for up to 10 μs.

Figure 1.7 1.3 GHz klystron and modulator system at CSU

Table 1.2 Parameters of L-band (1.3 GHz) normal conducting linac at CSU

Parameter	Symbol	Value
L-Band RF Gun Frequency [GHz]	$f_{L-band\ gun}$	1.3
L-Band RF Gun Potential Capability [MV]	$E_{L-band\ gun}$	6
L-Band Macropulse Length [μs]	$\sigma_{L-band\ gun}$	10
L-band Gun Bunch Charge [nC]	$q_{L-band\ gun}$	3
Shunt Impedance [MΩ/m]	r_{sh}	53
Unloaded Quality Factor (Measured at LANL)	Q_0	16114

1.3.3. Titanium: Sapphire ($Ti:Al_2O_3$) Laser System

In addition to the 6-MeV electron linac, the CSUAL houses a Titanium: Sapphire ($Ti:Al_2O_3$) laser system, donate by the Boeing Corporation for use as a photocathode drive laser for the linear accelerator as well as for use in other experiments (Figure 1.8). Related parameters are given in Table 1.3.

Table 1.3 Parameters for drive-laser system

Micro Oscillator		
Parameter	Symbol	Value
Average Power [mW]	P_{ave}	> 300
Repetition Rate [MHz]		<81.25
Pulse width [fs]		< 35 (with ext. comp.)
Legend Elite Duo Amplifier		
Parameter	Symbol	Value
Average Power (at 800 nm) [W]	P_{ave}	> 10 (at 1kHZ)
Average Power (at 256 nm) [W]	P_{ave}	> 1 (at 1kHZ)
Pulse Duration [fs]		40 (FWHM)

Electron bunches of a few nanocoulombs (nC) will be emitted from a high-quantum efficiency (QE) cathode via the photoelectric effect at burst rates of up to 81.25 MHz.

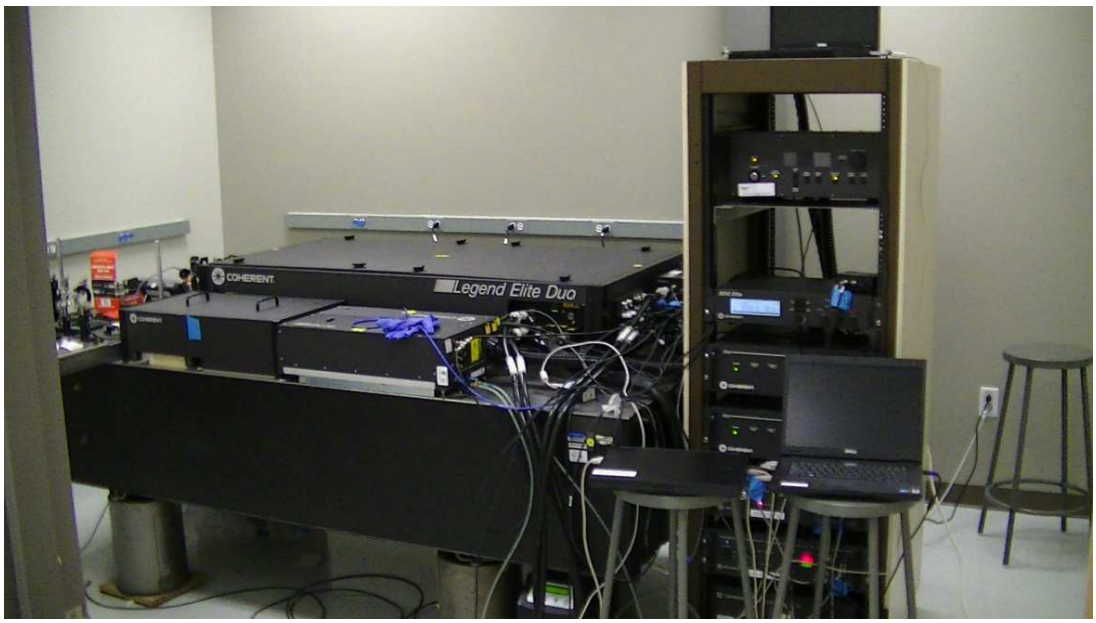

Figure 1.8 Coherent Titanium: Sapphire ($Ti:Al_2O_3$) laser system

1.3.4. Achieving Higher Energies Using Conventional Linac System

To generate a 6 MV potential in our linac, only 1.8 MW is needed. Any more would damage the linac. This leaves us 18 MW from the klystron to work with. The absolute simplest way to get more potential is to just add more L-band sections after our L-band photoinjector. There would be enough power to readily reach 60 MV of potential in this way. In addition to that, L-band accelerating structures and transmission components such as waveguides and power dividers are pretty affordable as the tolerances are rather relaxed. Such a system would be roughly 5 to 6 meters in length and represents the baseline to which was compared to our alternative concept, the co-linear X-band energy booster.

2. CO-LINEAR X-BAND ENERGY BOOSTER (CXEB) CONCEPT

Our idea is to instead utilize the power in the electron beam from our L-band linac system as a drive source for an X-band linac structure. This will allow us to increase our beam energy without the need for expensive, specialized X-band klystrons. It also has the potential to make the overall system more compact, and also might provide us a way to increase our energy a modest amount without significant investment.

Recent developments in the so-called X-band frequency regime drew our attention to create a unique concept that could help increase energies of accelerators in general. X-band RF cavities have an intrinsically high shunt impedance, so one is able to generate high gradients in the X-band accelerating cavities with a relatively low input RF power. The novel concept is a co-linear, X-band energy-booster (CXEB) accelerator system. It relies on the use of X-band accelerating structures powered by an energetic electron beam that passes through it; therefore, it does not require a separate X-band RF power source. The design details of the system that will allow us to explore how to achieve our goal of reaching the maximum practical net potential across the X-band accelerating structure while driven solely by the beam from the L-band system are given in this dissertation. This beam can then be used for subsequent purposes, such as the electron-beam power source for a free-electron laser (FEL) system. The basic parameters of the system are given in Table 2.1.

Table 2.1 Basic parameters of the CXEB system

Parameter	Symbol	Value
Frequency of Titanium:Sapphire Laser [MHz]	f_{laser}	81.25
Resonance Frequency of L-Band RF Gun [GHz]	$f_{L-band\ gun}$	1.3
Maximum Energy of L-Band RF Gun [MeV]	$E_{L-band\ gun}$	6
Maximum Macropulse Length of L-band RF Gun [μs]	$\tau_{L-band\ gun}$	10
Resonance Frequency of X-band PEC and MAC [GHz]	$f_{X-band\ PEC\ \&\ MAC}$	11.7

The CXEB concept has some features that are common to the CLIC) and AWA. In here, these two concepts can be explored briefly.

AWA and CLIC differ between each other according to the accelerating cavity structure design and overall layout. For instance, while CLIC is mainly focused on metallic accelerating structures that are running with two separate beams in a parallel configuration, AWA is mainly concerned with dielectric (quartz) loaded accelerating structures used in a co-linear fashion.

The CXEB uses features of both. It is co-linear like the AWA, but uses all copper structure with a final frequency in the X-band similar to CLIC.

2.1. Standing-Wave (SW) Cavity Case

Before studying the travelling-wave (TW) case, which is the primary subject for the first part of this dissertation, it is useful to look at the on-resonance standing-wave (SW) case to both understand the advantage of the SW structure and its limitations.

In our previous study [31], we showed that by using a standing wave (SW), X-band (11.7 GHz) cavity tuned to the 9th harmonic of our 1.3-GHz linac and driven by the beam from this linac we could potentially increase our beam energy by a modest amount. In that paper it was shown that our 6-MeV electron bunch energy could periodically be boosted to 11 MeV upon passage through both the L-band and a relatively short and simple X-band linac structure, but there was a fundamental limit to that configuration.

As a bunch passes through a structure, it loses energy to the cavity and this result in an induced voltage of:

$$V_b = 2kq \tag{2.1}$$

where q is the charge of a bunch passing through the cavity and k is the mode loss parameter [32,33].

$$k = \frac{\omega_{rf} R_{sh}}{4Q_0} \tag{2.2}$$

where ω_{rf} is the angular frequency of the RF mode R_{sh} is the effective mode shunt impedance in ohms and Q_0 is the mode unloaded quality factor. Following passage through the cavity, the field decays with a time constant of [ibid, 33]:

$$\tau = \frac{2Q_0}{\omega_{RF}} \tag{2.3}$$

The maximum equilibrium integrated voltage, V_{max}, is reached when the integrated voltage added by the passing bunch equals the decay during the time between passages.

$$V_{max} = \frac{V_b}{\left(1-e^{-T_0/\tau}\right)} \tag{2.4}$$

where T_0 is the time between bunch passages. Assuming T_0 is much less than τ, that the length of the cavity is equal to L, and using Equations 2.3 and 2.4, the expected result is found as:

$$V_{max} = IR_{sh} = Ir_{sh}L \tag{2.5}$$

where I is the average beam current passing through the cavity. (The assumption here is that the electron bunch length is much less than the X-band wavelength.). Figure 2.1 shows the voltage build up over time in a representative SW X-band structure with relevant parameters given in Table 2.2.

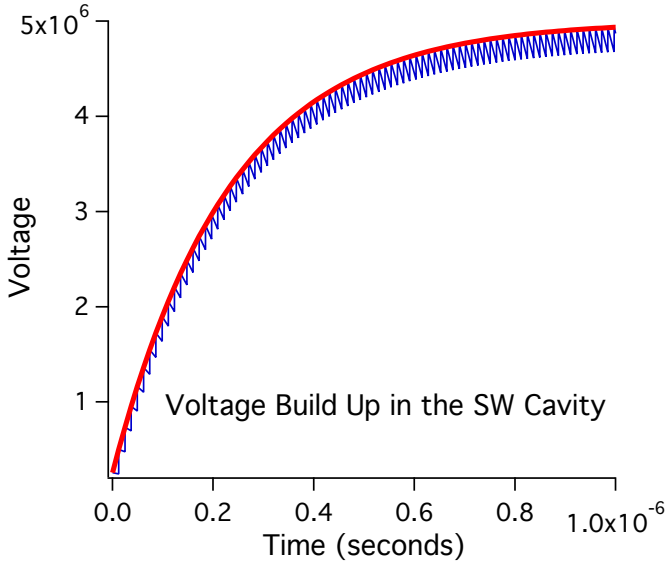

Figure 2.1 The voltage build-up in the X-band, SW, PEC structure. The blue line shows the sawtooth nature of the field over time and the red is the "smooth" buildup over time

Table 2. 2 The basic parameters of the SW cavity system

Parameter	Symbol	Value
Resonance Frequency of X-band PEC [GHz]	f_0	11.7
Average Drive Beam Current [A]	I	0.1
Length of SW X-band PEC [m]	L	0.46
Shunt Impedance per Unit Length [MΩ/m]	r_{sh}	107
Unloaded Quality Factor	Q_o	8540
Bunch Separation [ns]	T_o	12.3
Achieved Energy at the End of PEC [MeV]	E_{final}	11

The basic setup for this simple configuration is shown in Figure 2.2. The L-band system provides the beam to power the X-band cavity. For a given shunt impedance, average beam current, and maximum achievable potential Equation 2.5 can be used to determine the length of the SW structure. Using the parameters values from above and limiting the maximum potential to 5 MV leads to a structure length of 46 cm. This potential in the X-band structure comes at the expense of power provided by the drive beam. The drive beam, originally at a potential of 6 MV upon entry to the X-band structure, thus exits the X-band structure at a potential of 1 MV. If one periodically shifts the phase of emission off the L-band cathode by 20 degree at L-band, this is equivalent to a 180 degree shift at X-band, thus placing the resulting bunch at the peak accelerating voltage of the X-band structure. The X-band structure thus acts as both a decelerator of the primary drive beam and an accelerator to the periodically boosted beam. Given that we had only 6 MV of potential to start with, we could gain on resonance no more than 6 MV in the X-band structure as that was the limit of the drive beam. A drop of 5 MV seemed reasonable and so the net potential in our design was limited to 11 MV, 6MV from the RF gun and 5 MV from the X-band structure. This was a very simple arrangement that would allow us to generate an 11-MeV beam from our L-band system that was originally limited to 6 MeV. In this configuration most of the beam is used to power the X-band linac and loses energy, but a shift of 20 degrees at L-band allows the low-current, delayed beam to pass through the X-band structure on crest and gain energy. Our desire to achieve even higher energies for several applications, however, drove us to our present design configuration described below.

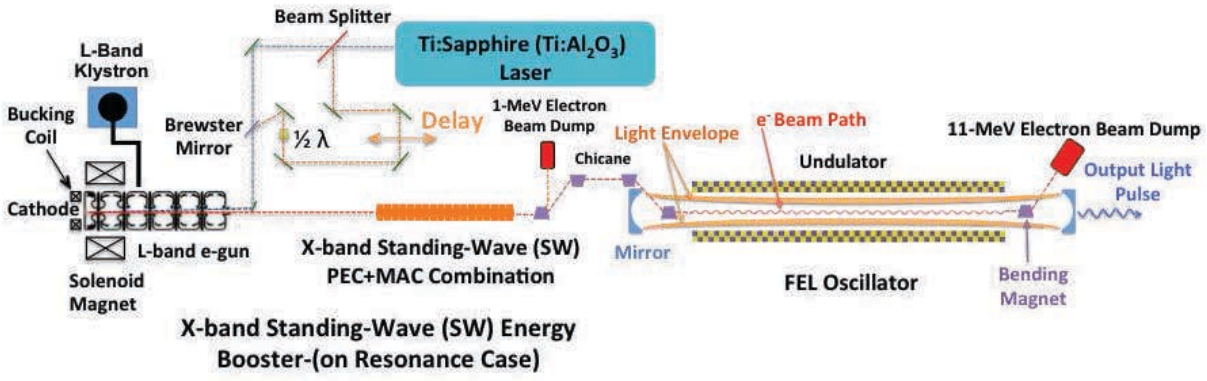

Figure 2.2 The basic system configuration used to boost the bunch energy from 6 MeV out of the L-Band linac to 11 MeV after the X-band linac in the SW case.

Before moving on to the travelling-wave case, we wish to clarify our derivation of the SW case. Implicit in the work was the fact that the X-band structure was tuned precisely to the harmonic frequency of the 1.3 GHz L-band structures. This, of course, is not necessary, and indeed one may be able to achieve even higher energies if the X-band system is tuned off resonance to the L-band system. In this manner the maximum integrated potential in the X-band structure can be higher than the initial potential of the drive beam. This is because the off-resonance drive beam will not experience the full decelerating potential of the structure. The structure will then need to be made longer to fully decelerate the drive beam, but the integrated potential across the entire structure would be more than in the on-resonance case. The low-current bunches would then need to be delayed by something different than 20 degrees, but that is a simple modification [ibid, 27]. The full analysis of the off-resonant case will not be discussed in here.

2.2. Travelling-Wave (TW) Cavity Case

In our alternative arrangement, a similar co-linear, beam-driven configuration is utilized but now based on two separate travelling-wave (TW) X-band structures, one used as an X-band power

generator and part time accelerator (the decelerator), and one purely as an accelerator. This configuration is shown in Figure 2.3.

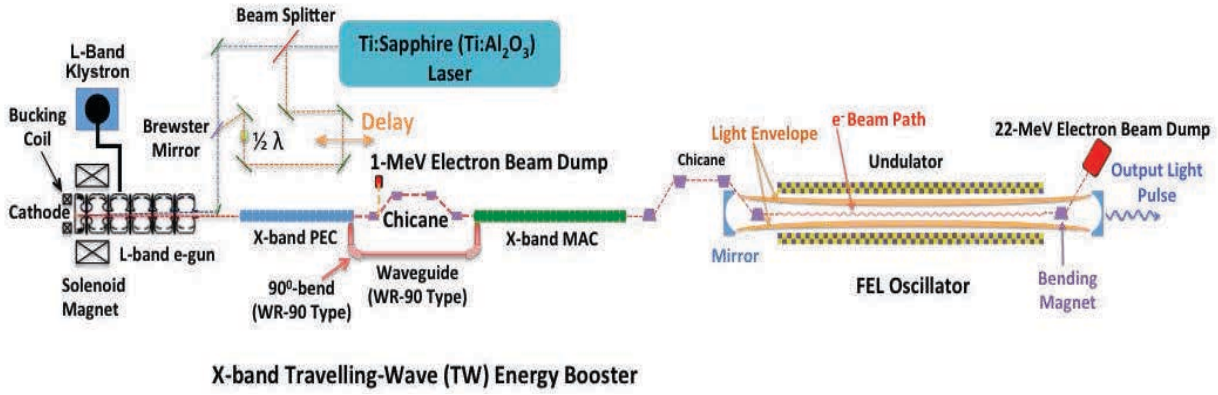

Figure 2. 3 General layout of the Co-linear X-band Energy Booster (CXEB) system

In the SW case above, roughly 500 kW of power is dissipated in the X-band structure, and this is sufficient to generate a field of greater than 10 MV/m, but the available power from the klystron is not being used very effectively, after all there is potentially 18 MW available. The limitation comes about from the fact that the drive beam can only afford to lose 5 MV of potential and all the power is delivered exclusively to the SW structure. It is better to instead extract the power available in the beam and feed it into another X-band structure to achieve an even higher overall potential. This can be accomplished with a travelling-wave (TW) structure.

The work performed and nicely presented at CERN [34] with the references therein will be followed closely. This provides the framework for the solution; however, our configuration is uniquely different than that a CERN, i.e. co-linear versus parallel, and therefore truly constitutes a new concept.

As a bunch travels through a TW structure it sets up fields much in the same manner as in the SW structure. Due to the TW mode of the structure, and the beam propagation direction, the power in the fields travels towards the downstream output coupler and exits the structure. The group velocity, v_g, governs power flow; typically $\vartheta_g \ll c$. If the period between bunches, T_o, is less than L/ϑ_g then the fields from subsequent bunches add to the fields in the cavity. Assuming a bunch period that is a sub-harmonic of the RF frequency, the fields add coherently and the field seen at the output coupler can be quite large. A simplified picture of the process is shown in Figure 2.4.

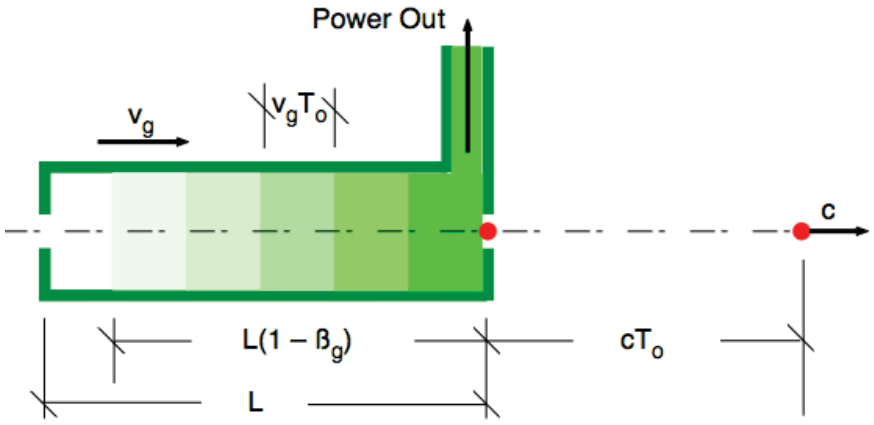

Figure 2. 4 The field build-up in a beam-powered TW structure (ibid, 34 - Graphic modeled after Figure 4.5)

The filling time of the structure is given by

$$t_{fill} = L/\vartheta_g\,(1-\beta_g) \tag{2.6}$$

To calculate the field at the output coupler of the structure one must sum up the contribution of all bunches passing through the structure over one fill time. To do this correctly one must account for ohmic losses experienced by the field as the energy flows from one end of the

structure to the other and also adjust downward the average beam current by a form factor dependent on the bunch longitudinal profile.

Upon doing this one find that the field at the structure output coupler is:

$$E_b = \frac{1}{2}\frac{r_{sh}}{Q}\omega_{RF}\frac{L}{\vartheta_g}IF\eta_\Omega \tag{2.7}$$

where I is the average beam current given by $\mathrm{q/T_o}$, F is the bunch form factor that for a Gaussian bunch of duration σ_t is given by $\mathrm{e}^{-(\sigma_t\omega_{RF})^2/2}$, and

$$\eta_\Omega = \frac{1-e^{-a}}{\alpha}, \quad \tau = \frac{\omega_{RF}}{2Q\vartheta_g}, \quad \alpha = L\tau \tag{2.8}$$

Continuing to follow closely the derivation in reference [ibid, 34] the following expression is found

$$\frac{r_{sh}}{Q}\omega_{RF} = \frac{E_b^2}{d\chi/ds} \tag{2.9}$$

where $\mathrm{d}\chi/\mathrm{ds}$ is the stored energy in the field per unit length of the cavity. The flow of energy travels at the rate of the group velocity; therefore, the power exiting the coupler and available for other purposes is given by

$$P = \frac{d\chi}{dt} = \frac{d\chi}{ds}\frac{ds}{dt} = \frac{E_b^2}{(r_{sh}/Q)\omega_{RF}}\vartheta_g \tag{2.10}$$

Combining this with Equation 2.7 gives the result we are looking for, the power exiting the output coupler

$$P = \frac{1}{4}\frac{r_{sh}}{Q}\frac{\omega_{RF}}{\vartheta_g}L^2I^2F^2\eta_\Omega^2 \tag{2.11}$$

The entire derivation leading to this result makes some assumptions. One is that the energy is added to the cavity in a smooth fashion. For the approximation to be good requires that the number of bunches contributing to the field,

$$N_{fill} = \frac{L}{\vartheta_g T_0}(1 - \beta_g) \tag{2.12}$$

be large.

These equations can then be used to determine the required properties of the cavity to achieve a desired output power level; however, additional constraints need to be applied. In particular, generated power can only be equal to or less than the power in the beam.

Assuming a linear increase of the field along the length of the cavity, which is equivalent to saying that N_{fill} is large, the peak, integrated potential that the beam experiences upon traversing the cavity is then

$$\hat{V} = \frac{1}{2} E_b L \tag{2.13}$$

This needs to be set a reasonable value when compared to the incoming potential of the beam. Similarly, the generated power can be used to estimate the mean voltage, $\langle V \rangle$, experienced by the bunch.

$$P = \langle V \rangle I \eta_\Omega \tag{2.14}$$

Using Equations 2.7, 2.11, 2.13, and 2.14, the mean voltage of the bunch can be found as

$$\langle V \rangle = \hat{V} F \tag{2.15}$$

These equations will be used in the design of the overall system.

3. X-BAND RF CAVITY DESIGN

Chapter 2 provides a theoretical guide for the overall design; however, in this chapter we study the practical design of RF structures that could be fabricated and used in our concept.

3.1. X-band RF Cavity Design Study

A consistent description [35, 36] of X-band cavity geometries is used, Figure 3.1, where a is the iris radius, R is the cavity radius, h ($= 2r_1$) is the disc thickness, r_1 is the radius of the iris poles, l is the single cell length and λ is the wavelength of the fundamental excited mode. In our studies for SW X-band RF cavity design π mode and for TW X-band RF cavity design $2\pi/3$ and $5\pi/6$ modes were chosen. For each of these designs it is considered the boundary conditions [37] and dispersion properties of disk-loaded waveguides confine the accelerating mode to be an integer multiple of cell lengths, i.e. for 2π/3 mode the one full period every 3 cells [38]. The details of each design will be provided below.

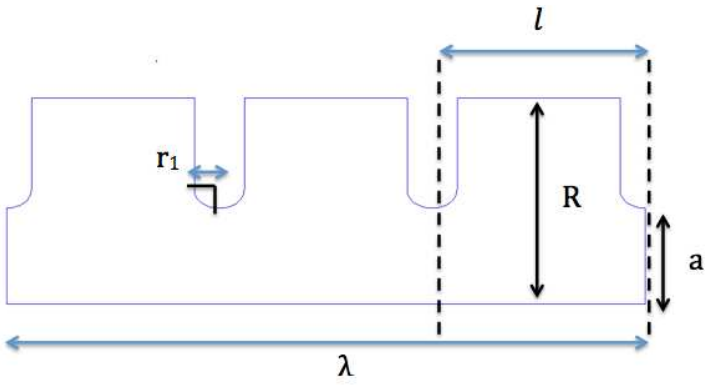

Figure 3. 1 Schematic view of a generic X-band RF cavity

3.1.1. SW Power Extraction Cavity Design

In general, the aim is to transfer energy from the L-Band RF wave to the electron beam, consisting of bunches of charged particles, and then from the electron beam to the RF wave induced in the X-band structure, thus a proper structure design that maximizes this interaction was needed.

We have described two concepts, one that utilizes a simple standing wave cavity, but has some limitations; the other uses a travelling wave design. In this subsection we will describe the design of the SW structure and follow it in subsequent subsections with the TW designs.

A standing wave is described by the following equation

$$E = E_0 \sin(kx) \sin(\omega_{RF} t) \tag{3.1}$$

where k is the wavenumber and ω_{RF} is the angular (or radial) radio frequency. The simplest cavity mode that will generate such a field is the π-mode ($2\pi/2$ or one full period in two cells). In addition to ensure the design operated in the π-mode additional adjustments were made to ensure that the structure was resonant at 11.7 GHz, that it had high effective shunt impedance, and that the iris dimensions were sufficient to ensure clean beam transport and minimize to some degree the effect of higher-order modes. Table 3.1 shows the output from the design program SUPERFISH [39, Appendix C] following our optimization of the geometry using three different values for the iris to wavelength ratio, $a/\lambda = 0.2, 0.15$ and 0.1.

Table 3.1 SW X-band PEC parameters

Parameter	Symbol	Value		
Phase Advance per Cell [Radian]	ψ	π		
Iris radius to Wavelength Ratio	a/λ	0.20	0.15	0.10
Iris Radius [m]	a	0.00256		
Disk Thickness [m]	h	0.002		
Cell Radius [m]	R	0.010747	0.010271	0.009975
Unloaded Quality Factor	Q_0	8958	8681	8512
Resonance Frequency [GHz]	f_0	11.7		
Shunt Impedance per Unit Length [MΩ/m]	r_{sh}	62.4	83	107

Equation 2.5 shows that there is a trade-off between the length and shunt impedance. To keep the structure short chose $a/\lambda = 0.1$ was chosen. This is at the expense of a smaller aperture; however, for our beam conditions this aperture size was considered sufficient. Figure 3.2 shows the electric and magnetic field distributions from SUPERFISH for the optimized X-band SW geometry.

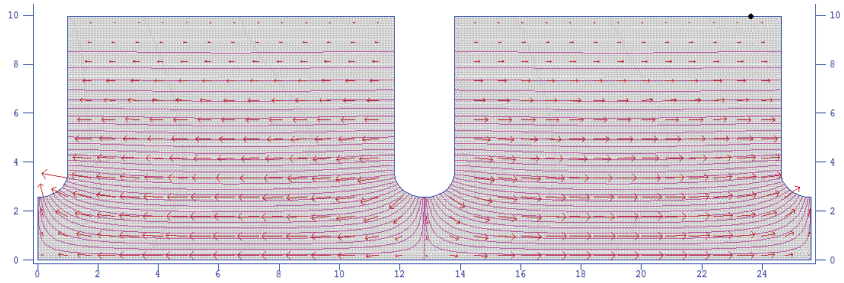

(a)

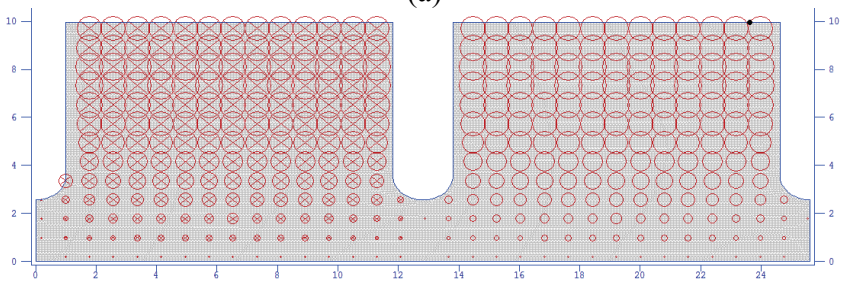

(b)

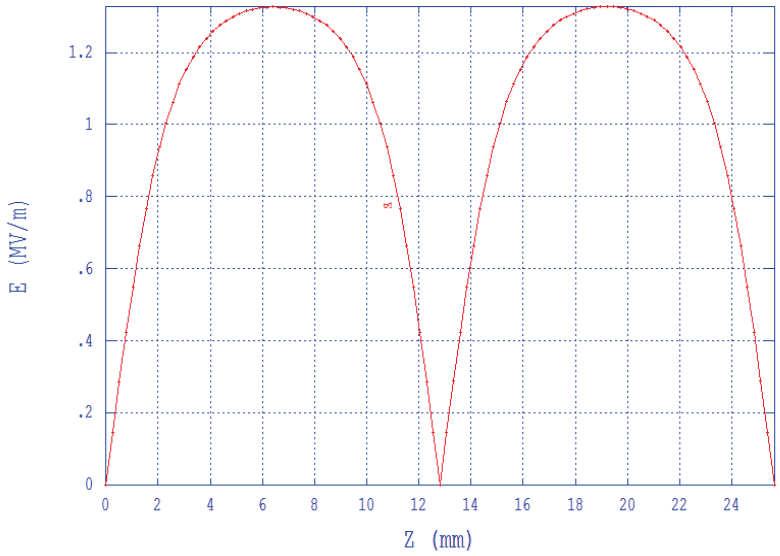

(c)

Figure 3. 2 (a) The electric field distributions (b) the magnetic field distributions and (c) the magnitude of the electric field for $a/\lambda = 0.10$ SW X-band PEC

3.1.2. TW Power Extraction Cavity (PEC) Design

In a typical resonant travelling wave structure configuration, power is fed into one end of the structure and then travels to the other end were a load absorbs the remaining power. Losses occur along the way, and if the structure properties remain invariant along the length the net obtained field decreases as a function of length along the structure. Such structures are referred to as constant impedance structures. To improve the overall performance constant gradient structures were developed. Here typically the iris decreases along the length and with this the impedance increase to compensate the loss of power thus maintaining the gradient as a function of length [40]. This additional complexity of design is not necessary in our design as the beam provides the power in a uniform fashion along the length of the structure.

In our power extraction cavity (PEC) or decelerator we have chosen to use a $2\pi/3$ TW mode as such a mode allows us to achieve a relatively higher shunt impedance value and therefore a shorter structure. In here, the main item of note is the iris radius as discussed earlier. The r_{sh}/Q_0 suffers if this is made too large as shown in Figure 3.3 while making it too small limits the current that can be passed safely through the structure.

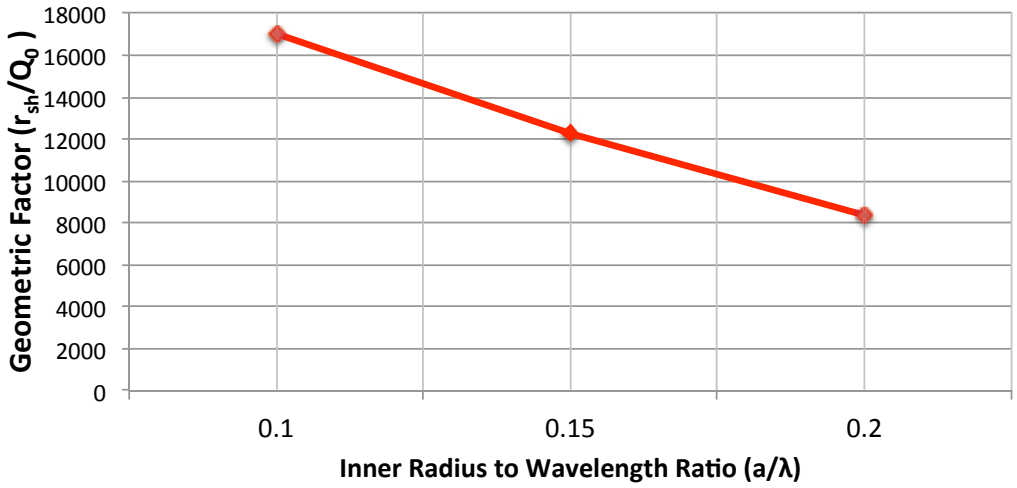

Figure 3.3 The r_{sh}/Q_0 versus a/λ for a $2\pi/3$ phase advance

Another important parameter that needs to be optimized for effective deceleration in the PEC is the group velocity, with a lower group velocity preferable as it as it allows for more bunches to contribute to the fields for a given overall length (Eq. 2.12). The group velocity versus iris radius to wavelength ratio values for the X-band PEC are shown in Figure 3.4.

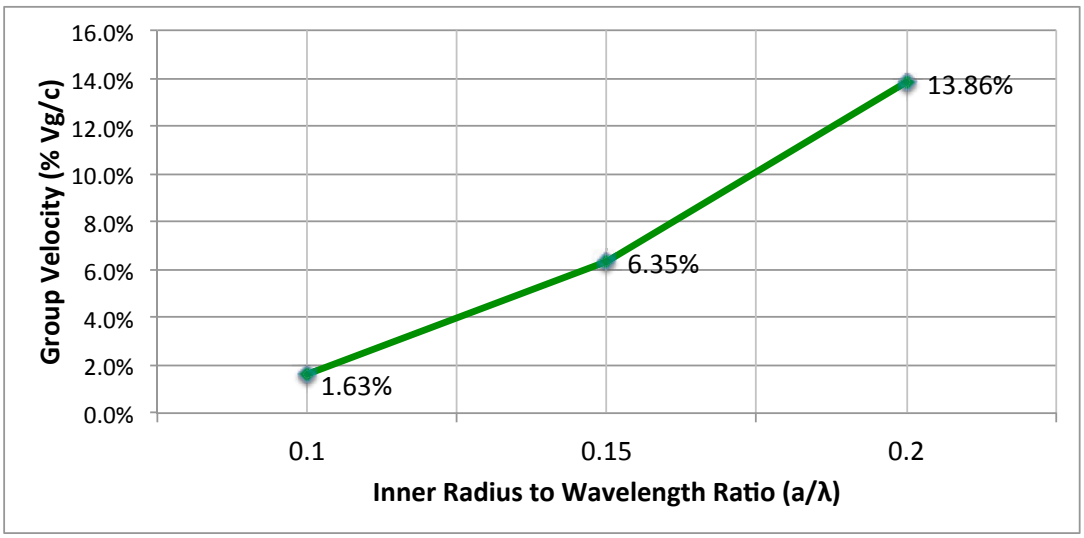

Figure 3.4 The relative velocity versus a/λ for a $2\pi/3$ phase advance

Figure 3.5 shows the cavity fields, both the electric and magnetic, as computed by SUPERFISH for both the Neumann and Dirichlet boundary conditions as specified at the end walls.

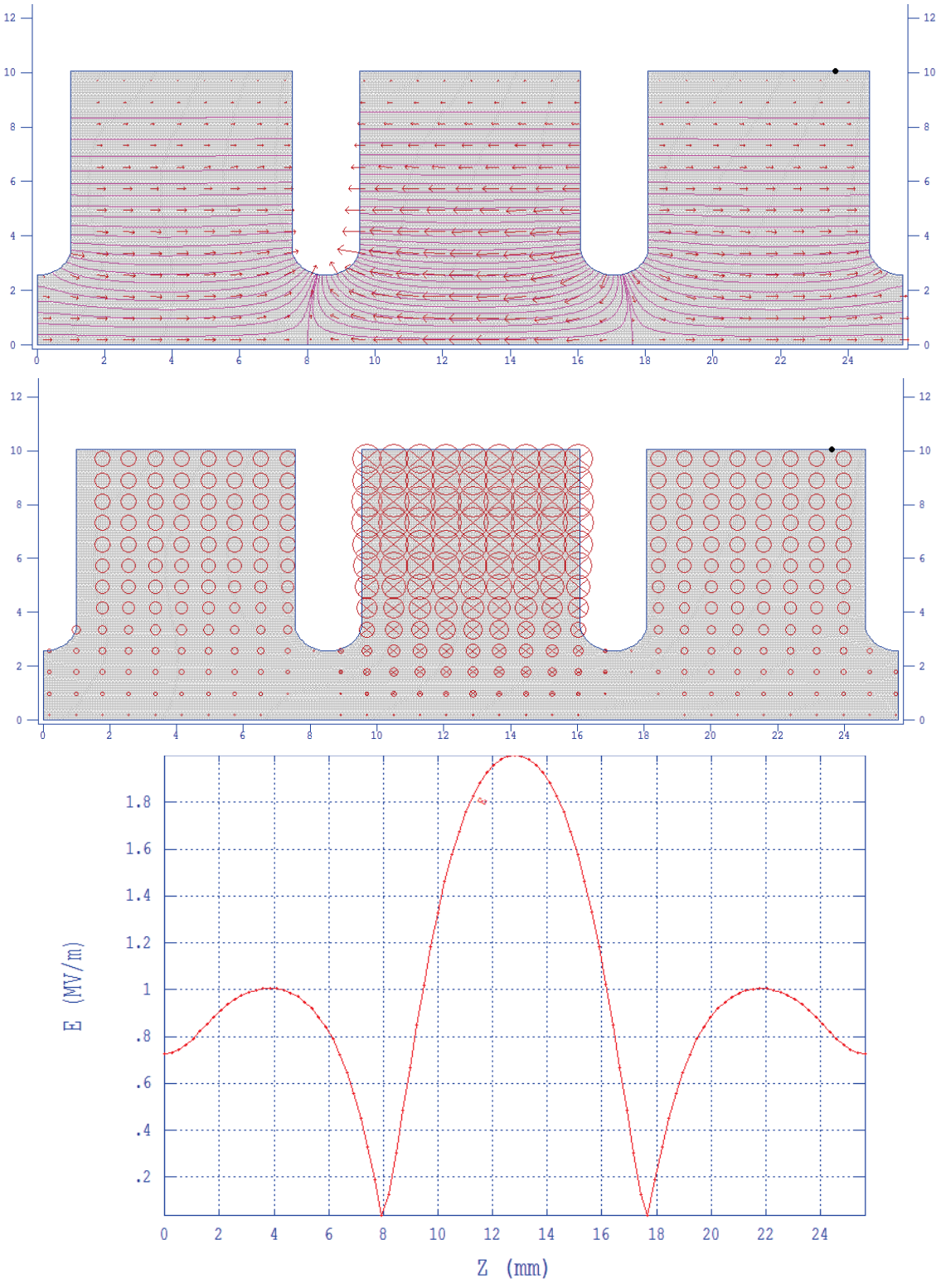

(a)

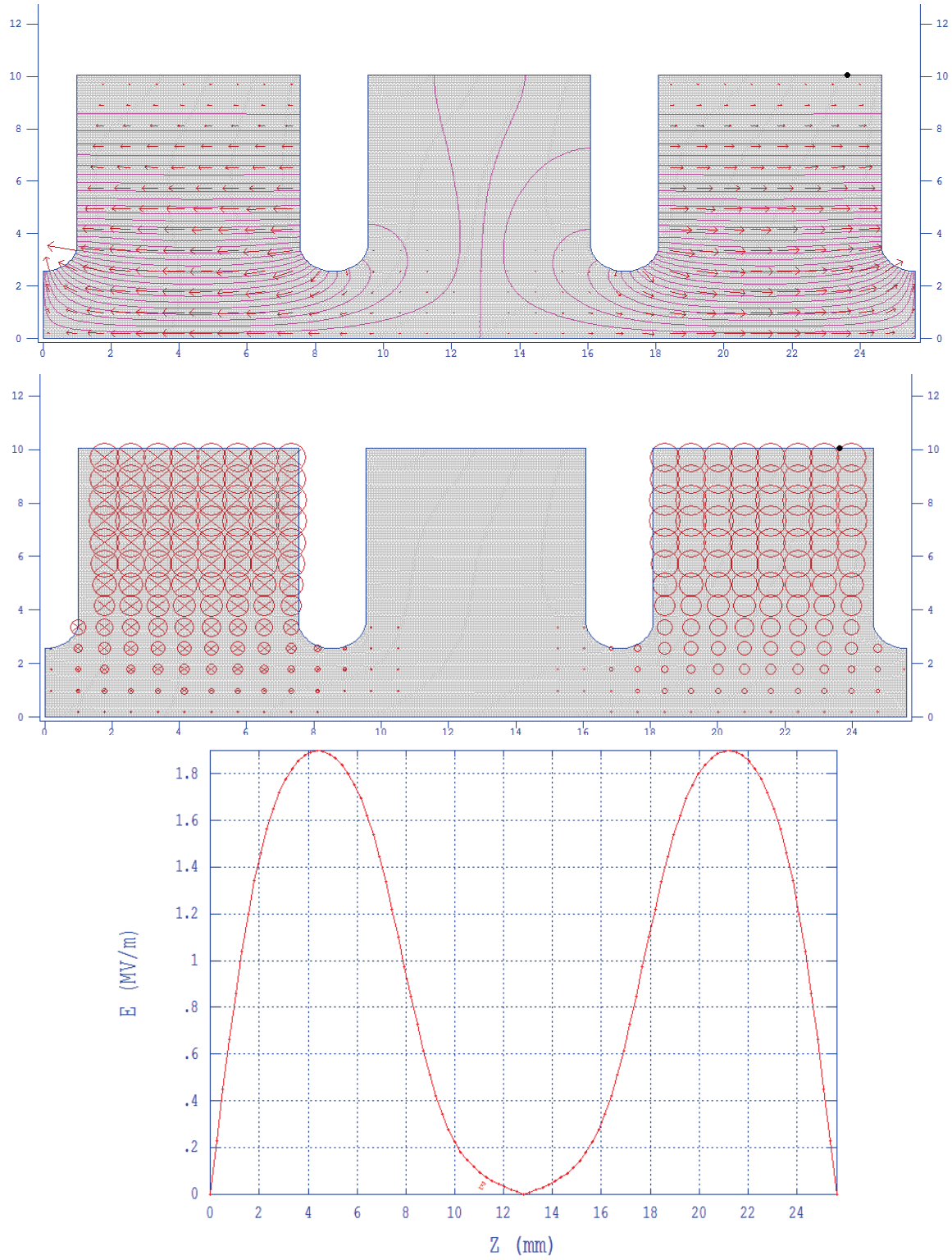

(b)

Figure 3. 5 The electric and magnetic field distributions, and magnitude of electric field for $a/\lambda = 0.10$ TW PEC in (a) the Neumann boundary condition at end walls for $2\pi/3$ mode (b) and the Dirichlet boundary condition at end walls for the $2\pi/3$ mode

The final choices of parameters for our proposed PEC, as computed by the design code SUPERFISH, are given in Table 3.2.

Table 3. 2 The parameters for the Power Extraction Cavity (PEC)

Parameter	Symbol	Value
Resonance Frequency [GHz]	f_0	11.7
Phase Advance per Cell [Radian]	ψ	$2\pi/3$
Iris radius to Wavelength Ratio	a/λ	0.10
Iris Radius [m]	a	0.00256
Disk Thickness [m]	h	0.002
Cell Radius [m]	R	0.01006
Unloaded Quality Factor	Q_0	6456.1
Shunt Impedance per Unit Length [MΩ/m]	r_{sh}	110.3
Group Velocity [m/s]	ϑ_g	1.63c

3.1.3. TW Main Accelerator Cavity (MAC) Design

Originally, it was chosen to use a 5π/6-mode TW main accelerating cavity (MAC) design which is given at Appendix D in detail. Even though the 5π/6-mode MAC can provide a better performance, a 2π/3-mode TW MAC design which is the same design as PEC but with a different length and couplers on both ends was chosen to avoid the expense of the overall higher system cost.

3.2. Optimization Results

In this section, the optimization studies were performed to achieve the maximum gradient in the system in an efficient way.

3.2.1. L-Band Photocathode RF Gun and Drive Laser Considerations

The L-band (1.3 GHz) photocathode RF gun is powered by a 20-MW klystron (Thomson TV2022) capable of providing full power for 10 μs. The resistive losses at 6 megavolt (MV) are 1.8 MW; therefore, there is an abundance of power for the beam. At full potential the on-axis longitudinal field at the cathode is 26 MV/m. Here it is assumed the use of a high quantum efficiency cathode (1%) and the maximum current density will be limited to $10\ \mathrm{A/mm^2}$. The cathode radius will also be limited to 2 mm. This should allow us, via use of proper focusing through a reasonably short PEC, to avoid inadvertent beam losses.

The drive laser will be assumed to provide a transverse top-hat distribution with a 2-mm radius and Gaussian distribution in the longitudinal direction. The laser power is adjusted to generate a peak current density of 10 A/mm^2 and the bunch length, and therefore total charge per bunch, is adjusted to maximize the overall X-band power. The pulse frequency of the laser system is set at 81.25 MHz, the 16th sub-harmonic of 1.3 GHz and the 144th sub-harmonic of 11.7 GHz.

3.2.2. Optimization Results for PEC

The output power in Equation 2.11 was maximized by varying the laser pulse length and the PEC length while constraining the mean voltage $\langle V \rangle$ to 5 MV, ensuring that N_{fill} is equal to or larger than 10, and that the maximum charge per bunch is less than 7.4 nC. 5 MV was chosen so that upon passage of the PEC the originally 6-MeV electron beam would be at 1 MeV and therefore allow us to maintain adequate control of the spent beam. The 7.4 nC comes from a

calculation of the current required to achieve a fully matched condition between the klystron, waveguide and cavity system.

Tables 3.3 and 3.4 provide some of the primary numbers and outputs of the optimization. Our optimization shows that for this simple case 1.13 MW X-band RF power can be generated from a 233-mA beam (average current during the 10 μs L-band RF pulse) passing through a 61.2-cm X-band TW PEC.

The cavity length was varied during the optimization to achieve the maximum power output subject to the constraint that at least 10 bunches participated in the power build-up in the cavity. This ensures that the N_{fill} condition is at least roughly met.

Table 3.3 Calculated values for the PEC

Parameter	Symbol	Value
Cavity Length [m]	L	0.612
Ohmic Reduction	η_Ω	0.97
Form Factor	F	0.96
Field at the end of PEC [MV/m]	E_b	17
PEC Power Available [MW]	P	1.13
Peak Voltage seen by the Bunch [MV]	$\hat{V}$	5.2
Average Voltage seen by the Bunch [MV]	$\langle V \rangle$	5
Number of Contributed Bunches	N_{fill}	10

Table 3. 4 The optimized parameters for the photocathode gun and drive laser system

Parameter	Symbol	Value
Charge per Bunch [nC]	q	2.86
Current during L-band Pulse [mA]	I	233
Laser Frequency [MHz]	f_{laser}	81.25
RF Repetition Rate [Hz]	R_{RF}	10
L-band RF pulse Length [μs]	T_{pulse}	10
Duty Factor	D	10^{-4}
Bunch Duration (FWHM) [ps]	t_{bunch}	9.1

The power generated, 1.13 MW, is significantly less than the ~18 MW potentially available. The limitation is due to the choice of laser system. It is limited to 81.25 MHz. This is the 16th sub-harmonic of the 1.3 GHz L-band system. If there were a way to provide an identical set of conditions, but at the full 1.3 GHz, then the power generated at X-band would be roughly 1.13 MW x 16 = 18 MW. This clearly shows the potential of such a co-linear configuration to convert the power at one frequency to the power at another more favorable frequency that is suitable for accelerating beams.

3.2.3. MAC Length Optimization

In a constant impedance structure, the field drops as a function of length due to ohmic losses. In order to maximize the energy gain in a given length *L,* the condition should be met according to Equation 3.2 or 3.3 which is discussed in detail and given by Equation B.107 or B.108 in Appendix B.

$$t_f \cong 2.52\frac{Q}{\omega} \tag{3.2}$$

$$L = 2.52 \frac{Q \vartheta_g}{\omega} \tag{3.3}$$

Using these equations and the parameters given in Table 3.2, the optimum length of a single MAC structure was calculated as 1.08 m.

3.2.4. Maximum Achievable Gradient

The simplest configuration would be to immediately transport the power via waveguide from the PEC coupler to a single $2\pi/3$ mode 1.08-m long MAC structure. Assuming for the time being that there are no ohmic losses in the waveguide or losses due to imperfect coupler matching, the full 1.13 MW would be available to drive the 110.3*1.08 = 119 MΩ load of the single structure $2\pi/3$ mode MAC. This in turn would produce an 11.6 MV potential across the structure. It can thus be seen that the merits of the slightly more complicated configuration when compared to the single SW structure arrangement. The SW case would allow us to boost our 6 MeV beam up to 6 MeV + 5 MeV = 11 MeV. In the simplest TW configuration shown in Figure 2.8 maximum energy gain is 6 MeV + 5 MeV + 11.6 MeV = 21.6 MeV, a significant gain over the on-resonance SW configuration.

Performance of the system can be enhanced even further, but at the expense of more complexity. Figure 3.6 (a) and (b) show two additional configurations. In case (a) the power is divided by two and feeds two separate MAC structures, while in (b) the power is divided by four and feeds four MAC structures. These configurations are predicated on the fact that the net accelerating potential increases for a given power available as the square root of the net shunt impedance, thus if there were no power loss in the waveguide system, the four-structure configuration would

result in a net potential across all MACs of 2*11.6 = 23.2 MeV. Unfortunately there are losses in the waveguide system. A rough estimate for these losses is 0.134 dB/m. The waveguide run from the exit of the PEC to each MAC in the four-structure case is estimated to be roughly 5 m for a total of 0.67 dB in power loss, thus the effective power available from the PEC is reduced from 1.13 MW to 966 kW. This is then split four ways to power each of the four 119 MΩ structures. The potential across each is then 5.4 MV or a total of 21.6 MV across all four MAC structures. This brings the total potential across the entire system to the sum of 6 MV from the L-Band, plus 5 MV from the PEC, plus 4*5.4 = 21.6 MV for the MAC or 32.6 MV total, a boost of 5.4 over that of the 6 MV delivered by the L-band system alone. Table 3.5 provides a summary of these results.

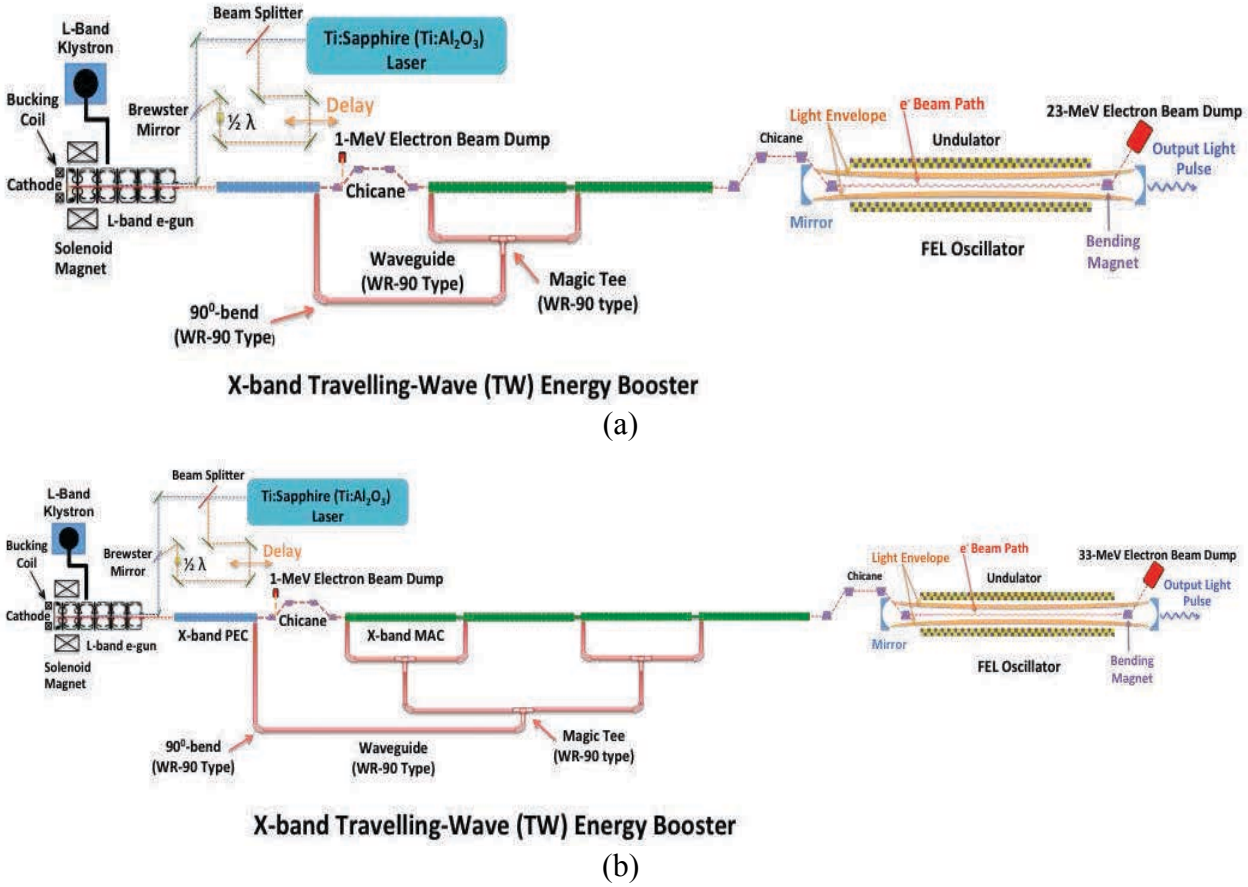

Figure 3.6 (a) The two MAC case and the (b) four MAC case for the CXEB system

Table 3.5 The available potential and the maximum energy gain values for MAC

Parameter	Symbol	Value
Number of X-band MAC Cells	-	126
Total Length per Section [m]	L	1.08
Available Gradient (1 Section) [MV/m]	E_{a_1}	20.0
Available Gradient (2 Sections) [MV/m]	E_{a_2}	14.3
Available Gradient (4 Sections) [MV/m]	E_{a_4}	10.1
Maximum Energy Gain (1 section) [MeV]	W_{max_1}	21.6
Maximum Energy Gain (2 sections)* [MeV]	W_{max_2}	23.1
Maximum Energy Gain (4 sections)* [MeV]	W_{max_3}	32.6

*Includes waveguide power losses

4. ADVANCED FREQUENCY AND TIME DOMAIN SIMULATIONS USING ACE3P SUITE

For more refined results, 3-dimenional (3D) frequency and time domain simulations were performed using the high-performance parallel computing capabilities of the National Energy Research Scientific Computing Center (NERSC) [45] together with the SLAC National Accelerator Laboratory's Advanced Computational Electromagnetics Code Suite ACE3P (Advanced Computational Electromagnetics 3D Parallel) [46-49, Appendix C]. The 3D computer-aided design (CAD) and post-processing were done using the Trelis [50] and Paraview [51] software, respectively. Detailed information about the computer capabilities used at NERSC and the ACE3P code are given in Appendix D. In this chapter more realistic simulations were performed for both the PEC and MAC, and 3D designs for the various other ancillary RF system parts in frequency domain [52] while following the related references [53-56, ibid, 33, 34]. The related theoretical descriptions are given at Appendix B in detail. Furthermore, the field build up in the PEC was simulated in time domain [57] and then compared the results were found in Chapters 2 and 3.

4.1. Frequency Domain (FD) X-band TW PEC and MAC Designs Using OMEGA3P

Some important parameters for our X-band PEC are simulated using OMEGA3P [58], the eigen-frequency solver of the ACE3P Suite. The phase advance per cell, which is $2\pi/3$ for X-band PEC and MAC, applies to single cell travelling-wave structures using periodic boundary conditions (PBC) at both end of each structure.

4.1.1. X-Band TW PEC and MAC Design Using Periodic Boundary Conditions (PBC) in OMEGA3P

Our simulations studies was started to evaluate how different symmetry conditions effects the PEC and MAC parameters and because we would like to increase our central processing unit (CPU) time efficiency on the supercomputing facility. In this part of our study, while travelling wave boundary condition were applied [59] at the both ends of the half and quarter PEC single cell geometries, the mesh size was kept constant and similar to what was used for the whole cell. The parameter comparison results and the magnitude of the electric and magnetic fields for the each model of the single cell of our TW X-band PEC using OMEGA3P, eigen-frequency solver of ACE3P are given in Table 4.1 and Figure 4.1[60].

Table 4.1 Parameter comparison of TW X-band PEC single cell for different symmetries using OMEGA3P

Parameter	Symbol	Value		
Symmetry Condition		Full Model	Half Symmetry	Quarter Symmetry
Mesh Number		11591	8955	5962
Finite Element Method (FEM) Order		2	2	2
Inner radius to Wavelength Ratio	a/λ	0.2	0.2	0.2
Cell Radius [m]	R	0.0110275	0.00110275	0.0110275
Resonance Frequency [GHz]	f_0	11.69559	11.699435	11.699753
Unloaded Quality Factor	Q_0	6646.03	6649.69	6649.14

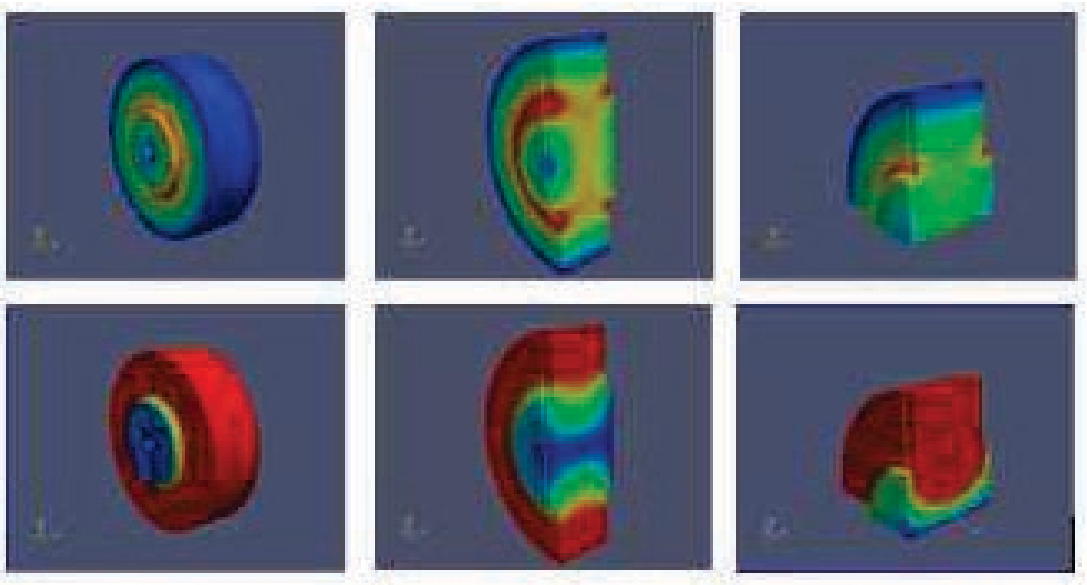

(a) (b) (c)

Figure 4.1 Magnitude of electric (a) and magnetic (b) fields of the single TW X-band PEC using OMEGA3P for different symmetries

The magnitude of the electric and magnetic fields for our single cell TW X-band PEC using OMEGA3P is shown in Figure 4.2.

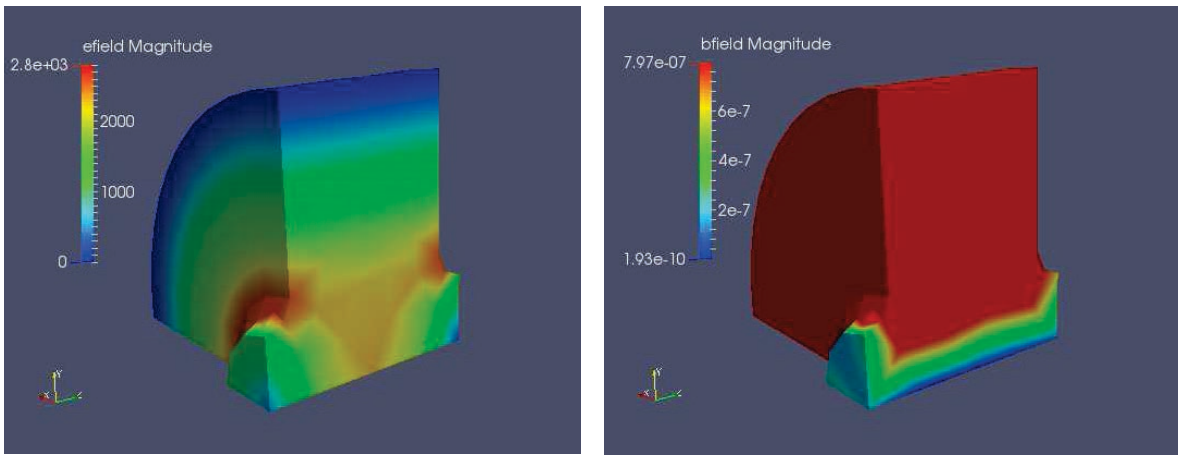

(a)

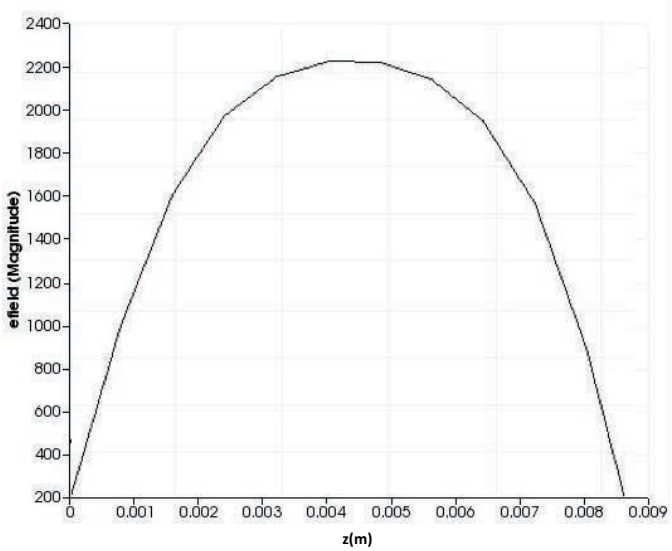

(b)

Figure 4.2 (a) The electric and magnetic field distributions, and (b) magnitude of electric field for the single cell TW X-band PEC using OMEGA3P

Some important parameter comparisons for the single cell of our TW X-band PEC using quarter symmetry in OMEGA3P and previous SUPERFISH results are given in Table 4.2 to show the accuracy of the results.

The fields calculated by OMEGA3P will later be used in a full simulation of the process.

Table 4.2 Parameters for TW X-band PEC using OMEGA3P and SUPERFISH

Parameter	Symbol	SUPERFISH	ACE3P
Resonance Frequency [GHz]	f_0	11.700176	11.699852
Phase Advance per Cell [Radian]	ψ	$2\pi/3$	$2\pi/3$
Inner Radius to Wavelength Ratio	a/λ	0.10	0.10
Unloaded Quality Factor	Q_0	6456.11	6448.53
Shunt Impedance per Unit Length [MΩ/m]	r_{sh}	110.329	110.2

4.2.1. Coupler Designs for X-band PEC and MAC Using OMEGA3P and S3P

Coupler design is an important consideration because the power transfer needs to be done as efficiently as possible from the PEC to the MAC structure. Furthermore, the coupler type must be chosen properly. Because our TW power is high (in the MW range) a waveguide type coupler was chosen that has a slot at the upper end of the last RF cell of the PEC to out couple the power from the primary mode into a standard waveguide. This is as opposed to a coaxial-based coupler that would not be able to sustain the power levels. A regular WR-90 type X-band rectangular waveguide was attached to a tapered section between the slot and waveguide [59-63]. PBC were applied on both ends of a PEC single cell and adjustments are made to achieve the desired frequency as shown in Figure 4.3.

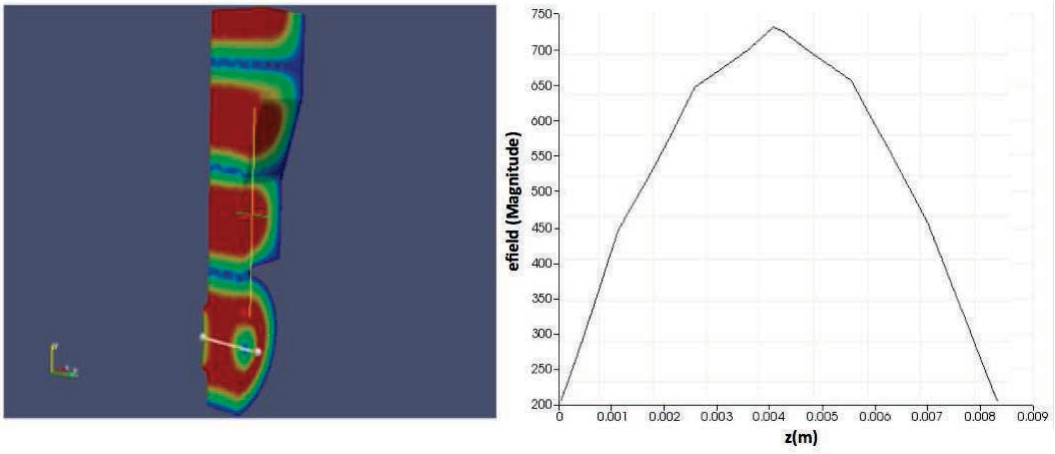

Figure 4.3 OMEGA3P result of the coupler cavity cell using PBC

To check our results the coupler design was evaluated with another technique using waveguide boundary condition (WBC) at the waveguide port end to evaluate; however, with this technique, because the WBC is broadband the neighbor cell was shortened [64-72] to reach the desired mode and frequency. This coupler again matches the TE_{10} mode of the WR-90 type waveguide

following the tapered waveguide section. The coupling constant is adjusted to provide a proper match under equilibrium conditions shown in Figure 4.4 using S3P [73].

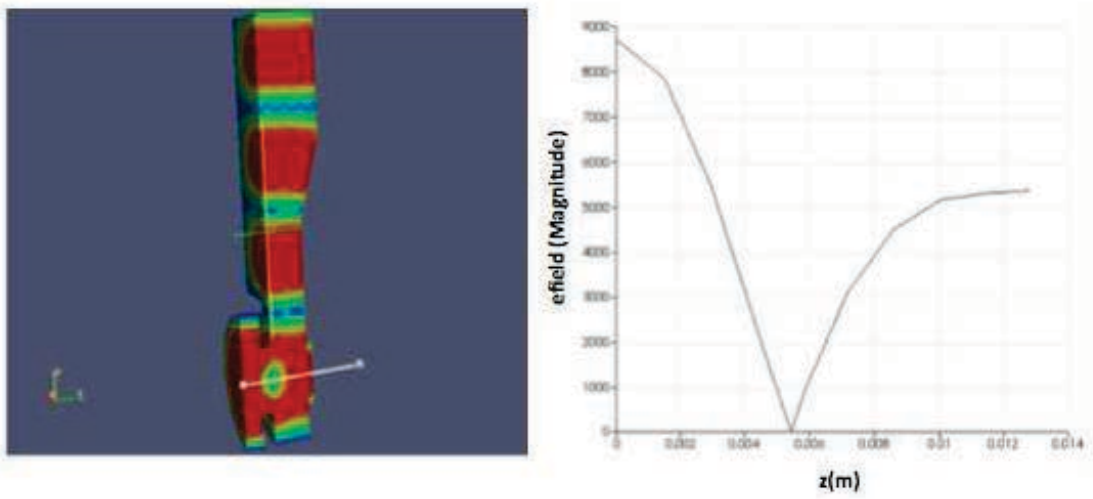

Figure 4.4 S3P result of the coupler cavity using WBC

Once adjusted correctly the coupler cavity structure was attached to 2 regular X-band PEC cells as the $2\pi/3$ phase advance per cell repeats itself every 3 cells. The attached 3-cell PEC structure is shown in Figure 4.5 following the optimization of the reflection coefficient using S3P. The plot on the right shows the absolute value of the on-axis longitudinal electric field as a function of position along the length of the structure and the $2\pi/3$ nature of the field distribution [ibid 58].

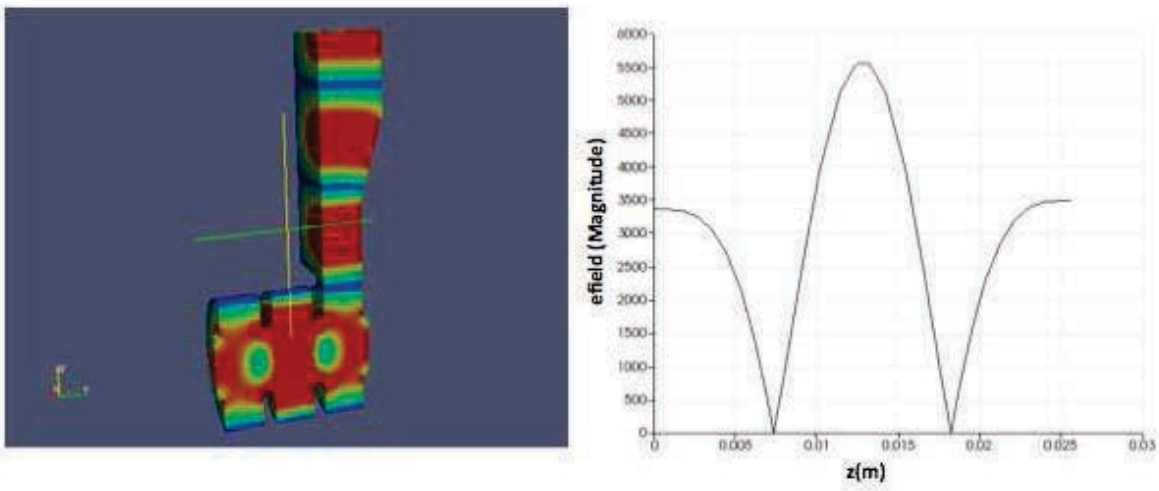

Figure 4.5 S3P result of X-band PEC and attached coupler cavity result using WBC

Finally, the coupler cavity structure was attached to the full X-band PEC and MAC structures as shown in Figures 4.6 and 4.7. As it is shown in both figures the electric field distribution are well balanced at the desired mode $(2\pi/3)$ and frequency.

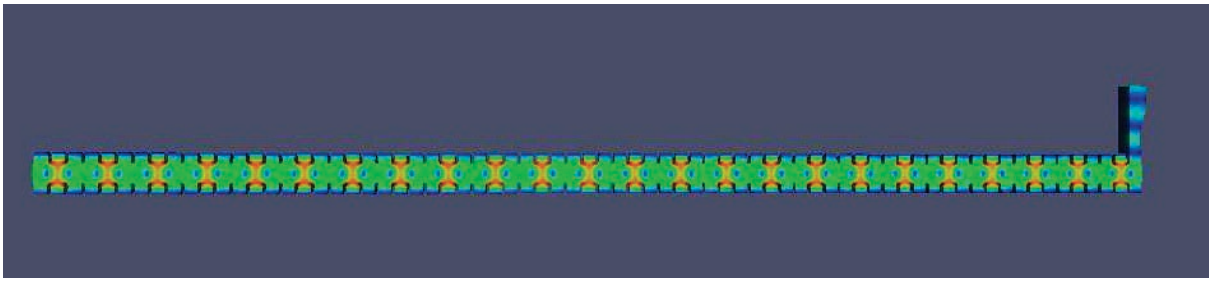

(a)

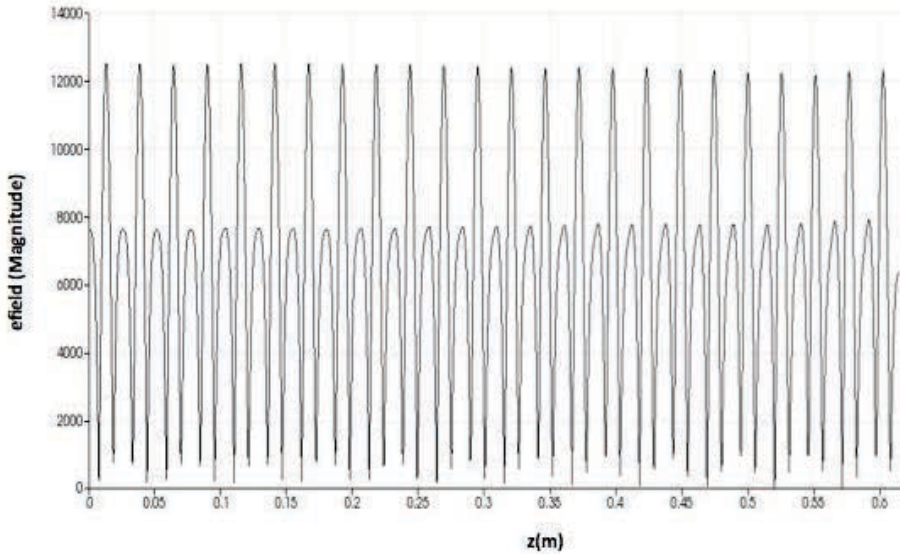

(b)

Figure 4.6 (a) The electric field distribution and (b) the electric field magnitude of 72-cell X-band PEC using WBC in S3P

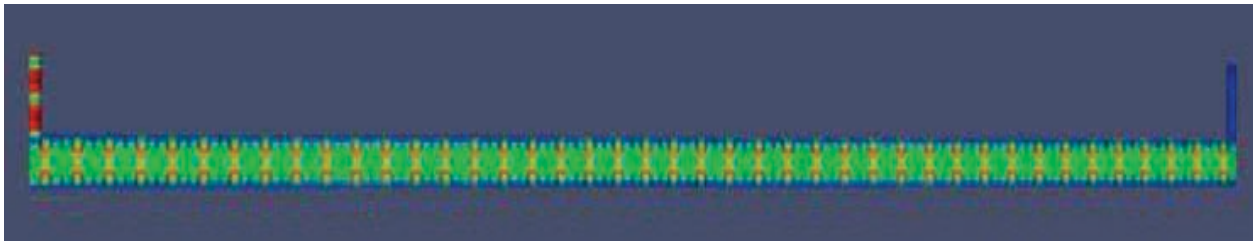

(a)

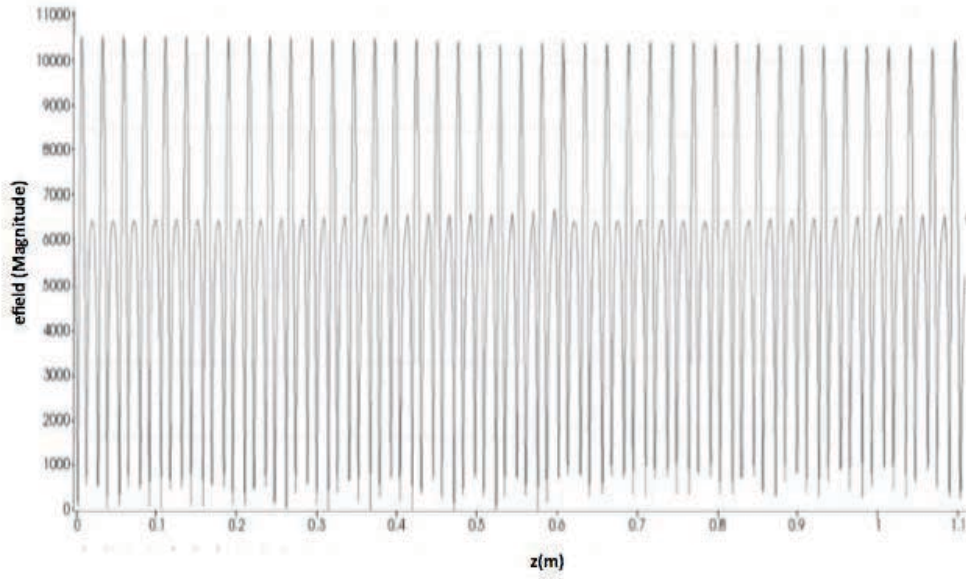

(b)

Figure 4.7 (a) The electric field distribution and (b) the electric field magnitude of 126-cell X-band MAC using WBC in S3P

4.3.1. X-band Transmission Components Simulations Using S3P

ACE3P's frequency-domain solver for evaluating scattering parameters, S3P, was again used for the simulations of WR-90 type of the passive transmission components such as the straight waveguide sections, E and H bends, magic tees, and waveguide loads that are used in the CXEB system. While all of the components are broadband, the simulation was performed at 11.7 GHz and using the TE_{10} mode within the waveguide. The electric and magnetic field distributions of each component are shown in Figures 4.8, 4.9, 4.10, 4.11, 4.12 and 4.13.

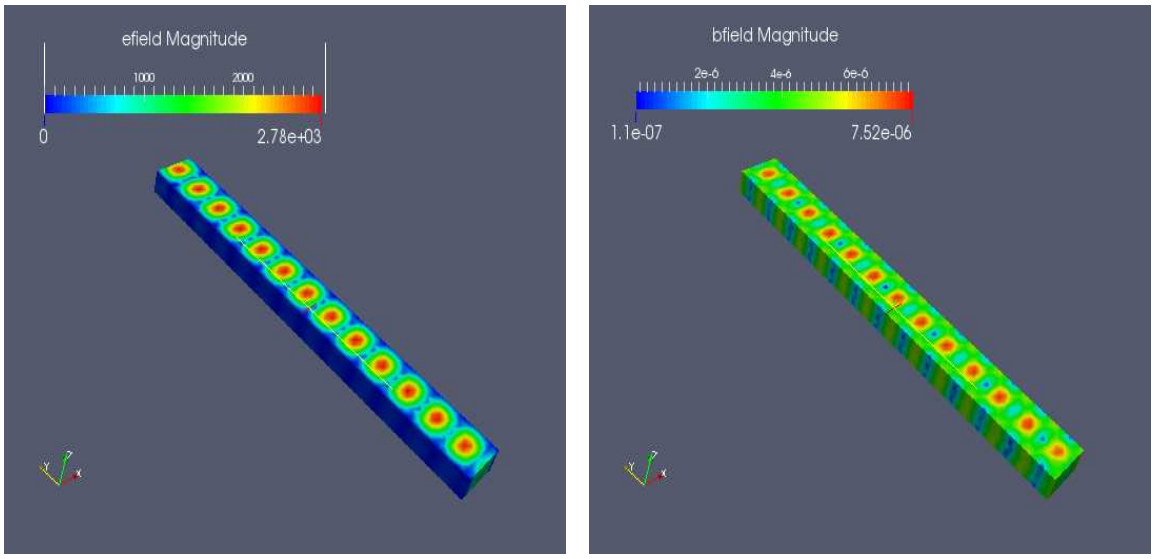

(a) (b)

Figure 4.8 (a) The electric and (b) the magnetic field magnitudes of a WR-90 straight waveguide sections at 11.7 GHz.

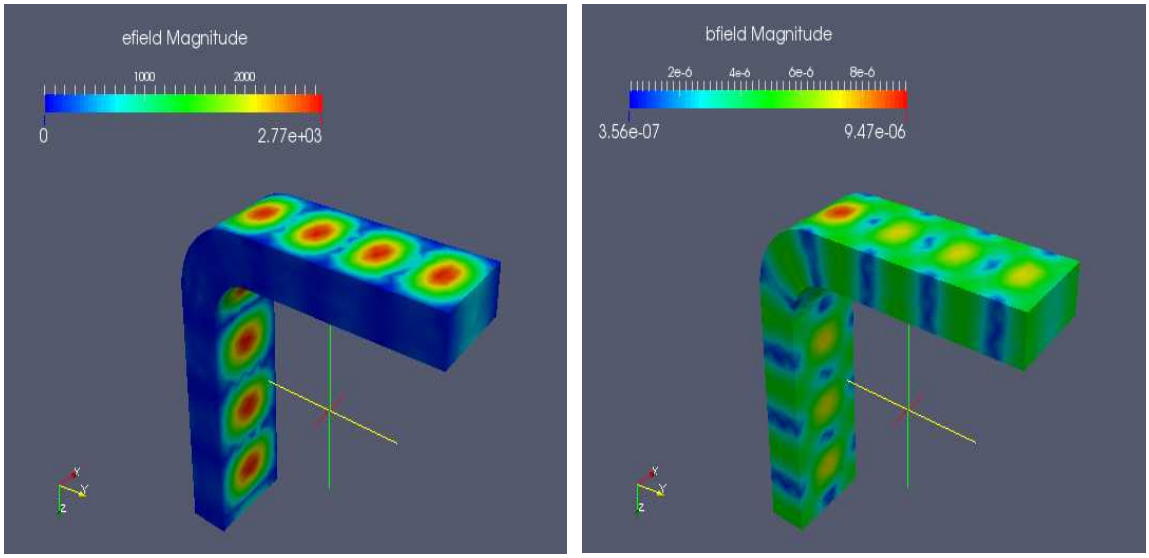

(a) (b)

Figure 4.9 (a) The electric and (b) the magnetic field magnitudes of a WR-90 E-bend at 11.7 GHz

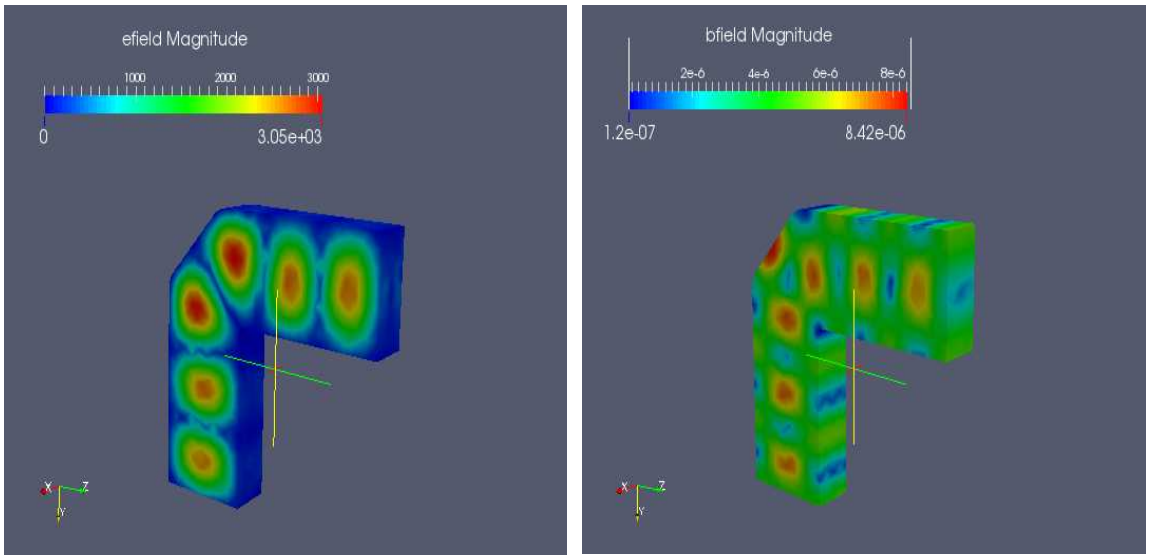

(a) (b)

Figure 4.10 (a) The electric and (b) the magnetic field magnitudes of a WR-90 H-bend at 11.7 GHz

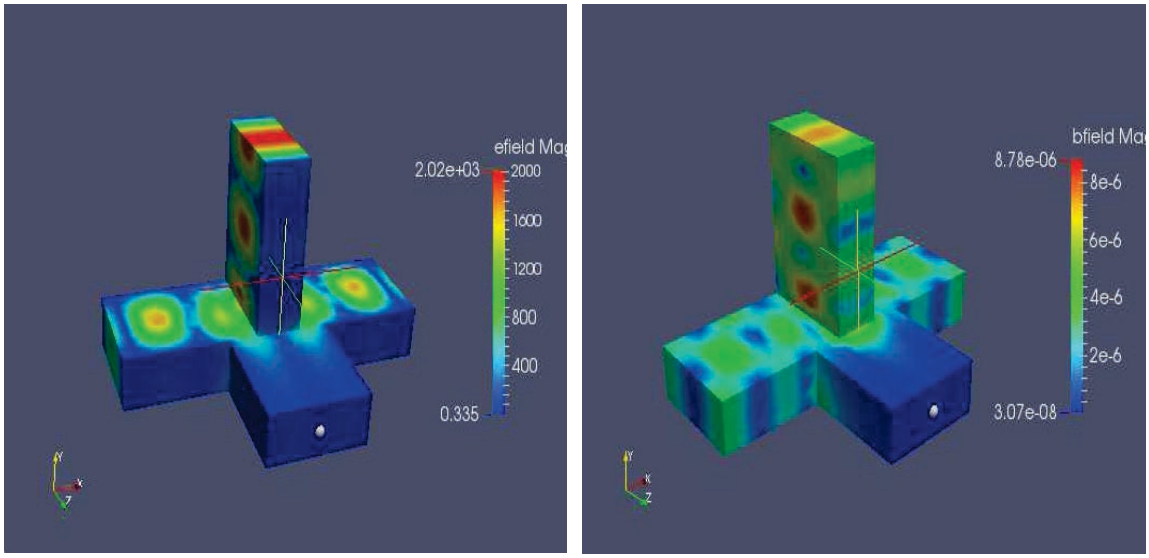

(a) (b)

Figure 4.11 (a) The electric and (b) the magnetic field magnitudes of a WR-90 Magic tee, used for horizontal power division, at 11.7 GHz

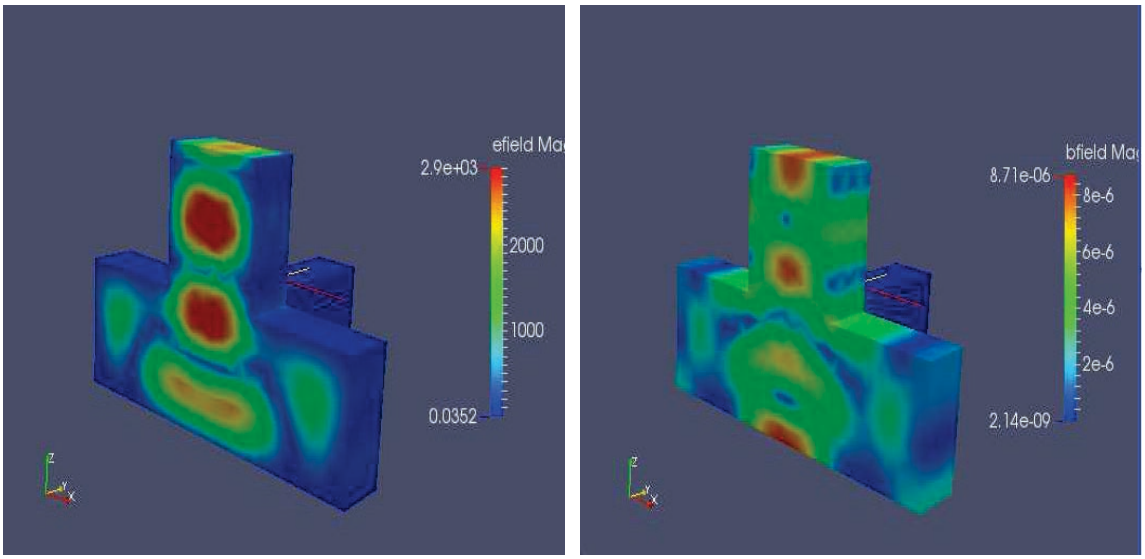

(a) (b)

Figure 4.12 (a) The electric and (b) the magnetic field magnitudes of a WR-90 Magic tee, used for vertical power division, at 11.7 GHz

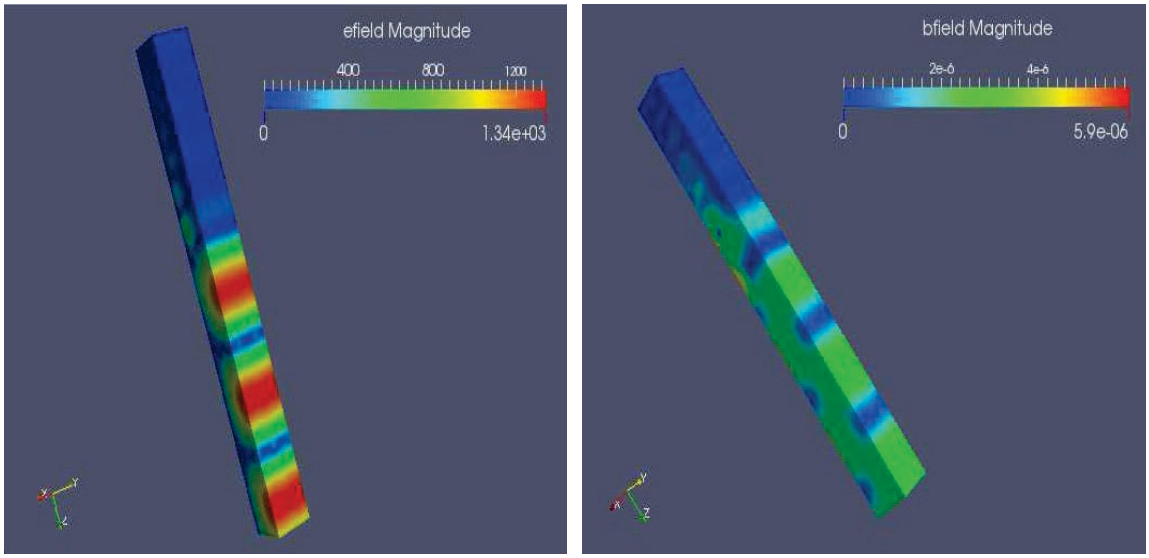

(a) (b)

Figure 4. 13 (a) The electric and (b) the magnetic field magnitudes of a WR-90 RF load for residual power absorption at the end of MAC structures at 11.7 GHz

4.2. Time-Domain (TD) Wakefield Excitation in the X-band PEC Using T3P

T3P was used for the time domain verification our calculations given above. First, the excitation of the PEC with a single bunch was observed and then continue with multiple bunches.

4.2.1. Single Bunch Excitation in X-band PEC

A symmetric Gaussian bunch distribution [74] was defined in T3P [75] using a single 2.86 nC bunch

Figures 4.14 (a) and (b), respectively, shows the wakefield excitation and impedance spectrum, of a single 2.86 nC, 1 mm long bunch that has travelled through the 72-cell X-band PEC structure. This compares favorably to Equation 2.11 and Tables 3.3 and 3.4.

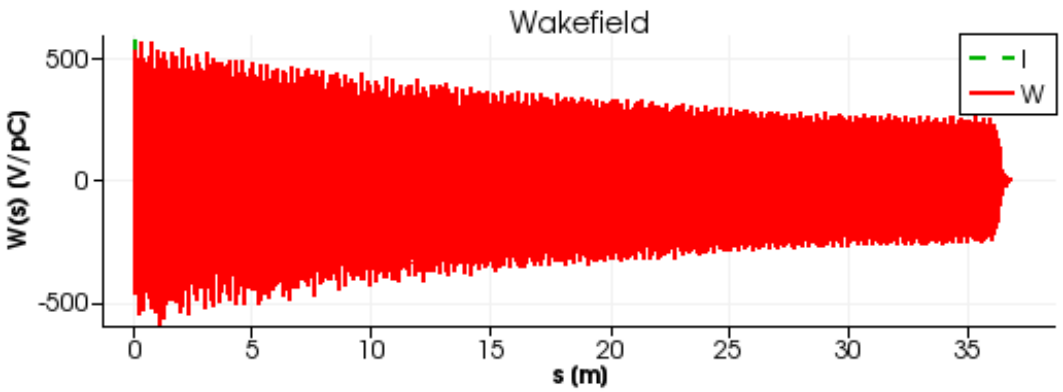

(a)

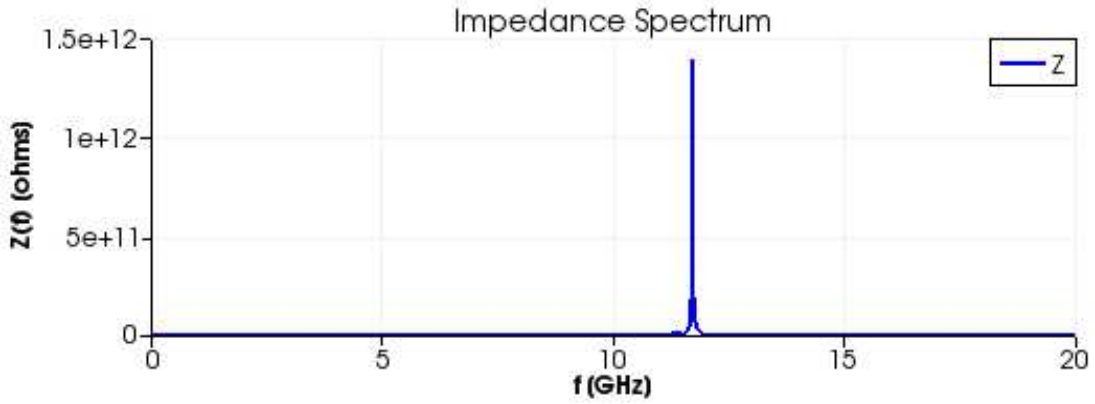

(b)

Figure 4.14 (a) Wakefield excitation of a single bunch for the length optimization of the X-band PEC (b) Impedance spectrum of the X-band PEC using a single bunch

4.2.2. Multibunch Excitation in X-band PEC

When multiple bunches pass through the PEC each spaced from one another by a multiple of RF periods the fields coherently add. To show this effect a bunch train of 20 symmetric Gaussian bunches spaced by 12.3 ns were passed through the PEC. Each bunch was set to have 2.86 nC and the following bunch lengths 4, 2 and 1 mm were simulated. As a reminder the form factor ($F(\sigma) = e^{-(k\sigma)^2/2}$) is 0.62 for the longest bunch length (4 mm) and 0.97 for the shortest one (1 mm) where, k is the wavenumber of the 11.7 GHz mode.

The electric field build-up due to the coherent wakefield excitation of the 72-cell X-band PEC for using 4, 2 and 1 mm bunch lengths and the resultant spectrums of each case are shown in Figures 4.15, 4.16 and 4.17, respectively. The related parameters and extracted X-band power results are given in Table 4.3.

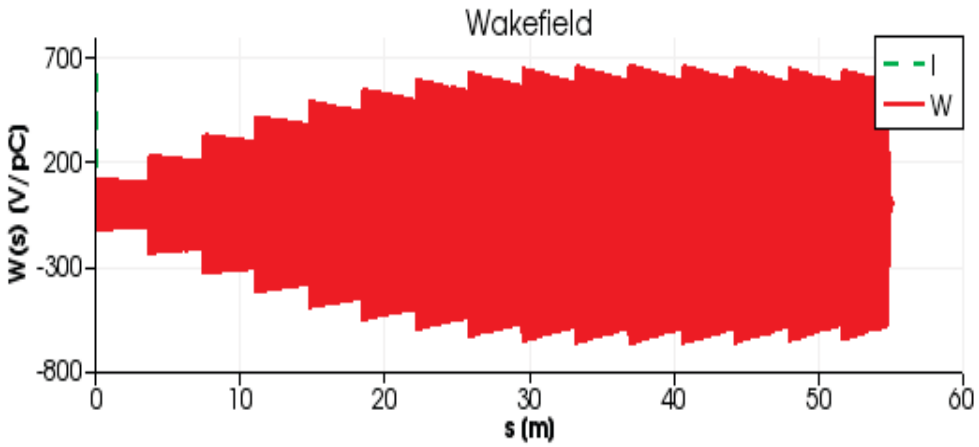

(a)

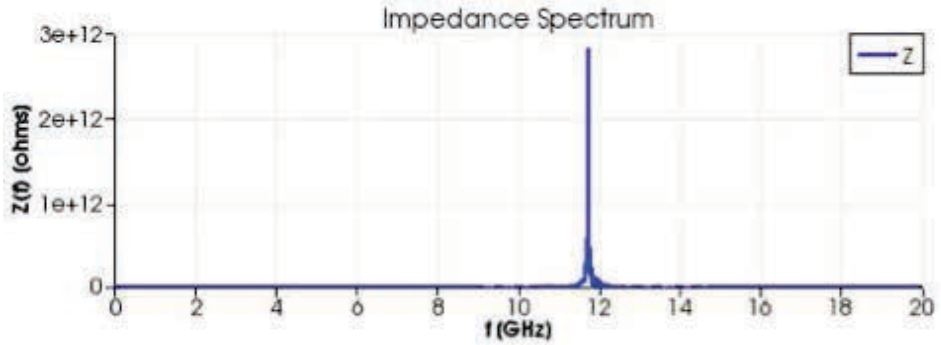

(b)

Figure 4.15 (a) Wakefield excitation of 20 Gaussian bunches with 12.3 ns bunch separation, 2.86 nC bunch charge and 4 mm bunch length in the X-band PEC (b) Impedance spectrum of the X-band PEC wakefield excitation for 20 Gaussian bunches with 12.3 ns bunch separation, 2.86 nC bunch charge and 4 mm bunch length

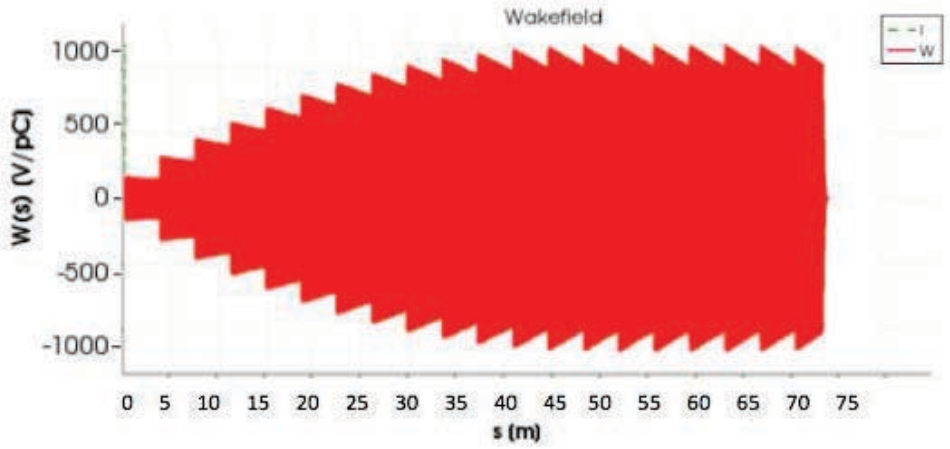

(a)

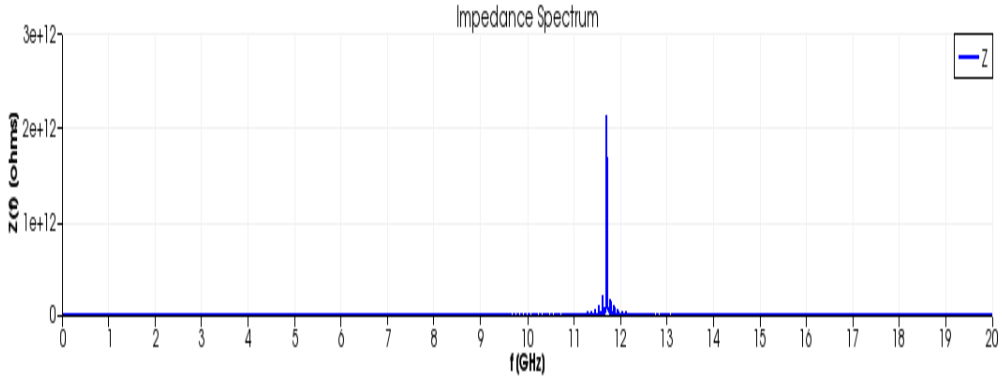

(b)

Figure 4.16 (a) Wakefield excitation of 20 Gaussian bunches with 12.3 ns bunch separation, 2.86 nC bunch charge and 2 mm bunch length in the X-Band PEC (b) Spectrum of X-band PEC wakefield excitation for 20 Gaussian bunches with 12.3 ns bunch separation, 2.86 nC bunch charge and 2 mm bunch length

Because of the consistency for achieving the steady-state condition at the 10^{th} bunch in Figure and 4.15 and 4.16, in order to keep the CPU time shorter for the 1 mm bunch length case, the simulation was performed with 8 bunches and is shown in Figure 4.17 [76].

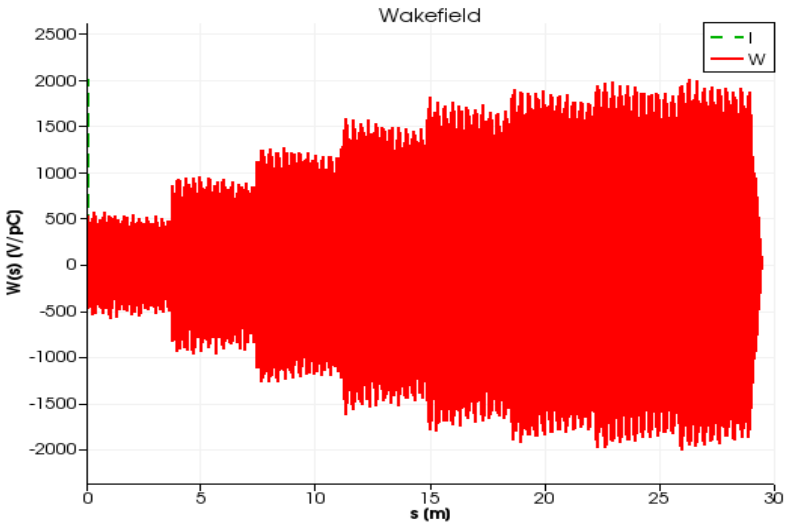

(a)

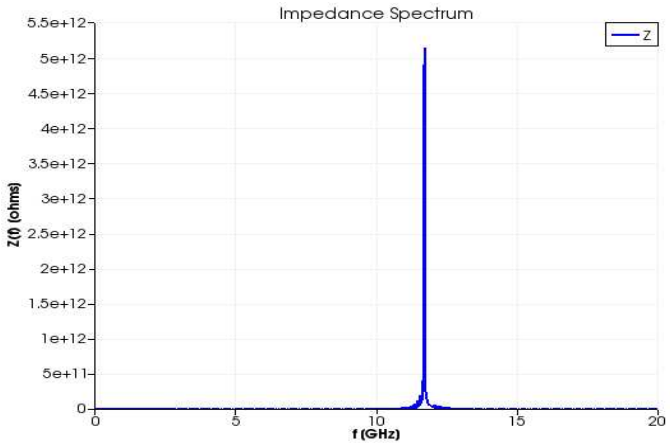

(b)

Figure 4.17 (a) Wakefield excitation of 8 Gaussian bunches with 12.3 ns bunch separation, 2.86 nC bunch charge and 1 mm bunch length (b) Spectrum of X-band PEC wakefield excitation for 20 Gaussian bunches with 12.3 ns bunch separation, 2.86 nC bunch charge and 1 mm bunch length.

If the wake potential W(s) in Figure 4.17 (a) is multiplied by the total charge 2.86 nC in the bunch then the energy loss found is the desired ~5 MeV and an output power of 1.14 MW is

achieved at the end of the X-band PEC. This result is consistent with the result we found earlier for the extracted power 1.13 MW thus providing confidence in our original calculations.

Table 4.3 Extracted X-band Power for 4, 2 and 1 mm bunch lengths in 72-cell PEC

Parameter	Symbol	Value		
Number of X-band PEC Cells		72		
Bunch Charge [nC]	q	2.86		
Bunch Separation [ns]	T_0	12.3		
Group Velocity [m/s]	ϑ_g	1.63c		
Bunch Length [mm]	σ	4	2	1
Form Factor	F	0.62	0.89	0.97
Extracted X-band Power [MW]	P_{out}	0.51	0.95	1.14

5. CSU APPLICATION FOR CXEB

In this part of the study, our novel concept was applied to a practical application, an FEL, to validate the usage of the system in real life applications.

5.1. Repetitive Bunches at Full Energy

Our drive-laser system is capable of providing a 10-μs, 81.25-MHz burst of pulses at a 10-Hz repetition rate that are suitable for extracting electron bunches off the high-quantum efficiency photocathode. A simple 5%/95% beam splitter can then be used to separate the laser into two components, one used to generate the primary drive beam and the other used to generate the beam that will be accelerated. The optical delay between the two components of the laser will be adjusted so that there is a 20-degree difference at 1.3 GHz (42.7 ps). Since the X-band system is tuned to the 9^{th} harmonic of 1.3 GHz, this difference is exactly 180 degrees at 11.7 GHz. Shining both laser beams on the photocathode simultaneously will then create a train of bunches. The train of bunches will alternate in charge with one having 19 times the amount of charge in it compared to the next bunch and with the separation of these bunches being such that both will be accelerated by the L-band system while the X-band system will decelerate the high-current beam and accelerate the low-current beam. Figure 5.1 provides a graphical representation of the laser pulse train.

Appealing to the linear nature of the fields we can consider the low-charge, low-current beam separate from the high-charge, high-current beam and consider the effects on both independently and together as they pass through the PEC. From Equation 2.7 it is seen that the fields

experienced by the beams scale linearly with the beam current. As such, and in our case, the fields generated by the high-current beam are 19 times that of the low-current beam. However, because the low-current beam is 180-degrees out of phase with the high-current beam, it experiences a net accelerating field that is dominated by the fields generated from the high-current beam.

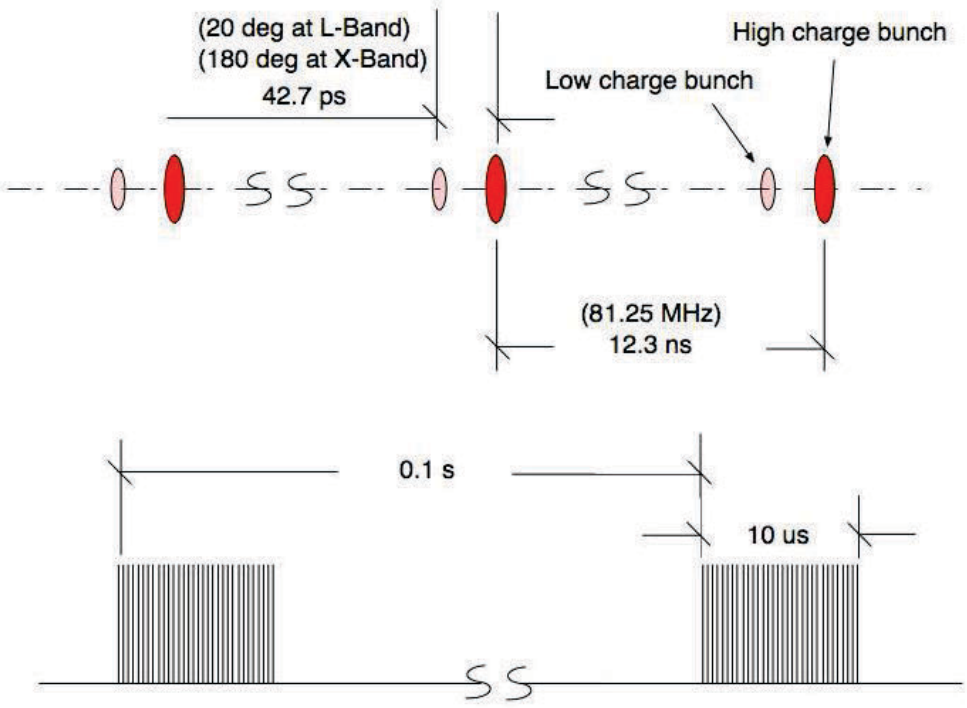

Figure 5.1 The basic timing configuration. The top shows the repetitive nature of the resulting electron bunch train with a high-charge bunch followed by a low-charge bunch while the bottom shows the 10-μs bursts occurring at a 10-Hz repetition rate.

It is also seen that the power extracted from the PEC is quadratic in the current according to Equation 2.11. Thus the power available for extraction is completely dominated by the high-current beam.

In our design example, Table 3.3, the high-current beam will lose 5 MV in passing through the PEC, but the low-current beam will gain 5 MV and therefore upon exiting the PEC will be at a beam energy of 11 MeV.

A small magnetic chicane will then be placed immediately following the PEC. The low-energy, high-current beam will then be directed to a beam dump by the fields of the first dipole in the chicane, while the low-current, 11-MeV beam will travel through the chicane and then onward to the MAC. Assuming a configuration as shown in Figure 3.6 (b) the low-current beam will be further accelerated by the MAC and reach a full energy of 32.6 MeV. It can now be used for practical applications, in our case we choose to explore its use in driving a free-electron laser oscillator at a shorter wavelength than would be achievable with the L-band accelerator alone.

5.2 One Application Example: An Infrared (IR) Free-Electron Laser (FEL)

At CSU we have a 1.25-m long undulator magnet [77] originally designed for a free-electron laser (FEL) system. The undulator has a period of $\lambda = 2.5$ cm and a normalized field strength of $K = 1.0$. An electron with a normalized, relativistic beam energy of γ passing down the length of an undulator will emit light of wavelength:

$$\lambda = \frac{\lambda_{und}}{2\gamma^2}\left(1 + \frac{K^2}{2}\right) \tag{5.1}$$

In our case, with a 32.6-MeV electron beam, the light emitted will be in the infrared (IR) at 4.6 μm.

A typical configuration for an FEL oscillator is shown in Figure 5.2. The electron bunch passes through the field of the undulator and generates a pulse of light. This pulse is then reflected back to the other mirror of the cavity. The mirrors are spaced such that the round trip time of the light matches the period between bunches therefore allowing the light to interact over and over with a fresh bunch. If the bunches are of sufficient quality then FEL gain is achieved and laser-like pulses are generated at the resonant wavelength of the system.

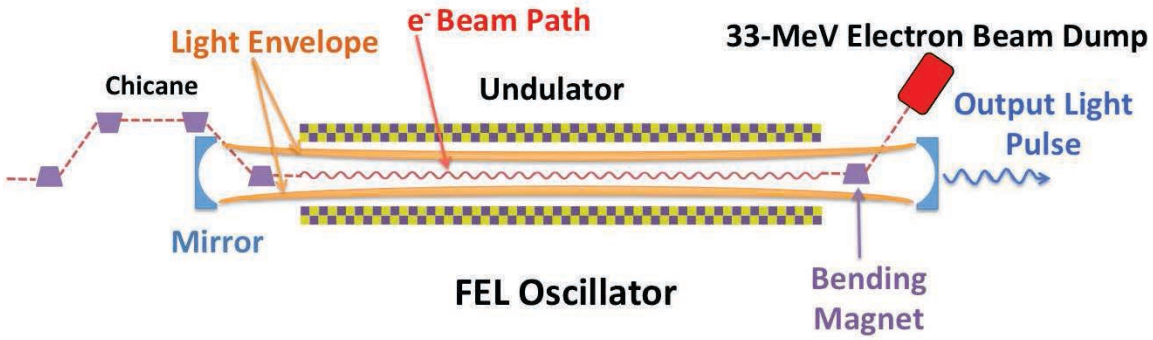

Figure 5.2 Conceptual configuration for an FEL oscillator

Figure 5.3 shows the output of a PERSEO [78] simulation of the FEL output power as a function of round trips in the FEL oscillator. For the beam conditions given in Table 5.1, saturation of the FEL process is achieved in roughly 80 round trips. The cavity length, 1.85 m, was chosen to match the 12.3-ns bunch spacing of the 32.6-MeV electron bunches coming from the MAC. This implies a time to saturate of roughly 1 μs and so provides roughly 9 μs of lasing action for the 10-μs, L-band RF pulse. The average power emitted by the FEL during the 10- μs pulse is 426 W. The 10^{-4} duty factor (D) drops this down to a time-averaged power of 42.6 mW.

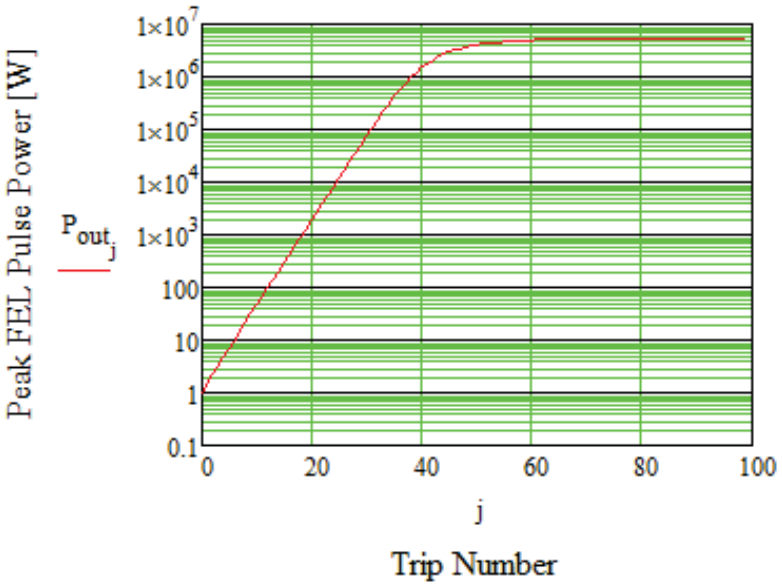

Figure 5.3 The growth of the intra-cavity FEL power as a function of round trip number

Table 5.1 FEL parameters and output

Parameter	Symbol	Value
Peak Bunch Current [A]	I_{peak}	6.3
Bunch Length (FWHM) [ps]	t_{bunch}	9.1
Bunch Energy Spread	$\Delta E/E$	1%
Normalized Emittance [μm]	ε_n	2
Beta Function in Undulator [m]	β	0.51
Duty Factor	D	10^{-4}
Cavity Output Coupler	Γ	10%
Beam Energy [MeV]	E	32.6
Output Wavelength [μm]	λ	4.6
Average Power During Burst [W]	P_{burst}	426
Time-Averaged Output Power [mW]	P	42.6

6. CONCLUSION

In this dissertation, the novel co-linear X-band energy booster (CXEB) configuration explored. Our system converts power from a readily available L-band power amplifier into power at X-band. This power is then used to drive X-band structures that have high shunt impedance in a manner that could conceivably shorten the effective length of an accelerator and thus reduce overall costs.

Our novel concept then was applied to a practical application, an FEL design in the IR wavelength region, to validate the usage of the system in real life applications.

In addition, our concept can also be well used to convert high power at X-band to power at much higher frequencies (~100 GHz) at W-band or (~200 GHz) at G-band. This power can then be used as a source for accelerating structures that have extremely high shunt impedance per unit length ($> 350\ \mathrm{M\Omega/m}$) implying that very high gradients could be achieved (~150 MV/m). Such systems can be used to design very high-energy particle accelerators in a compact manner. Our calculations and simulations are also applicable to the facilities (CLIC, AWA and FACET) in the related laboratories (CERN, ANL and SLAC, respectively) that are mention previously to further increase their capabilities.

In conclusion, a promising, compact, efficient and cost-effective particle accelerator concept that can be used for a variety of purposes such as driving an oscillator FEL was designed. The theory and simulations of the complete system including the power generation in the time domain were

provided. These full 3D, realistic simulations benefited from the use of SLAC's ACE3P simulation suite running on the high power parallel computing capabilities of the NERSC.

Ultimately it is our hope that the CXEB concept can be used to yield a new generation of robust and compact accelerator designs that are suitable for a myriad of applications such as in industry, public health, imaging and environmental research while not only saving overall costs but also the system performance.

REFERENCES

[1] Aicheler, M., Burrows, P., Draper, M., Garvey, T., Lebrun, P., Peach, K., Phinney, N., Schmickler, H., Schulte, D. and Toge, N., 2012. *A Multi-TeV linear collider based on CLIC technology: CLIC Conceptual Design Report*(pp. 2012-1). Geneva, Switzerland: CERN.

[2] Stohr, J., 2011. Linac Coherent Light Source II (LCLS-II) Conceptual Design Report (No. SLAC-R-978). SLAC National Accelerator Laboratory (SLAC).

[3] Bini, S., Chimenti, V., Marcelli, A., Palumbo, L., Spataro, B., Dolgashev, V.A., Tantawi, S., Yeremian, A.D., Higashi, Y., Grimaldi, M.G. and Romano, L., 2012. Development of X-band accelerating structures for high gradients.*Chinese physics C*, *36*(7), p.639.

[4] Higo, T., Higashi, Y., Matsumoto, S., Yokoyama, K., Doebert, S., Grudiev, A., Riddone, G., Wuensch, W., Zennaro, R., Adolphsen, C. and Dolgashev, V., 2010. Advances in X-band TW Accelerator Structures Operating in the 100 MV/m Regime. *THPEA013, IPAC10, Kyoto*.

[5] Alesini, D., Gallo, A., Spataro, B., Marinelli, A. and Palumbo, L., 2007. Design of couplers for traveling wave RF structures using 3D electromagnetic codes in the frequency domain. *Nuclear Instruments and Methods in Physics Research Section A: Accelerators, Spectrometers, Detectors and Associated Equipment*, *580*(3), pp.1176-1183.

[6] Wang, J.W., Lewandowski, J.R., Van Pelt, J.W., Yoneda, C., Riddone, G., Gudkov, D., Higo, T. and Takatomi, T., 2010, May. Fabrication technologies of the high gradient accelerator structures at 100MV/m range. In *this conference, IPAC10, THPEA064, Kyoto, Japan*.

[7] Wang, J.W., Adolphsen, C., Bowden, G.B., Burke, D.L., Cornuelle, J., Dolgashev, V.A., Fowkes, W.B., Jobe, R.K., Jones, R.M., Ko, K. and Kroll, N., 2000. Design, Fabrication and Measurement of the First Rounded Damped Detuned Accelerator Structure (RDDS1). *arXiv preprint physics/0009025*.

[8] Mirapeix, F., Castillo, J., Ortiz, A., Añel, J., Urzainki, A., Aldalur, X. and Amores, J., 2011. STATUS OF THE MANUFACTURING OF ACCELERATING STRUCTURES FOR LINACS.

[9] Wilson, I. "The compact linear collider CLIC." *Physics Reports* 403 (2004): 365-378.

[10] Rosenzweig, J. B. "Particle Wake-field Accelerators." In *Proc. Linear Accelerator Conf*, p. 835. 1992.

[11] Litos, M., E. Adli, W. An, C. I. Clarke, C. E. Clayton, Sébastien Corde, J. P. Delahaye et al. "High-efficiency acceleration of an electron beam in a plasma wakefield accelerator." *Nature* 515, no. 7525 (2014): 92-95.

[12] Wootton, K. P., J. McNeur, and K. J. Leedle. "Dielectric laser accelerators: designs, experiments, and applications." *Reviews of Accelerator Science and Technology* 9 (2016): 105-126.

[13] Compact Linear collider (CLIC) website: http://clic-study.web.cern.ch/

[14] Cappelletti, A., Dolgashev, V., Lewandoski, J., Tantawi, S., Weathersby, S. and Zelinski, J., 2011. Demonstration of the high RF power production feasibility in the CLIC power extraction and transfer structure [PETS]. *Nuclear Instruments and Methods in Physics Research Section A: Accelerators, Spectrometers, Detectors and Associated Equipment*, *657*(1), pp.78-81.

[15] Argonne Wakefield Accelerator (AWA) Facility website: https://www.anl.gov/hep/group/argonne-wakefield-accelerator-facility

[16] Gao, F., M. E. Conde, W. Gai, C. Jing, R. Konecny, W. Liu, J. G. Power, T. Wong, and Z. Yusof. "Design and testing of a 7.8 GHz power extractor using a cylindrical dielectric-loaded waveguide." *Physical Review Special Topics-Accelerators and Beams* 11, no. 4 (2008): 041301.

[17] Hogan, M. J., T. O. Raubenheimer, A. Seryi, P. Muggli, T. Katsouleas, C. Huang, W. Lu et al. "Plasma wakefield acceleration experiments at FACET." *New Journal of Physics* 12, no. 5 (2010): 055030.

[18] Amann, J., and K. Bane. *Facility for Advanced Accelerator Experimental Tests at SLAC (FACET) Conceptual Design Report*. No. SLAC-R-930. Stanford Linear Accelerator Center (SLAC), 2009.

[19] Caldwell, A., K. Lotov, P. Muggli, E. Gschwendtner, and M. Wing. *AWAKE design report: a proton-driven plasma wakefield acceleration experiment at CERN*. No. CERN-SPSC-2013-013. 2013.

[20] Gschwendtner, Edda, Erik Adli, L. Amorim, Robert Apsimon, Ralph Assmann, A-M. Bachmann, Fabian Batsch et al. "AWAKE, the advanced proton driven plasma wakefield acceleration experiment at CERN." *Nuclear Instruments and Methods in Physics Research Section A: Accelerators, Spectrometers, Detectors and Associated Equipment* 829 (2016): 76-82.

[21] Leemans, W. P., P. Volfbeyn, K. Z. Guo, S. Chattopadhyay, C. B. Schroeder, B. A. Shadwick, P. B. Lee, J. S. Wurtele, and E. Esarey. "Laser-driven plasma-based accelerators: Wakefield excitation, channel guiding, and laser triggered particle injection." *Physics of Plasmas* 5, no. 5 (1998): 1615-1623.

[22] Geddes, C. G. R., Cs Toth, J. Van Tilborg, E. Esarey, C. B. Schroeder, D. Bruhwiler, C. Nieter, J. Cary, and W. P. Leemans. "High-quality electron beams from a laser wakefield accelerator using plasma-channel guiding." *Nature* 431, no. 7008 (2004): 538-541.

[23] Esarey, Eric, Phillip Sprangle, Jonathan Krall, and Antonio Ting. "Overview of plasma-based accelerator concepts." *IEEE Transactions on Plasma Science* 24, no. 2 (1996): 252-288.

[24] Hooker, Simon Martin. "Developments in laser-driven plasma accelerators." *Nature Photonics* 7, no. 10 (2013): 775-782.

[25] Milton, S., Biedron S., Burleson, C. Carrico, J. Edelen, C. Hall, K. Horovitz, A. Morin, L. Rand, N. Sipahi, T. Sipahi, P.J.M. van der Slot, A. Dong, H. Yehudah. The CSU Accelerator and FEL Facility. 34th International Free Electron Laser Conference (FEL 2012), Nara, Japan, Aug. 26-31, 2012, pp. 373-376. JACOW, Geneva, Switzerland, 2012.

[26] Milton, S., Biedron S., Harris, J., Martinez, J., D'Audney, A., Edelen J., Hall C., Horovitz K., Morin A., Rand L., Sipahi N., Sipahi, T., Williams, J., Medicine Bear, S., Carrico, C., Moin, N., Van Keuren, J., van der Slot, P.J.M., Bos, A., Dong, A., Kang, L., Kenny, K., Smith. J. Status of the CSU

Accelerator and FEL Facility. Directed Energy Professional Society (DEPS) Fourth Annual Advanced High-Power Lasers Meeting Proceedings, Santa Fe, New Mexico, USA, June 24-27, 2013.

[27] Ernst, G.J., Witteman, W.J., Verschuur, J.W.J., Haselhoff, E.H., Mols, R.F.X.A.M., Bouman, A.F.M., Botman, J.I.M., Hagedoorn, H.L., Delhez, J.L. and Kleeven, W.J.G.M., 1992. Status of the "TEU-FEL" project. *Nuclear Instruments and Methods in Physics Research Section A: Accelerators, Spectrometers, Detectors and Associated Equipment*, *318*(1), pp.173-177.

[28] Ernst, G.J., Witteman, W.J., Verschuur, J.W.J., Mols, R.F.X.A.M., Oerle, B.V., Bouman, A.F.M., Botman, J.I.M., Hagedoorn, H.L., Delhez, J.L. and Kleeven, W.J.G.M., 1995. The" TEU-FEL" project. *Infrared Physics and Technology*,*36*(1), pp.81-98.

[29] Schrage, D.L., Young, L.M., Aikin, D.J., Clark, W.L., DePaula, R.F., Gladwell, C., Martinez, F.A., Naranjo, A.C., Roybal, P.L. and Stovall, J.E., 1993. University of Twente photocathode linac. *Nuclear Instruments and Methods in Physics Research Section B: Beam Interactions with Materials and Atoms*,*79*(1-4), pp.721-725.

[30] Milton, S., Biedron S., Harris, J., Martinez, J., D'Audney, A., Edelen J., Einstein, J., C. Hall, Horovitz, K., Morin, A., Sipahi, N., Sipahi, T., Williams, J., Carrico, C., and van der Slot, P.J.M. "Colorado State University (CSU) Accelerator and FEL Facility.", In 5th International Particle Accelerator Conference (IPAC'14) Proceedings, Dresden, Germany, June 15-20, 2014, pp. 3937-3939. JACOW, Geneva, Switzerland, 2014.

[31] Sipahi, Taylan*, Sipahi, Nihan*, Sandra Biedron, Stephen Milton, and Chris Adolphsen. Passively Driving X-band Structure to Achieving Higher Beam Energies." *In 6th International Particle Accelerator Conference (IPAC'13) Proceedings, Shanghai, China, May 12-17, 2013*(pp. 1304-1306). JACOW, Geneva, Switzerland, 2013.

[32] P. B. Wilson, "High Energy Electron Linacs: Applications to Storage Ring RF Systems and Linear Colliders", SLAC-PUB-2884 (1991).

[33] Wangler, Thomas P. *RF Linear accelerators*. John Wiley & Sons, 2008.

[34] E. Adli, “A Study of the Beam Physics in the CLIC Drive Beam Decelerator”, CERN-THESIS-2010-024.

[35] Dehler, M., Candel, A. and Lee, L., 2010. Numerical Validation of the CLIC/SwissFEL/FERMI Multi Purpose X Band Structure. *LINAC2010, Tsukuba, Japan, MOP073*, p.223.

[36] Spataro, B., Alesini, D., Bacci, A., Ficcadenti, L., Mostacci, A., Palumbo, L. and Parodi, R., 2008. A bi-periodic X-Band cavity for SPARC. *Nuclear Instruments and Methods in Physics Research Section A: Accelerators, Spectrometers, Detectors and Associated Equipment*, *586*(2), pp.133-142.

[37] Wang, J. W. "RF Properties of Periodic Accelerating Structures For Linear Colliders* r--m." (1989).

[38] Christou, Chris. "X-band linac technology for a high repetition rate light source." *Nuclear Instruments and Methods in Physics Research Section A: Accelerators, Spectrometers, Detectors and Associated Equipment* 657, no. 1 (2011): 13-21.

[39] Menzel, M. T., and H. K_ Stokes. *Users guide for the POISSON/SUPERFISH group of codes*. No. LA-UR--87-115. Los Alamos National Lab., NM (United States), 1987.

[40] Sipahi, T., Sipahi, N., Biedron, S., and Milton, S. X-band RF Power Generation via an L-band Accelerator System and Uses. Directed Energy Professional Society (DEPS) 16th Annual Directed Energy Symposium Proceedings, Huntsville, Alabama, March 10-14, 2014.

[41] Sipahi, T., Sipahi, N., Biedron, S., and Milton, S. Passively Driving X-Band Structures to Achieve Higher Beam Energies. *In 25th North American Particle Accelerator Conference (NA-PAC’13), Pasadena, California, USA, Sept. 29 – Oct. 4, 2013(pp. 1001-1003).* JACOW, Geneva, Switzerland, 2014.

[42] Sipahi, N., Sipahi, T., Biedron, S., and Milton, S. X-band RF power Generation via L-band Accelerator System and Uses. *In 25th North American Particle Accelerator Conference (NA-PAC’13),*

Pasadena, California, USA, Sept. 29-Oct. 4, 2013(pp. 951-953). JACOW, Geneva, Switzerland, 2014.

[43] Sipahi, T., Biedron, S., and Milton, S. 2014. Achieving Higher Energies Via Passively Driven X-band Structures. *In 5th International Particle Accelerator Conference (IPAC'14) Proceedings, Dresden, Germany, June 15-20, 2014*(pp. 3933-3936). JACOW, Geneva, Switzerland, 2014.

[44] Sipahi, T., Biedron, S., and Milton, S. 2015, Co-linear X- Band Energy Booster (XCEB) Cavity and RF System Details. *In 6th International Particle Accelerator Conference (IPAC'15) Proceedings, Richmond, Virginia, USA, May 3-8, 2015*(pp. 3421- 3424). JACOW, Geneva, Switzerland, 2015

[45] National Energy Research Scientific Computing Center (NERSC) website: http://www.nersc.gov/

[46] Ko, K., Candel, A., Ge, L., Kabel, A., Lee, R., Li, Z., Ng, C., Rawat, V., Schussman, G. and Xiao, L., 2010. Advances in parallel electromagnetic codes for accelerator science and development. *LINAC2010, Tsukuba, Japan*, pp.1028-1032.

[47] Candel, A., Kabel, A., Lee, L.Q., Li, Z., Ng, C., Schussman, G. and Ko, K., 2009. State of the art in electromagnetic modeling for the Compact Linear Collider. In *Journal of Physics: Conference Series* (Vol. 180, No. 1, p. 012004). IOP Publishing.

[48] Sjobak, K.N., Adli, E.A. and Grudiev, A., 2013. *Surface field optimization of accelerating structures for CLIC using ACE3P on remote computing facility*(No. CERN-ACC-2013-0196).

[49] Sjobak, K.N., Adli, E., Wuensch, W. and Grudiev, A., 2012, May. Design of an accelerating structure for a 500 GeV CLIC using ACE3P. In *Conf. Proc.* (Vol. 1205201, No. CERN-ATS-2012-122, p. THPPC011).

[50] Trelis Software website: http://www.csimsoft.com/

[51] Paraview Software website: http://www.paraview.org/

[52] Private communication, Cho-Kuen Ng, 2014

[53] Jackson, John David. "Classical electrodynamics." (1999): 841-842.

[54] Slater, John Clarke. "Microwave electronics." (1950).

[55] Collin, Robert E. "Field theory of guided waves." (1960).

[56] Pozar, D.M., 2006. *Microwave engineering*. Publishing House of Electronics Industry.

[57] Private communication, Oleksiy Kononenk, 2016

[58] Lee, L.Q., Ng, C., Li, Z. and Ko, K., 2009. Omega3P: A parallel finite-element eigenmode analysis code for accelerator cavities (No. SLAC-PUB-13529).

[59] Sipahi, T., Biedron, S. and Milton, S., 2016, June. Frequency Domain Simulations of Co-linear X-band Energy Booster (CXEB) RF Cavity Structures and Passive RF Components with ACE3P. In *7th International Particle Accelerator Conference (IPAC'16), Busan, Korea, May 8-13, 2016*(pp. 480-482). JACOW, Geneva, Switzerland.

[60] Sipahi, Taylan, Sandra Biedron, and Stephen Milton. "Frequency Domain Simulations of RF Cavity Structures and Coupler Designs for Co-Linear X-Band Energy Booster (CXEB) with ACE3P." In *North American Particle Accelerator Conf.(NAPAC'16), Chicago, IL, USA, October 9-14, 2016*, pp. 191-194. JACOW, Geneva, Switzerland, 2017.

[61] Westbrook, E. "Microwave impedance matching of feed waveguides to the disk-loaded accelerator structure operating in the 2π/3 mode." *SLAC-TN-63-103* (1963)

[62] Kamigaito, O. "Circuit-model representation of external-Q calculation." *Physical Review Special Topics-Accelerators and Beams* 9, no. 6 (2006): 062003.

[63] Kageyama, Tatsuya. *A simple method using MAFIA to calculate external Q values of waveguide-loaded cavities*. No. KEK-89-4. National Laboratory for High Energy Physics, 1989.

[64] Wei, Zhao, Tang Xiao, Shi Rong-Jian, and Hou Mi. "Coupler design for an L-band electron linac." *Chinese physics C* 36, no. 8 (2012): 765.

[65] Jin, K. "A calculation means for RF couplers numerical simulation design." *Nuclear Instruments and Methods in Physics Research Section A: Accelerators, Spectrometers, Detectors and Associated Equipment* 539, no. 1 (2005): 100-104.

[66] Jana, P. K., Vinit Kumar, and Nita S. Kulkarni. "Design of RF power coupler for 5 MeV, 3 KW traveling wave electron Linac." In *Proceedings of the Indian particle accelerator conference*. 2013.

[67] Tang, Z. X., And Y. J. Pei. "Design of An Accelerating Tube For Medical Standing-Wave Accelerator Based on Genetic Algorithm's Optimal Calculation."

[68] Rong, W. A. N. G., and PEI Yuan-Ji JIN Kai. "A Calculation Method for RF Couplers Design Based on Numerical Simulation by Microwave Studio." (2006).

[69] Pei, S., J. Zhang, M. Hou, X. Li, and B. Wang. "RF Characteristic Studies On The Whole Accelerating Structure For The Bepcii Linear Accelerator."

[70] Wang, T. F., L. E. Thode, and R. K. Cooper. "Cavity-waveguide coupling through a large aperture." In *paper WE3-25 of this conference*. 1988.

[71] Jin, K., Y. J. Pei, D. M. Jiang, Y. Z. Liu, Q. J. Lai, M. H. Zhao, and H. Zhao. "X-band travelling wave accelerator structure R&D." In *Particle Accelerator Conference, 2001. PAC 2001. Proceedings of the 2001*, vol. 5, pp. 4089-4091. IEEE, 2001.

[72] Alesini, David, Alessandro Gallo, Bruno Spataro, Agostino Marinelli, and Luigi Palumbo. "Design of couplers for traveling wave RF structures using 3D electromagnetic codes in the frequency domain." *Nuclear Instruments and Methods in Physics Research Section A: Accelerators, Spectrometers, Detectors and Associated Equipment* 580, no. 3 (2007): 1176-1183.

[73] Design, D.C., 2004. X-Band Linear Collider R&D In Accelerating Structures Through Advanced Computing.

[74] Sipahi, T., Biedron, S., and Milton, S. "Wakefield Excitation in Power Extraction Cavity (PEC) of Co-linear X-band Energy Booster (CXEB) in Time Domain with ACE3P.", In 7th International Particle Accelerator Conference (IPAC'16) Proceedings, Busan, Korea, May 8-13, 2016, pp. 480-482. JACOW, Geneva, Switzerland, 2016.

[75] Candel, Arno, Z. Li, C. Ng, V. Rawat, G. Schussman, Kwok Ko, I. Syratchev, A. Grudiev, and W. Wuensch. *ACE3P Computations of Wakefield Coupling in the CLIC Two-*

Beam Accelerator. No. SLAC-PUB-14281. SLAC National Accelerator Laboratory (SLAC), 2010.

[76] Sipahi, Taylan, Sandra Biedron, and Stephen Milton. "Wakefield Excitation in Power Extraction Cavity of Co-Linear X-Band Energy Booster in Time Domain with ACE3P." In *North American Particle Accelerator Conf. (NAPAC'16), Chicago, IL, USA, October 9-14, 2016*, pp. 195-197. JACOW, Geneva, Switzerland, 2017.

[77] Verschuur, J.W.J., Ernst, G.J. and Witteman, W.J., 1992. The "TEUFEL" undulator. *Nuclear Instruments and Methods in Physics Research Section A: Accelerators, Spectrometers, Detectors and Associated Equipment*, *318*(1), pp.847-852.

[78] L. Giannessi, PERSEO, www.perseo.enea.it

[79] Linear Coherent Light Source: website: https://lcls.slac.stanford.edu/

[80] Linear Coherent Light Source II website: https://portal.slac.stanford.edu/sites/lcls_public/lcls_ii/Pages/default.aspx

[81] Thomas Jefferson Laboratory website: https://www.jlab.org/FEL/

[82] Deutsches Elektronen-Synchrotron
A Research Centre of the Helmholtz Association website https://flash.desy.de/

[83] Alice Free Electron Laser website: https://www.fels-of-europe.eu/fel_facilities/test_facilities/alice/

[84] Elettra and Fermi Lightsources website: https://www.elettra.trieste.it/index.html

[85] Sparc project website: http://www.lnf.infn.it/acceleratori/sparc/

[86] The Paul Scherrer Institute website: https://www.psi.ch/swissfel/

[87] CLIO Free Electron website: https://www.fels-of-europe.eu/fel_facilities/ir_facilities/clio/

[88] MAX IV Free Electron Laser website: https://www.fels-of-europe.eu/fel_facilities/x_ray_facilities/max_iv_fel/

[89] SACLA XFEL website: http://xfel.riken.jp/eng/index.html

[90] Hanna, S. M. "Applications of X-band technology in medical accelerators." In *Particle Accelerator Conference, 1999. Proceedings of the 1999*, vol. 4, pp. 2516-2518. IEEE, 1999.

[91] Quyet, N. H., M. Uesaka, H. Iijima, K. Dobashi, A. Fukasawa, F. Ebina, H. Ogino, and M. El-Ashmawy. "Compact x-band (11.424 Ghz) linac for cancer therapy." In *Proc. EPAC*. 2004.

[92] Eckman, C., P. Buaphad, Y. Kim, T. Downer, A. Andrews, B. N. Lee, B. C. Lee, and S. Y. Ryoo. "Design of a Compact X-band LINAC Structure for KAERI-RTX-ISU Medical CyberKnife Project." PAC, 2013.

[93] Sathe, Shridhar K., Suzanne S. Teuber, and Kenneth H. Roux. "Effects of food processing on the stability of food allergens." *Biotechnology advances* 23, no. 6 (200[5): 423-429.

[94] Fermilab Accelerator Complex website: http://www.fnal.gov/pub/science/particle-accelerators/accelerator-complex.html

[95] CERN Large Hadron Collider website: https://home.cern/topics/large-hadron-collider

[96] Japan Proton Accelerator Research Complex: http://j-parc.jp/Acc/en/index.html

[97] Spallation Neutron Source website: https://neutrons.ornl.gov/sns

[98] European Spallation Source website: https://europeanspallationsource.se

[99] Halbach, Klaus, and R. F. Holsinger. "SUPERFISH-a computer program for evaluation of RF cavities with cylindrical symmetry." *Part. Accel.* 7, no. LBL-5040 (1976): 213-222.

[100] T. Sipahi, M.Sc.Thesis “Resonance Frequency Calculation of a Narrow Gap Reentrant Klystron Cavity”, Ankara University, 2013.

[101] N. Sipahi, M.Sc.Thesis “Equivalent Circuit Properties and Quality Factor of a Narrow Gap Reentrant Klystron Cavity”, Ankara University, 2013.

[102] Krawczyk, F., Nathan A. Moody, Felix A. Martinez, Gerald O. Bolme, Karen A. Young, Dinh C. Nguyen, and Lloyd M. Young. "Initial RF measurements of the cw normal-conducting RF injector." *Proceedings of the LINAC08, Victoria, BC, Canada* (2008).

[103] Alesini, D., A. Falone, M. Migliorati, A. Mostacci, F. Palpini, L. Palumbo, and B. Spataro. "Design and RF measurements of an X-band accelerating structure for linearizing the longitudinal emittance at SPARC." *Nuclear Instruments and Methods in Physics Research Section A: Accelerators, Spectrometers, Detectors and Associated Equipment* 554, no. 1 (2005): 1-12.

[104] Hopper website: http://www.nersc.gov/users/computational-systems/hopper/ (retired)

[105] Top 500 Supercomputer website: https://www.top500.org/

[106] Edison website: http://www.nersc.gov/users/computational-systems/edison/

[107] Cori website: http://www.nersc.gov/users/computational-systems/cori/

[108] Kononenko, O., Ge, L., Ko, K., Li, Z., Ng, C.K. and Xiao, L., Advances In Massively Parallel Electromagnetic Simulation Suite ACE3p.

[109] ANSYS software website: http://www.ansys.com/

[110] HFFS User Guide Version 10

[111] ANSYS Academic Research HFSS Release 16.1

[112] Fukuda, Y., T. Hayakawa, E. Ichihara, K. Inoue, K. Ishihara, H. Ishino, Y. Itow et al. "Evidence for oscillation of atmospheric neutrinos." *Physical Review Letters* 81, no. 8 (1998): 1562.

[113] Ahmad, Q. Retal, R. C. Allen, T. C. Andersen, J. D. Anglin, G. Bühler, J. C. Barton, E. W. Beier et al. "Measurement of the Rate of ν e+ d→ p+ p+ e− Interactions Produced by B 8 Solar Neutrinos at the Sudbury Neutrino Observatory." *Physical Review Letters* 87, no. 7 (2001): 071301.

[114] Direct Evidence for Neutrino Flavor Transformation from Neutral-Current Interactions in the Sudbury Neutrino Observatory

[115] CERN Neutrinos to Gran Sasso (CNGS) website: https://home.cern/about/accelerators/cern-neutrinos-gran-sasso

[116] Gschwendtner, E., Pardons, A., Bruno, L., Clement, M., Efthymiopoulos, I., Elsener, K., Meddahi, M., Rangod, S. and Vincke, H., 2007. First operational experience with the CNGS facility.

[117] Gschwendtner, E., Cornelis, K., Efthymiopoulos, I., Ferrari, A., Pardons, A., Vincke, H., Wenninger, J., Autiero, D., Sala, P. and Guglielmi, A., 2010, June. Performance and operational experience of the CNGS facility. In *Applications of High Intensity Proton Accelerators* (Vol. 1, pp. 132-136).

[118] Japan Proton Acceleretor Research Complex (J-PARC) website: https://j-parc.jp/index-e.html

[119] Abe, K., Abgrall, N., Aihara, H., Ajima, Y., Albert, J.B., Allan, D., Amaudruz, P.A., Andreopoulos, C., Andrieu, B., Anerella, M.D. and Angelsen, C., 2011. The T2K experiment. *Nuclear Instruments and Methods in Physics Research Section A: Accelerators, Spectrometers, Detectors and Associated Equipment*, *659*(1), pp.106-135.

[120] Sekiguchi, T., Bessho, K., Fujii, Y., Hagiwara, M., Hasegawa, T., Hayashi, K., Ishida, T., Ishii, T., Kobayashi, H., Kobayashi, T. and Koike, S., 2015. Development and operational experience of magnetic horn system for T2K experiment. *Nuclear Instruments and Methods in Physics Research Section A: Accelerators, Spectrometers, Detectors and Associated Equipment*, *789*, pp.57-80.

[121] Fermilab website: http://www.fnal.gov/

[122] Patterson, R. B. "The NOvA experiment: status and outlook." *Nuclear Physics B-Proceedings Supplements* 235 (2013): 151-157.

[123] Mena, Olga, and Stephen Parke. "Physics potential of the Fermilab NuMI beamline." *Physical Review D* 72, no. 5 (2005): 053003.

[124] Derwent, P., Holmes, S. and Lebedev, V., 2015. An 800-MeV superconducting LINAC to support megawatt proton operations at Fermilab.*arXiv preprint arXiv:1502.01728*.

[125] Hylen, J., Smart, W., Wehmann, A., Menary, S., Malensek, A.J., Johnson, D., Morfin, J., Koizumi, G. and Lucas, P., 1997. Conceptual design for the technical components of the Neutrino Beam for the Main Injector. *Batavia, IL: Fermi National Accelerator Laboratory Report TM-2018*.

[126] Abramov, A.G., Galyaev, N.A., Garkusha, V.I., Hylen, J., Novoskoltsev, F.N., Ryabov, A.D. and Zarucheisky, V.G., 2002. Beam optics and target conceptual designs for the NuMI project. *Nuclear*

Instruments and Methods in Physics Research Section A: Accelerators, Spectrometers, Detectors and Associated Equipment, *485*(3), pp.209-227.

[127] Adamson, P., Anderson, K., Andrews, M., Andrews, R., Anghel, I., Augustine, D., Aurisano, A., Avvakumov, S., Ayres, D.S., Baller, B. and Barish, B., 2016. The NuMI neutrino beam. *Nuclear Instruments and Methods in Physics Research Section A: Accelerators, Spectrometers, Detectors and Associated Equipment*, *806*, pp.279-306.

[128] Chen, H. "Proposal for a new experiment using the booster and NuMI neutrino beamlines: MicroBooNE." *FERMILABPROPOSAL-0974* (2007).

[129] Bazarko, Andrew O., and MiniBooNE Collaboration. "MiniBooNE: Status of the booster neutrino experiment." *Nuclear Physics B-Proceedings Supplements* 91, no. 1-3 (2001): 210-215.

[130] Sousa, A., 2015. First MINOS+ data and new results from MINOS. *arXiv preprint arXiv:1502.07715*.

[131] McFarland, K.S., 2006. MINERvA: a dedicated neutrino scattering experiment at NuMI. *arXiv preprint physics/0605088*.

[132] Ayres, D.S., Drake, G.R., Goodman, M.C., Grudzinski, J.J., Guarino, V.J., Talaga, R.L., Zhao, A., Stamoulis, P., Stiliaris, E., Tzanakos, G. and Zois, M., 2007. The NOvA Technical Design Report.

[133] Acciarri, R., Wachala, T., Bishai, M., Davies, G.S., Singh, J., Gendotti, A., Marteau, J., Goodman, M.C., Sanchez, F., James, C. and Stewart, J., 2016.*Long-Baseline Neutrino Facility (LBNF) and Deep Underground Neutrino Experiment (DUNE) Conceptual Design Report Volume 1: The LBNF and DUNE Projects* (No. arXiv: 1601.05471).

[134] Acciarri, R., Acero, M.A., Adamowski, M., Adams, C., Adamson, P., Adhikari, S., Ahmad, Z., Albright, C.H., Alion, T., Amador, E. and Anderson, J., 2015. Long-Baseline Neutrino Facility (LBNF) and Deep Underground Neutrino Experiment (DUNE) Conceptual Design Report Volume 2: The Physics Program for DUNE at LBNF. *arXiv preprint arXiv:1512.06148*.

[135] Strait, J., McCluskey, E., Lundin, T., Willhite, J., Hamernik, T., Papadimitriou, V., Marchionni, A., Kim, M.J., Nessi, M., Montanari, D. and Heavey, A., 2016. Long-Baseline Neutrino Facility (LBNF) and Deep Underground Neutrino Experiment (DUNE) Conceptual Design Report Volume 3: Long-Baseline Neutrino Facility for DUNE June 24, 2015. *arXiv preprint arXiv:1601.05823*.

[136] Acciarri, R., Acero, M.A., Adamowski, M., Adams, C., Adamson, P., Adhikari, S., Ahmad, Z., Albright, C.H., Alion, T., Amador, E. and Anderson, J., 2016. Long-baseline neutrino facility (LBNF) and deep underground neutrino experiment (DUNE) conceptual design report, volume 4 the DUNE detectors at LBNF. *arXiv preprint arXiv:1601.02984*.

[137] Papadimitriou, V., et al. Design of The LBNF Beamline*. IPAC-2016-TUPMR025.

[138] Strait, J., 2015. *DUNE Physics* (No. FERMILAB-CONF-15-611-ND). Fermi National Accelerator Laboratory (FNAL), Batavia, IL (United States).

[139] Hylen, J. et al., "NuMI Facility Technical Design Report," Fermilab-TM-2018, Sept., 1997.

[140] Andrews, R., Chen, A.Z., Childress, S.C., Moore, C.D., Papadimitriou, V. and Campbell, M.R., 2013. Status of the Design of the LBNE Neutrino Beamline.*arXiv preprint arXiv:1301.6985*.

[141] Papdimitriou, V. (Fermilab) for the Collaboration, "Design of the LBNF Beamline", FERMILAB-CONF-17-022-AD.

[142] Kopp, S.E., 2007. Accelerator neutrino beams. *Physics reports*, *439*(3), pp.101-159.

[143] van der Meer, Simon. *A directive device for charged particles and its use in an enhanced neutrino beam*. No. CERN-61-07. CERN, 1961.

[144] Pellico, W., Domann, K., Garcia, F.G., Gollwitzer, K., Seyia, K. and Zwaska, B., 2012. FNAL-The Proton Improvement Plan (PIP). *THPME075, IPAC*, *14*.

[145] Holmes, S., Derwent, P., Lebedev, V., Mishra, S., Mitchell, D. and Yakovlev, V.P., 2015. PIP-II Status and Strategy. *Proc. of IPAC2015, Richmond, VA, USA*, pp.3982-3985.

[146] Lebedev, Valeri. *The PIP-II Conceptual Design Report*. No. FERMILAB-DESIGN-2017-01; FERMILAB-TM-2649-AD-APC. Argonne National Laboratory (ANL), Argonne, IL (United States); Fermi National Accelerator Laboratory (FNAL), Batavia, IL (United States), 2017.

[147] He, Y., CLASSE Seminar, "Magnetic Focusing Horns for Neutrino Experiments", CHESS, Cornell University, December 17, 2010.

[148] Anderson, E. Kris, Status Update ongoing efforts for NuMI Horn 1 Stripline Redesign and Horn Change Out, All Experiment's Meeting, July 06, 2015.

[149] Hurh, P. (on behalf of the Target System Department Engineering and Operations Team), "NuMI Horn Stripline Failure, Analysis, and Recovery or the Case of the Cracked Stripline", in Proc. the 6th High Power Targetry Workshop, Rutherford Appleton Laboratory at Merton College, University of Oxford, UK, 11-15 April 2016.

[150] ANSYS Academic Research, Maxwell 3D Release 16.1

[151] Sipahi, T., Biedron, S., Hylen, J., Milton, S., and Zwaska, R. Simulations of High Current NuMI Magnetic Horn Striplines at FNAL. *In 7th International Particle Accelerator Conference (IPAC'16), Busan, Korea, May 8-13, 2016*(pp. 1230-1232). JACOW, Geneva, Switzerland, 2016.

[152] Sipahi, T., Zwaska, R., Biedron, S., Hylen, J., and Milton. S., "Simulations of High Current NuMI Magnetic Horn Striplines at FNAL." *PoS* (2016): 941.

[153] Sipahi, T., Biedron, S., Hylen, J., Milton, S., and Zwaska, R. "Simulations Of High Current Magnetic Horn Striplines at Fermilab", In 2016 North American Particle Accelerator Conference Proceedings NAPAC'16, Chicago, IL, USA, October 9-14, 2016.

[154] Sipahi, T., et al. "High Current Striplines for Neutrino Beams.", In 6th Euro-Asian Pulsed Power Conference (EAPPC 2016) with the 21st International Conference on High-Power Particle Beams (BEAMS) and the 15th International Conference on Megagauss Magnetic Field Generation and related topics (MEGAGAUSS) proceedings, Estoril, Portugal, 18-22 September, 2016.

[155] Private communications Kris E. Anderson, 2016.

[156] Private communications, Jim Hylen, 2016-2017.

APPENDICES

APPENDIX A: INVENTION AND DEVELOPMENT OF PARTICLE ACCELERATORS

A1. Description of a Particle Accelerator

A particle accelerator is a machine that accelerates charged elementary particles, such as electrons, positrons or protons, to higher energies. This can be done in particle accelerators delivering energy to a charged-particle beam by application of an electric field.

A2. DC versus RF Acceleration

The particle accelerators can be categorized into two classes as electrostatic and electrodynamic (or electromagnetic) particle accelerators.

The first particle accelerators were electrostatic accelerators, developed in the early 1930s, in which the beam gains energy from a constant (static) electric field. In this types of accelerators each particle acquires an energy equal to the product of its electric charge times the potential drop, and the use of electrostatic fields led to a unit of energy called the electronvolt (eV), equal to the product of the charge times the voltage drop. If a particle has a charge q and mass m and move through a potential difference of V then it will gain a kinetic energy (E_{kin}) of:

$$E_{kin} = \frac{m\vartheta^2}{2} = qV \qquad \text{(A.1)}$$

Obviously, the achievable kinetic energy for particles in these devices is determined by the accelerating voltage, which is limited by electric breakdown to no more than a few tens of megavolts (MV).

An old ordinary television with a cathode ray tube (CRT) is a small-scale example of this class. The most common types are the Cockcroft–Walton generator and the Van de Graaff generator. A variation of the Van de Graaff accelerator is the Tandem accelerator, which can produce accelerating potentials twice as high as that from a single Van de Graaff accelerator.

On the other hand, because of the high voltage ceiling imposed by electric discharge, in order to accelerate particles to higher energies, techniques involving dynamic fields rather than static fields are used. In that sense electrodynamic (electromagnetic) accelerators use changing electromagnetic fields either magnetic induction or oscillating radio frequency (RF) fields to accelerate particles. Linear induction accelerators and betatrons are the examples of magnetic induction accelerators to accelerate particles. Another branch of this class, was first developed in the 1920s, is the basis for most modern large-scale accelerators have led to the name resonance accelerators in time, which includes the linear accelerator (linac), cyclotron, and synchrotron. The ideal particle orbit in an RF accelerator mentioned above can be either a straight line for a linac, a spiral for a cyclotron, or a circle for a synchrotron. Since in these types the particles can pass through the same accelerating field multiple times, the output energy is not limited by the strength of the accelerating field. Radio frequency (RF) accelerators bypass this limitation by applying a harmonic time-varying electric field to the beam, which is localized into bunches, such that bunches always arrive when the field has the correct polarity for acceleration. The time

variation of the field removes the restriction that the energy gain be limited by a fixed potential drop. The beam is accelerated within electromagnetic cavity structures, in which a particular electromagnetic mode is excited from a high frequency external power source. For acceleration, the beam particles must be properly phased with respect to the fields, and for sustained energy gain they must maintain synchronism with those fields.

In classical electrodynamics, the interaction between electromagnetic fields and moving charged particles is described by two sets of equations. While the modern Maxwell's equations describe how electrically charged particles and currents or moving charged particles give rise to electric and magnetic fields, the Lorentz force law completes that picture by describing the force acting on a moving point charge q in the presence of electromagnetic fields. For a particle of charge q in an electromagnetic field, the Lorentz force on particle with charge q and velocity $\boldsymbol{\vartheta}$ in an electric field **E** and a magnetic field **B**, is given by:

$$\mathbf{F} = q\mathbf{E} + q(\boldsymbol{\vartheta} \times \mathbf{B}) \tag{A.2}$$

Relating the Lorentz force to particle momentum or kinetic energy, has been known from definitions in classical mechanics:

$$\Delta\mathbf{p} = \int \mathbf{F}dt \tag{A.3}$$

$$\Delta E_k = \int \mathbf{F}d\boldsymbol{s} \tag{A.4}$$

where $d\boldsymbol{s} = \boldsymbol{\vartheta}dt$

$$\Delta E_k = \int \mathbf{F}\boldsymbol{\vartheta}dt \tag{A1.5}$$

$and\ \Delta E_k = \beta\Delta c\mathbf{p}$, where $\beta = \frac{\boldsymbol{\vartheta}}{c}$

Then, the Lorentz force can be expressed in terms of fields and the change of kinetic energy becomes:

$$\Delta E_k = \int \mathbf{F} ds = q \int [\mathbf{E} + (\boldsymbol{\vartheta} \text{ x } \mathbf{B})]\, ds \tag{A.6}$$

$$\Delta E_k = q \int \mathbf{E} ds + \frac{q}{c} \int (\boldsymbol{\vartheta} \times \mathbf{B})\, \boldsymbol{\vartheta}\, dt \tag{A.7}$$

In the first part of the integral electric field **E** which is in the same direction of particle motion increases the particle kinetic energy and cause acceleration. This acceleration is independent of the particle velocity even the particle at rest $\boldsymbol{\vartheta} = 0$.

The second part of the integral depends on the particle velocity and it is normal to the propagation direction and magnetic field direction. Since then, the term vanishes due to the scalar product $(\boldsymbol{\vartheta} \times \mathbf{B})\boldsymbol{\vartheta} = 0$. It causes only a deflection of the particle's trajectory by changing the direction of momentum vector.

In the circular accelerator, particles move in a circular trajectory using electromagnets until they reach the desired energy. The advantage of circular accelerators over linacs is the ring topology allows continuous acceleration, as the particle can transit indefinitely. Another advantage is that a circular accelerator is smaller than a linear accelerator of comparable power, such as a linac can be very long to have the equivalent power of a circular accelerator.

Depending on the energy and the type of accelerated particle, circular accelerators have a disadvantage in that the particles emit synchrotron radiation (SR). When any charged particle is accelerated, it emits electromagnetic radiation and secondary emissions. As a particle travelling in a circle orbit is always accelerating towards the center of the circle and it continuously radiates

towards the tangent of the circle. This radiation is called synchrotron light and depends highly on the mass of the accelerating particle. Certain accelerators such as synchrotrons are built specially for producing synchrotron light. On the other hand for this reason, many high-energy electron accelerators are linacs.

As mentioned above both the circular and linear particle accelerators have their own advantageous and disadvantageous. The decision can be made according to the required application. In our case, because of the main interest in the first part of this dissertation is related to linear type RF particle accelerators, the scope is narrowed to linacs starting from the invention and development of RF linac in the next subsection.

A3. Invention and Development of RF Linac

Technological base of the linac is a consequence of the science includes the discoveries of electromagnetism by Faraday, Maxwell, and Hertz in the nineteenth century and the discovery of superconductivity in the twentieth century. The improvements in classical physics, especially classical mechanics, and electromagnetism, as well as relativity theory provide the development of linac in the second half of the twentieth century significantly.

In 1924, Gustav Ising proposed the first accelerator that used time-dependent fields, consisting of a straight vacuum tube, and a sequence of metallic drift tubes with holes for the beam. The concept proposed by Ising was not tested at that time, but the publication was very important because it influenced Rolf Wideröe.

The first RF linear accelerator was conceived and demonstrated experimentally by Wideröe in 1927 in Germany. This linac was the forerunner of all modern RF accelerators and inspired E. O. Lawrence to the invention of the cyclotron.

The first formal proposal and experimental test for a linac was by Rolf Wideröe in 1928, but linear accelerators that were useful for research in nuclear and elementary particle research did not appear until after the developments of microwave technology in World War (WW) II, stimulated by radar programs. Since then, the progress has been rapid, and today, the linac is not only a useful research tool, but is also being developed for many other important applications.

The original Wideröe linac concept was not suitable for acceleration to high energies. Linac development required higher-power microwave generators, and accelerating structures better adapted for high frequencies and for acceleration requirements of high-velocity beams. High-frequency power generators, developed for radar applications, became available after WW II. At this time, a new and more efficient high-frequency proton accelerating structure, based on a linear array of drift tubes enclosed in a high-Q cylindrical cavity, the drift-tube linac (DTL) concept, was proposed by Luis Alvarez and coworkers at the University of California. Around the same time another a new and efficient accelerating structure for relativistic electrons was proposed, consisting of an array of pillbox-cavity resonators with a central hole in each end wall for propagation of both the beam and the electromagnetic energy, called the disk-loaded or iris-loaded waveguide, and this development led eventually to the 3-km Stanford Linear Accelerating Center (SLAC) linac. From these two projects the first modern proton and electron linac were born [ibid 27].

The modern linacs typically consist of sections of specially designed waveguides or high-Q resonant cavities that are excited by RF electromagnetic fields, usually in the very high frequency (VHF) and ultra-high frequency (UHF) microwave frequency ranges. The accelerating structures are tuned to resonance and are driven by external, high-power radio frequency (RF) power tubes, such as klystrons, or various types of gridded vacuum tubes. The efficiencies of these tubes typically range from about 40 to 65%. The output electromagnetic energy from the tubes is transported in conventional transmission lines or waveguides to the linac structure. The accelerating structures must efficiently transfer the electromagnetic energy to the beam, and this is accomplished in two ways. First, the resonant buildup of the fields in the high-Q structure transforms the low field levels of the input waveguide into high fields within the structure and produces a large ratio of stored electromagnetic energy relative to the ohmic energy dissipated per cycle. Second, through an optimized configuration of the internal geometry, the structure can concentrate the electric field along the trajectory of the beam promoting maximal energy transfer. The most useful figure of merit for high field concentration on the beam axis and low ohmic power loss is the shunt impedance.

One of the main advantages of the linacs is its capability for producing high-energy, and high-intensity charged-particle beams of high beam quality, where high beam quality can be related to a capacity for producing a small beam diameter and small energy spread. Other attractive characteristics of the linacs are strong focusing can be easily provided to confine a high-intensity beam; the beam traverses the structure in a single pass, and therefore repetitive error conditions causing destructive beam resonances are avoided; because the beam travels in a straight line, there is no power loss from synchrotron radiation, which is a limitation for high-energy electron

beams in circular accelerators; injection and extraction are simpler than in circular accelerators, since the natural orbit of the linac is open at each end; special techniques for efficient beam injection and extraction are unnecessary; the linac can operate at any duty factor, all the way to 100% duty or a continuous wave (CW), which results in acceleration of beams with high average current.

The linacs have been one of the most significant examples of high-technological research tool for almost about a century. We can expect that the linear accelerator will have a promising future. The straight-line trajectory avoids power losses caused by synchrotron radiation that accompanies circular RF accelerators. The capability for providing strong focusing allows high-quality and high-intensity beams that enable precision measurements to be made, and provides high-power beams for many applications. We can anticipate continuing progress in areas such as RF light sources, colliding beams, high-power beams, high frequency RF power and microwave technology, and RF superconductivity. In addition to basic science research fields further developments in these areas will lead the compact linacs to new performance levels with higher currents, better beam quality, and lower power requirements, so the expansion of new applications for linacs in the medical and industrial areas are confidently expected in near future.

A4. RF Linacs in Global Facilities

One of the most important decision point of RF linacs is the choice of technology between room-temperature (normal-conducting) and cryo (superconducting) operation. The favor for a specific technology depends on several parameters such as the beam energy, beam current, beam power and duty factor. While normal-conducting copper RF structures are preferable for low-duty cycle

applications the superconducting niobium RF cavities are chosen for CW mode or long pulse length application because of low wall losses.

Electron-positron linear colliders are preferred over circular colliders because synchrotron radiation losses, experienced by relativistic electrons in circular accelerators, are avoided. Furthermore, because of the strong focusing in a linac, high beam quality is achieved, which is required for high luminosity and a high collision rate. Stanford Linear Collider (SLC) which was the electron–positron linear collider at SLAC National Laboratory (originally Stanford Linear Accelerator Center) and the Los Alamos Neutron Science Center (LANSCE) formerly known as the Los Alamos Meson Physics Facility (LAMPF) multi-purpose proton linac at Los Alamos National Laboratory (LANL) are the two historically significant large linac projects [ibid 27].

RF electron linacs also provide high-quality electron beams for free-electron lasers LCLS [79] and II (SLAC) [80], JLab FEL (JLAB) [81], FLASH (DESY) [82], ALICE FEL (Daresbury Laboratory) [83], FERMI (Elettra) [84], SPARC FEL (INFN) [85], Swiss FEL (PSI) [86], CLIO FEL (d'Orsay) [87], MAX-IV FEL (Lund University) [88] and SACLA (RIKEN) [89].

In addition to large scale R&D facilities which use electron linacs have large variety of usages in medical applications [90]; such as cancer therapy (in 10–20-MeV energy range) [91], medical irradiations [92], and also in industrial applications; such as radiation processing of food including sterilization [93].

High intensity proton accelerators; such as Main Injector-MI (Fermilab) [94], Large Hadron Collider-LHC (CERN) [95] and Main Ring-MR (Japan Proton Accelerator Research Complex-J-PARC) [96], and spallation neutron sources; such as Spallation Neutron Source (SNS) [97], European Spallation Source (ESS) [98] have included protons linacs as injectors to high-energy synchrotrons for elementary particle and nuclear physics, material and life science research.

APPENDIX B: RADIO FREQUENCY (RF) CAVITY FUNDAMENTALS

B1. Electromagnetic Waves in a Bounded Media and Determination of Modes

Electromagnetic waves in free space are transverse electromagnetic TEM type which means both the electric (**E**) and magnetic field (**B**) vectors are perpendicular to the direction of propagation of the wave as shown in Figure B.1.

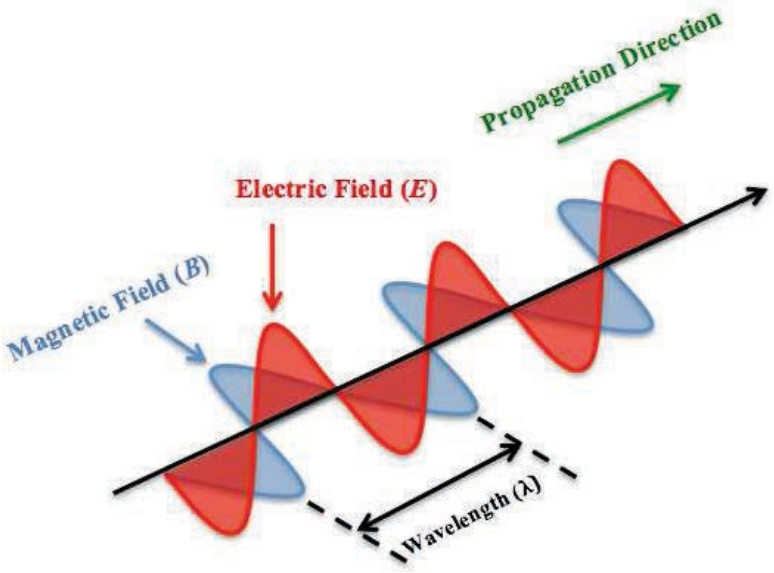

Figure B.1 TEM behavior of electromagnetic waves in nature

The only practical way to transmit high frequency electromagnetic waves is to confine them in an arbitrary shape hollow conductor tube. It is desirable that the conductivity of the wall material is large to minimize wall losses. (Skin depth (δ) and consequent wall loss are inversely proportional to $\sqrt{w\sigma}$ where w is angular frequency and σ is the conductivity.)

In this bounded media (a waveguide or a resonator), where the boundaries are conductors, TEM wave type is no longer possible because boundary conditions cannot be satisfied.

Waveguides most commonly used are either rectangular or circular, but the cross section shape can be arbitrary as long as it does not change abruptly along the waveguide. In either case, there is a lower limit in the wave frequency allowed for propagation (cutoff frequency), similar to the case of wave propagation in plasma. Waves having frequencies lower than the cutoff frequency cannot be propagated in a waveguide. The origin of the cutoff phenomena is in the boundary conditions at the conductor wall that should be satisfied by the electric and magnetic fields, and consequent deviation from the TEM nature.

For a waveguide that is filled with air, the wave equation for the electromagnetic fields is given by:

$$\left(\boldsymbol{\nabla}^2 - \frac{1}{c^2}\frac{\partial^2}{\partial t^2}\right)\mathbf{E}(\mathbf{r}, t) = 0 \tag{B.1}$$

$$\left(\boldsymbol{\nabla}^2 - \frac{1}{c^2}\frac{\partial^2}{\partial t^2}\right)\mathbf{H}(\mathbf{r}, t) = 0 \tag{B.2}$$

Each equation has three components. Obviously for a rectangular waveguide Cartesian coordinates provide simplicity for the solution. Equation B.2 can be decomposed into three scalar wave equations such as: E_x, E_y and E_z. For Equation B.2 these are H_x, H_y and H_z.

In a cylindrical waveguide, the cylindrical coordinates $\rho, \emptyset, z$ can be most convenient. Unlike the Cartesian coordinates, the vector wave equation in the cylindrical coordinates cannot be separated into three scalar wave equations because of the complexity in the vector Laplacian. However, the axial (z) component of the vector wave equation reduces to a scalar wave equation in the cylindrical coordinates in a different wave. These two solution suggests the possibility of the entire electromagnetic fields in a waveguide can be described by two axial components, E_z

and H_z, because both electric and magnetic field components are not entirely independent but constrained through the Maxwell's equations. As long as the waveguide cross section does not change along the axis to describe electromagnetic fields in a waveguide, it is sufficient to solve the following two scalar wave equations:

$$\left(\boldsymbol{\nabla}^2 - \frac{1}{c^2}\frac{\partial^2}{\partial t^2}\right) E_z(r,t) = 0 \tag{B.3}$$

$$\left(\boldsymbol{\nabla}^2 - \frac{1}{c^2}\frac{\partial^2}{\partial t^2}\right) H_z(r,t) = 0 \tag{B.4}$$

The transverse components, $E_\perp$ and $H_\perp$, can be fully described by the axial fields, E_z and H_z. Due to fact that solving a scalar wave equation is simpler than solving a vector wave equation we start the derivation of wave equations from Maxwell's equations.

$$\nabla \times \mathbf{E} = -\mu_0 \frac{\partial \mathbf{H}}{\partial t} \tag{B.5}$$

$$\nabla \times \mathbf{H} = \varepsilon_0 \frac{\partial \mathbf{E}}{\partial t} \tag{B.6}$$

Since the direction of wave (and also the energy) propagation is along the waveguide (in z direction), we may assume the phase function as:

$$e^{i(wt - k_z z)}$$

where k_z is the axial wavenumber in the z direction. For the assumed phase function, the gradient operator along the z axis and time derivative can be replaced by:

$$\frac{\partial}{\partial z} \rightarrow -ik_z, \qquad \frac{\boldsymbol{\partial}}{\boldsymbol{\partial t}} \rightarrow iw$$

The electric and magnetic fields can be written with their axial and transverse component decompositions as:

$$\mathbf{E} = E_\perp + E_z \tag{B.7}$$

$$\mathbf{H} = H_{\perp} + H_z \tag{B.8}$$

Then, Equations B1.5 and B1.6 can be written as:

$$\nabla_{\perp} \times E_{\perp} + \nabla_{\perp} E_z \times e_z - ik_z e_z \times E_{\perp} = -iw\mu_0 (H_{\perp} + H_z) \tag{B.9}$$

$$\nabla_{\perp} \times H_{\perp} + \nabla_{\perp} H_z \times e_z - ik_z e_z \times H_{\perp} = iw\varepsilon_0 \, (E_{\perp} + E_z) \tag{B.10}$$

Because of $e_z$is unidirectional constant vector $\nabla_{\perp} \times e_z = 0$ the Equation B.9 can be rewritten for the transverse components as:

$$E_{\perp} = \frac{-i}{w\varepsilon_0} (\nabla_{\perp} H_z \times e_z - ik_z e_z \times H_{\perp}) \tag{B.11}$$

If Equation B.11 substitute into Equation B.9 then the transverse magnetic field can be entirely written in terms of axial fields as:

$$H_{\perp} = \frac{-i}{(w/c)^2 - k_z^2} (k_z \nabla_{\perp} H_z - w\varepsilon_0 \, k_z \nabla_{\perp} E_z \times e_z) \tag{B.12}$$

Similarly, the transverse electric field in terms of the axial fields can be written as:

$$E_{\perp} = \frac{-i}{\left(\frac{w}{c}\right)^2 - k_z^2} (k_z \nabla_{\perp} E_z + w\mu_0 \nabla_{\perp} H_z \times e_z) \tag{B.13}$$

Obviously, it is indicated that if the axial fields, E_z and H_z are known, the tranverse components of the electric and magnetic fields can be calculated.

The different modes occur due to the boundary conditions imposed by the conductive walls of the waveguide. At a conducting surface, there can be no tangential electric field (there can be no component of the electric field parallel to the walls on the waveguide (or resonator), only perpendicular to them). Similarly, at a conducting surface, there can be no component of the magnetic field perpendicular to the surface (the magnetic field can only be parallel to the walls of the waveguide (or resonator)). Modes having no axial electric fields, $E_z = 0$; are called Transverse Electric (TE) modes and modes having no axial magnetic fields, $H_z = 0$; are called

Transverse Magnetic (TM) modes. Due to the fact that the electric field of TE modes is determined by the axial magnetic field H_z from:

$$E_\perp = \frac{-iw\mu_0}{\left(\frac{w}{c}\right)^2 - k_z^2} \nabla_\perp H_z \times e_z \tag{B.13}$$

and TM modes are determined by the axial electric field E_z from:

$$H_\perp = \frac{iw\varepsilon_0}{\left(\frac{w}{c}\right)^2 - k_z^2} \nabla_\perp E_z \times e_z \tag{B.12}$$

The wave propagation along the waveguide can be explained in terms of its reflection from wall to wall. A waveguide of rectangular cross-section has four walls, as shown in Figure B.2. The number of half wavelengths between two parallel planes determine the wave mode (TE_{mn} or TM_{mn}) with m and n being the number of half waves in the x and y direction, respectively. In the case of a resonator, a third subscript is needs to be added, indicating the number of half wavelengths in the z direction. These modes, which describe the configuration of electromagnetic fields in a waveguide or resonator, are called waveguide or cavity modes.

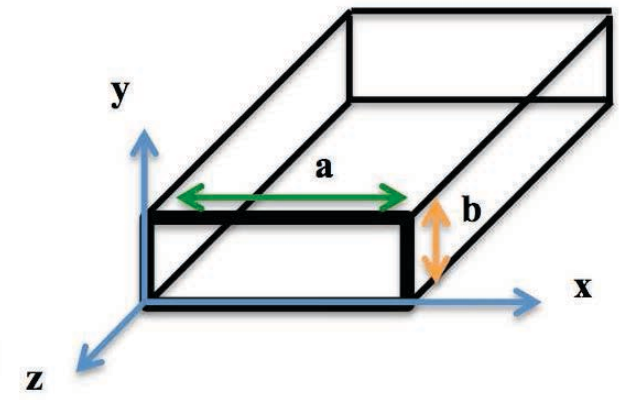

Figure B.2 Rectangular Waveguide

As it is mentioned earlier there are two types of waves in a hollow waveguide with only single type conductor:

TE-waves have $\mathbf{E} = (E_x, E_y, 0)$ and $\mathbf{H} = (H_x, H_y, H_z)$

TM-waves have $\mathbf{E} = (E_x, E_y, E_z)$ and $\mathbf{H} = (H_x, H_y, 0)$

The wall material is assumed to have a sufficiently large conductivity so that in the lowest order approximation the wall material can be regarded as a perfect conductor. Such approximation is not bad, as long as the skin depth is small enough and the field penetration into the wall is negligible. The boundary conditions are that the tangential components of the electric field and the normal derivative of the tangential components of the magnetic field are zero at the boundaries.

In general, boundary conditions are specified either by the value of a field component (Dirichlet condition), or by the derivative of a field component along the normal to the boundary (Neumann condition). A good physical insight is obtained by assuming the boundaries to be perfect conductors where the tangential component of the electric field (E_t) and the normal component of the magnetic field (H_n) must be zero.

$$E_t = 0, H_n = 0 \tag{B.13}$$

The second condition can be also stated, as the normal derivative of the tangential magnetic field at the boundary is zero.

$$\left(\frac{\partial H_t}{\partial n} = 0\right) \tag{B.14}$$

B2. TE Mode in Rectangular Waveguide

As clearly mentioned above a TE wave has $E_z = 0$ and $H_z \neq 0$. Consequently, all **E** field components are transverse to the propagation direction. Therefore for TE modes, the solution is needed for the magnetic field (**H**) which obeys the following scalar wave equation:

$$\left(\boldsymbol{\nabla}^2 - \frac{1}{c^2}\frac{\partial^2}{\partial t^2}\right)\mathbf{H} = 0 \tag{B.15}$$

It can be written more explicitly as:

$$\left(\frac{\partial^2}{\partial x^2} + \frac{\partial^2}{\partial y^2} + \frac{\partial^2}{\partial z^2} - \frac{1}{c^2}\frac{\partial^2}{\partial t^2}\right)\mathbf{H} = 0 \tag{B.16}$$

The wave equation applies to each field component, however we are mostly interested in the H_z. Then Equation B.5 can be rewritten as :

$$\left(\frac{\partial^2}{\partial \mathrm{x}^2} + \frac{\partial^2}{\partial \mathrm{y}^2} + \frac{\partial^2}{\partial \mathrm{z}^2} - \frac{1}{\mathrm{c}^2}\frac{\partial^2}{\partial \mathrm{t}^2}\right)\mathrm{H_z} = 0 \tag{B.17}$$

The solution of the wave equation is usually expressed as the product of functions of one variable:

$$H_z(x, y, z, t) = X(x)\, Y(y)\, Z(z)\, T(t) \tag{B.18}$$

For sinusoidally varying fields $T(t)$ is proportional to $e^{i\omega t}$ and the propagation in the z direction is given with $Z(z)$ is proportional to e^{-ikz}. The constant k indicates the phase advance of the wave per unit length. $X(x)$ and $Y(y)$ are the trigonometric functions, so longitudinal field in z direction can be expressed as:

$$H_z = H_z(x, y)e^{i(wt - k_z z)} \tag{B.19}$$

Noting $\frac{\boldsymbol{\partial}}{\boldsymbol{\partial z}} = -ik_z$, $\frac{\boldsymbol{\partial^2}}{\boldsymbol{\partial z^2}} = -k_z^2$ and $\frac{\boldsymbol{\partial}}{\boldsymbol{\partial t}} = iw$, $\frac{\boldsymbol{\partial^2}}{\boldsymbol{\partial t^2}} = -w^2$ the Equation B1.5 can be rewritten as:

$$\left(\frac{\partial^2}{\partial x^2} + \frac{\partial^2}{\partial y^2} + \left(\frac{w}{c}\right)^2 - k_z^2\right)H_z(x, y) = 0 \tag{B.20}$$

This is a two dimensional Helmholtz equation and can be solved by the method of separation of variables as done for the Laplace equation. The boundary conditions for $H_z(x,y)$ can be achieved by vanishing the tangential components of the electric field at the wall of the waveguide in Figure B.2.

$$\nabla_{\perp} H_z(x,y) = 0 \text{ at } x = 0, a \text{ and } y = 0, b \tag{B.21}$$

This condition can be satisfied by:

$$H_z(x,y) = H_0 cos\left(\frac{m\pi}{a}x\right) cos\left(\frac{n\pi}{b}y\right) \tag{B.22}$$

where m or n are integers and either of them can be zero but not simultaneously. Substitution of Equation B.22 in Equation B.8 yields dispersion relation which determines the axial wave number k_z for a given frequency ω and dimensions of the waveguide where c is the speed of light.

$$\omega^2 = c^2\left[\left(\frac{m\pi}{a}\right)^2 + \left(\frac{n\pi}{b}\right)^2 + k_z^2\right] \tag{B.23}$$

The minimum frequency allowed for wave propagation ($k_z > 0$) in a waveguide occurs at $k_z = 0$ and is given by

$$\omega_c = c\sqrt{\left(\frac{m\pi}{a}\right)^2 + \left(\frac{n\pi}{b}\right)^2} \tag{B.24}$$

Only waves having frequencies higher than ω_c can exist in the waveguide. Thus, this frequency is called the cutoff frequency (ω_c).

For a given cross section of a rectangular waveguide ($a > b$), the smallest cutoff frequency for TE_{mn} mode occurs when m = 1, n = 0 and the cutoff frequency is TE_{10} mode is given as angular frequency, which is the rate of change of the phase of a sinusoidal waveform, in radians per second $\left[\frac{Radians}{Second}\right]$ by:

$$\omega_{c,10} = \frac{\pi c}{a} \tag{B.25}$$

or as ordinary frequency, which is the number of occurrences of a repeating event per unit time corresponding to one crest per second, Hertz [Hz]:

$$f_{c,10} = \frac{c}{a} \tag{B.26}$$

B3. TM Mode in Rectangular Waveguide

To accelerate charged particles, a longitudinal electric field, as the waves of the TM type have (or distorted TE waves can also be used). Similar to TE mode the wave equation can be written for TM mode using electric field (**E**). The wave equation applies to each field component, however we are mostly interested in the longitudinal electric field (E_z). For TM modes, E_z satisfying the Helmholtz equation is given:

$$\left(\frac{\partial^2}{\partial x^2} + \frac{\partial^2}{\partial y^2} + \left(\frac{w}{c}\right)^2 - k_z^2\right) E_z(x, y) = 0 \tag{B.27}$$

with the boundary conditions $E_z = 0$ at $x = 0, a$ and $y = 0, b$.

This condition can be satisfied by:

$$E_z(x, y) = E_0 sin\left(\frac{m\pi}{a} x\right) sin\left(\frac{n\pi}{b} y\right) \tag{B.28}$$

where m and n are nonzero integers. The cutoff frequency of the TM mode is:

$$\omega_c = c\sqrt{\left(\frac{m\pi}{a}\right)^2 + \left(\frac{n\pi}{b}\right)^2} \tag{B.29}$$

The longitudinal electric field (E_z) can be written considering the explanations for the derivation that was used in Equation B.7 earlier as:

$$E_z = E_z(x, y) e^{i(wt - k_z z)} \tag{B.30}$$

The exponent $(wt - kz)$ is typical for a travelling wave (TW). If it moves the with wave crest it will be equal to zero $(wt - kz = 0)$. Then the phase velocity (ϑ_{ph}) can be expressed as:

$$\frac{z}{t} = \frac{w}{k} = \vartheta_{ph} \tag{B.31}$$

B4. TE and TM Mode Profiles for Rectangular Waveguide

For TE mode the electric field of in the y direction can be written as:

$$E_y(x, z, t) = E_0 sin\left(\frac{\pi}{a}x\right) e^{i(k_z z - \omega t)} \tag{B.32}$$

From $\mathbf{H} = \frac{1}{i\omega\mu_0}\boldsymbol{\nabla} \times \mathbf{E}$ the corresponding magnetic field components can be written as:

$$H_x = \frac{k}{\omega\mu_0} E_0 sin\left(\frac{\pi}{a}x\right) e^{i(k_z z - \omega t)} \tag{B.33}$$

$$H_z = -i\frac{\pi/a}{\omega\mu_0} E_0 cos\left(\frac{\pi}{a}x\right) e^{i(k_z z - \omega t)} \tag{B.34}$$

Similarly this calculation can be done for TM mode using the magnetic field in y direction H_y and applying to $\mathbf{E} = \frac{1}{i\omega\varepsilon_0}\boldsymbol{\nabla} \times \mathbf{H}$. Then the field components will be:

$$H_y(x, z, t) = H_0 cos\left(\frac{\pi}{a}x\right) e^{i(k_z z - \omega t)} \tag{B.35}$$

$$E_x = \frac{k}{\omega\varepsilon_0} E_0 cos\left(\frac{\pi}{a}x\right) e^{i(k_z z - \omega t)} \tag{B.36}$$

$$E_z = i\frac{\pi/a}{\omega\varepsilon_0} E_0 sin\left(\frac{\pi}{a}x\right) e^{i(k_z z - \omega t)} \tag{B.37}$$

According to these the general characteristics of electric and magnetic field profiles of TE and TM modes of a rectangular waveguide for $l = \frac{\lambda}{2}$ shown as Figure B.3.

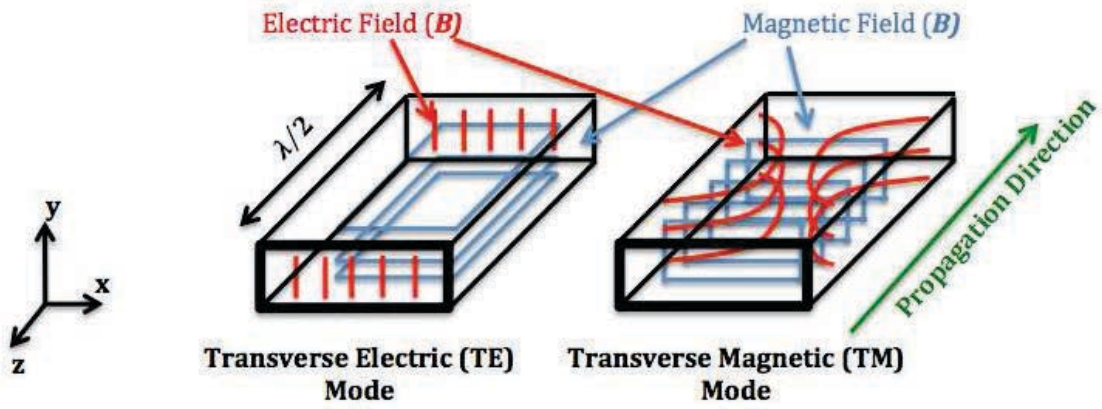

Figure B.3 Electric (**E**) and magnetic (**B**) field profiles of TE and TM modes of a rectangular waveguide

B5. Transmitted Power (Poynting Vector)

Poynting vector represents the directional energy flux density, the rate of energy transfer per unit area, of an electromagnetic field. The SI (Système International) unit of the Poynting vector is the Watt per square meter (W/m^2). If the direction of energy propagation is in a waveguide in the z direction the Poynting vector is, therefore expected to be direct as in the same direction.

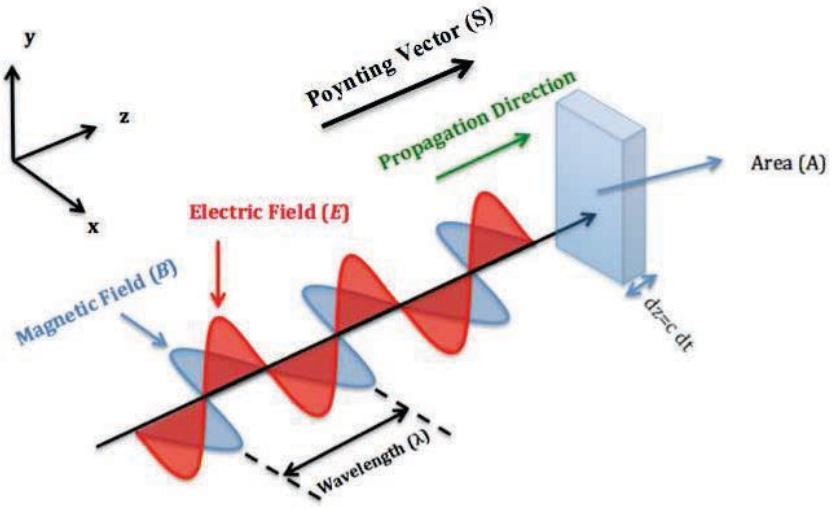

Figure B.4 Direction of Poynting Vector

In the Cartesian coordinates, the z component of the Poynting vector is given by:

$$S_z(\mathbf{E}\times\mathbf{H}^*)_z = E_x H_y^* - E_y H_x^* \tag{B.38}$$

For the TE mode, the Poynting vector can be written as:

$$S_z = -E_y H_x^* \tag{B.39}$$

The power transmitted in the waveguide shown in Figure B.2 can be found by integrating the Poynting vector in the axial direction given by:

$$P_{peak} = \int_0^a dx \int_0^b dy\, S_z(x) \tag{B.40}$$

The Poynting flux can be written as:

$$S_z = \frac{k_z}{\omega\mu_0} E_0^2 sin^2\left(\frac{\pi}{a}x\right) \tag{B.41}$$

Then,

$$P_{Peak} = \frac{k_z}{\omega\mu_0} E_0^2 \int_0^a sin^2\left(\frac{\pi}{a}x\right) dx \times b \tag{B.42}$$

$$= \frac{k_z}{\omega\mu_0} E_0^2 \frac{ab}{2} \tag{B.43}$$

$$\frac{k_z}{\omega\mu_0} = \sqrt{\frac{\varepsilon_0}{\mu_0}}\sqrt{1-\left(\frac{f_c}{f}\right)^2} \tag{B.44}$$

$$= E_0^2 \frac{ab}{2}\sqrt{\frac{\varepsilon_0}{\mu_0}}\sqrt{1-\left(\frac{f_c}{f}\right)^2} \tag{B.45}$$

and

$$P_{RMS} = E_0^2 \frac{ab}{4}\sqrt{\frac{\varepsilon_0}{\mu_0}}\sqrt{1-\left(\frac{f_c}{f}\right)^2} \tag{B.46}$$

Similarly for the TM mode,

$$P_{Peak} = \frac{k_z}{\omega\varepsilon_0} H_0^2 \frac{ab}{2} \tag{B3.47}$$

and

$$P_{RMS} = H_0^2 \frac{ab}{4} \frac{\sqrt{\frac{\varepsilon_0}{\mu_0}}}{\sqrt{1-\left(\frac{f_c}{f}\right)^2}} \tag{B.48}$$

B6. TE and TM Modes in Rectangular Resonator

If the resonator case considered (both end of the waveguide closed with a metallic plate) for the length l in the z direction the boundary conditions on the cavity walls force the fields to exist only at certain quantized resonant frequencies. In this case, the waveguide form complete standing waves in all directions (all three Cartesian components of the wave vector are quantized, and therefore the modes can be written as TE_{mnp} and TM_{mnp}). Here, it is sufficient to consider TM modes because after suitable coordinates changes, TM modes can be recovered from TE modes. Then, Equation B.28 and B.29 can be expressed as:

$$E_z(x,y) = E_0 sin\left(\frac{m\pi}{a}x\right) sin\left(\frac{n\pi}{b}y\right) cos\left(\frac{p\pi}{l}z\right) \tag{B.49}$$

$$\omega_c = c\sqrt{\left(\frac{m\pi}{a}\right)^2 + \left(\frac{n\pi}{b}\right)^2 + \left(\frac{p\pi}{l}\right)^2} \tag{B.50}$$

B7. TE and TM Mode in Cylindrical (Pillbox) Cavity

Electromagnetic waves in a cylindrical cavity can also be divided into TE and TM modes, as in rectangular waveguides, in cylindrical coordinates using the axial components E_z and H_z to satisfy the scalar wave equation.

In accelerator cavities generally cylindrical cross sections are preferred. The electromagnetic field in this type of conductor tubes is rotationally symmetric as shown in Figure B.5.

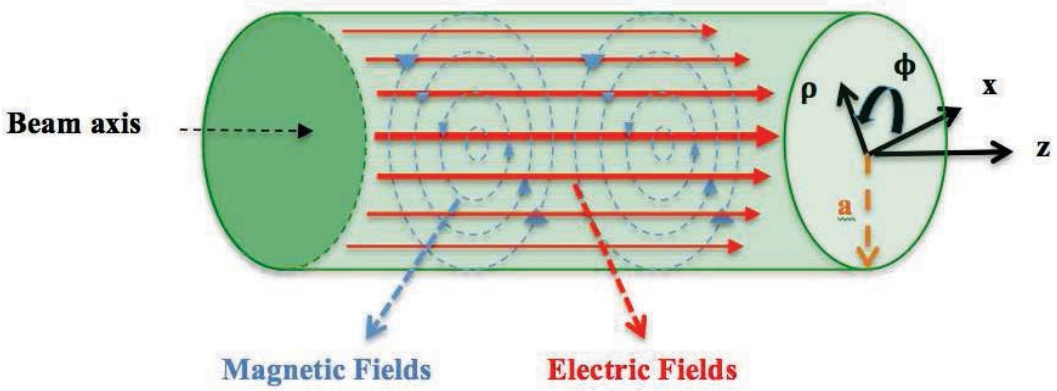

Figure B. 5 The electric (**E**) and the magnetic (**B**) field profiles of TM modes pillbox cavity

In this case the wave equation can be written in cylindrical coordinates as:

$$\frac{\partial^2 E_z}{\partial z^2} + \frac{1}{r}\frac{\partial}{\partial r}\left(r\frac{\partial E_z}{\partial r}\right) - \frac{1}{c^2}\frac{\partial^2 E_z}{\partial t^2} = 0 \tag{B.51}$$

and the solution :

$$E_z = Z(z)\,R(r)\,T(t) \tag{B.52}$$

Expressing $Z(z)$ and $T(t)$, we can have a equation for $R(r)$:

$$\frac{d^2R}{dr^2} + \frac{1}{r}\frac{dR}{dr} + \left(\frac{w^2}{c^2} - k_z^2\right)R = 0 \tag{B.53}$$

where,

$$k^2 = \frac{w^2}{c^2} - k_z^2 \tag{B.54}$$

Equation B.54 is the dispersion relation and well-known Bessel equation in zero order. The solution for $k^2 > 0$ can be given with the first kind of Bessel function in zero order:

$$R(r) = AJ_0(ka) \tag{3.55}$$

where A is a constant. At the boundary of cylinder that has a radius a the Equation 3.55 vanishes:

$$J_0(ka = x) = 0 \tag{3.56}$$

This equation has many roots (Figure B.6) and each root corresponds to a mode of the TM wave. The first root (x_{m1}) occurs at 2,405 ($ka = 2.405$) for TM_{01} mode (Table B.1).

Table B.1 Zeros of the Bessel functions of the first kind

m	x_{m1}	x_{m2}	x_{m3}
0	2.405	5.520	8.654
1	3.832	7.016	10.173
2	5.136	8.417	11.620

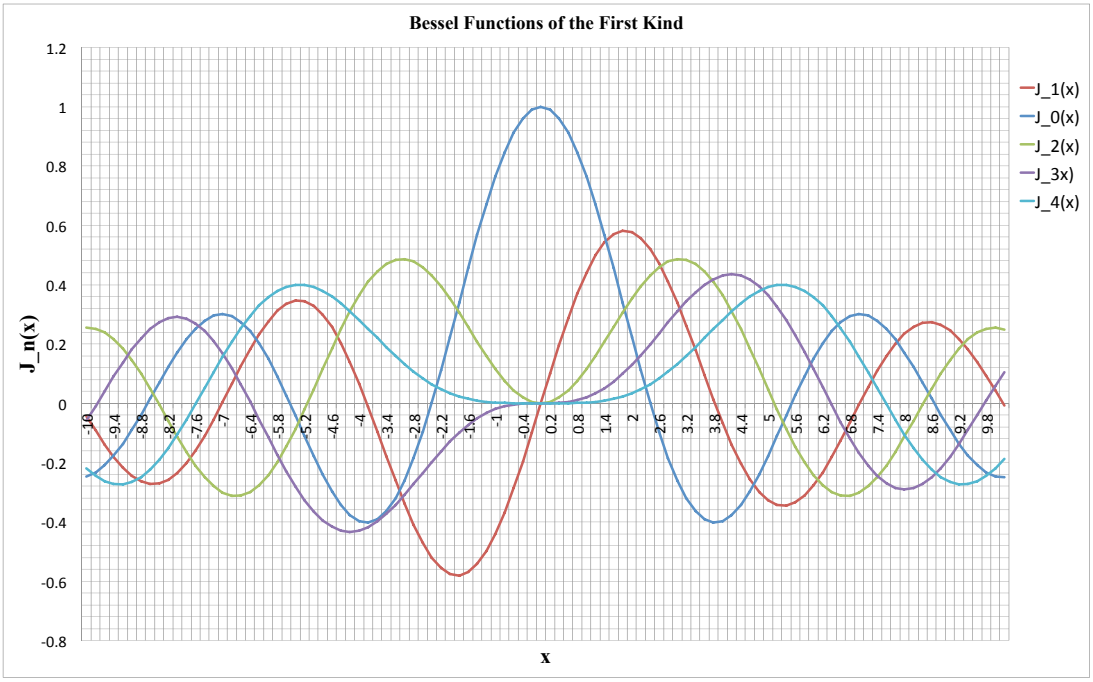

Figure B.6 Plot of first kind Bessel functions

Similar derivation can be done for TE mode in a cylindrical cavity and solution can be given with second kind of Bessel function in zero order (J_0'), however as it is mentioned before the interested in this studies is mainly focused on TM mode accelerating cavity structures.

The electric field is maximum where $J_0(x)$ is maximum and magnetic field is maximum at $J_0'(x')$ maximum for a TM_{01} mode pillbox cavity shown in Figure B.5. The electric and magnetic field characteristics of such kind of cavity is shown in Figure B.7.

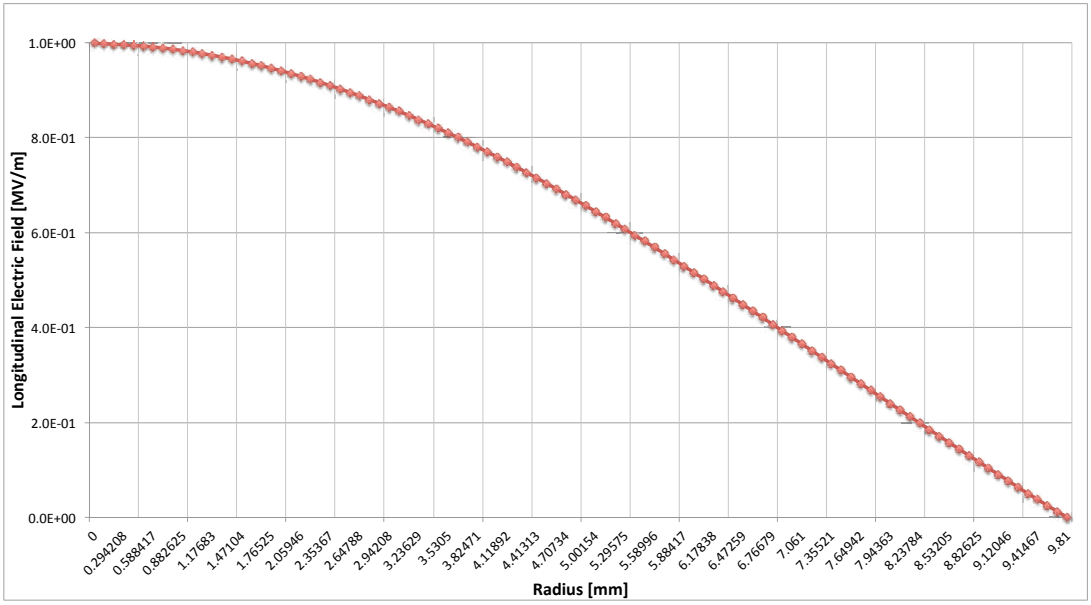

(a)

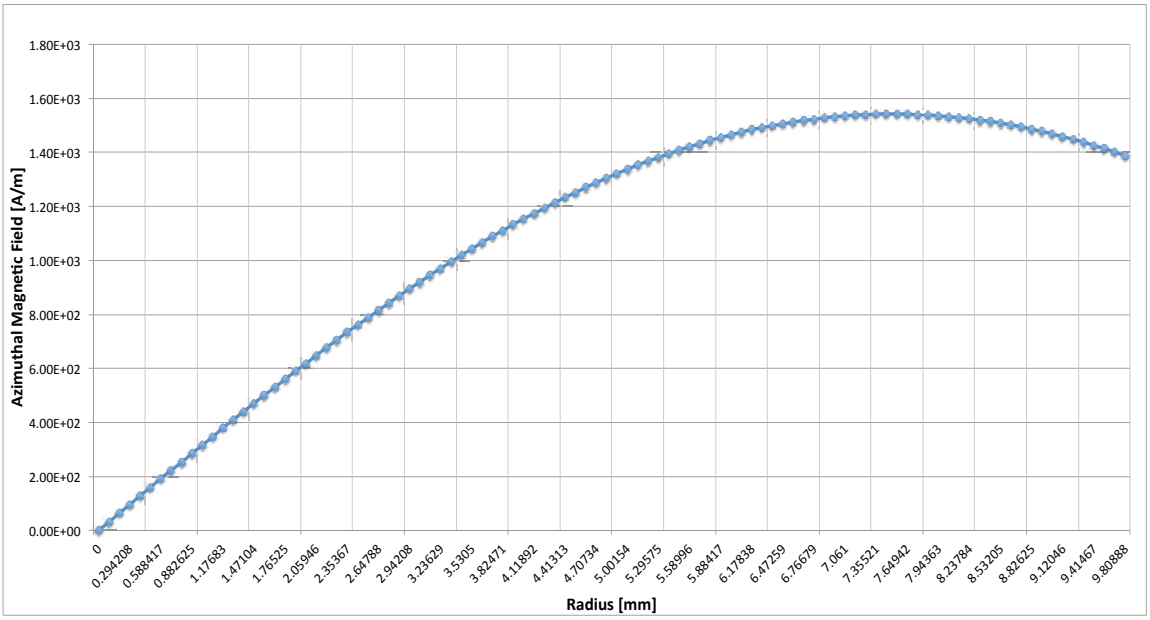

(b)

Figure B.7 (a) Electric and (b) magnetic field characteristics of a TM_{01} pillbox RF cavity

B8. Dispersion (Brillouin) Diagram of a Pillbox Cavity

It is known that a wave does not occur monochromatically in nature and a real wave exists in the form of a wave group consists of a superposition of waves of different frequencies and wave numbers.

Plotting w versus $f(k)$ from dispersion relation from Equation B.54 the Brillouin diagram can be achieved. The slope of the radius vector from the origin to a point on the hyperbola gives the phase velocity, which is the velocity of any phase of the wave travels:

$$\frac{w}{k} = \vartheta_{ph} \tag{B.57}$$

If the individual waves have very small phase velocity spreads, the wave envelope will tend to move with a velocity called the group velocity. In that case, the energy flow of the

electromagnetic wave helps to understand the group velocity due to electromagnetic energy can be described in terms of the motion of a wave packet whose frontier edge moves almost with group velocity, instead of the phase velocity. According to this the group velocity can be though as the velocity which energy propagates and in that case the slope of a point on the hyperbola gives the group velocity as it is shown in Figure B.8.

$$\frac{dw}{dk} = \vartheta_g \tag{B.58}$$

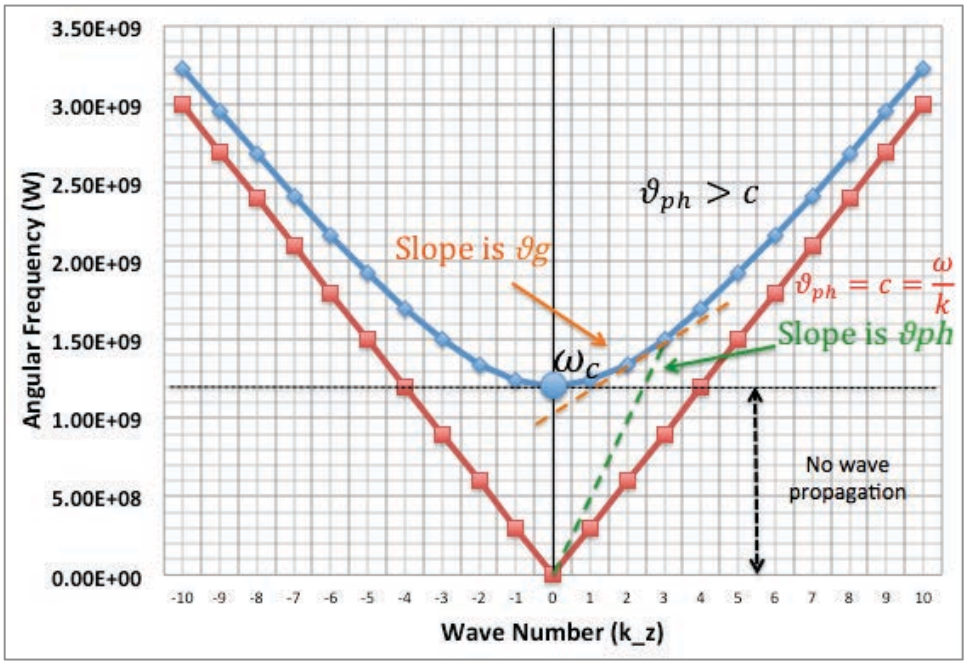

Figure B.8 Dispersion (Brillouin) diagram of a cylindrical (pillbox) cavity

B9. Slow-wave (Disc-loaded) Cavity

It is known that the phase velocity is greater than speed of light $(\vartheta_{ph} > c)$ in a pillbox cavity. A synchronism needs to be done between the TM-wave and particle, which means that the wave velocity (phase velocity ϑ_{ph}), and the particle velocity (ϑ_p) must be equal. Since $\vartheta_{ph} > c$ in a

pillbox cavity, in order to use electromagnetic waves for accelerating particles waves needs to be slowed down. This can be done inserting array of discs in a pillbox cavity as shown in Figure B.9. The purpose of these discs is to increase the capacitance per unit length of the cavity which contributes to slowing down the phase velocity of electromagnetic waves.

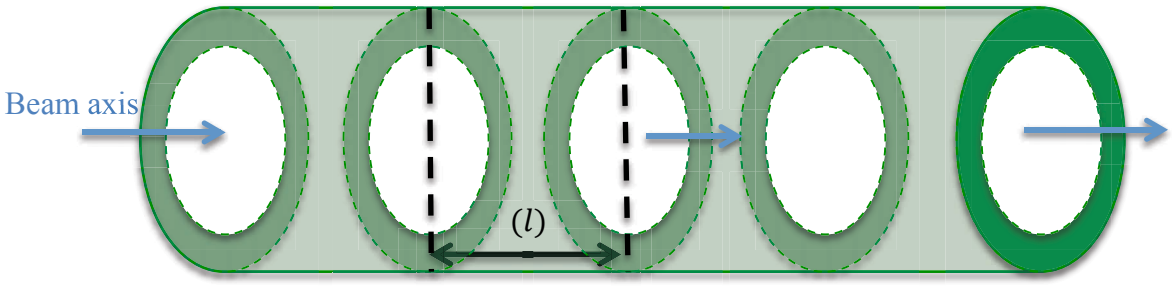

Figure B.9 Slow-wave disc-loaded cavity

The solution of this case can be achieved from wave equation applying Floquet's theorem for periodic structures, which states that for a given mode of oscillation and at a given frequency the wave function is multiplied by a constant such as $e^{-ik_0 l}$, when moving from one period (or cell length) (l) to the next one and also applying Fourier series to that periodic case as follows:

$$E_z(r,z,t) = E_z(r,z)e^{i(wt-k_0 z)} \tag{B.59}$$

$$E_z(r,z+l) = E_z(r,z) \tag{B.60}$$

$$E_z(r,z) = \sum^n a_n(r)e^{-i(2\pi n/l)z} \tag{B.61}$$

Introducing the expression above into wave equation for rotational symmetric waves provide the dispersion relation for periodic structures as:

$$e^{iwt}\sum^n a_n(r)e^{-i\left(k_0+\frac{2\pi n}{l}\right)z}\left[\frac{d^2a_n(r)}{dr^2}+\frac{1}{r}\frac{da_n(r)}{dr}+k^2a_n(r)\right]=0 \tag{B.62}$$

where,

$$k^2 = \left(\frac{w}{c}\right)^2 - \left[k_0+\frac{2\pi n}{l}\right]^2 \tag{B.63}$$

For each "n" there is a travelling wave with its own phase velocity.

$$\vartheta_{ph} = \frac{w}{k_0 + \frac{2\pi n}{l}} = \frac{w}{k_n} \tag{B.64}$$

The phase velocity is slowed down (compare Equation B.57 and Equation B.64) and now and n value can be found for the condition of acceleration that has ($\vartheta_{ph} = \vartheta_p$).

Now, $\vartheta_{ph} < c$ and then $k^2 < 0 = k'^2$ or $k = ik'$. The solution of the wave equation is can be expressed with Bessel functions of imaginary argument, which are called modified Bessel functions (I_0).

$$a_n(r) = A_n I_0(k'r) \tag{B.65}$$

where A_n is a constant.

In this case some assumptions need to be done to have the dispersion relation, so there is not any direct analytical solution. For a given frequency and the radius of the waveguide the dispersion relation can be solved numerically to determine the aspect ratio between cavity radius and iris radius of the obstacle.

B10. Travelling-wave (TW) and Standing-wave (SW) Disc-Loaded Cavities

In a disc-loaded pillbox cavity at each obstacle, the iris acts as a scatterer, resulting in a transmitted and a reflected wave. When the spacing between irises approaches multiple of the wavelength then the transmitted and reflected waves from successive irises interfere strongly and the dispersion curve differs drastically from that of an empty cavity.

In the cavity the electromagnetic energy propagates in both –z ($\vartheta_g < 0$) or +z ($\vartheta_g > 0$) directions. If it propagates in +z direction at the end of the cavity this energy can either be dissipated into a matched load or be reflected back by a shorting end wall. An RF cavity working in the first case is called travelling-wave (TW) disc-loaded structure. A generic TW disc-loaded structure is shown in Figure B.10.

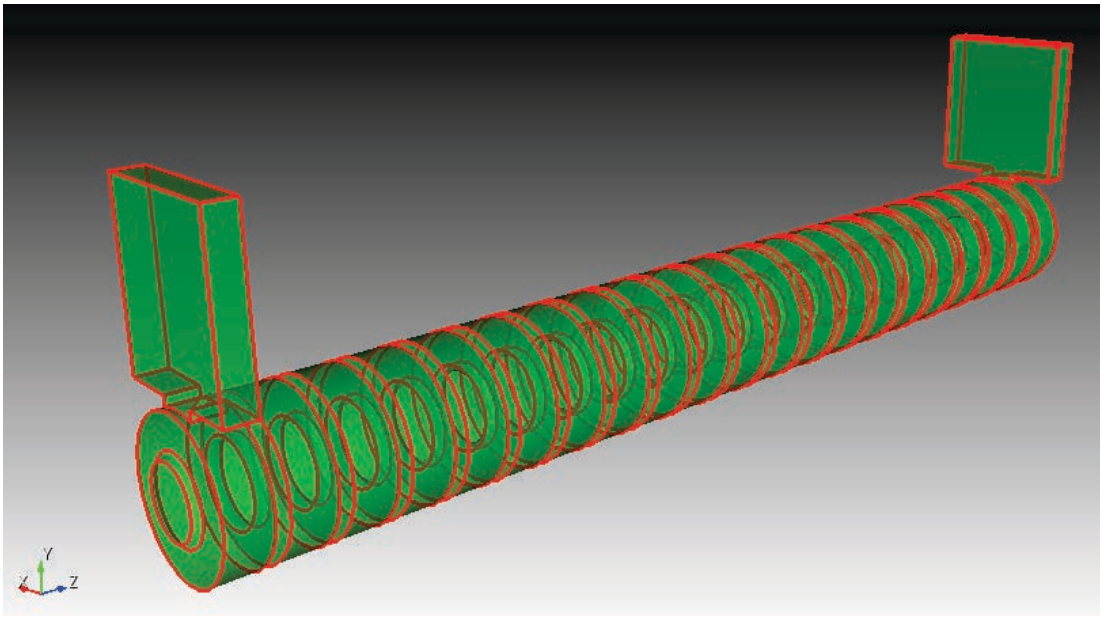

Figure B.10 The generic TW disc-loaded structure

For a given frequency, there has been an infinite series of space harmonics, from $n = -\infty$ to $n = -\infty$ and all space harmonics have the same group velocity, but different phase velocities. A TW cavity operates with the $n = 0$ space harmonic, because of the wave amplitude is largest in this case. The structure is usually designed so that the dispersion curve crosses the $\vartheta_p = c$ line for a phase advance per period (k_0) of $\frac{\pi}{2l}$ to $\frac{2\pi}{3l}$ as shown in Figure B.11. This type of RF cavities can be divided into two different categories as constant-impedance (CI) and constant-gradient (CG) TW structures. A constant-impedance structure has a uniform cell structure and electric

field attenuated (E_a) along the structure varies. In a constant-gradient structure the electric field attenuated along the structure is constant, therefore the structure dimensions have to be suitably varied along the accelerator.

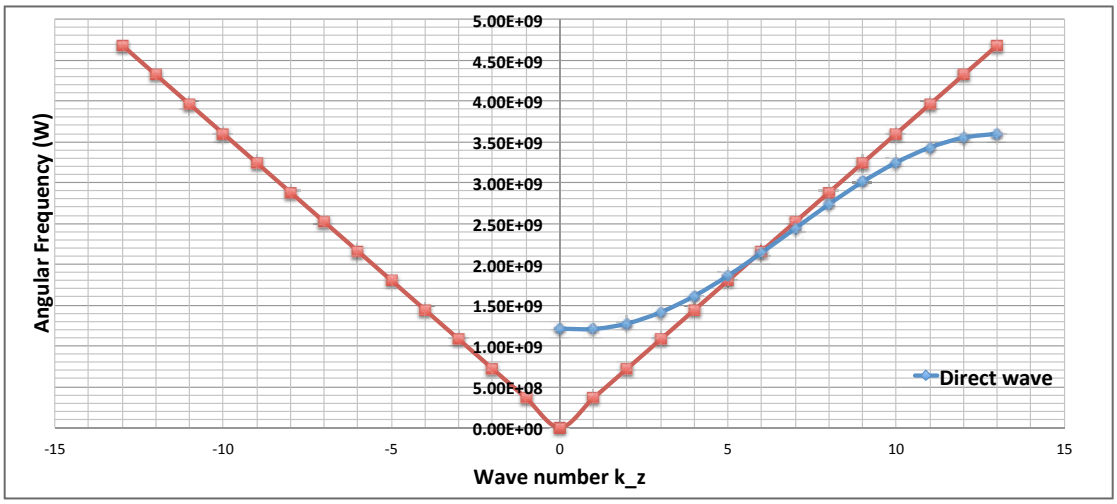

Figure B. 11 Dispersion (Brillouin) diagram of a travelling-wave (TW) disc-loaded cavity (each wave number represents 30° in phase)

If the energy is reflected back and forth between end walls, as in the second case, this type of RF cavity is called standing-wave (SW) disc-loaded structure. A generic SW disc-loaded structure is shown in Figure B.12.

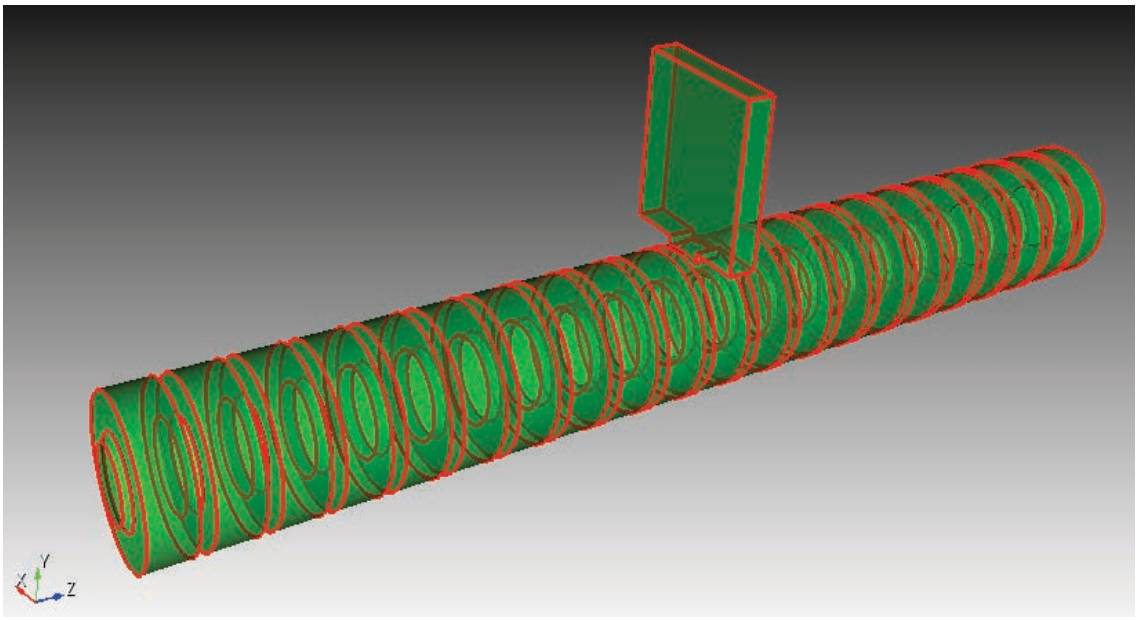

Figure B.12 The generic SW disc-loaded structure

A direct and a reflected sinusoidally varying wave, travelling with the same velocity but in opposite directions as shown in Figure B.13, combine to create a standing-wave pattern, so a standing-wave accelerator uses both the direct and the reflected wave to accelerate particles.

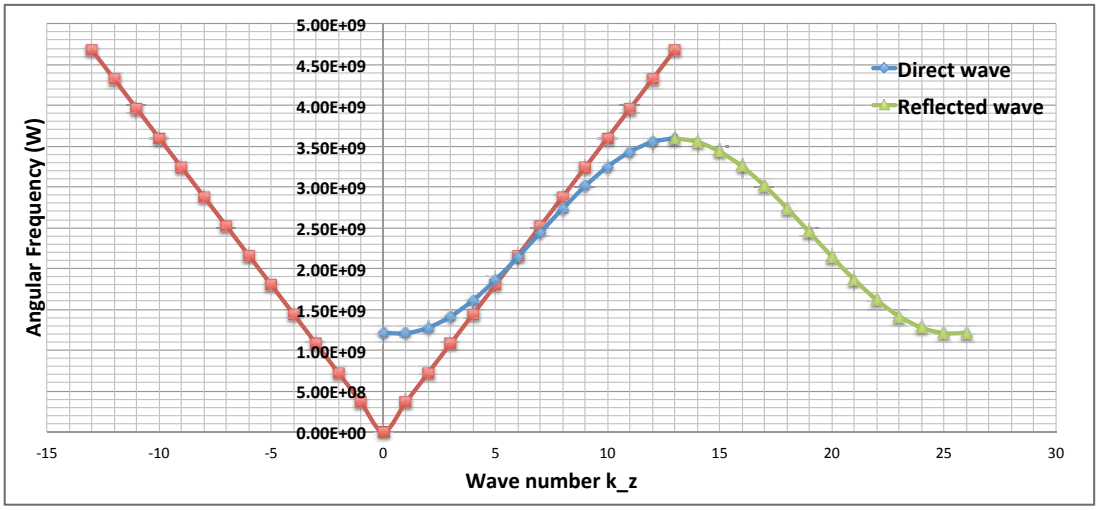

Figure B.13 Dispersion (Brillouin) diagram of a standing-wave (SW) cavity (each wave number represents 30° in phase)

B11. Figures of Merit for RF Cavity Design

In addition to wave and related mode characteristics mentioned so far some resonator (accelerating cavity) design parameters needs to be defined to better understand how they function. For that purpose there are several figures of merit commonly used for the characterization of the accelerating cavities.

Quality Factor ($\boldsymbol{Q}$)

Quality factor is the dimensionless parameter that indicates the ratio of the stored energy (U_s) in the oscillating resonator (excited accelerating cavity) to the dissipated energy per cycle (U_d) by damping processes. It is the measure of the strength of the damping of accelerating cavity's oscillations and determines the maximum energy the cavity can fill to with a given input power.

$$Q = 2\pi \times \frac{\mathrm{U_s}}{U_d} \tag{B.66}$$

$$Q = 2\pi f \times \frac{U_s}{P_d} \tag{B.67}$$

$$Q = \omega \times \frac{U_s}{P_d} \tag{B.68}$$

Stored Energy ($\boldsymbol{U_s}$)

Stored energy can be obtained integrating the Poynting vector over the volume as:

$$\int_{Vol} \frac{\partial}{\partial t}\left(\frac{\varepsilon_0}{2}|\mathbf{E}|^2 + \frac{\mu_0}{2}|\mathbf{H}|^2\right) dv \tag{B.69}$$

Energy is stored via electric field and magnetic field in the system, so when the energy is all stored in E field it is given by:

$$U_s = \frac{\varepsilon_0}{2}\int |\mathbf{E}|^2 \, dv \tag{B.70}$$

and when it oscillates at back to the B field by:

$$U_s = \frac{\mu_0}{2} \int |\mathbf{H}|^2 \, dv \tag{B.71}$$

It can be calculated for a pillbox cavity in terms of electric field peak (E_0) as:

$$U_s = \frac{\pi}{2} \varepsilon_0 l a^2 E_0 J_1^2(2.405) \tag{B.72}$$

Dissipated Power (P_d)

The dissipated power (P_d) is the power loss because of the resistance in the accelerating cavity walls. It is given by:

$$P_d = \frac{1}{2} \int_{Surf} R_s |\mathbf{H}|^2 ds \tag{B.73}$$

where R_s is the surface resistance can be written in terms of skin depth $\delta = \sqrt{\frac{2}{\omega \mu_0 \mu_r \sigma}}$ and conductivity (σ) as:

$$R_s = \sqrt{\frac{\pi f \mu_0 \mu_r}{\sigma}} = \frac{1}{\sigma \delta} \tag{B.74}$$

P_d can be calculated for a pillbox cavity in terms of electric field peak (E_0) as:

$$P_d = \pi \frac{\varepsilon_0}{\mu_0} a R_s E_0^2 J_1^2(2.405)[l + a] \tag{B.75}$$

Accelerating Voltage (V_0)

Accelerating voltage is the effective voltage ($V_0 T$), which T is the reduction fraction of the peak voltage between cavity walls caused by the sinusoidal time variation of the field in the cavity, seen by a charged particle while passing along the accelerating cavity.

Transit-time Factor (T)

The transit-time factor (T) is the ratio of the acceleration voltage (V_0) to the voltage which a particle can see with infinite velocity. An electric field on the axis seen by a particle with a velocity (v_p) can be expressed from Equation 3.58 as:

$$E_z(r,z,t) = E(r,z)\cos(wt + \emptyset) \tag{B.76}$$

where, $\emptyset$ represents the phase term $k_z z$.

The axial electric field amplitude E_0, which is $\frac{V_0}{l}$, where V_0 is the axial RF voltage in an accelerating cavity cell that has a length l:

$$V_0 \equiv \int_{-l/2}^{l/2} E(0,z)\, dz \tag{B.77}$$

Then, the energy gain can be expressed with Panofsky equation [ref] as:

$$\Delta W = qE_0 T \cos\emptyset\, l \tag{B.78}$$

Regardless of $\emptyset$, the energy gain of a particle in a harmonically time-varying field is always less than the energy gain in a constant direct current (DC) field equal to that seen by the particle at the center of the cavity cell. This is known as the transit-time effect. The transit-time factor (T) is the ratio of the energy gained in the time-varying RF field to a DC field of voltage $V_0 \cos\emptyset$. And it provides the reduction in the energy gain caused by the sinusoidal time variation of the field in the cavity cell. It provides more realistic accelerating field by taking into account the time variation of the field during particle transit through the structure. In the general form it is expressed as:

$$T = \frac{\int_{-l/2}^{l/2} E(0,z)\cos\omega t dz}{\int_{-l/2}^{l/2} E(0,z) dz} \tag{B.79}$$

Accelerating Gradient (E_a)

Accelerating gradient is the effective voltage per unit length:

$$E_a = \frac{V_0 T}{l} = E_0 T \tag{B.80}$$

Shunt impedance (R_{sh})

Shunt impedance is the measure of the strength which an eigenmode of an accelerating cavity interacts with charged particles on a defined line. It relates the accelerating voltage and the power dissipation by:

$$R_{sh} = \frac{V_0^2}{P_d} \tag{B.81}$$

Group velocity (ϑ_g)

Group velocity can be defined as the velocity of the electromagnetic energy flow in terms of the power (P_z) of the travelling wave, and the stored energy per unit length (U_s):

$$\vartheta_{EM-energy\ flow} = \vartheta_g = \frac{P_z}{U_s} \tag{B.82}$$

B12. Accelerating Field and Power Attenuation in a CI-TW Disc-Loaded Cavity

Along a TW structure the electric field is attenuated and certain amount of power is dissipated in the cavity walls. Due to the fact that in here, it is convenient to introduce some important relationships between the longitudinal accelerating field amplitude (E_z) and the power (P_{TW}) of the travelling wave, and the stored energy per unit length (U_s).

The travelling-wave power can be obtained by integrating the Poynting vector over a radial aperture (a):

$$P_{TW} = \int_0^a E_r \, H_\theta 2\pi r d \tag{B.83}$$

The dissipated power (P_d) in the resistive cavity walls can be written in terms of travelling-wave power along the propagation direction as:

$$-\frac{P_{TW}}{dz} \tag{B.84}$$

The group velocity, ϑ_g, is also the energy flow velocity, and relates the TW power to the stored energy per unit length U_s from Equation B.82 as:

$$P_{TW} = \vartheta_g U_s \tag{B.85}$$

Eliminating U from Equation B.54 and Equation B.68 yields a differential equation for TW power:

$$\frac{dP_{TW}}{dz} = -\frac{\omega P_{TW}}{Q\vartheta_g} \tag{B.86}$$

Using the definition for the field attenuation per unit length as $\alpha_0 = \frac{\omega}{2Qv_g}$, this equation becomes:

$$\frac{dP_{TW}}{dz} = -2\alpha_0 P_{TW} \tag{B.87}$$

In this thesis the main interest is CI disc-loaded TW structure for practical fabrication reasons. Due to this type of structure has uniform cell geometry these parameters are independent of z. This is very useful while we are introducing the power attenuation along the structure due to attenuation per unit length is constant, so then the solution to the Equation B.87 can be written as:

$$P_{TW}(z) = P_0 e^{-2\alpha_0 z} \tag{B.88}$$

If the same procedure applied to the accelerating gradient:

$$\frac{E_a}{dz} = -\frac{\omega E_a}{2Q\vartheta_g} = -\alpha_0 E_a \tag{B.89}$$

Then the solution will be:

$$E_a(z) = E_0 e^{-\alpha_0 z} \tag{B.90}$$

The relationship between TW power and accelerating gradient can be expressed in terms of the parameters defined above:

$$E_a^2 = \frac{\omega R_{sh} P_{TW}}{Q \vartheta_g} \tag{B.91}$$

The total power attenuation at the end of the structure ($z = L$) can be found using Equations B.88 and B.90 as:

$$P_{TW}(L) = P_0 e^{-2\alpha_0 L} \tag{B.92}$$

$$E_a(L) = E_0 e^{-\alpha_0 L} \tag{B.93}$$

$\alpha_0 L$ describes the total power attenuation for the structure. This can be defined as the total power attenuation parameter as:

$$\tau_0 = \alpha_0 L = \frac{\omega L}{2 Q v_g} \tag{B.94}$$

Then, the travelling wave power and accelerating gradient along the structure can be expressed in terms of input power P_0 and field E_0 as:

$$P_{TW}(z) = P_0 e^{-2\tau_0} \tag{B.95}$$

$$E_a(z) = E_0 e^{-\tau_0} \tag{B.96}$$

The main aim in here is to maximize the energy gain of the particle. This can be done optimizing the length of the travelling-wave structure. The energy gain of a synchronous particle of charge q riding at a phase $\emptyset$ relative to the crest of the wave can be given with the integral as:

$$\Delta W = qV = q\cos\emptyset \int_0^L E_a(z) dz \tag{B.97}$$

the solution of this integral can be found for a given input field E_0 at the beginning of the structure ($z = 0$) from Equation B.96 as:

$$= qE_0L\frac{1-e^{-\tau_0}}{\tau_0}\cos\emptyset \tag{B.98}$$

Equation B.98 will be maximum for $\tau_0 \cong 1.26$ and then maximum energy gain can be written as:

$$\Delta W_{max} = qV_{max} = 0.57qE_0Lcos\emptyset \tag{B.99}$$

The same result for ΔW_{max} can be achieved in terms of P_0 by writing the equation relates P_0 to E_0 as:

$$= q\sqrt{2R_{sh}P_0L}\frac{(1-e^{-\tau_0})}{\sqrt{\tau_0}}\cos\emptyset \tag{B.100}$$

where,

$$E_o^2 = 2R_{sh}\alpha_0P_0 \tag{B.101}$$

and then,

$$\Delta W_{max} = 0.903\sqrt{R_{sh}P_0L}cos\emptyset \tag{B.102}$$

If the R_{sh} and P_0 are known the energy gain over the structure depends on τ_0 according to Equation B.100. From Equation B.94 in addition to L value if Q is also known the optimum ϑ_g can be determined. τ_0 can be controlled by the group velocity which can be given in the form of Equation B.103 for a disc-loaded TW accelerator as:

$$\vartheta_g = \frac{\mathrm{d}\omega}{dk_z} = \frac{2(2.405)c}{3\pi J_1^2(2.405)}\left(\frac{\mathrm{a}}{R}\right)^2 \sin\psi e^{-\alpha h} \tag{B.103}$$

where a is the inner radius of the cavity, R is the outer radius of the cavity, h is the disc thickness, ψ is the phase advance per cell can be found from

$$\psi = k_z l = \frac{2\pi}{\lambda} l \tag{B.104}$$

and α is the is the attenuation per unit length of the field for the TM_{01} mode can be written as:

$$\alpha = \sqrt{(2.405/a)^2 - \omega^2/c^2} \approx 2.405/a \tag{B.105}$$

The value of τ_0 also affects the filling time of the cavity, which defined as the time for the energy to propagate at the group velocity along the CI TW structure:

$$t_f = \frac{L}{\vartheta_g} = \tau_0 \frac{2Q}{\omega} \tag{B.106}$$

For the optimum case, $\tau_0 \cong 1.26$, in order to maximize the energy gain in a given length *L,* the following condition should be met in Equation B.106:

$$t_f \cong 2.52 \frac{Q}{\omega} \tag{B.107}$$

or

$$L = 2.52 \frac{Q\vartheta_g}{\omega} \tag{B.108}$$

and at the end of the accelerator structure Equations B.95 and B.96 consumption ratios of the input power and the field, and can be given as:

$$P_{TW}(L) = 0.08P_0 \tag{B.109}$$

$$E_a(L) = 0.28E_0 \tag{B.110}$$

According to figures of merit for RF cavities and the descriptions mentioned above the interest in this thesis is more likely a constant-impedance TW linear accelerator structure for several reasons, which are easy design and fabrication because of uniform cell structure, and efficient power extraction at the end of structure for the optimized case less than 10% of the input power goes into the matched load at the end of this structure as calculated in Equation B.109.

APPENDIX C: SOFTWARE COMPARISON AND SIMULATION METHODOLOGY

C1. Software Comparison

Computer simulation tools for RF structure design are a necessity due to the need for accurate predictions of fundamental parameters such as frequency (f), the quality factor (Q_0) and the shunt impedance (r_{sh}) etc. Each simulation code uses different approaches for the mesh generation and simulation techniques while calculating RF structure parameters. For this reason, some of the important properties (advantages and disadvantages) of the simulation codes that were used in this thesis are discussed in this appendix.

C1.1. SUPERFISH / POISSON

SUPERFISH is a well-known, semi open-source code used for RF structure simulation. It was developed and is maintained by the Los Alamos National Laboratory Computer group. It has been used for many years for the design of a large variety of RF structures. It is a 2-dimensional (2D) code with cylindrical symmetry and uses a finite difference method (FDM) for solving Maxwell Equations. The overall workflow of SUPERFISH [99] is shown in Figure C.1.

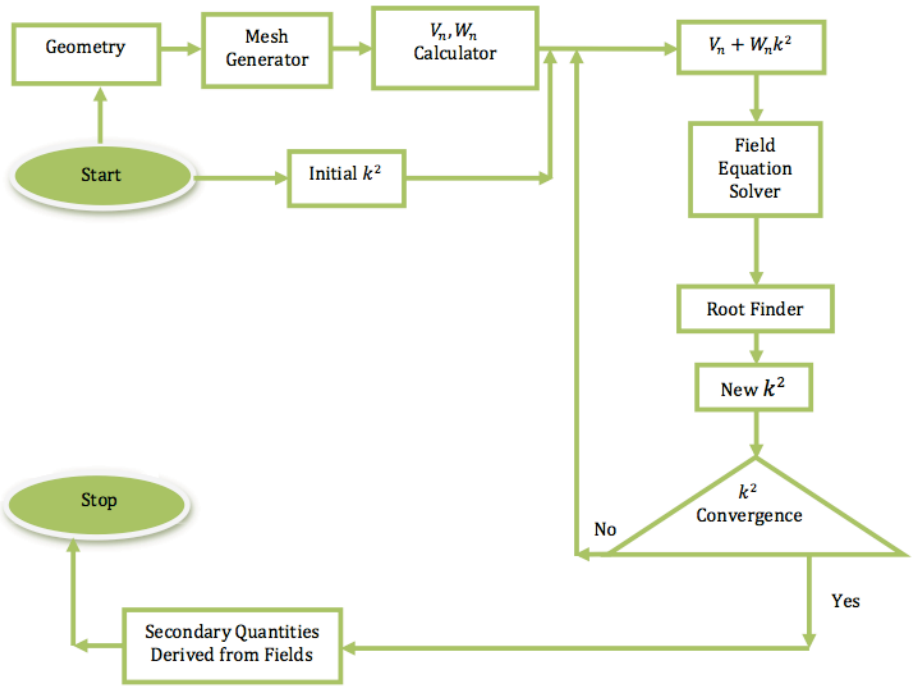

Figure C. 1 The workflow diagram of SUPERFISH

Its features are:

- Freely available code generated by LANL Computer Group
- Automesh (with manually-controlled adaptive mesh capability)

  Meshing scheme:

  - 2D-triangles
- Direct and iterative matrix solvers
- Eigen mode matrix solver

SUPERFISH was preferred for our 2D simulations because of its results Submissi, 101] had been consistent with actual measurements previously [102, 103], and its effectiveness in time and CPU usage.

C1.2. Advanced Computational Electromagnetics 3D Parallel (ACE3P) Suite

Advanced Computational Electromagnetics 3D Parallel (ACE3P) is a 3D massively parallel (>10k CPUs) electromagnetic simulation suite based on the high-order finite element method (FEM) for solving Maxwell Equations. It was implemented in C++/MPI and was developed by the SLAC National Laboratory. The suite consists of frequency and time domain modules for research and design of particle accelerators. It is ideally suited for the high-performance computing (HPC) platform at NERSC, Lawrence Berkeley National Laboratory (Berkeley Lab)-(LBNL or LBL). Use of these codes on the NERSC system enables one to perform large-scale electromagnetic simulations that can be used for improving existing facilities and optimizing the design of future machines. During this thesis the Hopper, Edison and Cori systems were used for the simulations performed. Some important specifications of each of these systems is discussed briefly here.

- **Hopper**

Hopper [104] was NERSC's first petaflop system, a Cray XE6, with a peak performance of 1.28 Petaflops/sec, 153,216 compute cores, 212 terabytes (TB) of memory, and 2 petabytes (PB) of storage. Hopper placed number 5 on the November 2010 Top 500 Supercomputer list [105]. It was retired on Dec 15, 2015.

- **Edison**

Edison [106] is a Cray XC30, with a peak performance of 2.57 petaflops/sec, 133,824 compute cores, 357 TB of memory, and 7.56 PB of storage.

- **Cori**

Cori [107], the NERSC's newest supercomputer is a Cray XC40. It ranked as the 5th most powerful supercomputer in the world on the November 2016 list of Top 500 supercomputers in

the world. It is unique among supercomputers of its size as it has two different kinds of nodes, 2,004 Intel Xeon "Haswell" processor nodes and 9,300 Intel Xeon Phi "Knight's Landing" nodes. Cori also features a 1.5 PB Cray Data Warp Burst Buffer with I/O operating at a world's-best 1.5 TB/sec.

The 3-dimensional (3D) computer-aided design (CAD) and post-processor are done using Trelis and Paraview softwares, respectively.

ACE3P consists of the following modules [108]:

- Omega3P, an electromagnetic eigen solver;
- S3P, a frequency-domain S-parameter solver;
- T3P, a time-domain solver for transients and wakefield computations;
- Track3P, a particle tracking code for multipacting and dark current studies;
- Pic3P, a particle-in-cell code for self-consistent particle and field interactions;
- TEM3P, a multi-physics code for integrated electromagnetic thermal and mechanical effects.

ACE3P can also be used directly in conjunction with:

- IMPACT, a beam dynamics code for realistic calculations of beam emittance in accelerators in the presence of wakefields, space charge, and radiative self-fields;
- Fluka, a radiation code for evaluating radiation effects in materials.

A typical ACE3P simulation workflow also includes pre-processing of the model and mesh building in Trelis and post-processing results in Paraview as shown in Figure C.2. While pre-processing and post-processing procedures can be both performed on a local desktop, ACE3P solvers run on supercomputers at NERSC.

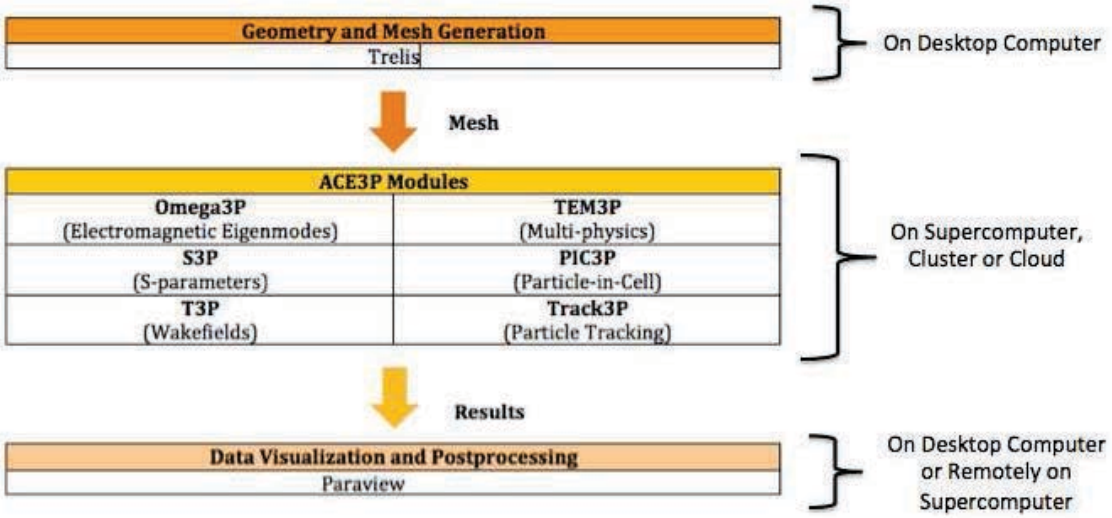

Figure C.2 The typical workflow of ACE3P

The capabilities of the code can be listed as:

- Code usage and HPC resources are free within US
- HPC speed (previously not possible)
- Import/export of 3D structures
- Automatic adaptive mesh generation and refinement

  Meshing scheme:

  - 3D-tetrahedrons
- Higher-order finite elements (p =1 to 6)
- Inclusion of skin effect and losses

- Direct and iterative matrix solvers
- Eigen mode matrix solver

ACE3P Suite was our preferred ultimate modeling tool due to its HPC capability that provided very quick turnaround time while achieving very accurate results for 3D RF structure designs both in the frequency (OMEGA3P and S3P) and time (T3P) domains.

C1.3. ANSYS

ANSYS software [102] is one of the well-known standard commercial tools for high-frequency electromagnetic field simulations. It uses FEM for solving Maxwell Equations. The general workflow of ANSYS is shown in Figure C.3 [109].

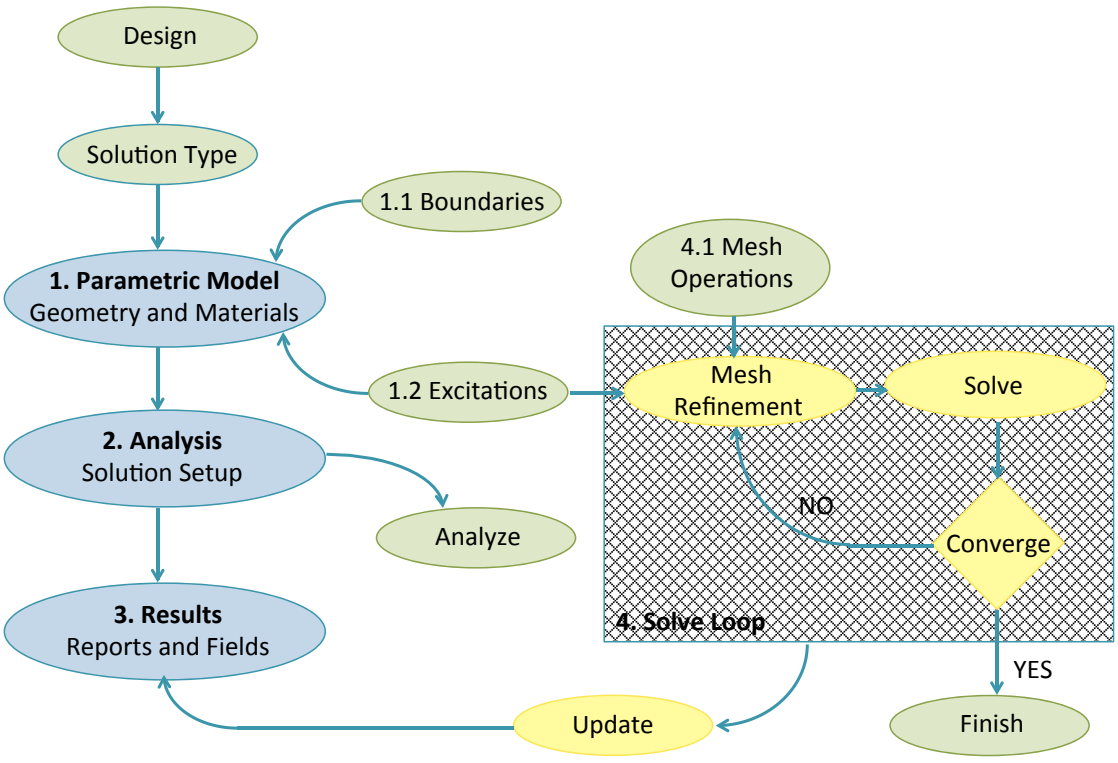

Figure C.3 The general workflow of ANSYS

The capabilities of the code can be listed as:

- HPC
- Accurate full-wave EM simulation
- Import/export of 3D structures
- Automatic adaptive mesh generation and refinement

  Meshing scheme:

  - 2D-triangles
  - 3D-tetrahedrons
- Adaptive Lanczos-Padé Sweep for fast frequency sweeps
- Inclusion of skin effect and losses
- Direct and iterative matrix solvers
- Eigen mode matrix solver

ANSYS software was used as a supporting code for our accuracy checks.

C2.Simulation Methodology

The parameters of a pillbox cavity can be determined analytically; however, for the modified pillbox (disc-loaded slow-wave) structures the solution of the dispersion relation are more readily done numerically. As a first check the simulated parameters of a pillbox cavity were compared to the known analytic solution. The following codes were checked: SUPERFISH, ANSYS High Frequency Structural Simulator (HFSS) [110] and ACE3P's OMEGA3P. The electric and magnetic field distributions for each code are shown in Figures C.4, C.5 and C.6. The parameter comparison between analytically calculated and simulated results are presented

and in Table C.1. The computed electromagnetic field distributions and parameters agree well with the analytical values discussed in detail at Appendix B.

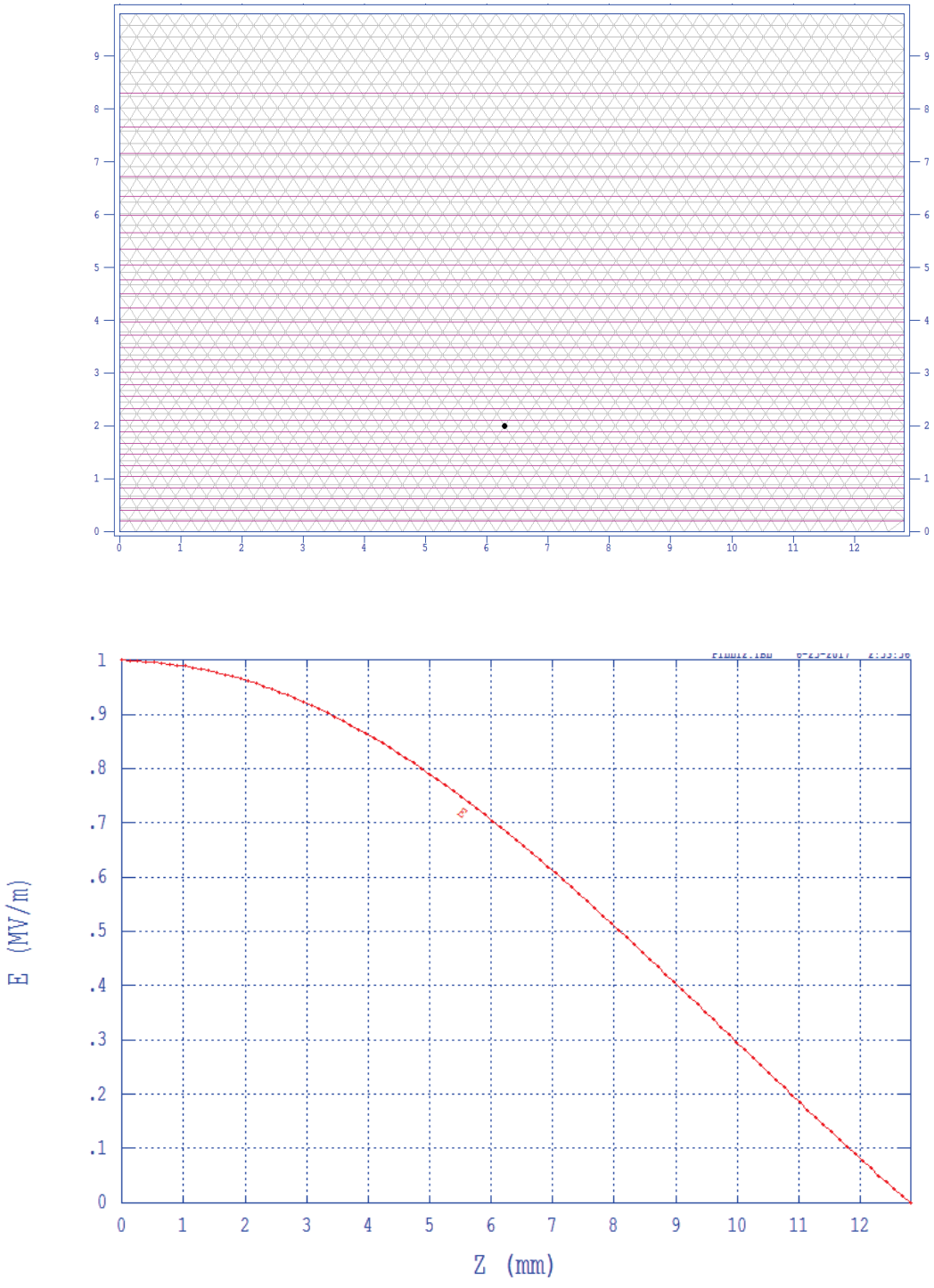

(a)

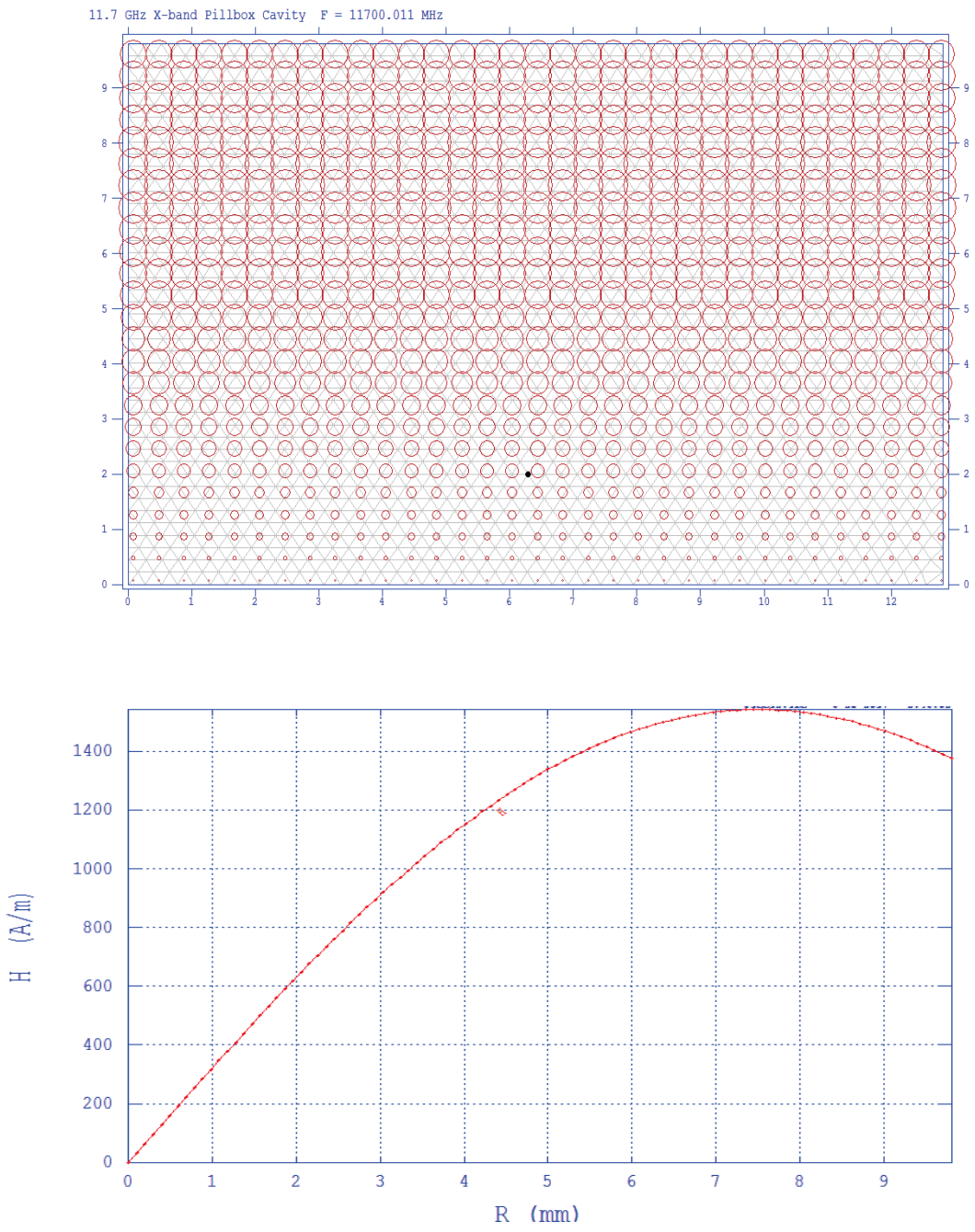

(b)

Figure C. 4 The (a) electric and (b) magnetic field distributions of a 11.7 GHz pillbox cavity using SUPERFISH (Vertical axis represent the radius (R) and horizontal axis represent axial distance (z) in the pillbox cavity cross section)

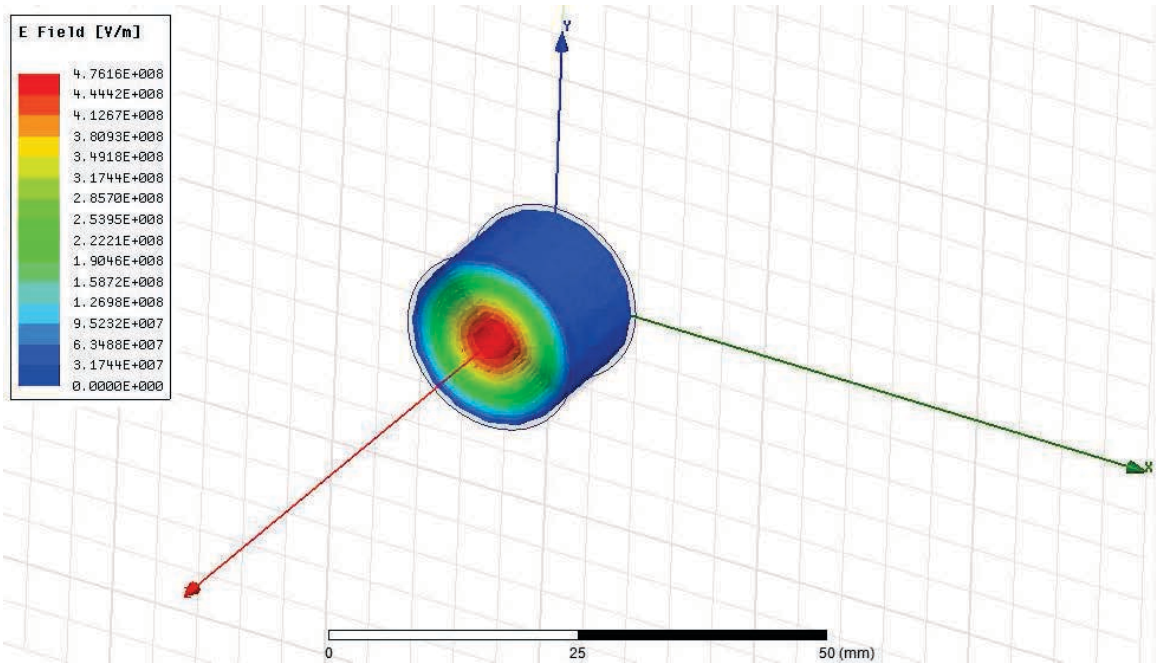

(a)

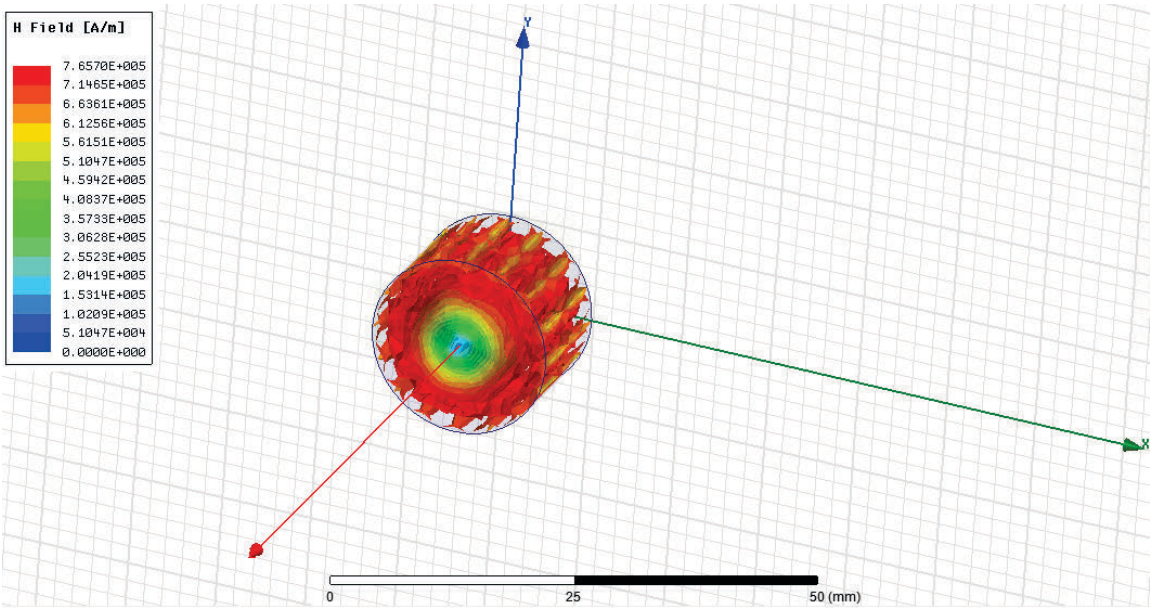

(b)

Figure C.5 (a) Electric and (b) magnetic field distribution of a 11.7 GHz pillbox cavity using HFSS

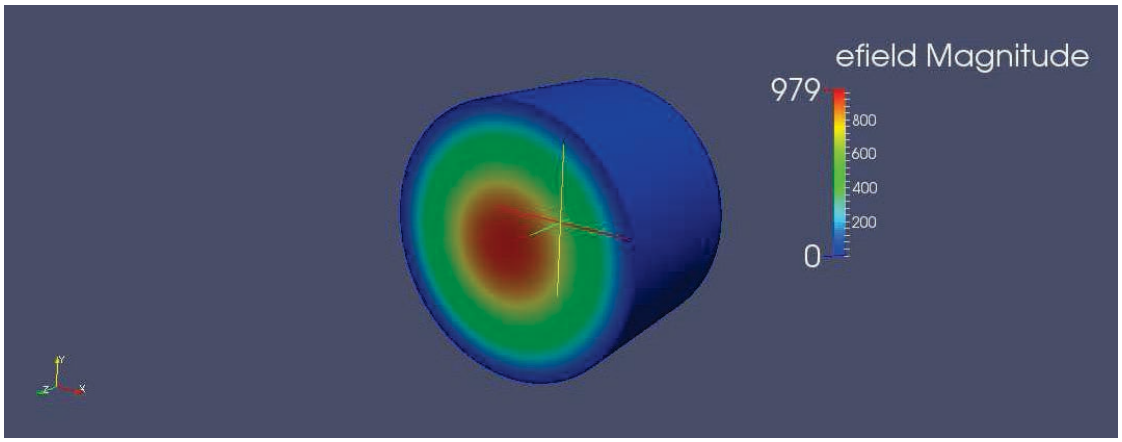

(a)

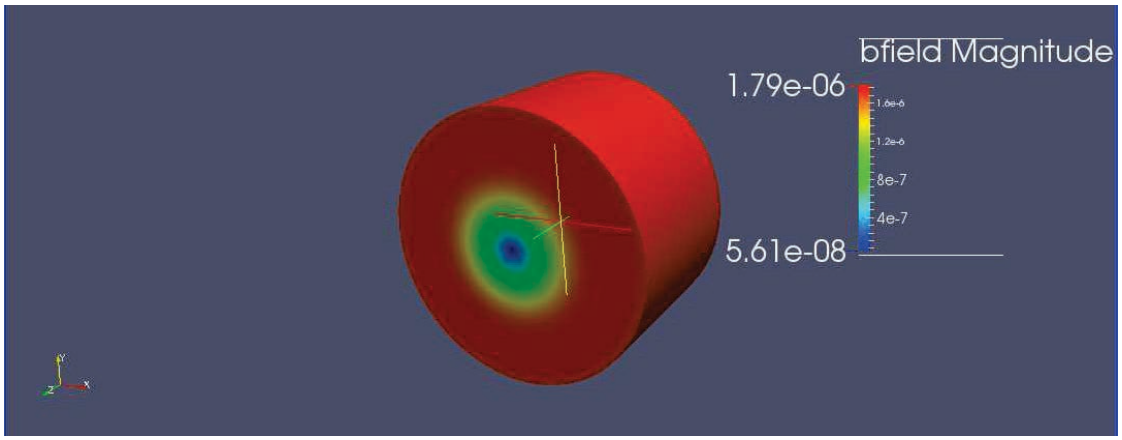

(b)

Figure C.6 (a) Electric and (b) magnetic field distribution of a 11.7 GHz pillbox cavity using OMEGA3P

Table C. 1 Analytical and simulation result comparison for a copper pillbox RF cavity

Parameters	Symbol	Analytical	SUPERFISH	OMEGA3P	HFSS
Cell Radius [m]	R	0.00987	0.00987	0.00987	0.00987
Resonance Frequency [GHz]	f_0	11.700	11.70001	11.70001	11.700012
Shunt Impedance per Unit Length [MΩ/m]	r_{sh}	4.42	4.28	4.32	4.3
Unloaded Quality Factor	Q_0	9170.5	9161.1	9168	9165
Stored Energy [μJ]	U_s	4.64	4.7	4.89	4.74
Dissipated Power [W]	P_d	37.2	38.32	37.8	38.1

APPENDIX D: ALTERNATIVE MAC DESIGN

The optimization for the MAC can follow a different path compared with the PEC.

D1. MAC Alternative Design Consideration

In this design our main aim is to maximize the energy gain in an optimum length and get the highest integrated potential through one or more cavities; therefore, our design was changed to a new geometry and phase advance from $2\pi/3$ to another mode, that of $5\pi/6$ which will be describe in detail below. Improvements in performance can be found by reducing the group velocity. To decrease the group velocity the iris radius value can be reduced, but at a certain point it is no longer practical to reduce the iris radius. Then, the only variable that can change the group velocity in Equation B.103 will be ψ. This argues for a large TW mode number defined as n in $2\pi/n$. This is shown in Figure D.1 where the relative velocity coming from the sine term is plotted versus n.

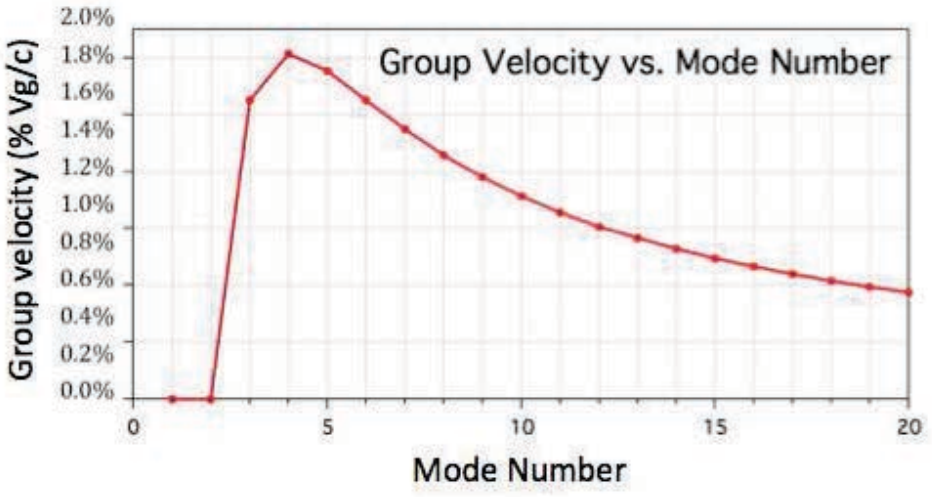

Figure D.1 The group velocity versus mode number

A value of n equal to 2 is the SW π-mode. This certainly would argue that that the $2\pi/3$ mode is not the best choice and that a mode number of more like 8 or 10 would be better and might still be practical.

On the other hand, as it is seen in Figure D.1, choosing a proper value such that 2<n<3 can give us the solution. For that reason, for an $a/\lambda = 0.1$ single cell geometry, moving the RF phase advance to $5\pi/6$ and using a longer cell length compared to that of the $2\pi/3$ mode in order to preserve synchronous acceleration of the electron bunch slows down the group velocity to 0.95% c as shown in Figure D.2. Further, it increases α, the damping constant along the length of the structure, allowing more efficient deposition of the RF power in the accelerating structure.

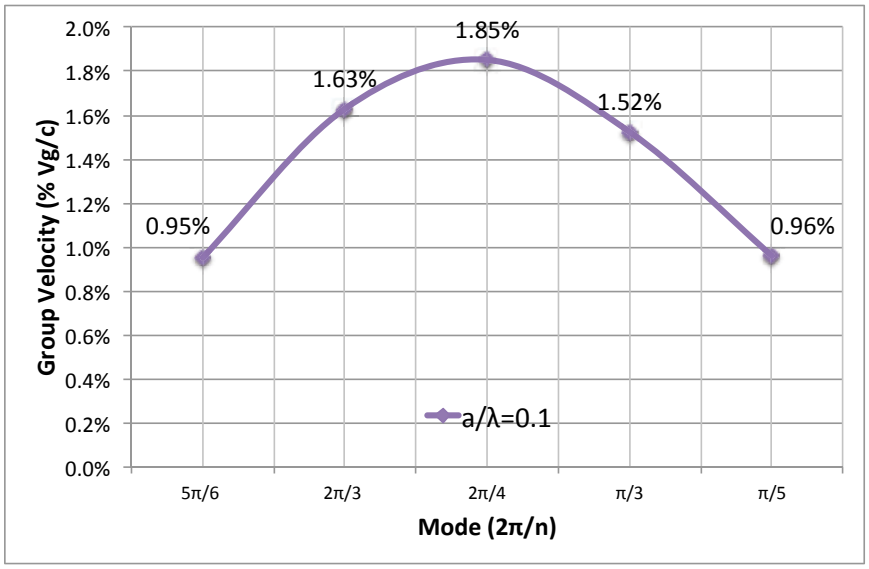

Figure D.2 Group velocity comparison for $2\pi/3$ and $5\pi/6$ mode $a/\lambda = 0.1$ single cell geometry

Figure D.3 shows the cavity fields, both the electric and magnetic, as computed by SUPERFISH for both the Neumann and Dirichlet boundary conditions as specified at the end walls for the accelerating cavity (ibid 43).

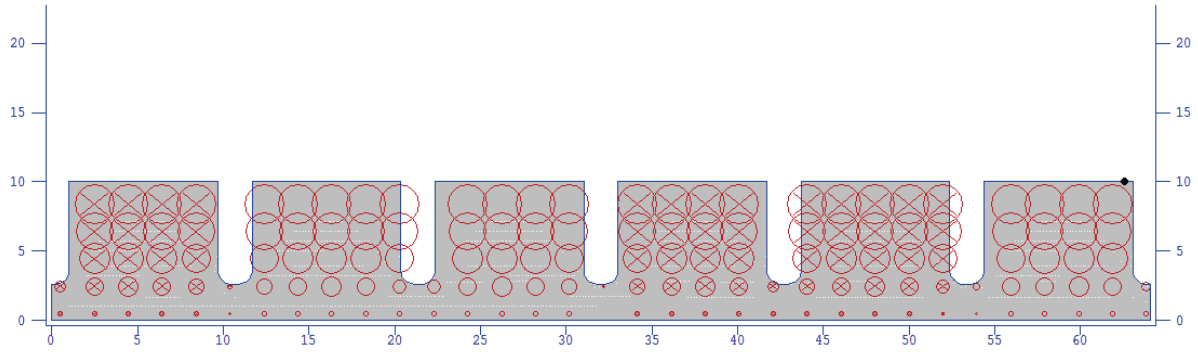

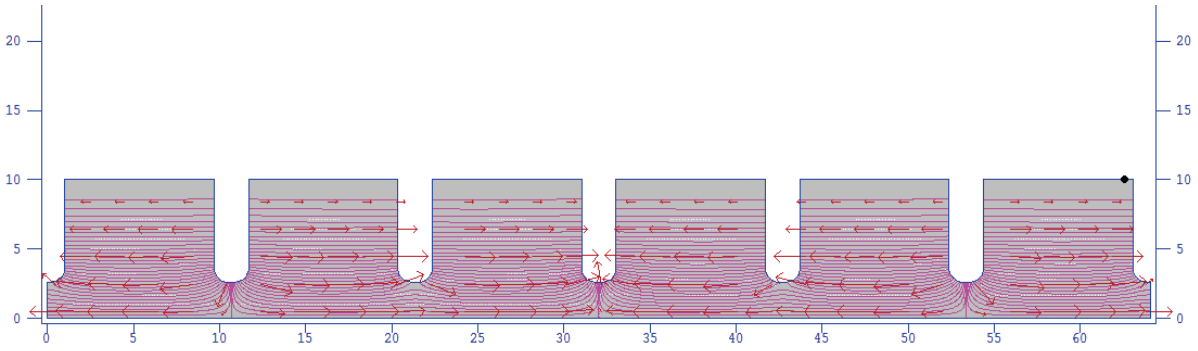

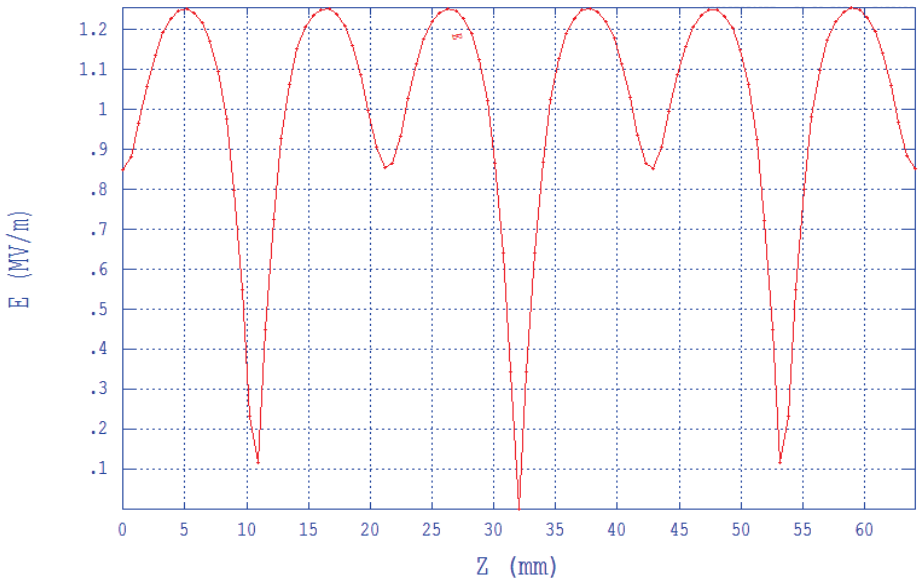

(a)

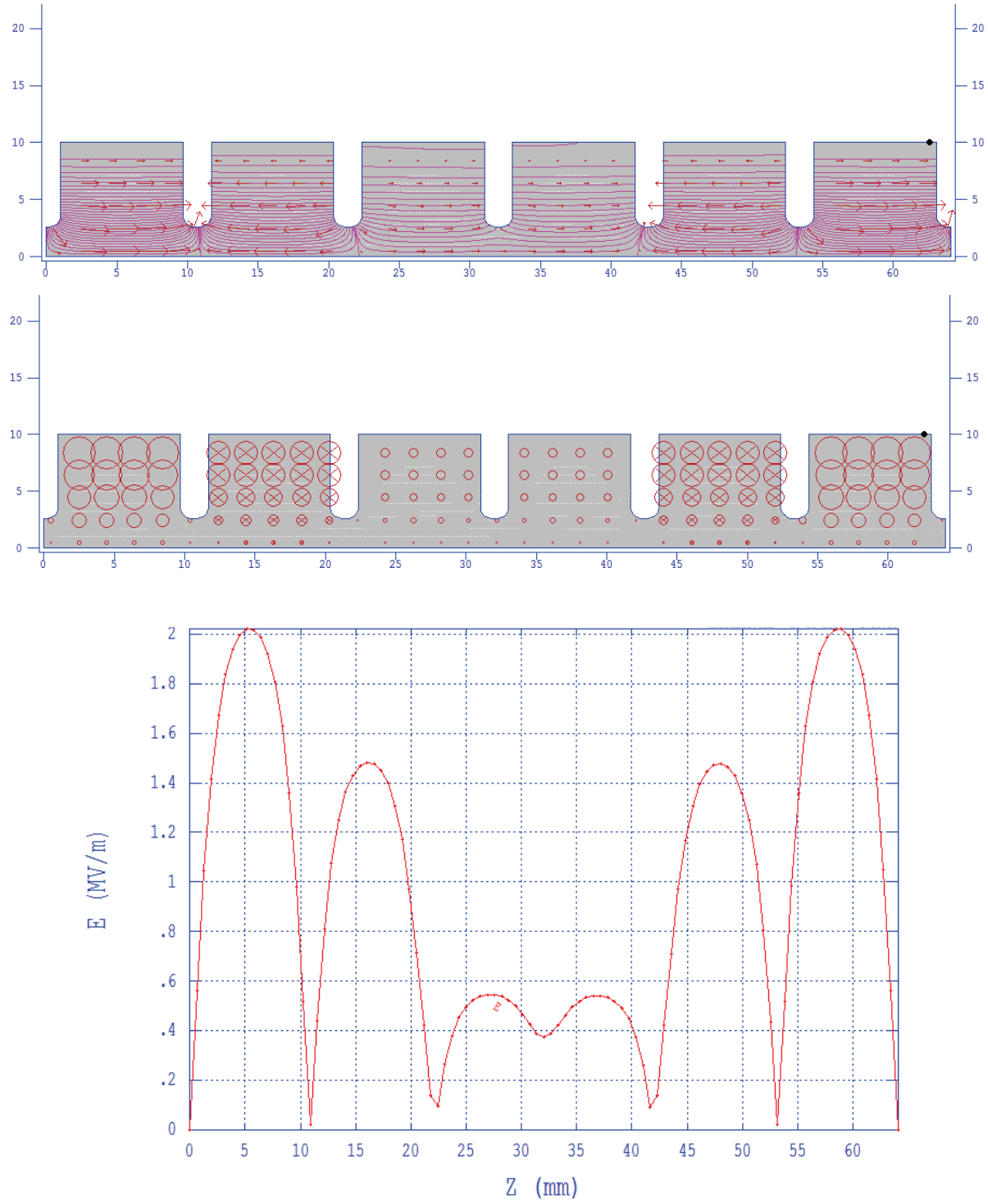

(b)

Figure D.3 The electric and magnetic field distributions, and magnitude of electric field for $a/\lambda = 0.10$ TW PEC in (a) the Neumann boundary condition at end walls for $5\pi/6$ mode (b) and the Dirichlet boundary condition at end walls for the $5\pi/6$ mode

Table D.1 gives the resulting geometry parameters for a $5\pi/6$-mode accelerating structure. This cavity will see a single, relatively low charge electron bunch, so the aperture requirements are not as severe. Further, our aim is to maximize the overall integrated voltage seen by the beam during its passage. This clearly argues for a $5\pi/6$-mode MAC structure that has higher shunt impedance and shorter than a $2\pi/3$-mode MAC.

Table D.1 Parameters for the $5\pi/6$ mode MAC

Parameter	Symbol	Value
Resonance Frequency [GHz]	f_0	11.7
Phase Advance per Cell [Radian]	ψ	$5\pi/6$
Iris Radius to Wavelength Ratio	a/λ	0.1
Iris Radius [m]	a	0.00256
Cell Radius [m]	R	0.01012
Disk Thickness [m]	h	0.002
Unloaded Quality Factor	Q_0	7598.7
Section Length [m]	L	0.7474
Shunt Impedance per Unit Length [MΩ/m]	r_{sh}	153.7
Group Velocity	ϑ_g	0.095c

In a constant impedance structure, the field drops as a function of length due to ohmic losses. As it is mentioned earlier in Chapter 3 and in detail at Appendix B in order to maximize the energy gain for a given length L, the condition should be met according to Equation 3.2 or 3.3 [equivalently Equation B.107 or B.108].

For the given values of $2\pi/3$ phase advance per cell design in Table 4.3, $L = 1.08$ m and $5\pi/6$ phase advance per cell design in Table D.1, $L = 0.747$ m.

Instead of using the simplest configuration to immediately transport the power via waveguide from the PEC coupler to a single $2\pi/3$ mode 1.08-m long MAC, the alternate, higher shunt impedance $5\pi/6$ mode ~0.75-m long MAC structure provides the same potential across the structure. The results for both cases are given in Table D.2.

Table D.2 The available potential and the maximum energy gain values using alternative $5\pi/6$ mode MAC

Parameter	Symbol	Value for $\psi = 2\pi/3$	Value for $\psi = 5\pi/6$
Number of X-band MAC Cell		126	72
Total Length per Section [m]	L	1.08	0.747
Available Gradient (1 Section) [MV/m]	E_{a_1}	20.0	20.0
Available Gradient (2 Sections) [MV/m]	E_{a_2}	14.3	14.3
Available Gradient (4 Sections) [MV/m]	E_{a_4}	10.1	10.1
Maximum Energy Gain (1 section) [MeV]	W_{max_1}	21.6	21.6
Maximum Energy Gain (2 sections)* [MeV]	W_{max_2}	23.1	23.1
Maximum Energy Gain (4 sections)* [MeV]	W_{max_3}	32.6	32.6

*Includes waveguide power losses

D2. Advanced 3D Simulation Results for Alternative $5\pi/6$-mode MAC

D2.1. Alternative TW X-Band $5\pi/6$-mode MAC Design Using PBC in OMEGA3P

Our L-band system is capable of generating beam for over 10 μs. This then argues for a structure with a very slow group velocity, as it will allow us to fill a longer cavity and capitalize on the long L-band RF pulses; however, as it is mentioned earlier this adds some complexity. The parameters for the alternative TW X-band MAC structure are given, as a comparison with SUPERFISH and OMEGA3P, in Table D.3. The magnitude of the electric and magnetic fields

for our single cell TW X-band MAC using OMEGA3P in Figure D.4 [13]. It is shown that the results are accurate with the previous results.

Table D.3 Parameters for alternative TW X-band $5\pi/6$-mode MAC using OMEGA3P and SUPERFISH

Parameter	Symbol	SUPERFISH	ACE3P
Phase Advance per Cell [Radian]	ψ	$5\pi/6$	$5\pi/6$
Inner Radius to Wavelength Ratio	a/λ	0.10	0.10
Resonance Frequency [GHz]	$f_{X-band\ MAC}$	11.6998	11.699723
Unloaded Quality Factor	Q_0	7598.7	7587.7
Shunt Impedance [MΩ/m]	r_{sh}	153.67	153.4

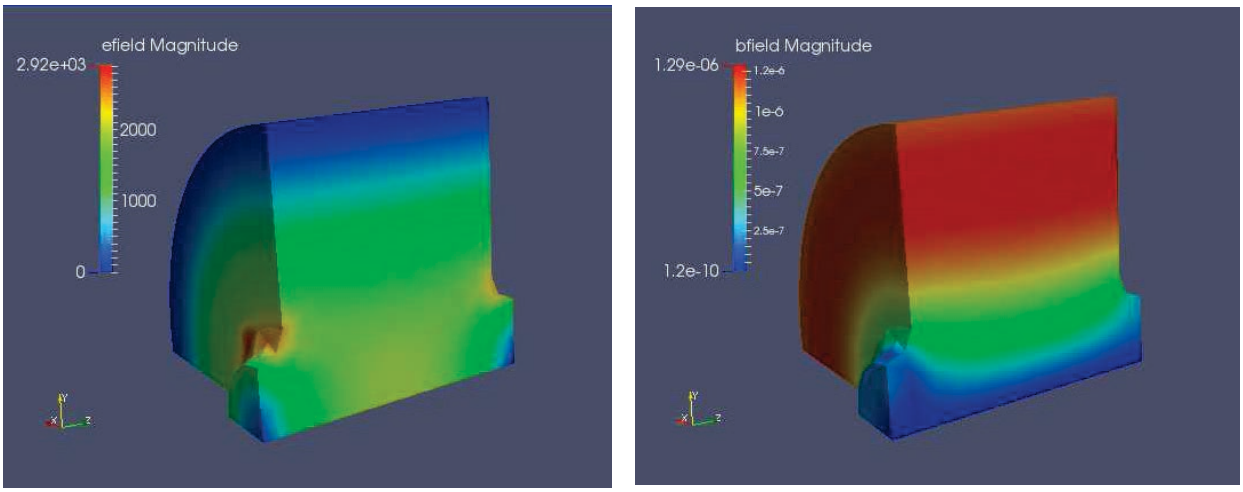

(a)

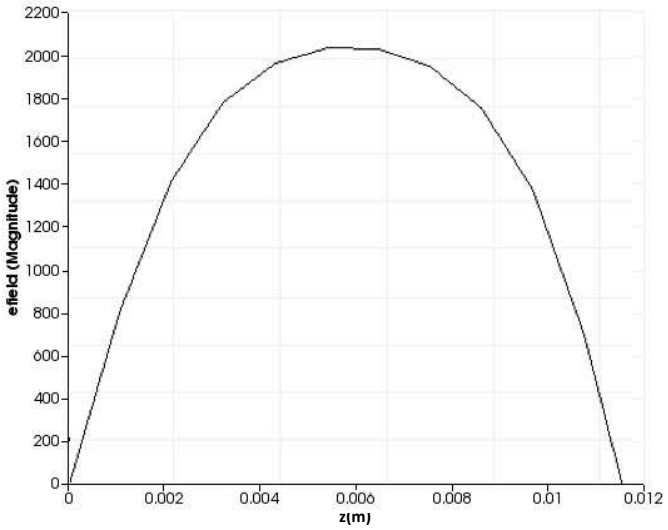

(b)

Figure D.4 (a) The electric and magnetic field distributions, and magnitude of electric field (b) magnitude of electric field for the single cell alternative TW X-band $5\pi/6$-mode MAC using OMEGA3P

D2.2. Coupler Design for Alternative TW X-band $5\pi/6$ -mode MAC Using OMEGA3P and S3P

The same procedure is used for the alternative MAC coupler structures but this time it is designed to operate on the $5\pi/6$ mode. The coupler cavity structure was attached to the 5 regular alternative-design X-band MAC cells as the $5\pi/6$ phase advance per cell repeats itself every 6 cells. The attached 6-cell MAC structure is shown in Figure D.5 for the optimization of the reflection coefficient using S3P.

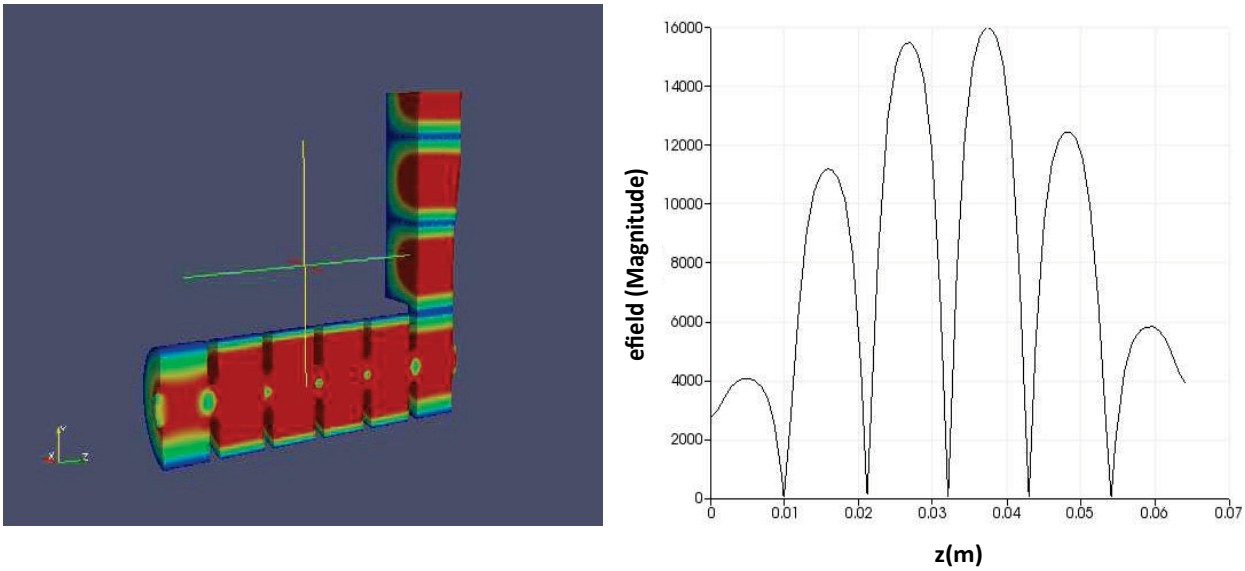

Figure D.5 S3P result of alternative TW X-band $5\pi/6$-mode MAC with attached coupler cavity using WBC

As a final design step the 72-cell alternative-design TW X-band $5\pi/6$-mode MAC with the attached input and output couplers at the both ends are shown in Figure D.6.

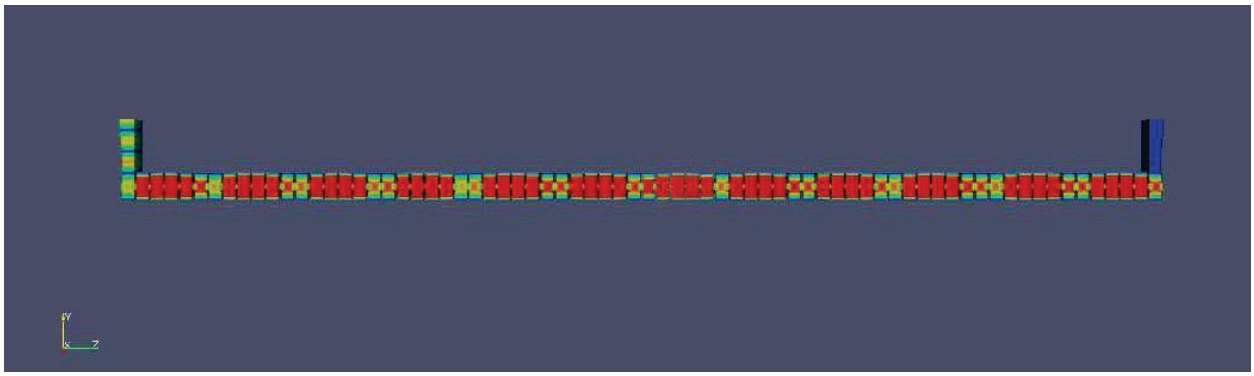

(a)

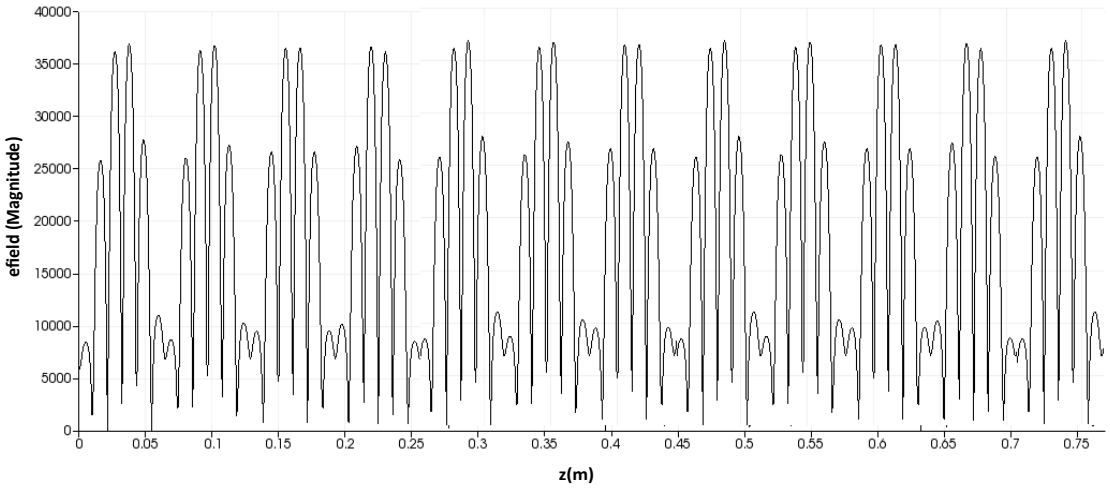

(b)

Figure D.6 S3P result of alternative TW X-band $5\pi/6$-mode MAC with attached input and output coupler cavities using WBC

APPENDIX E: ALTERNATIVE APPROACH FOR POWER EXTRACTION USING SMALLER BUNCH CHARGE AT 1.3 GHZ REPETITION RATE

As an alternative approach we explore the operation of the system when driven by 100 Gaussian bunches, each of which have 0.17875 nC bunch charge and with a bunch separation of 769 ps (1.3 GHz repetition rate) and a 4 mm bunch length.

This set up can be achieved using a Fabry-Perot interferometer, thus multiplying up the repetition rate of the laser system to 1.3 GHz. Even in this condition the high Q_0 of the X-band PEC can handle the decay in the field between excitations from the electron bunch. The charge per electron bunch goes down, but assuming no losses the average current would remain the same. Now, instead of 144 RF periods between excitations there would only be 9.

As this configuration adds more complexity and bring further modifications to the laser system this was done to crosscheck the simulations with high repetition rates and smaller bunch charges. As expected the extracted X-band power is decreases proportional to the square of the PEC length, bunch charge and form factor; however, the higher frequency term compensate it at the same rate.

The beam build-up due to the coherent wakefield excitation in the 18-cell X-band PEC using 4 mm bunch length with the 12.3 ns and 769 ps bunch separation cases. The relevant wakefield excitations and impedance spectrums are shown in Figures E.1 and E.2. The related parameters

and extracted X-band power result are given in Table E.1. The results are consistent with the Equation 2.11 for both cases.

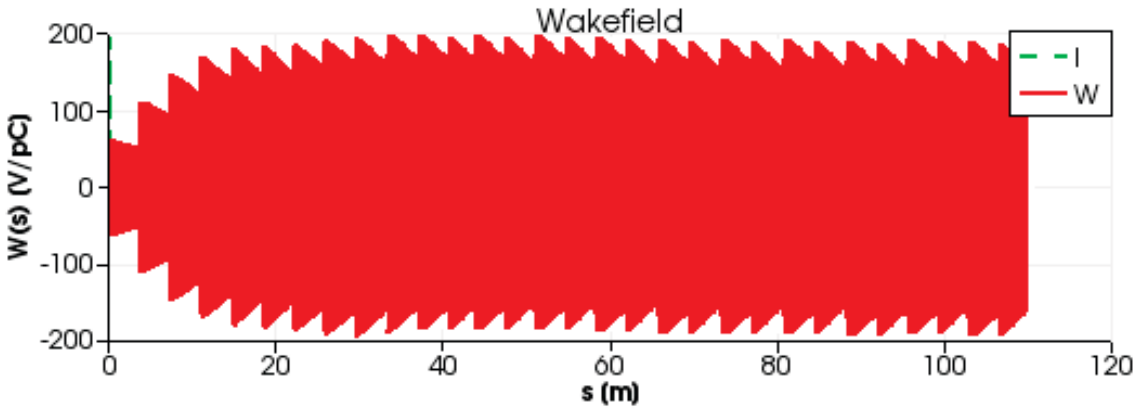

(a)

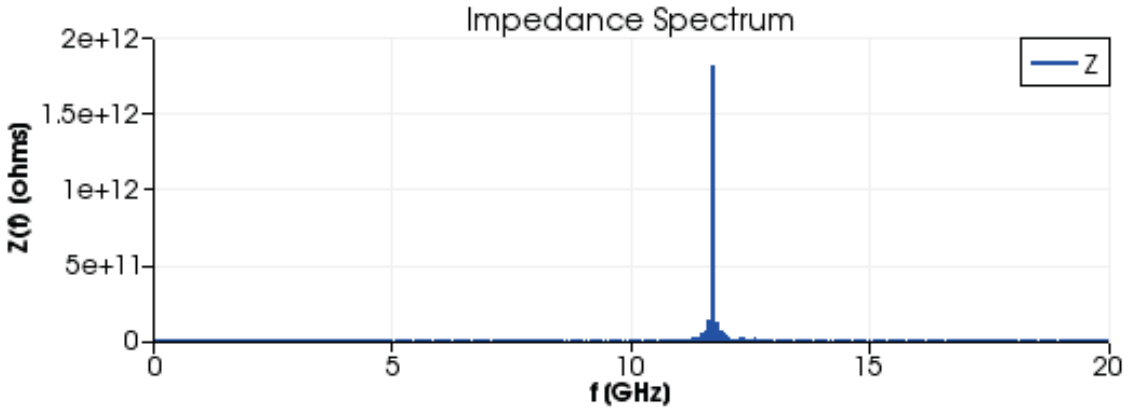

(b)

Figure E.1 (a) Wakefield excitation of 1 Gaussian bunches with 12.3 ns bunch separation, 2.86 nC bunch charge and 4 mm bunch length (b) Impedance spectrum of X-band PEC wakefield excitation for 30 Gaussian bunches with 12.3 ns bunch separation, 2.86 nC bunch charge and 4 mm bunch length

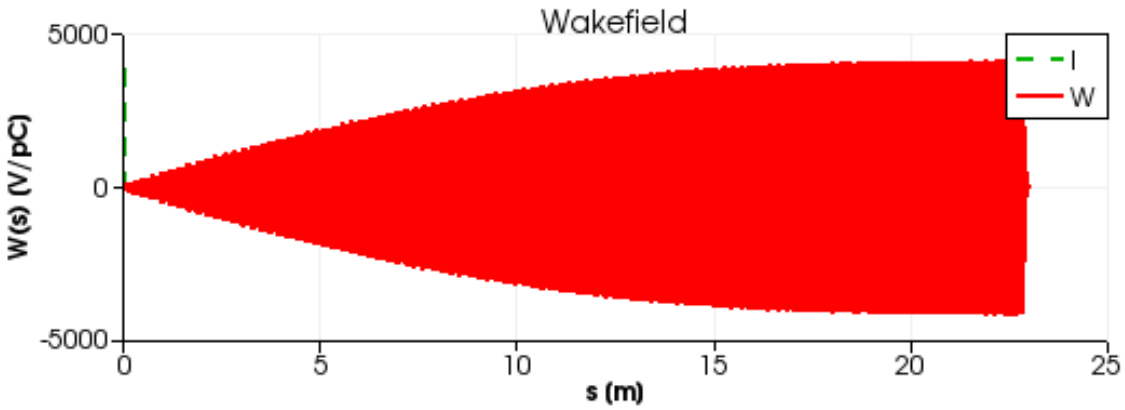

(a)

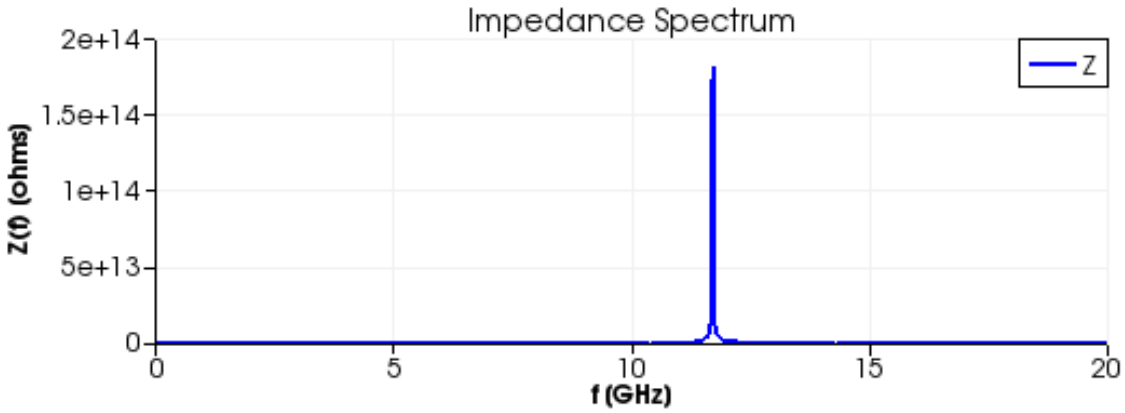

(b)

Figure E.2 (a) Wakefield excitation of 100 Gaussian bunches with 769 ps bunch separation, 0.17875 nC bunch charge and 4 mm bunch length (b) Impedance spectrum of X-band PEC wakefield excitation for 100 Gaussian bunches with 769 ps bunch separation, 0.17875 nC bunch charge and 4 mm bunch length

Table E.1 Extracted X-band Power for 4 mm bunch lengths in 18-cell PEC

Parameter	Symbol	Value for 81.25 MHz Repetition Rate	Value for 1.3 GHz Repetition Rate
Number of X-band PEC Cell		18	18
Bunch Charge [nC]	q	0.17875	2.86
Bunch Separation [ns]	T_0	0.769	12.3
Group Velocity [m/s]	ϑ_g	1.63c	1.63c
Bunch Length [m]	σ	0.004	0.004
Form Factor	F	0.62	0.62
Extracted X-band Power [MW]	P_{out}	0.0313	0.0313

APPENDIX F: IMPROVEMENTS TO THE ENGINEERING OF HIGH-CURRENT PULSED MAGNETIC HORN SYSTEMS AT FERMILAB

F.1. Introduction

The principles of neutrino sources and experiments have changed since the early days of the late 1950's. The components that are used for neutrino production need to be optimized according to desired experimental parameters. This part of the research includes the optimization studies of magnetic focusing components used for neutrino production at Fermilab.

F.2. Neutrino Sources

Neutrino sources can occur either artificially or naturally. Our main interest in here is artificial neutrino sources, however one of the most important discoveries in neutrino physics, the phenomenon of neutrino oscillations which shows that neutrinos have mass [112-114], came about not through the use of artificial neutrino sources, but by using neutrinos produced naturally in the Sun and in the Earth's atmosphere.

There are two principal types of artificial sources: fission reactors, producing electron-type antineutrinos from beta decays of fission fragments, and proton accelerators that produce muon-neutrinos (or antineutrinos) from pion decays in flight. Our focus will be on particle accelerator based neutrino production for this research.

Presently, there are several experiments that are using accelerator-based neutrinos worldwide: CERN, Switzerland [115-117]; Japan Proton Accelerator Research Complex (J-PARC), Japan [118-120]; and Fermi National Accelerator Laboratory (Fermilab), USA [121-123].

F.3. Fermilab

Fermi National Accelerator Laboratory (Fermilab) was founded in 1967 and located just outside Batavia, Illinois, near Chicago. It is a US Department of Energy (DOE) national laboratory specializing in high-energy particle physics (HEP). Since 2007 Fermilab has been operated by the Fermi Research Alliance, a joint venture of the University of Chicago, and the Universities Research Association Inc. (URA). Colorado State University jointed the URA in May 2015.

F.4. Fermilab Accelerator Complex

Fermilab's accelerator complex includes several particle accelerators and storage rings as shown in Figures F.1.

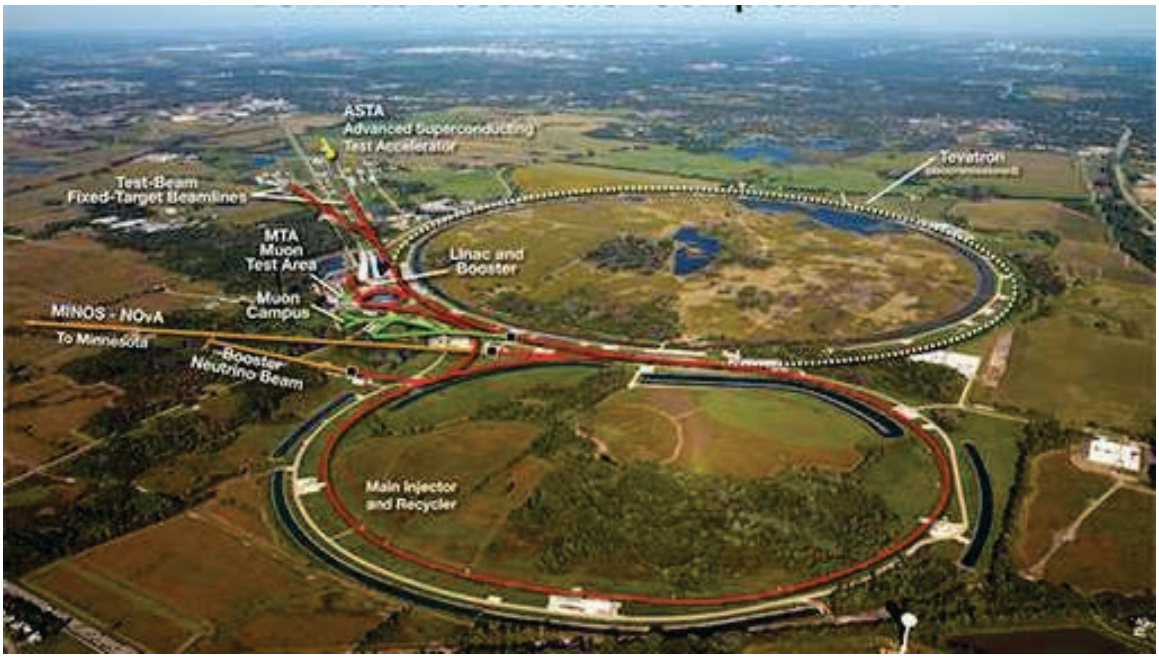

Figure F.1 The Fermilab accelerator complex (Figure courtesy of Fermilab)

It produces the world's most powerful, high-energy neutrino beam and provides proton beams for various experiments and accelerator and detector R&D programs. In addition the Proton Improvement Plan-II (PIP-II) [124] upgrade will provide the megawatt (MW) proton beam needed for the future neutrino experiments.

F.5. Fermilab Neutrino Experiments

The beams from the Fermilab accelerator complex, shown in Figure F.1, are used to drive many frontier short- and long- baseline neutrino experiments. The NuMI (Neutrino at Main Injector) [125-127] beamline at Fermilab has been providing intense neutrino beams for several experiments. The short baseline neutrino experiments MicroBooNE [128] and MiniBooNE [129] (acryonym BooNE - Booster Neutrino Experiment) focused on neutrino oscillations, and the long baseline experiments (MINOS - Main Injector Neutrino Oscillation Search [130], MINERvA [131], and NOVA - NuMI Off-axis ν_e Appearance Experiment [132]) will be

upgraded to provide beam for the future Long Baseline Neutrino Facility (LBNF) [133-137]. When completed LBNF will have the highest intensity neutrino beam in the world for the Deep Underground Neutrino Experiment (DUNE) [138].

F.5.1. NuMI/NOvA

Fermilab has been involved in a very active long baseline neutrino program since the initiation in 1998 and commissioning in 2005 of the NuMI project. The NuMI beamline [139], with a 400-kW design power and shown in Figure F.2, has been in operation for the MINOS neutrino oscillation program since that time. The accelerator infrastructure and the NuMI beam line were upgraded in 2012-2013 to 700 kW in order to provide higher neutrino intensities for NOvA.

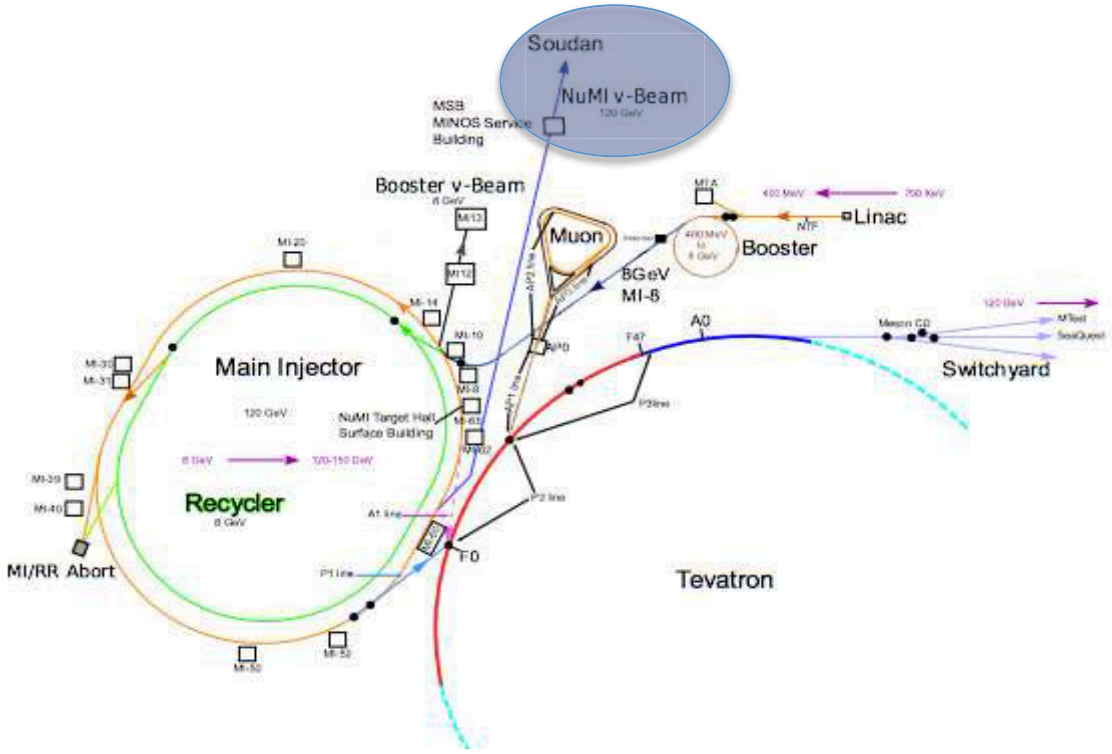

Figure F. 2 The NuMI/NOvA beamline at Fermilab [ibid 127] (Image courtesy of Fermilab)

F.5.2. LBNF/DUNE

Design and development for the next generation LBNF neutrino beam is a major project at Fermilab. Physics goals for LBNF require a new beamline, as shown in Figure F.3, with capabilities not attainable with the existing NuMI/NOvA beam parameters given in Table 6.1. This new beamline system at Fermilab will provide neutrino beams for the Deep Underground Neutrino Experiment (DUNE) (formerly the Long Baseline Neutrino Experiment (LBNE) [140]). DUNE is a proposed neutrino experiment with a near detector at Fermilab and a far detector at the Sanford Underground Research Facility (SURF) [141] located in Lead, South Dakota.

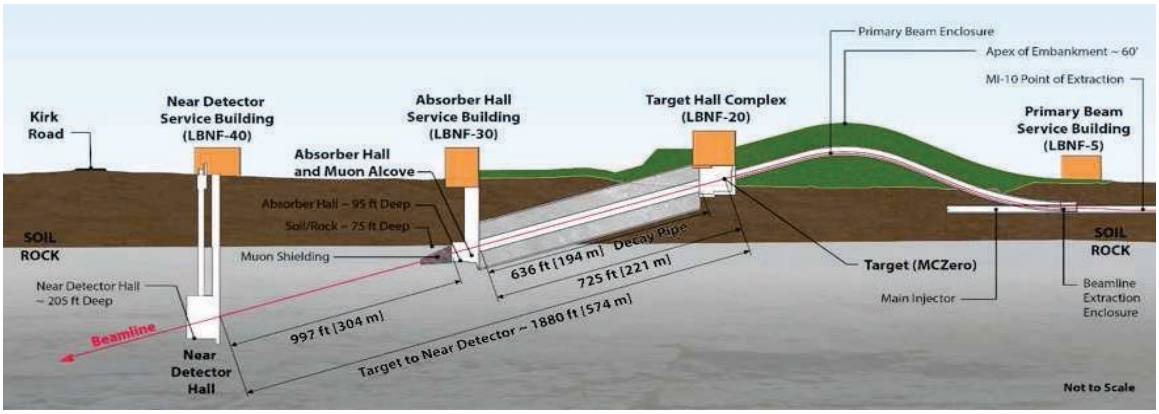

Figure F.3 Layout of the LBNF baseline (Image courtesy of Fermilab)

Table F.1 The beam parameters of the long baseline neutrino experiments at Fermilab

Parameters	NuMI/ MINOS	NuMI/NOvA	LBNF (Proposed)
Proton Beam Power [MW]	0.4	0.7	0.7 to 2.3
Proton Energy [GeV]	120	120	60 to 120
Repetition Rate [s]	1.87 μs	1.33 μs	1.33 μs
Protons per spill	4×10^{13}	4.9×10^{13}	4.9×10^{13} to 5×10^{14}
Baseline [km]	735	810	1300

F.6. Neutrino Production at Accelerator Based Neutrino Sources

To produce an intense neutrino beam, a proton beam of sufficient energy (in our case 120 GeV) and intensity is required. This proton beam is directed onto a target, usually made of Graphite or Beryllium, where they smash into the nucleus creating numerous particles including short-lived pions, the source of neutrinos and anti-neutrinos. This beam of pions has a broad energy spread and divergence requiring specialized magnetic focusing [142] to maximize the throughput to the downstream detectors. The pion beam is focused using large, high current magnetic devices that are shaped as and therefore referred to as magnetic horns. The focused pion beam is directed into a long decay volume, essentially a long evacuated tube, where they decay into muons and neutrinos or antineutrinos. This whole process is shown in Figure F.4.

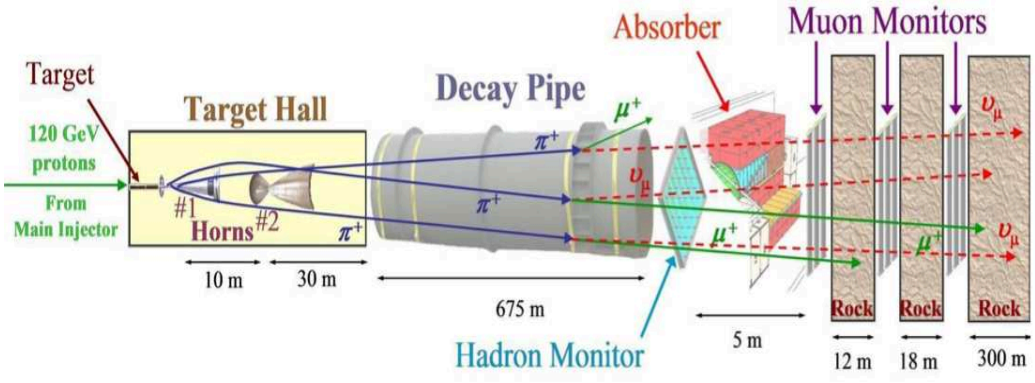

Figure F. 4 Stages of neutrino beam production and focusing scheme [ibid 127] (Image courtesy of Fermilab)

The design of the high-current horn and the associated striplines used to feed the current to the horn continue to evolve as existing experiments such as NuMI/NOvA are reconfigured for higher power proton beams of up to 1.2 MW. These horns must be even further refined and improved for the upcoming LBNF that will use even higher proton beam powers of up to 2.3 MW [144-147]. In its present state, there appears to be a design flaw with the striplines that lead to fatigue

failures. This is a particular concern as once the high-power proton beams are delivered to the target, all materials in this region; the horns in particular, can become highly radioactive making repair impossible and replacement necessary and extremely difficult. It is also of concern because of the desire to go to higher overall powers and thus higher average power requirements for the horns themselves. The design must be better understood and improved to make the horns and striplines robust for future operations.

F.7. Secondary Beam (Pion) Focusing Components in the Target Hall

Neutrino production starts in the Target Hall (or Target Station). The target station consists of a solid target, the pulsed magnetic focusing horns and the associated sub-systems such as the high-current striplines, cooling, and shielding infrastructure. A power supply that is outside of the shielding provides the required power to the magnetic horns.

F.7.1. Power Supply

Figure F.5 shows the pulsed power supply for the magnetic horns. A large capacitor bank dominates the pulsed power supply. Energy is stored in this capacitor bank and switched via silicon-controlled rectifiers (SCR) into the horn load. The supply produces a peak current of 200,000 A pulse at 722 V, over a 2.3 μs half sine wave every 1.33 s.

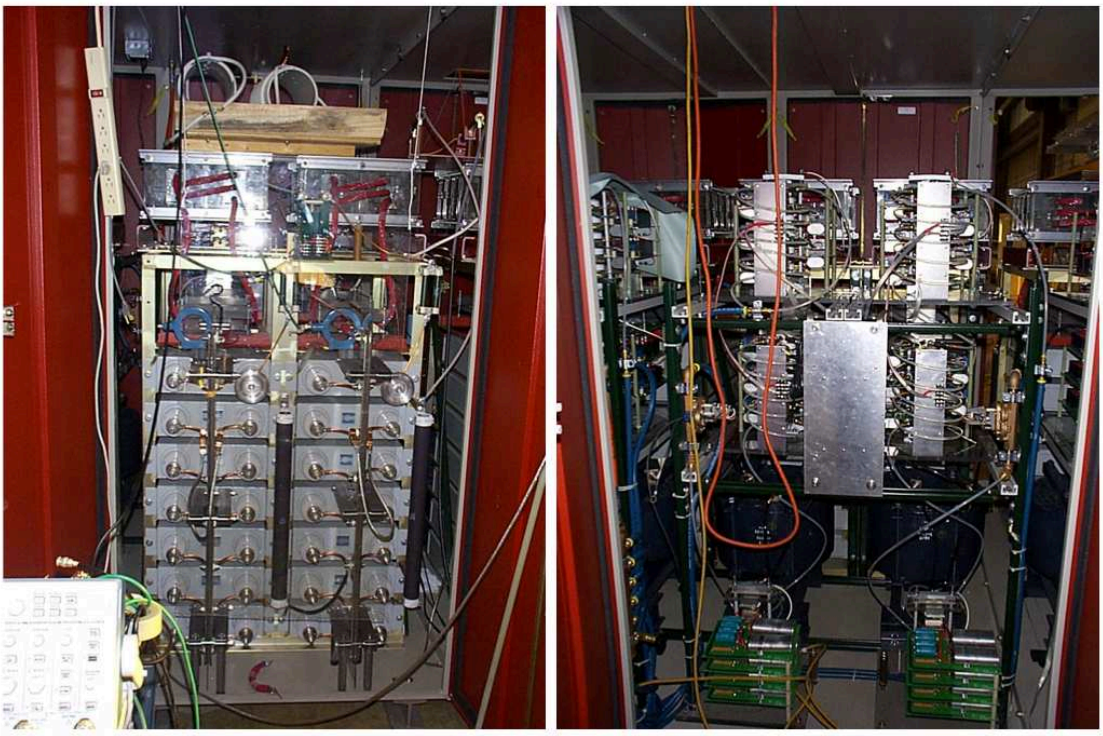

Figure F.5 Power supply of magnetic horn (Image courtesy of Fermilab)

F.7.2. High-Current Stripline

The magnetic horns are fed the pulsed, high-current from the power supply via the striplines (blue components shown in Figure F.6). The horns and stripline system are quite complex, expensive and very difficult to replace. Detailed and extensive design work as well as experimental testing is required to ensure they can withstand the severe conditions they will be subjected to.

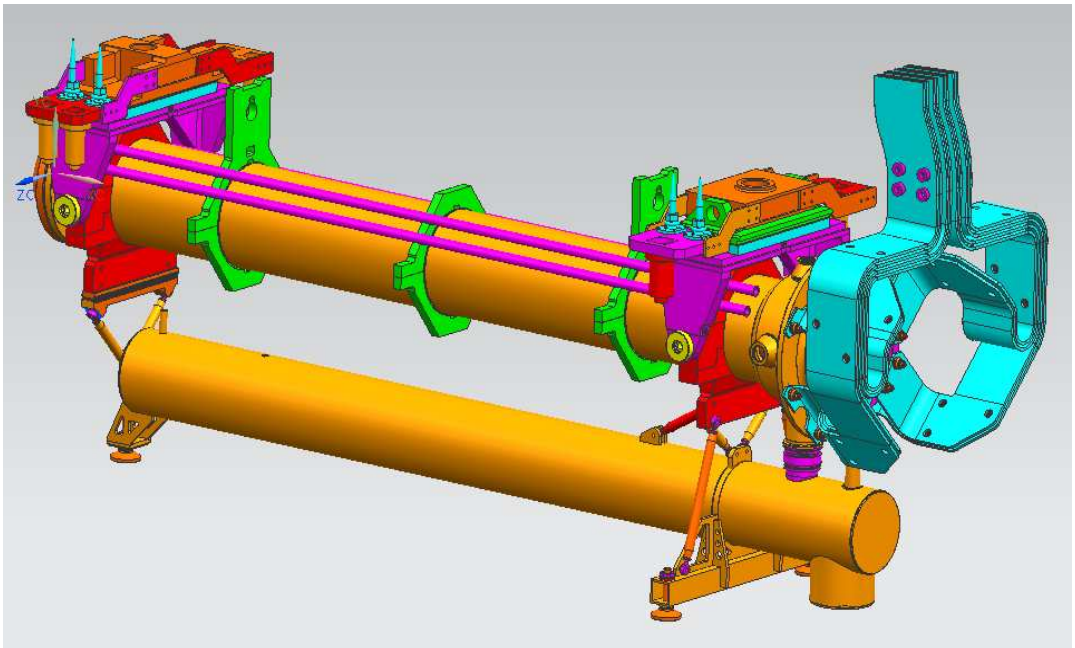

Figure F.6 3D CAD model of the attached magnetic horn (upper orange section) and the high current stripline (Turquoise colored component) with the cooling (lower orange section) and supporting infrastructure (light green section which holds the magnetic horn) (Image courtesy of Fermilab)

F.7.3. Pulsed Magnetic Horn

As mentioned above, the horns are essential components in producing intense neutrino beams and are used to produce toroidal magnetic fields, as shown in Figure F.7, that in turn are used to focus the pion beam.

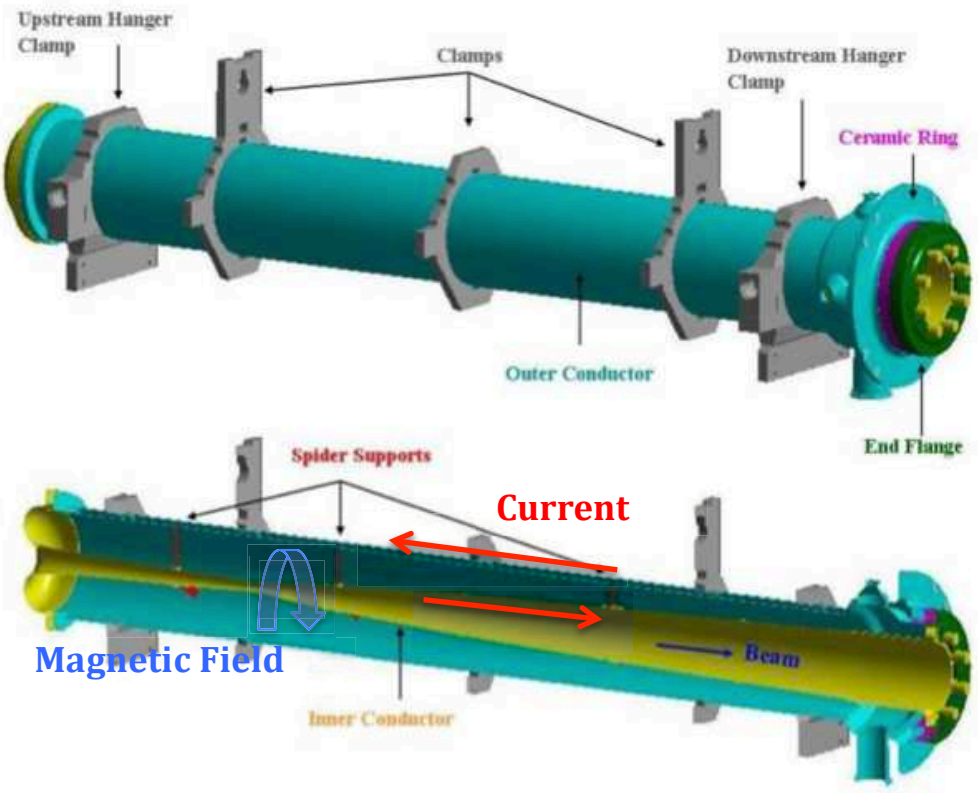

Figure F.7 The current and magnetic field representation at the magnetic horn [148] (Image courtesy of Fermilab)

The magnetic fields within the horn are used to focus into a roughly parallel beam the particles emerging from the target. These particles have a broad momentum and angular distribution, thus the complexity of the horn's field shape. This principle is illustrated in Figure F.8. Particles with very small angle at production never cross the inner conductor into the magnetic volume and can therefore continue in a straight line. Particles with somewhat larger production angles travel inside the magnetic volume, the more so for the larger angles. Within a given range of angles, these particles all form a parallel beam at the exit of the horn. In addition lower momentum particles are deflected more by the magnetic fields that those particles with higher momentum. The horn shape is designed to optimize this process. At even larger production angles, the field

in the horn is insufficient and the particles are not deflected enough. In order to focus a larger number of particles produced at various energies and angles, two or more horns can be used.

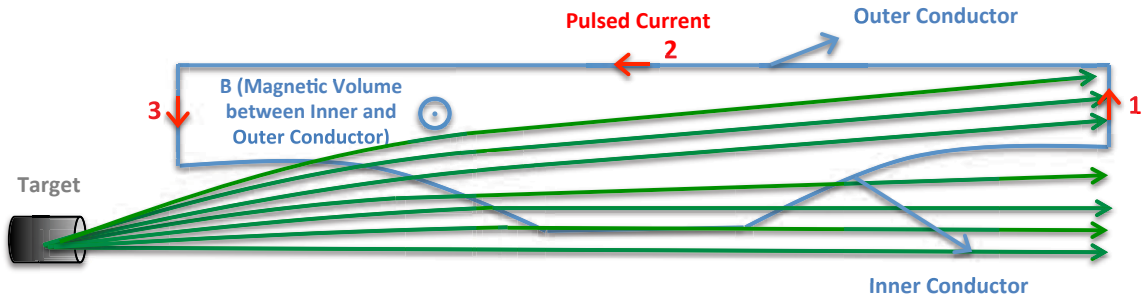

Figure F. 8 Focusing of charged Mesons (Pions and Kaons) in a magnetic horn (half symmetry)

F.8. Secondary Beam (Pion) Focusing Component Evaluation and Improvements

The magnetic horn and high-current stripline designs have been evolving as NuMI reconfigures for higher beam power and to meet the needs of the LBNF design. In 2013, the Fermilab Accelerator Complex and NuMI upgraded the proton beam power from 400 kW to 700 kW power. In anticipation to operations at 700 kW the so-called connection flag parts of the stripline were moved outward to lessen the anticipated additional beam heating and enhance the convective air-cooling of the target via directed airflow. Figure F.9 shows the previous 400-kW stripline design while Figure F.10 shows the modified stripline design for the 700 kW version. An additional result of this design change was a longer unclamped distance than in the original 400 kW design.

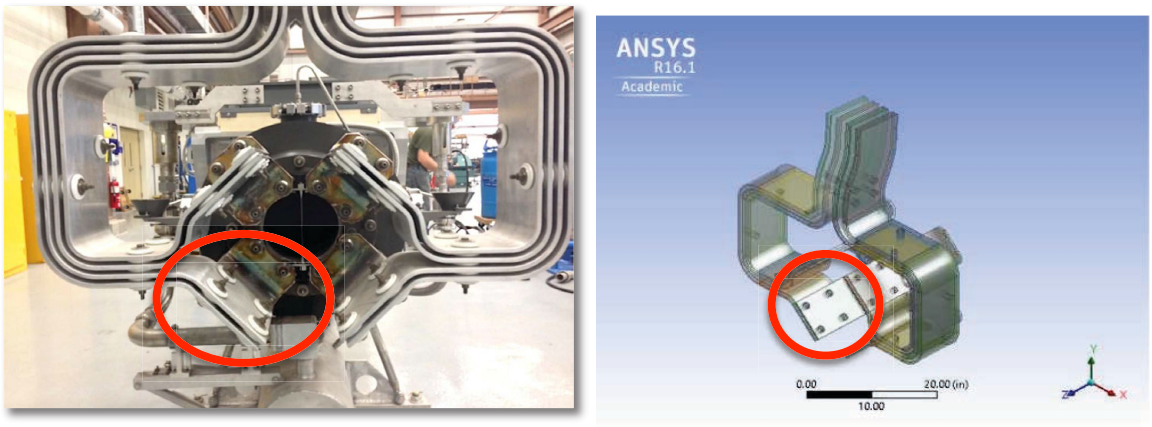

(a) (b)

Figure F.9 400 kW high-current stripline for NuMI (a) real design [149] and (b) 3D model

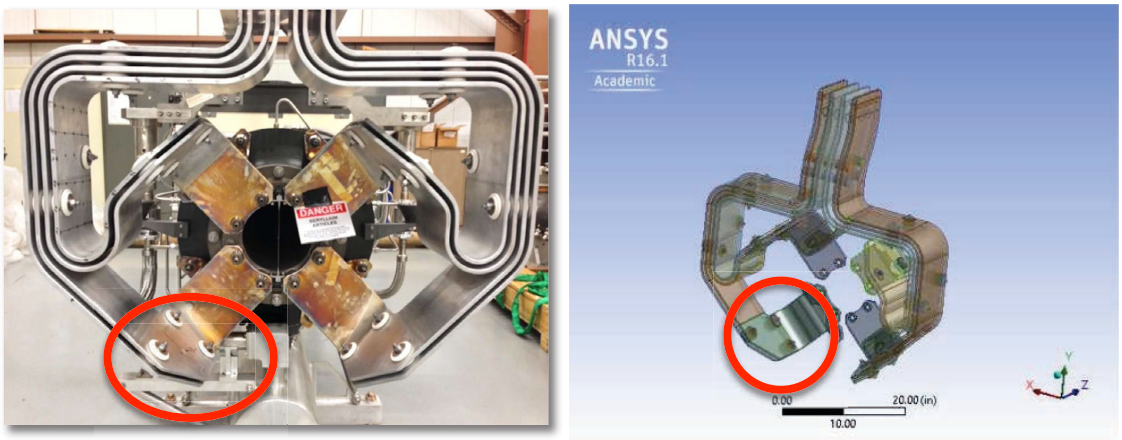

(a) (b)

Figure F.10 700 kW high-current stripline design for NOvA (a) real design [ibid 149] and (b) 3D model

In May 2015 the updated stripline of the NuMI Horn 1 failed right in the region of the connection flag (Figure F.11). Although the cycle lifetime for this component was originally projected to be 100 million cycles it failed after only 27 million cycles.

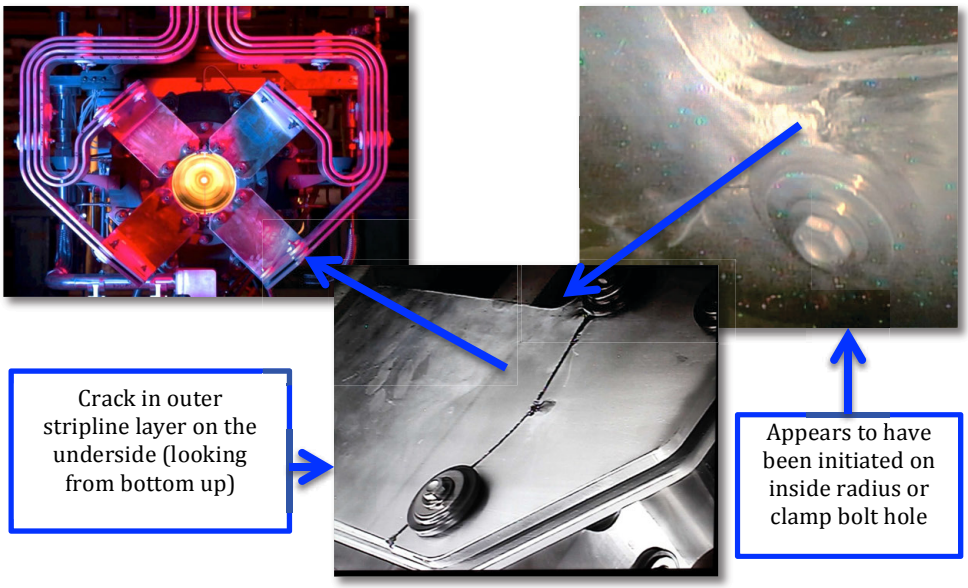

Figure F.11 The fatigue failure location of NuMI Horn 1 high-current stripline flag plate [150] (Courtesy of Fermilab)

Our study was to investigate the cause of this failure, recognizing that the failure was driven in part by the periodic magnetic forces experienced by the high-current striplines and also to explore alternative designs that would meet the overall system performance requirements of the high-power NuMI upgrades and LBNF designs. Calculations and simulations using LANL's magnetostatics kit (POISSON, PANDIRA and FORCE) [ibid 39] and ANSYS Maxwell 3D [151, Appendix C] codes were performed to evaluate the electromagnetic interactions in detail at critical stress points of the high-current stripline plates of the NuMI Horn 1 [152]. Also, calculations and simulations using ANSYS Electric were performed to evaluate the current density in detail at critical stress points of the high-current stripline plates of the NuMI Horn 1.

In addition to improving the design of the striplines so that they would be less susceptible to failure we were also interested in improving the uniformity of the current distribution along the length of the horn. To do this we investigated adding an electric current equalization section

between the high-current striplines and magnetic horn. However, to avoid excessive extra fabrication costs the length of the equalization section was optimized.

The results of these evaluations and optimizations are being used to support the development of new designs to handle increased electric current and higher beam power for the NuMI upgrades and for the LBNF design.

F.8.1. High-Current Stripline Simulations

Two different magnetic horns structures are given in Figures F.9 and F.10 have both advantages and disadvantages. The high current stripline shown in Figure F.9 is an older and larger version; however, it is more tolerant to thermal heating and is very robust. The high-current stripline shown in Figure F.10 has been designed as a more compact structure. Compared to the older design this one is not symmetric in the y-direction. In addition to this, the L-shaped flag plates have been changed to chamfered plates.

As seen in Figures F.9 and F.10 the high-current striplines are constructed as parallel conductors as this minimizes the impedance. Due to the electric current and resulting magnetic field a force occurs that plays an important role. Thus one needs to evaluate the behavior of the magnetic field and its related effects on the structure starting from the basic geometry.

F.8.1.1. Magnetic Field of Straight Current Carrying Cylinder Conductor

There are different metallic conductor plate combinations in the entire high-current stripline structure. Because of that it was started from first principles.

A constant current flowing through a cylindrical conductor generates a cylindrical magnetic field in the space surrounding it. The magnitude of this magnetic field can be expressed as in Equation F.1.

$$B = \frac{\mu_0 I}{2\pi d} \tag{F.1}$$

where I is the electric current, μ_0 permeability of free space, and d is the radial distance. First, to check the accuracy of the simulations codes with theoretical calculations a conductor of cylindrical cross-section (10 cm radius) carrying 1 Ampere (A) of constant current in the z direction (orthogonal to the page) was simulated. Then, the dimension of the conductors decreased from the larger dimensions (20 cm in radius) to real stripline plate equivalent cross-section dimension value (2.5 cm in radius) with well-optimized meshes at the end. The results are readily compared to the theoretical calculations. Figures F.12 and F.13 show the behavior of the simulated magnetic field in the radial direction as shown with the POISSON/PANDIRA and ANSYS Maxwell 3D solvers. As expected, the magnetic-field distribution in the x-y plane is in very good agreement with theory (to better than 1%). The results are given in Table F.2. Since the simulated values are consistent between POISSON and PANDIRA, the rest of the simulations were performed in LANL's kit with POISSON.

Table F.2 Magnetic field magnitude comparison generated through theory and simulation

Radius [m]	0.2	0.1	0.025
Theory [T]	$1\text{x}10^{-6}$	$2\text{x}10^{-6}$	$8\text{x}10^{-6}$
POISSON [T]	$1.004\text{x}10^{-6}$	$2.005\text{x}10^{-6}$	$8.012\text{x}10^{-6}$
PANDIRA [T]	$1.004\text{x}10^{-6}$	$2.004\text{x}10^{-6}$	$8.011\text{x}10^{-6}$
ANSYS Maxwell 3D [T]	$1.003\text{x}10^{-6}$	$2.008\text{x}10^{-6}$	$8.015\text{x}10^{-6}$

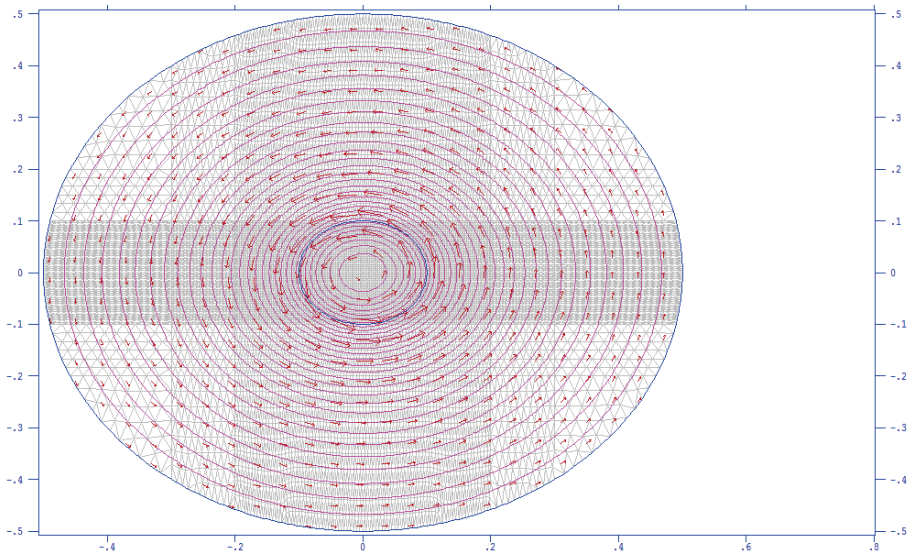

(a)

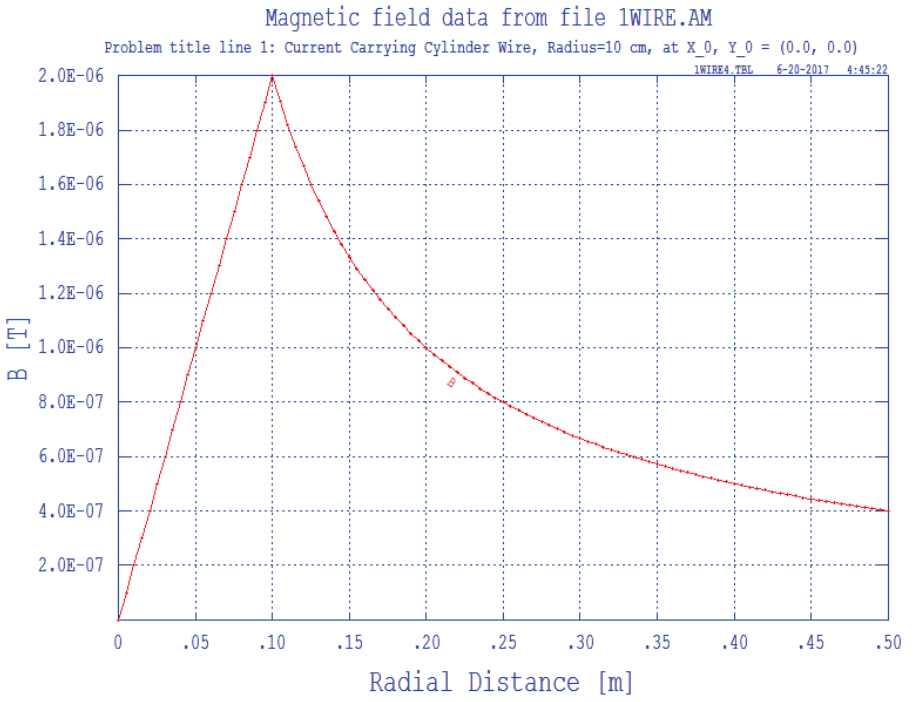

(b)

Figure F.12 POISSON/PANDIRA result (a) for the magnetic field map of a cylindrical conductor in the x-y cross-section (x-abscissa, y-ordinate) current carrying in the z direction (from out of page) (b) for the magnitude of magnetic field versus radial direction for a cylindrical conductor that has 10 cm in radius current carrying in the z direction

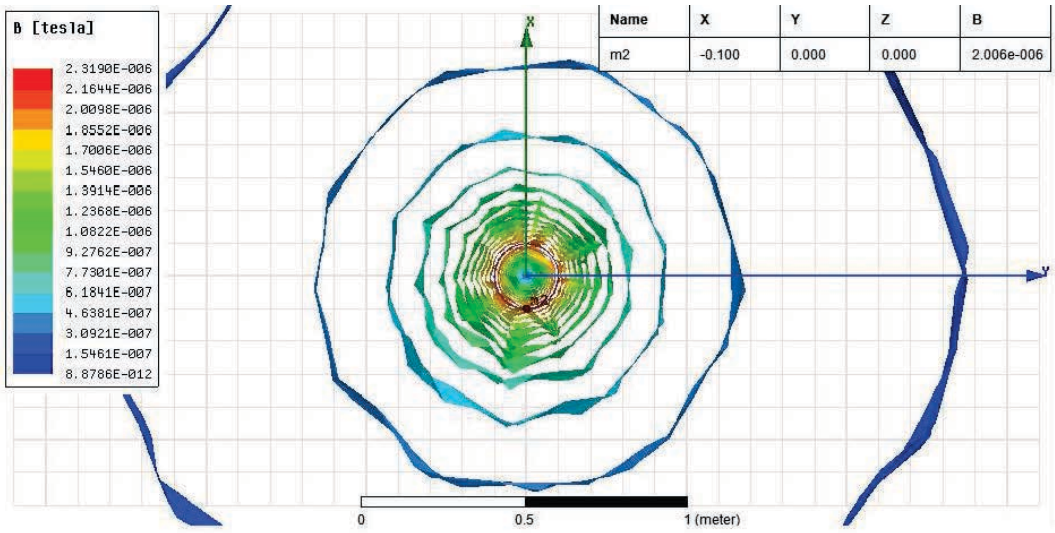

(a)

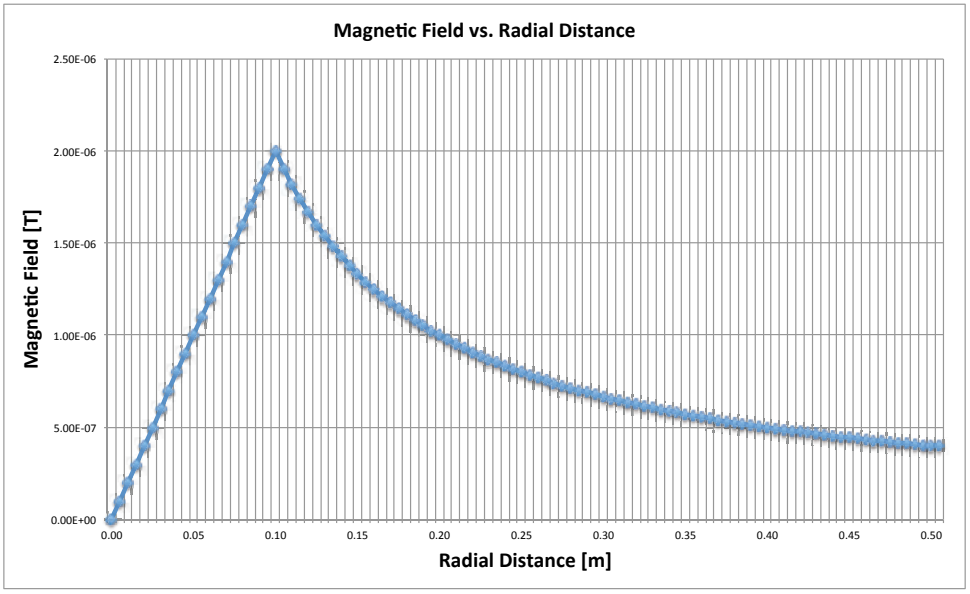

(b)

Figure F.13 (a) ANSYS Maxwell 3D Solver result (a) for the magnetic field map of a cylindrical conductor in the x-y cross section (x-abscissa, y-ordinate) current carrying in the z direction (from out of page) (b) for the magnitude of magnetic field versus radial direction for a cylindrical conductor that has 10 cm in radius current carrying in the z direction

As expected and seen in Figures F.12 (b) and F.13 (b), the magnetic field value is directly proportional to the radial distance (**B**~r) in the conductor and inversely proportional to the radial distance (**B**~1/r) the outside of the conductor. According to right hand rule (RHR), if the same electric current applied to the conductor in the opposite direction (–z) the magnitude of the magnetic field will be the same, however the direction will be the opposite.

F.8.1.2. Magnetic Force between Two Parallel Conductors

As a next step, the magnetic field interaction between two metallic conductors each carrying equal currents but opposite directions is evaluated. In this case, the magnetic fields being created by the moving charges can interact and create forces between the conductors.

The parallel conductors carrying currents in the same direction attract one another. Parallel conductors carry currents in the opposite direction and repel each other. The force on wire 1 due to the current in conductor 1 and the magnetic field produced by conductor 2 can be expressed as (force per unit length)

$$\frac{F_{Magnetic}}{Length} = \frac{\mu_0 I_1 I_2}{2\pi d} \quad . \qquad \text{(F.2)}$$

As a numerical evaluation, Ampere's force law is used to check the accuracy of both the LANL simulation kit and the ANSYS Maxwell 3D software.

First, the FORCE code was applied to determine the magnetic force results on conductor 1. The distance between each conductor is 1 meter (m), the applied electric currents are 1 A in the same direction and the radii of the conductors are 2.5 cm. The calculated result based on the theory is $2x10^{-7}$ N/m and the simulation results using Force and ANSYS Maxwell 3D are $2.014x10^{-7}$ N/m

and 2.0062x10^{-7} N/m, respectively. The results are shown in Figures F.14 and F.15. The errors are less than 1% when comparing with theory.

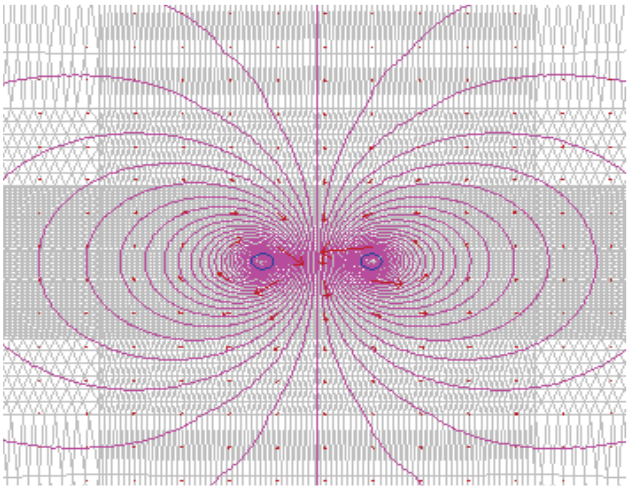

Figure F.14 POSSION result of the attractive behavior of the magnetic field for the cylindrical conductors carrying parallel currents in the same direction (Magnetic force (F_B) =2.01374 x 10^{-7} N/m)

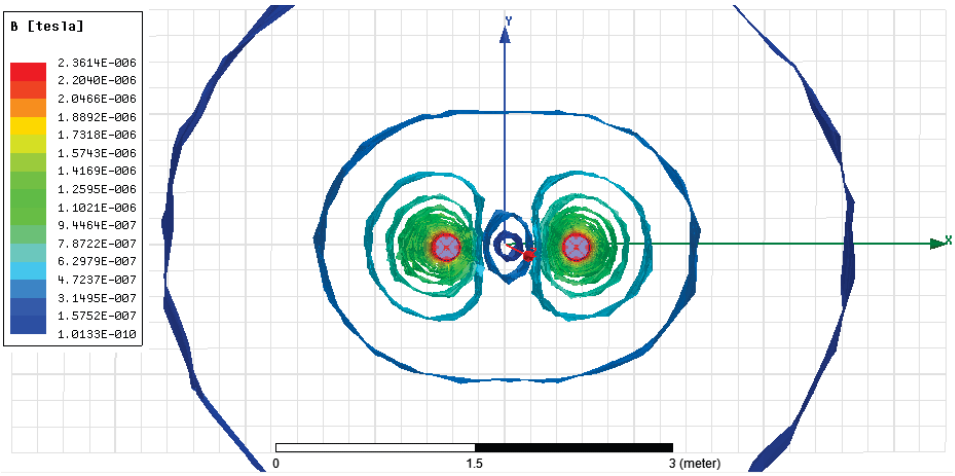

Figure F.15 ANSYS Maxwell 3D result of the attractive behavior of the magnetic field for the cylindrical conductors carrying parallel currents in the same direction (Magnetic force (F_B) = 2.0062 x 10^{-7} N/m)

The process was repeated for the same magnitude but oppositely directed electric current in the conductor. The calculated result based on the theory is 2x10^{-7} N/m and the simulation results

found using Force and ANSYS Maxwell 3D are 1.95956×10^{-7} and 2.0008×10^{-7} N/m, respectively. The results are shown in Figures F.16 and F.17.

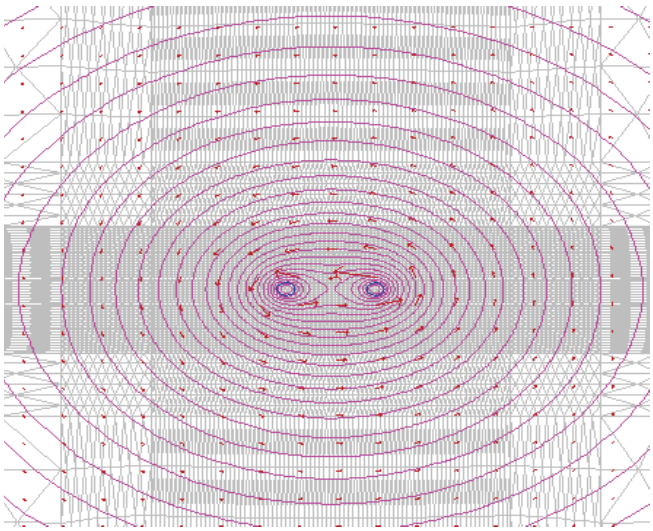

Figure F.16 POSSION result of the repulsive behavior of the magnetic field for the cylindrical conductors carrying parallel currents in the opposite direction (F_B=1.95956 x 10^{-7} N/m)

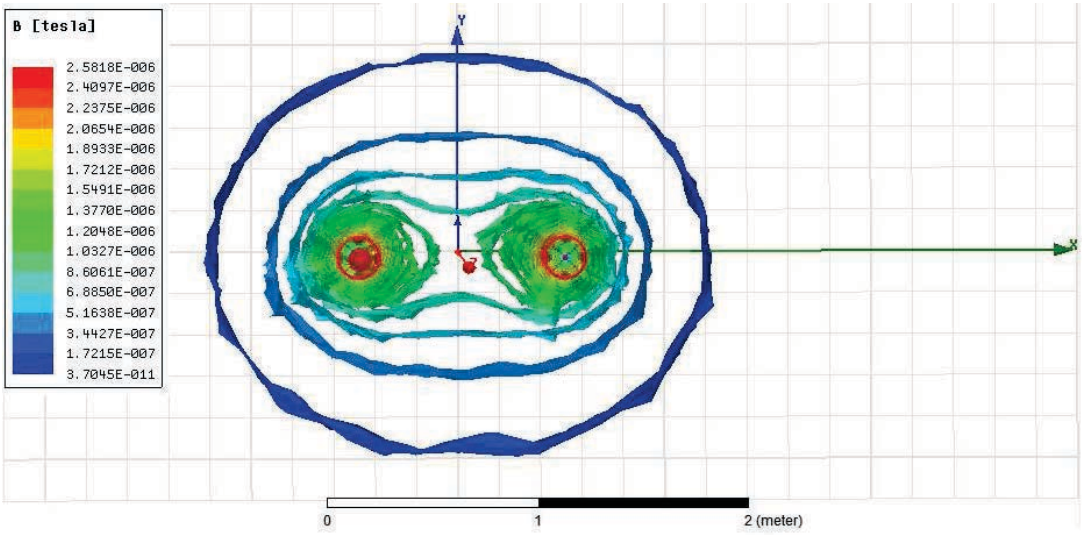

Figure F.17 ANSYS Maxwell 3D result of the repulsive behavior of the magnetic field for the cylindrical conductors carrying parallel currents in the opposite direction (F_B = 2.0008 x 10^{-7} N/m)

As a next step, the accuracy of the codes for sharp edge based conductors was examined. For this procedure while the other parameters kept exactly the same as the cylindrical conductor case, the

adaptive mesh configuration in ANSYS Maxwell 3D was changed from surface mesh for rounded geometries to a linear width mesh for geometries that have sharp edges. This provides more effective modeling of features for these types of geometries.

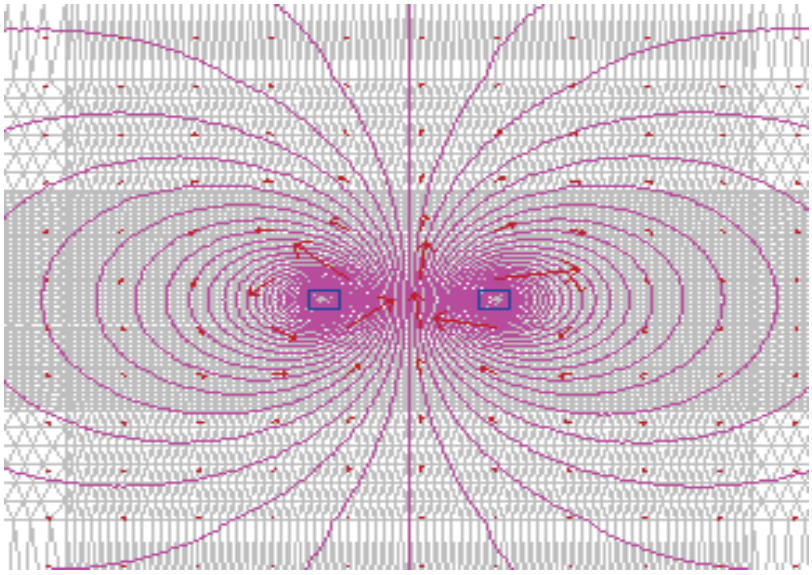

Figure F.18 POISSON result of the attractive behavior of the magnetic field for the square conductors carrying parallel currents in the same direction (F_B = 1.93572 x 10^{-7} N/m)

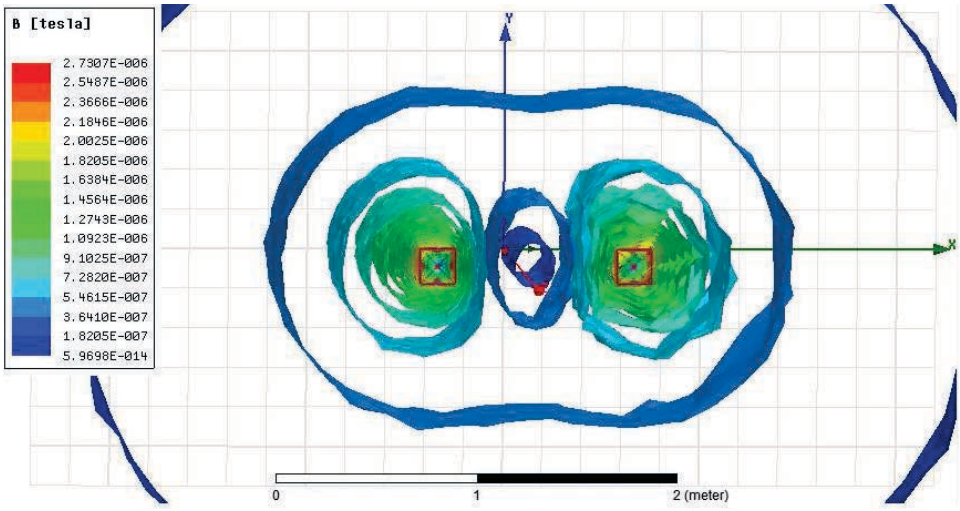

Figure F.19 ANSYS Maxwell 3D result of the attractive behavior of the magnetic field for the square conductors carrying parallel currents in the same direction (F_B = 1.982 x 10^{-7} N/m)

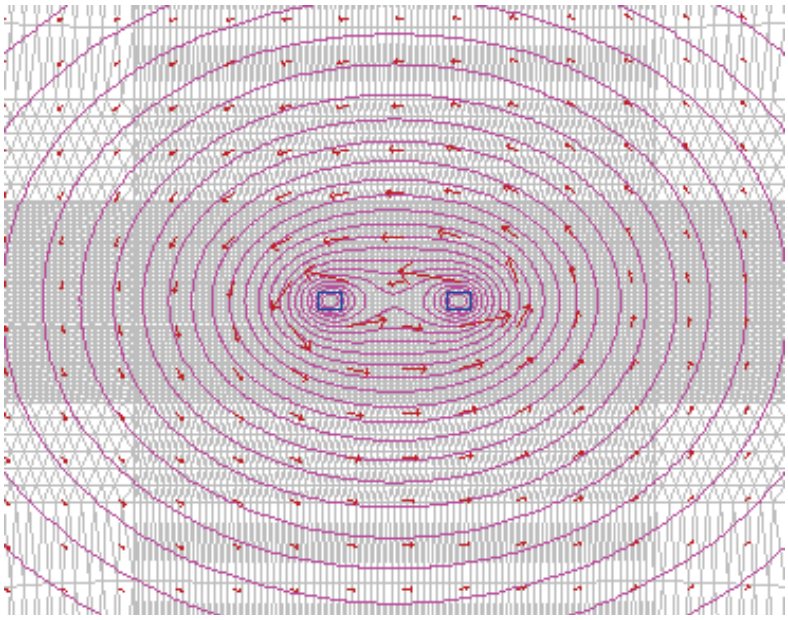

Figure F.20 POISSON result of the repulsive behavior of the magnetic field for the square conductors carrying parallel currents in the opposite direction (F_B = 2.03693 x 10^{-7} N/m)

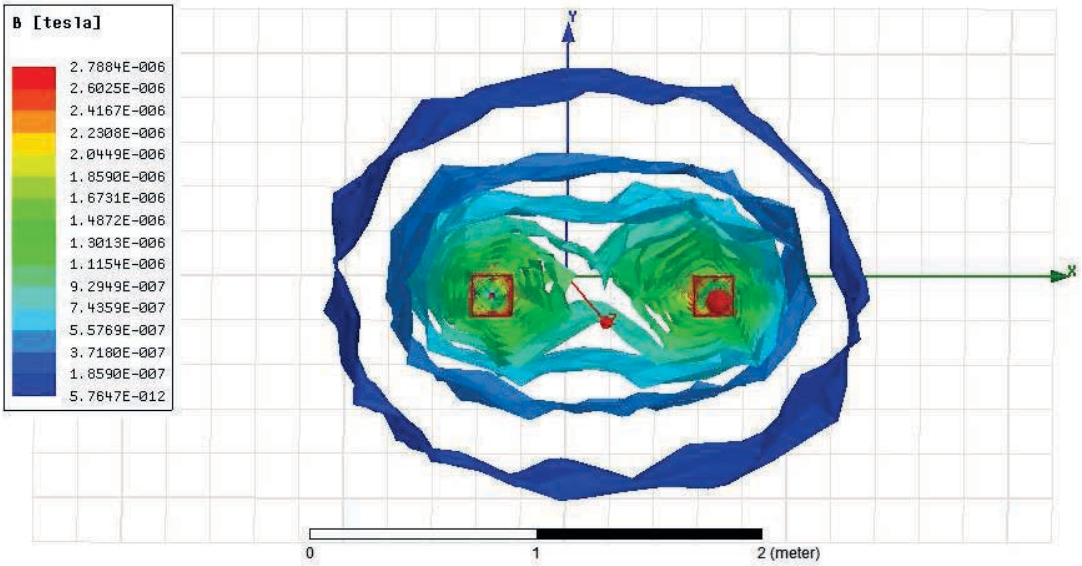

Figure F.21 ANSYS Maxwell 3D result of the repulsive behavior of the magnetic field for the square conductors carrying parallel currents in the opposite direction (F_B = 2.0241 x 10^{-7} N/m)

As expected, the results are consistent for all geometries both with parallel currents in the same direction (Figures F.18 and F.19), and parallel currents running opposite directions (Figures F.20 and F.21).

Now, the high-current striplines for Fermilab's horns will be examined.

F.8.1.3. Magnetic Field and Force Evaluation of High-Current Striplines

Four conductors are used to conduct the 200 kA into and out of the inner and outer conductor of the horn. This was shown in Figures F.9 and F.10 previously. The cross-section of all plates is 0.2032 m (8 inches) by 9.25×10^{-3} m (0.375 inches) and the distance between each plate is 9.25×10^{-3} m. Each carry an applied peak current of 50 kA, and the current flows with a polarity of + - - +. As such simulations were done for both relevant current polarity cases, + + and + -, Figures F.22 and F.23.

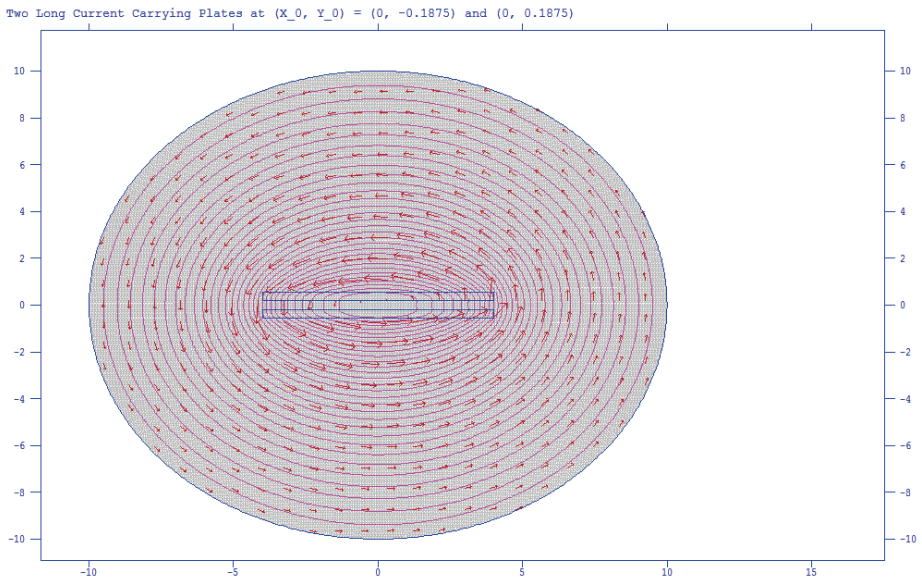

Figure F.22 POISSON result for the magnetic field map for cross section of parallel plates in x-y planes carrying 50 kA DC each in the same direction in the z direction

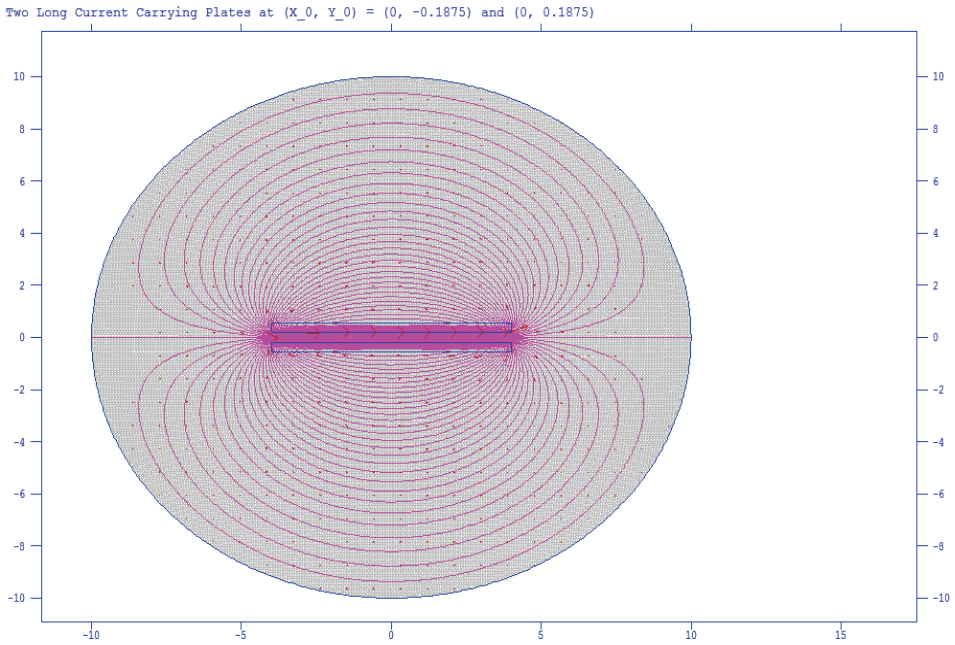

Figure F.23 POISSON result for the magnetic field map for cross section of parallel plates in x-y planes carrying 50 kA DC each in the opposite direction in the z direction

The magnetic force between two plates was found to be 6186 N/m.

The interactions of the straight sections using ANSYS Maxwell 3D are simulated once more as shown in Figure F.24 and F.25 before the evaluation of the critical stress points. Magnetic force is found as 6192 N/m between the plates that is shown in Figure F.25. This is consistent with POISSON result.

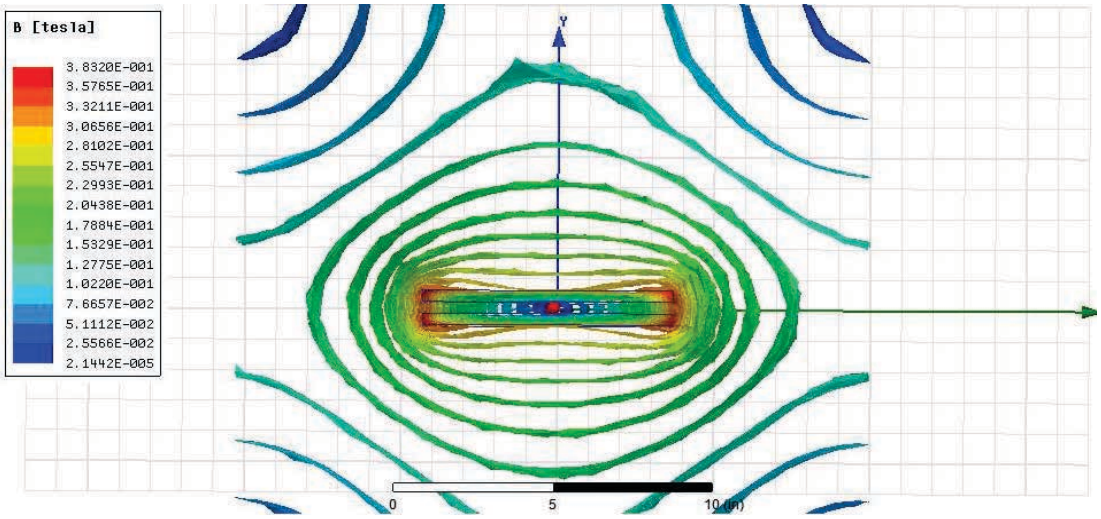

Figure F.24 ANSYS Maxwell 3D result for the magnetic field map for cross section of parallel plates in x-y planes carrying 50 kA DC each in the same direction

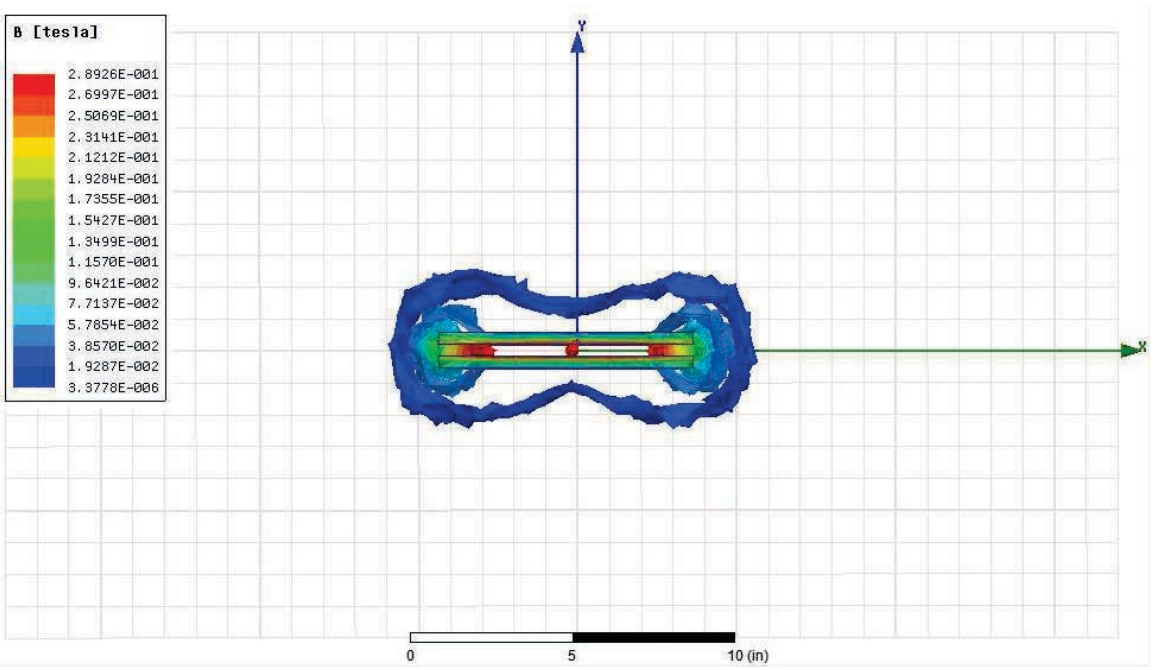

Figure F.25 ANSYS Maxwell 3D result for the magnetic field map for cross section of parallel plates in x-y planes carrying 50 kA DC each in the opposite direction

The flag plate of the stripline shown in Figure F.10 had a fatigue failure at its most critical stress locations. For the next step the magnetic field and related effects were evaluated for these 90-degree bends to see if they effects are the cause of the unexpected failure of the structure. The simulation results are given in Figures 6.26, 6.27 and 6.28. In Figure F.26, the plates have no bolt holes. In Figure F.27 and 6.28 bolt holes are included as in the real case of the flag plates for both the 400-kW and 700-kW design.

Simulations show that the magnetic field at the inner most corner is higher than in the straight sections even in the case without bolt holes. The average magnetic field on the flag plate of the 400-kW design is found to be ~ 0.28 T; however, at the inner corner section this field is ~ 0.39 T (Figure F.27 (a)). The average magnetic field on the flag plate of 700-kW design is found to be ~ 0.28 T; however, at the inner corner section this field is ~ 0.37 T (Figure F.26 (b)).

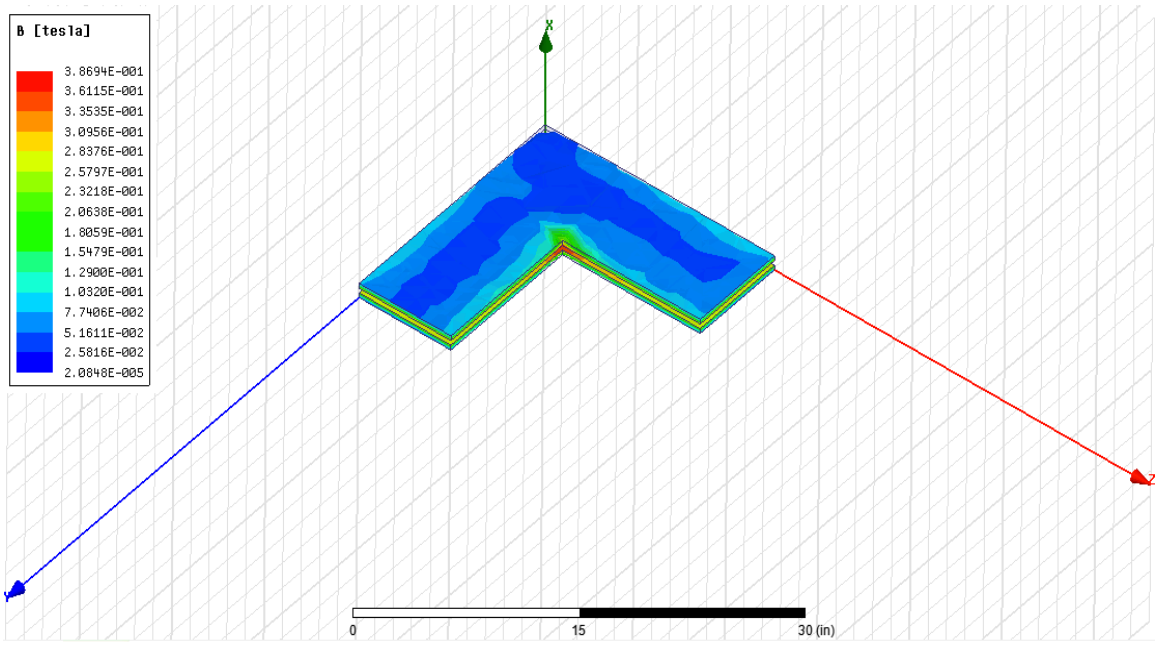

(a)

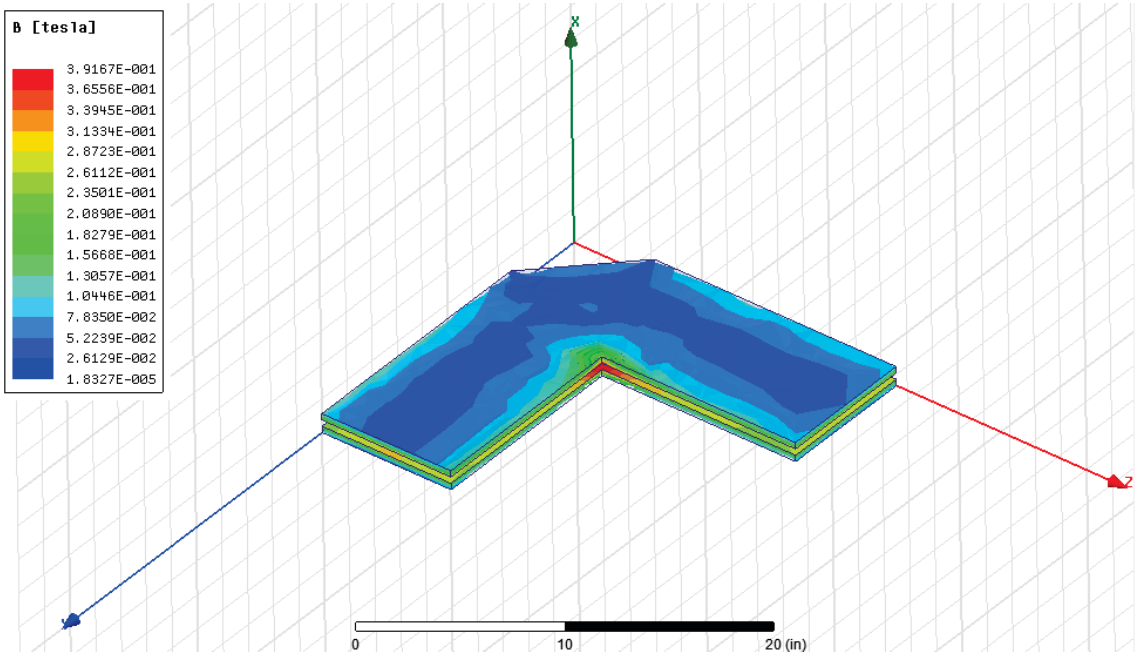

(b)

Figure F.26 ANSYS Maxwell 3D result for magnetic field map of (a) L-shaped and (b) chamfered L-shaped two parallel plates of the high-current stripline carrying 50 kA DC each in the opposite direction

Simulations show that the magnetic field at the inner most corner is much higher than in the straight sections for the case with bolt holes. The average magnetic field on the flag plate of 400-kW design is found to be ~ 0.28 T; however, at the inner corner section this field is ~ 0.56 T (Figure F.27 (a)). The average magnetic field on the flag plate of 700-kW design is found to be ~ 0.28 T; however, at the inner corner section this field is ~ 0.48 T (Figure F.27 (b)) [152].

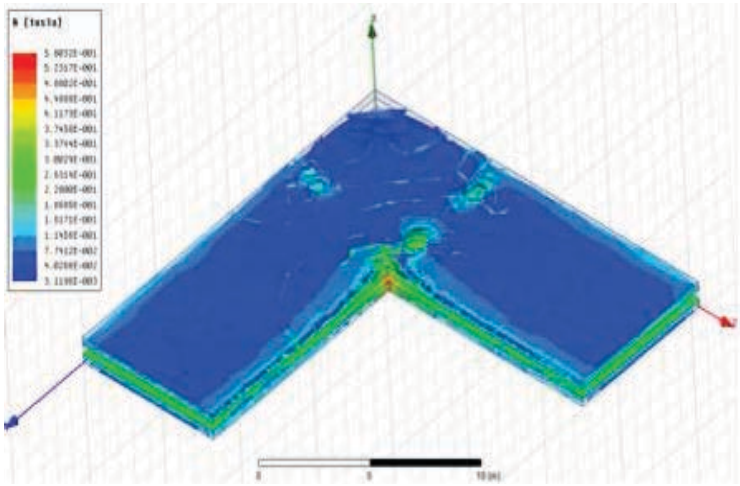

(a)

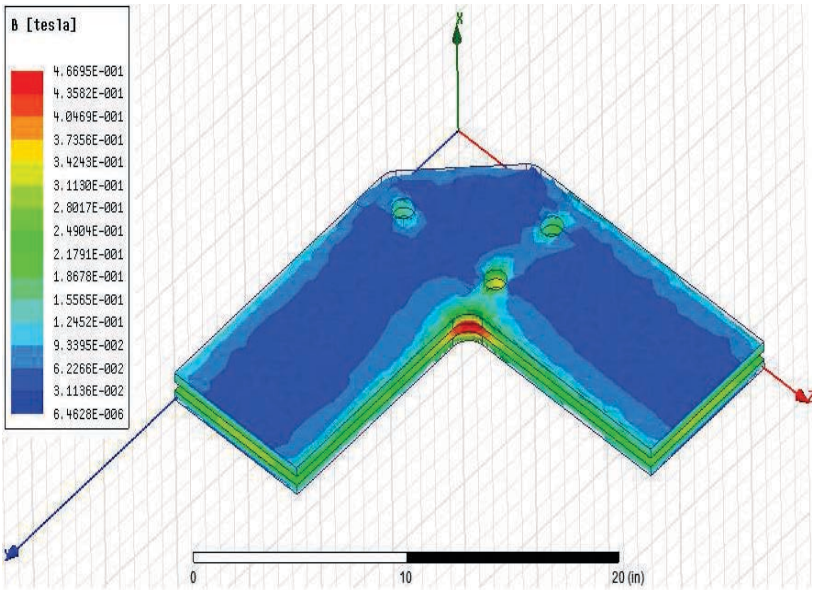

(b)

Figure F.27 ANSYS Maxwell 3D result for magnetic field map of (a) L-shaped and (b) chamfered L-shaped two parallel plates of the high-current stripline with bolt holes carrying 50 kA DC each in the opposite direction (+ -)

The average pressure on the flag plate of the 400-kW design is found to be ~ 2.6 x10^4 N/m^2; however, at the inner corner section this pressure is ~ 9.6 x 10^4. N/m^2. The related result is shown in Figure F.28 (a).

The average pressure on the flag plate of the 700-kW design is found to be ~3.2 x10^4 N/m^2; however, at the inner corner section this pressure is ~8.8 x10^4 N/m^2. The related result is shown in Figure 28 (b) [153].

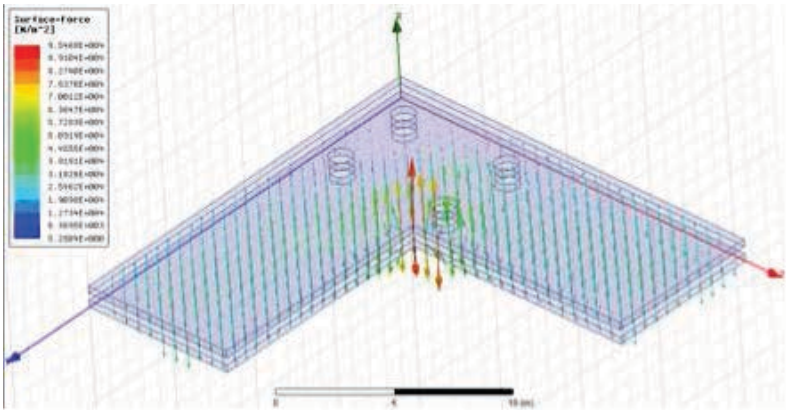

(a)

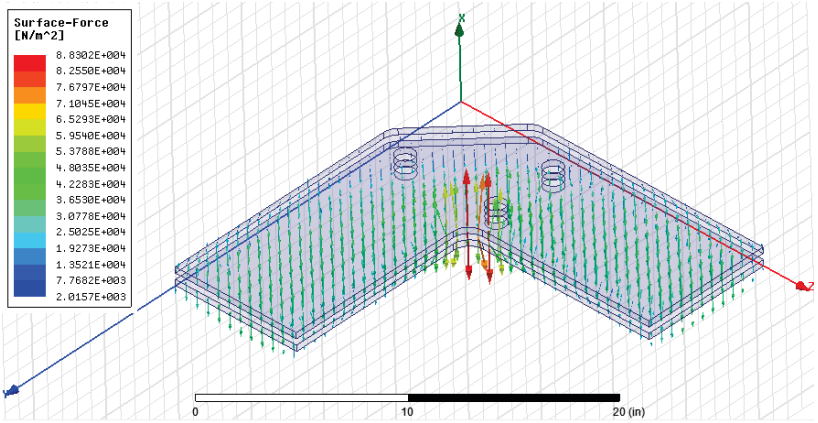

(b)

Figure F.28 ANSYS Maxwell 3D result for the pressure distribution of (a) L-shaped and (b) chamfered L-shaped two parallel plates of the high current stripline while carrying 50 kA DC each in the opposite direction (+ -)

F.8.1.3.1.1. ANSYS Electric Simulation Results for the Current Density of the High-Current Striplines

Current density calculations were done using the ANSYS Electric code applying 50 kA DC to each plate of the 400-kW and 700-kW high-current stripline geometry (half-symmetry) as shown in Figures F.29 and F.30, respectively.

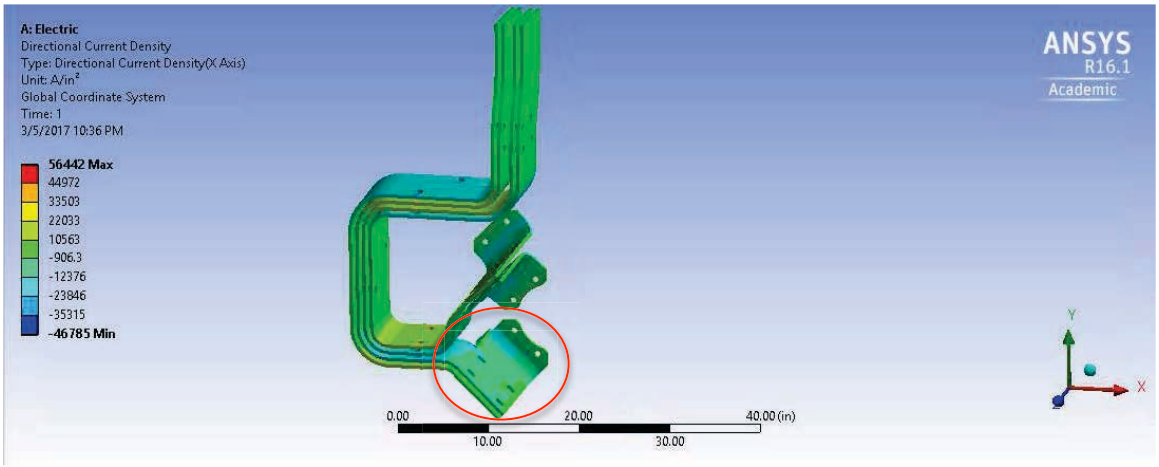

Figure F.29 400-kW half symmetric high-current stripline

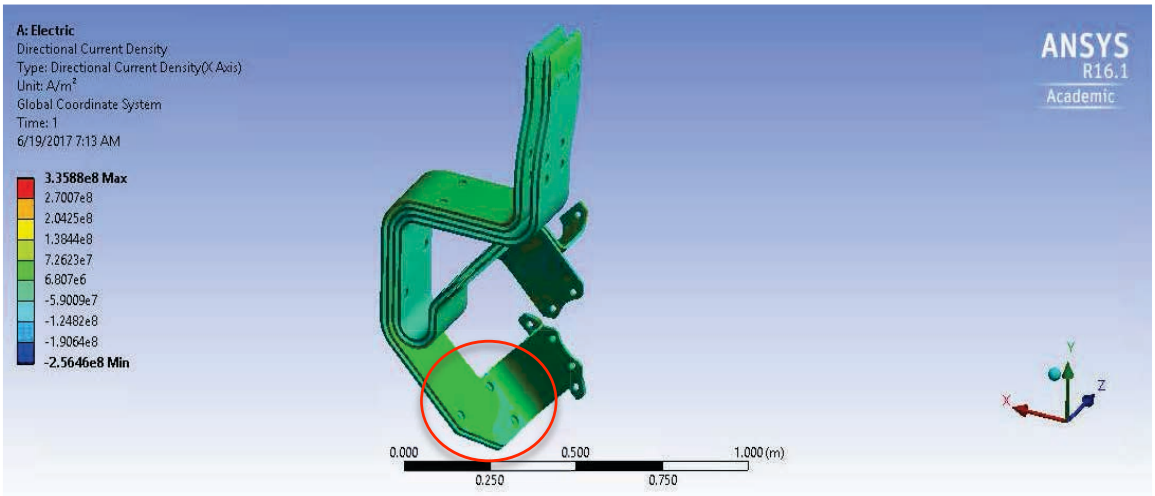

Figure F.30 700-kW half symmetric high-current stripline

As an initial check of the simulations first calculate the current density (**J**) was calculated in a straight section and compare it to that found by the simulation. The calculated value is 2.5833×10^7 A/m^2. The simulated value was found 2.5833×10^7 A/m^2 using ANSYS Electric (Figure F.31).

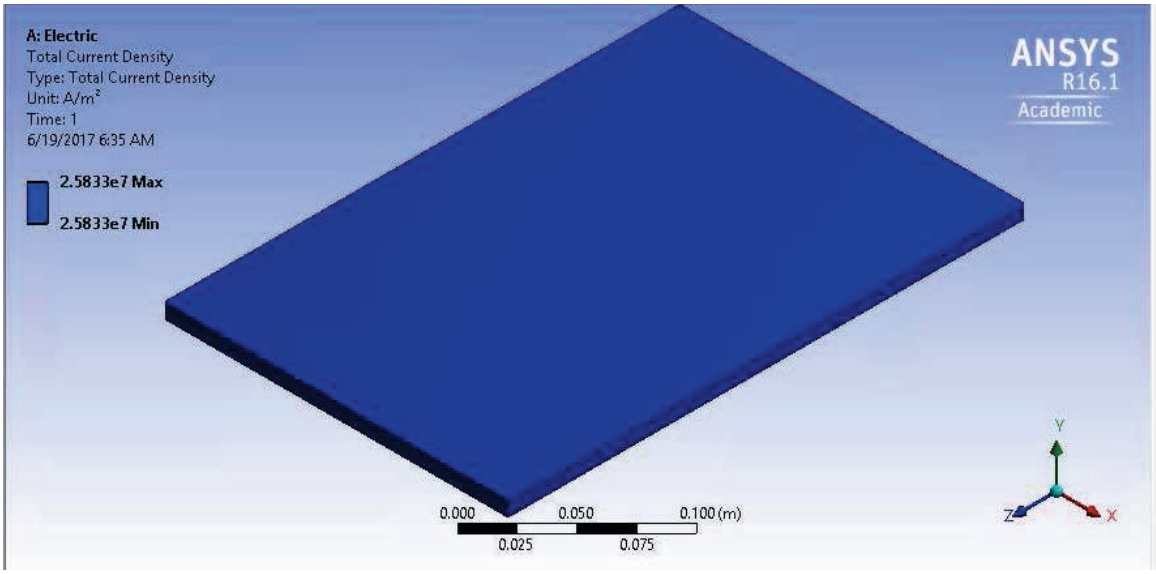

Figure F.31 ANSYS Electric result for total current density of the high-current stripline plate carrying 50 kA DC in the z direction

Next, the more realistic cases were evaluated; however, as our main aim is to investigate the failure at the flag plate of the 700-kW design the additional 4-bolt holes case was skipped here to keep consistency with the magnetic field simulations. A simple un-chamfered case was first performed (Figure F.32).

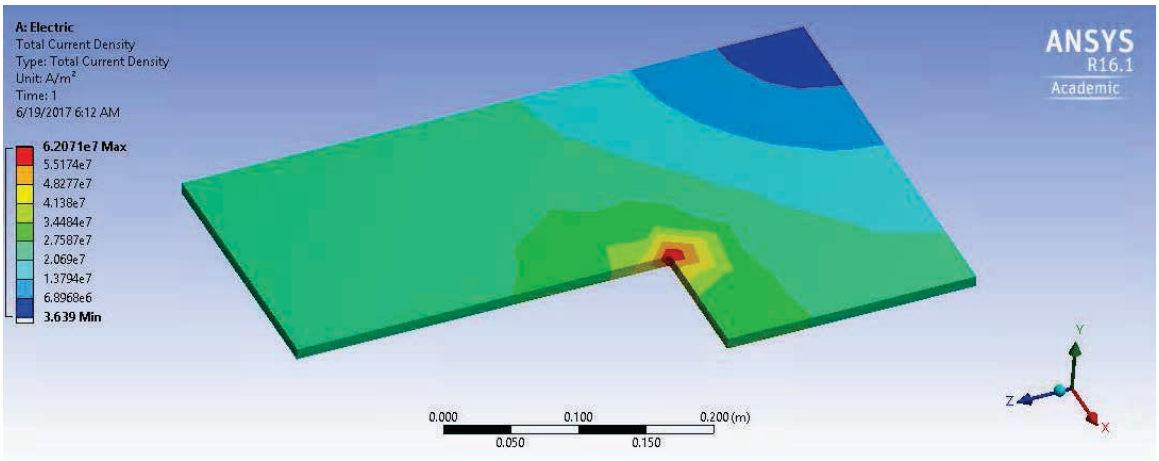

(a)

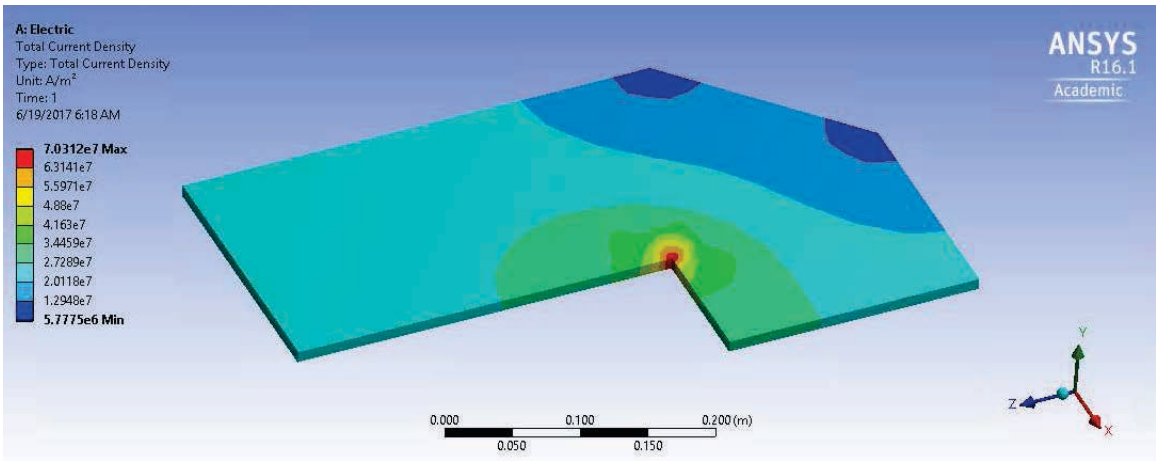

(b)

Figure F.32 ANSYS Electric result for total current density of (a) L-shaped (b) chamfered L-shaped high current stripline plate carrying 50 kA DC

When the identical current is applied to the chamfered L-shaped flag plate that includes the bolt holes as shown in Figure F.33, the current density at the inner corner was found to be ~3 times larger than the nominal straight plate case in Figure F.31.

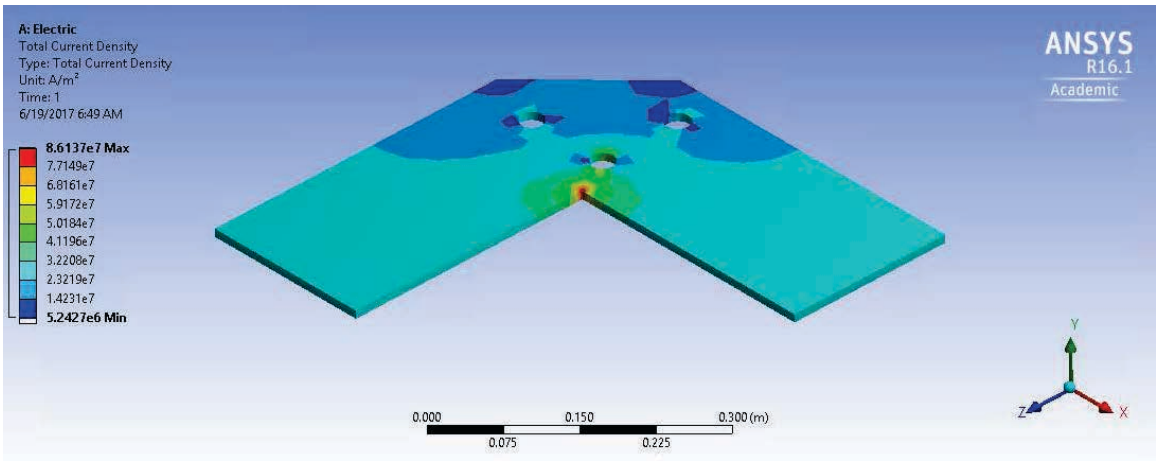

Figure F.33 ANSYS Electric result for total current density of (a) L-shaped and (b) chamfered L-shaped high-current stripline including bolt holes carrying 50 kA DC

As an intermediate summary, the magnetic force, pressure and current density at the critical locations of the flag plate parts of the 400-kW and 700-kW design of the magnetic Horn 1 stripline for NuMI/NOvA were evaluated [154, 155]. First, the results for the magnetic field and force that agreed well with theory were shown for straight plates of the striplines. Second, the results for the flag part of the stripline were evaluated step by step and it was shown that inclusion of the chamfering and bolt holes affected the current density and forces, but not critically. Then, the magnetic field and related effects such as the local pressures were simulated. Finally, the current density simulation was done.

The magnetic field was found to be ~2 times larger at the inner corner of the plates for the 400-kW design and ~1.7 times larger at the inner corner of the plates for the 700-kW design in Figure F.27 as compared to the straight plates case in Figure F.25. The pressure was found to be at the highest point in the inner corner ~3.5 times higher than seen on average for the 400-kW design and ~2.5 times higher than seen on average for the 700-kW as shown in Figure F.28. The current

density is found to be ~3 times larger in the inner corner that seen on the average for the 700-kW design as shown in Figure F.33.

According to these results, even though there is a higher stress point in the inner corner of the structure, the stress is not high enough to, in itself, cause structural damage, and so the damage is most likely coming from a combination of both heating and vibrational effects.

These research results are being implemented in the on-going design upgrades of the magnetic horn stripline designs to handle increased electrical current and higher beam power for the NuMI upgrades and for future LBNF designs. The corner sections need to be evaluated not only mechanically and thermally but also considering electromagnetic contributions. It is better if the inner corner radius of the plate is enlarged for the higher current required in the next designs.

F.8.1.4. Possible Solutions

F.8.1.4.1. The Short Term Solution

Since, the ANSYS Electromagnetic simulation results of the flag plates showed that the magnetic force is not high enough to cause the stress fracture by itself, these fractures are more likely related to fatigue failure due to insufficient damping of vibrational modes. There are possible solutions to avoid vibrational effects such as bolting the 700-kW stripline in a more rigid way as shown in Figure F.34.

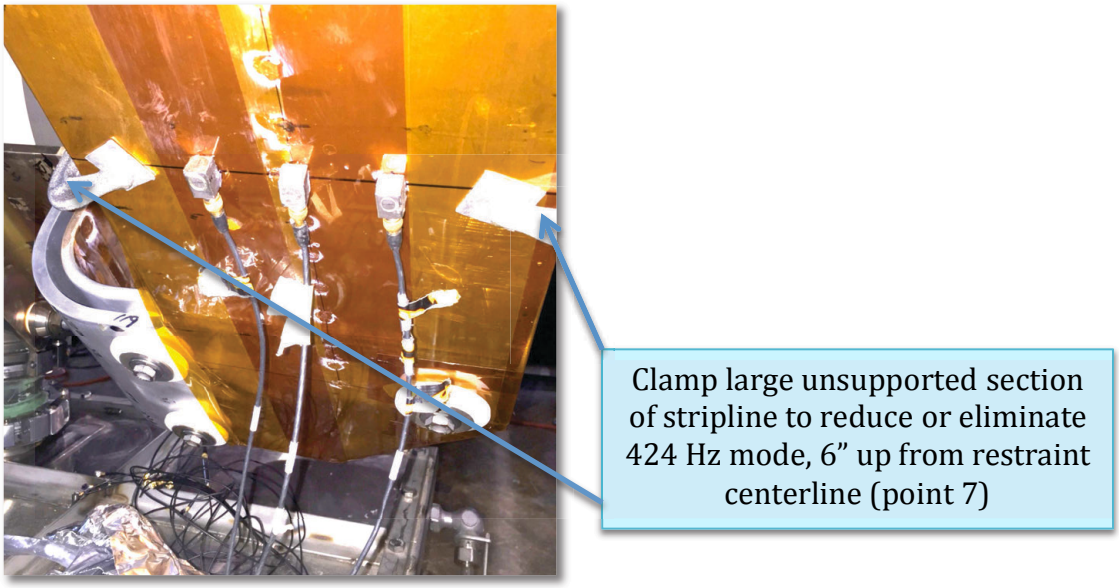

Figure F.34 Clamped large unsupported section of high current stripline [ibid 149] (Image courtesy of Fermilab)

F.8.1.4.2. The Long Term Solution

The new high-current stripline package for the 700-kW case is based upon the 400-kW stripline package design with some geometry, material and cooling improvements. This should lead to a more reliable long-term solution.

F.8.1.4.2.1. Geometry and Material Related Improvements

The planned geometry and material related improvements to the new design are shown in Figure F.35. A larger inner radius on the flag helps to reduce stress concentration. The use of Aluminum alloy 6013 for the flag regions provides higher fatigue and fracture toughness than alloy 6101. Extruding flags achieves better grain alignment transverse to the predicted crack propagation direction.

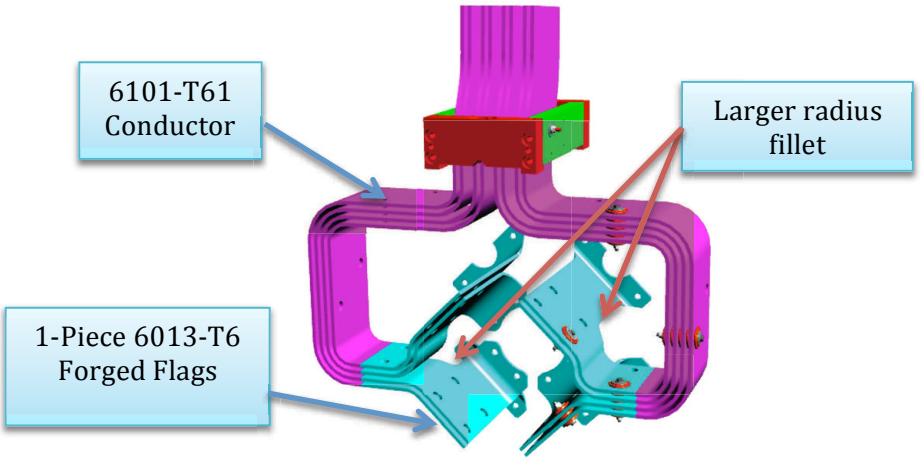

Figure F.35 Improved 700-kW high-current stripline design for the NuMI upgrade and LBNF design (ibid 149) (Image courtesy of Fermilab)

F.8.1.4.2.2. Thermal Effects Related Improvements

Cooling is essential, as Aluminum tends to soften when heated making it more prone to failure [155]. To cool the new-design stripline an air diverter is helpful to keep the temperature <100 ^{o}C (Figure F.36 (a))[ibid 149]. This appears achievable to 580 kW using the air cooling mechanism in Figure F.36 (b) [ibid 149].

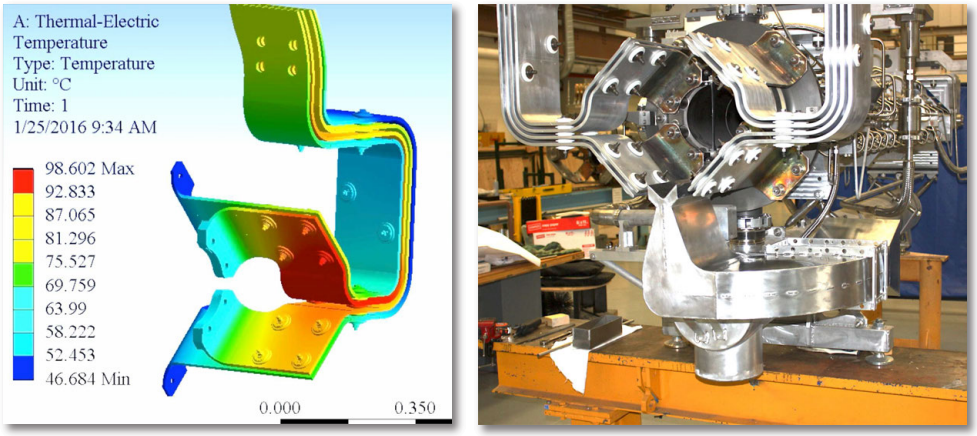

(a) (b)

Figure F.36 (a) Temperature simulation result and (b) air cooling mechanism of new design high-current stripline (Image courtesy of Fermilab)

F.8.2. Current Equalization Simulations for Pulsed Magnetic Horns

The current NuMI/NoVA configuration shown in Figure F.37 uses 2 horns, one after each other. However, for LBNF such an arrangement would require Horn 1 to be around 6 meters in length and this is not so practical to fabricate. In addition following decommissioning storage of such a large activated device becomes a problem. Due to such considerations a 3-horn configuration for LBNF is being considered as shown in Figure F.38.

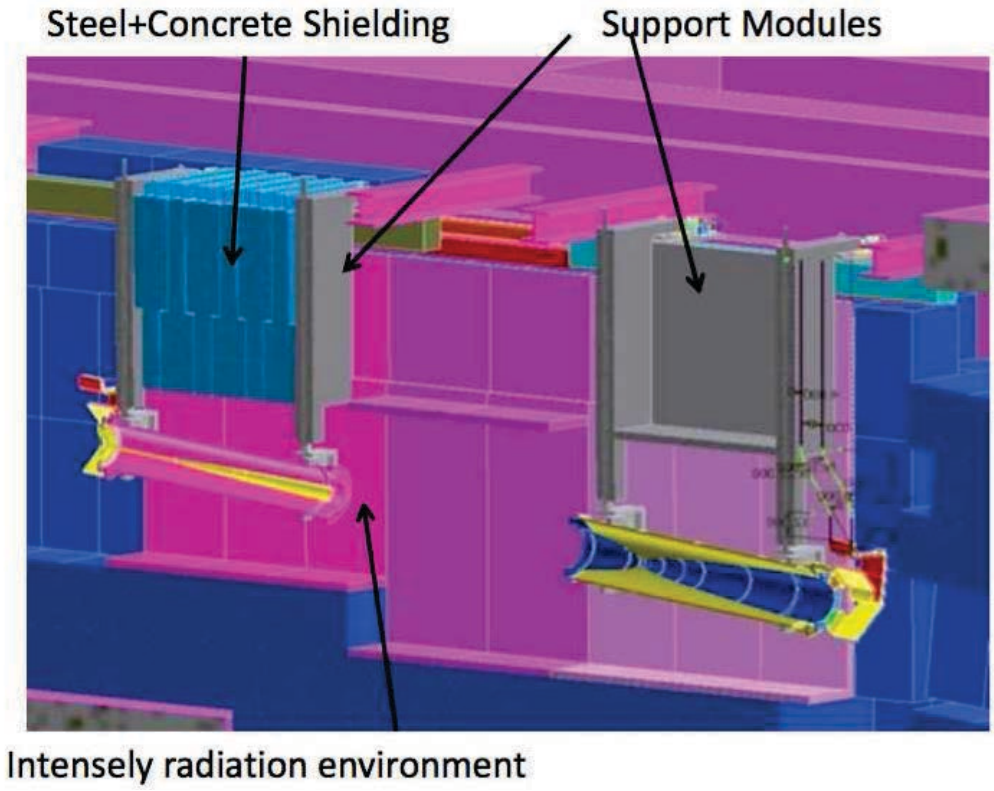

Figure F.37 2-horn configuration for NuMI/NOvA [idib 148] (Image courtesy of Fermilab)

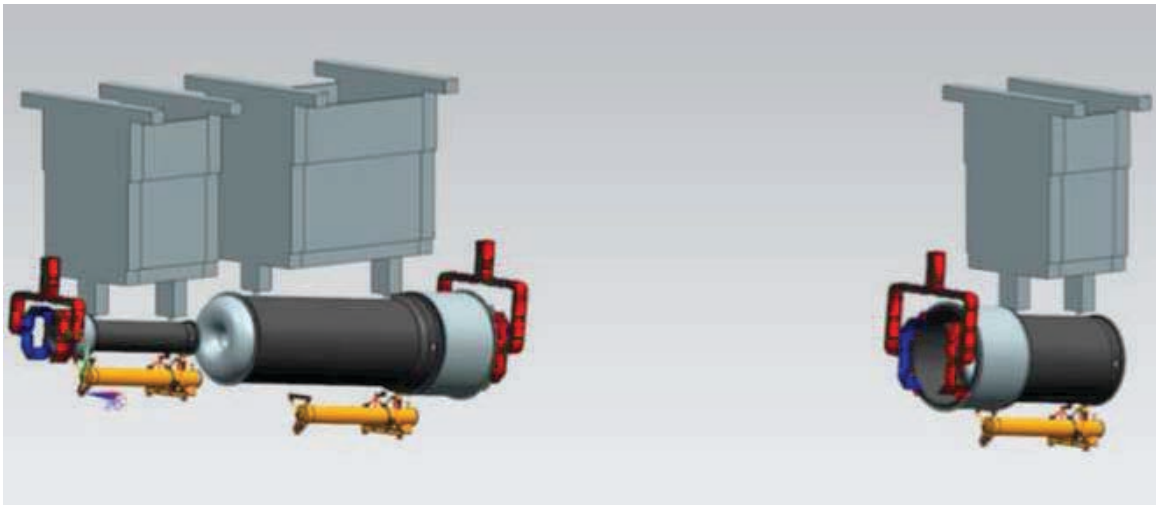

Figure F.38 3-horn configuration for LBNF [ibid 141] (Image courtesy of Fermilab)

The magnetic horns are fed through high-current stripline that are 90^0 apart from each other around the circumference of the horn. This caused an unbalanced current distribution at the early stages of the stripline end of the horn and obviously unbalanced magnetic fields along the horn. To avoid this unbalanced current distribution and magnetic field distribution along the pulsed magnetic horn structure a current equalization section was designed and optimized.

The key to understanding the equalization section is knowing where the pions are travelling that are being focused by the magnetic field.

The previous equalization section for NuMI/NOvA Horns 1 and 2 have the same radius with the magnetic horns however as shown in Figure F.39. Not all of the particles can be focused exactly parallel at the end of the horns as shown in Figure F.8 earlier and hit the equalization section this causes temperature increase at the equalization section of the horn due to the particle shower.

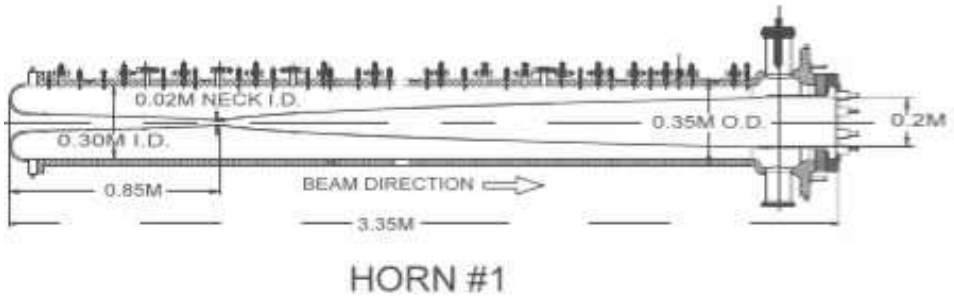

(a)

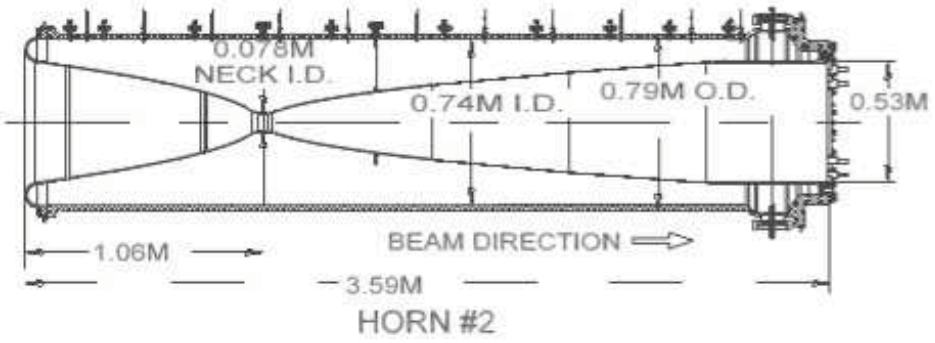

(b)

Figure F.39 Cross section of (a) NuMI/NoVA Horn 1 (b) Horn 2 [ibid 127] (Image courtesy of Fermilab)

In the case of the NuMI/NOvA horns, the relevant pions were more than 99% at lower radius than the inner conductor portion of the current equalization section.

As an example the magnetic field map simulation study was performed using ANSYS Maxwell 3D for the NuMI/NOvA Horn 1 (Figure F.40).

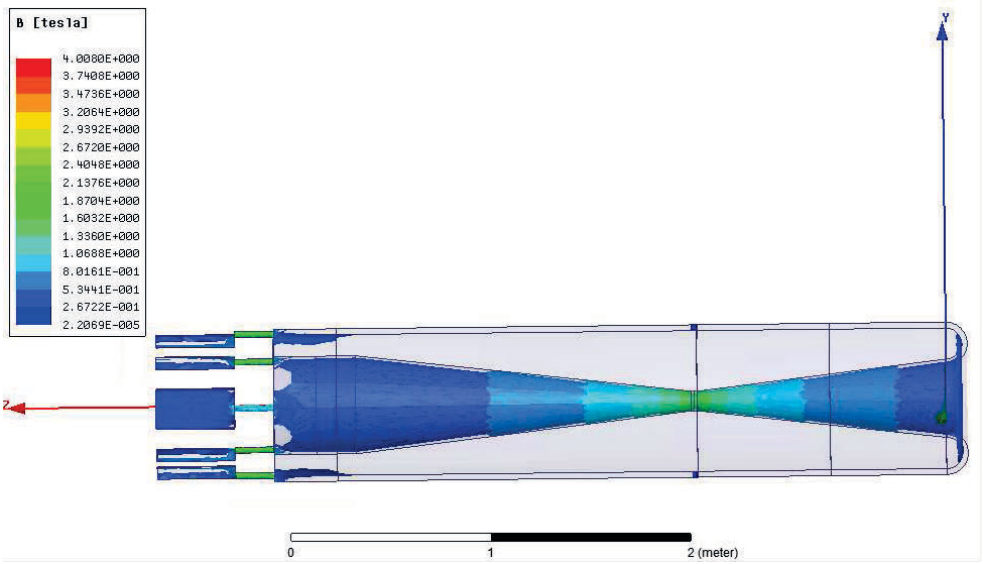

Figure F.40 NuMI/NOvA Horn 1

Compare with NuMI/NOvA Horn 1 the LBNF Horn B has some differences; such as straight sections after conical sections, so to evaluate this modification two straight sections added to NuMI/NOvA design. It is shown that, however, this modification effects the magnetic field the field is not totally damaged as shown in Figure F.41.

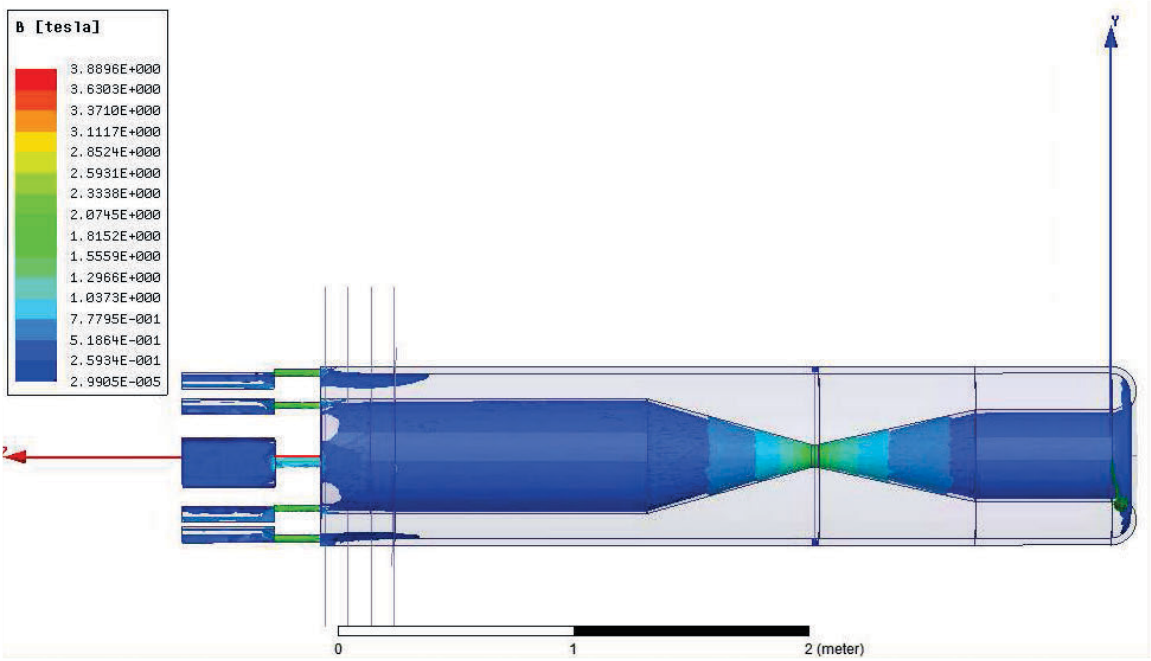

Figure F.41 Two straight section added NuMI Horn 1 design for LBNF Horn B

For LBNF Horn B, a significant fraction of the good pions are at radius larger than the long straight sections, and some go almost out to the outer conductor. That is why the equalization section inner conductor is pushed to very large radius - so that the pions are not affected by that field, but the long straight section is still focusing pions that are at larger radius than the inner conductor along that section. The main aim in here is not to destroy the focusing in that region by having magnetic field non-uniformities in that region.

Also, LBNF Horn B design has a larger outer conductor radius. To see the effect of the larger outer radius conductor an equalization section which has length of NuMI/NOvA equalization section but has a larger radius attached to these two designs shown in Figure F.42. From NuMI/NOvA experience [156], the radius for the equalization section of the magnetic horn was

increased to let the particles go through without hitting the equalization section for LBNF Horn B design as shown in Figure F.42 (b).

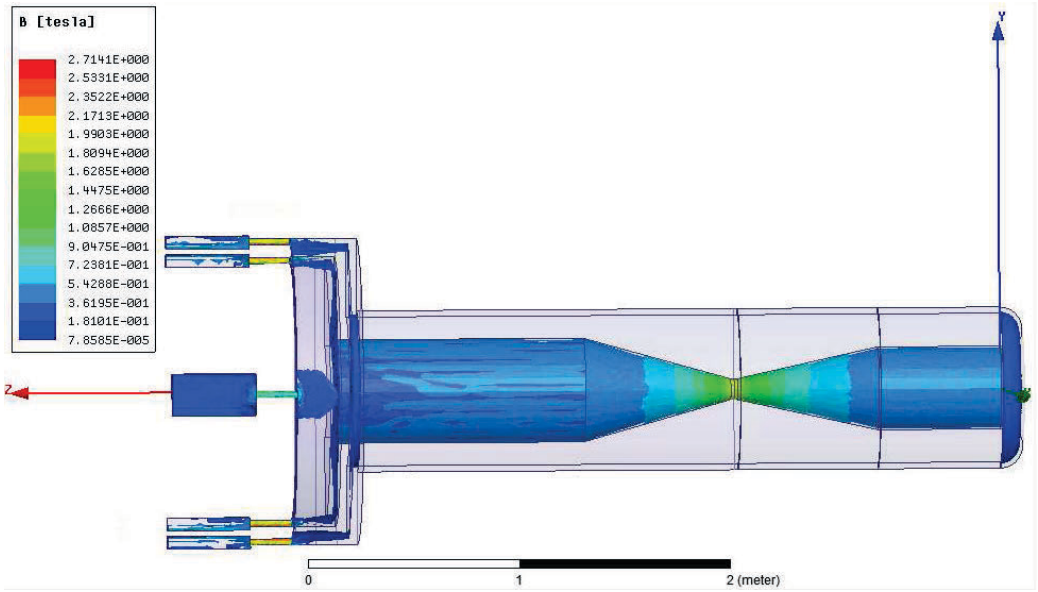

(a)

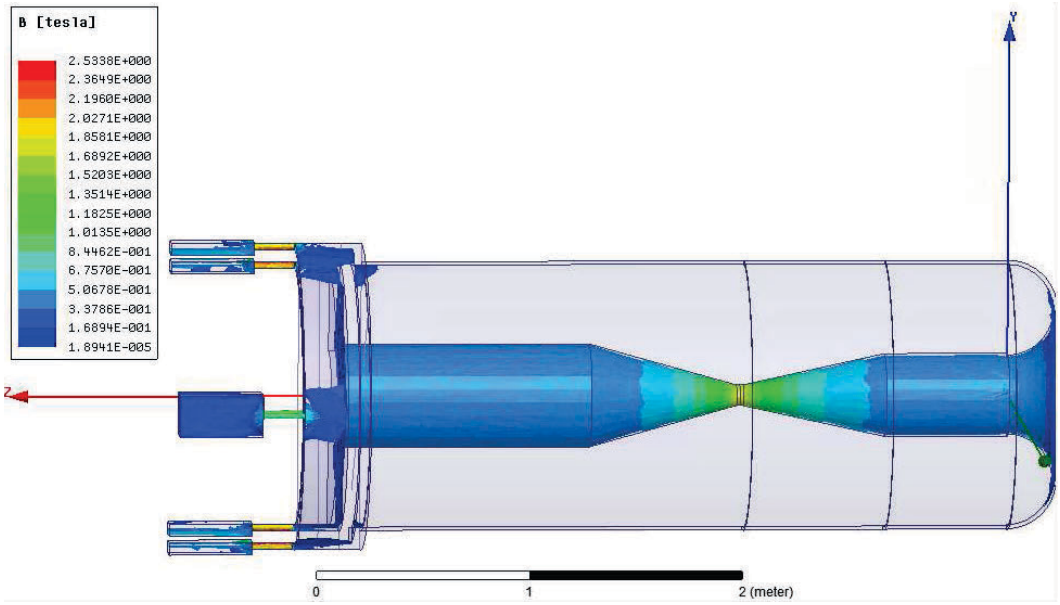

(b)

Figure F.42 (a) LBNF Horn B (a) with the smaller -NuMI like- outer conductor radius (b) with the larger outer conductor radius

Then, the equalization section length optimization study was performed using ANSYS Maxwell 3D for the LBNF Horn B. A 3-meter long equalization section, fed by 4x75=300 kA, was divided into shorter sections (every 25 cm) and the currents measure at 90^0 and 45^0 across the radius between outer and inner conductor of the equalization section. The magnetic field values are then averaged according the Equation 6.3.

$$\frac{B_{90^\circ}-B_{45^\circ}}{B_{90^\circ}+B_{45^\circ}} \tag{F.3}$$

The optimum length of the equalization section was defined when the averaged magnetic field value change was better than 1%, the required for the experimental case. What was found was that the optimum length value coincides roughly with the radius of the equalization section. This process was repeated for different radius values and the change of optimal length was always found proportional to the radius of the equalization section. Here, the result is presented for an equalization section that has a 75 cm radius (Figures F.43 and F.44).

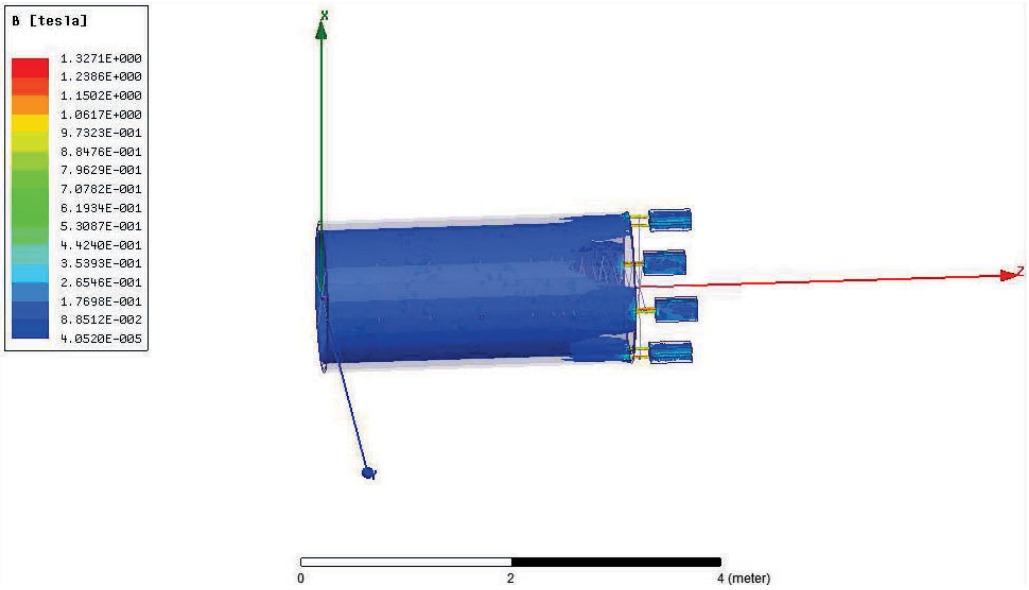

Figure F.43 The current equalization section for LBNF Horn B

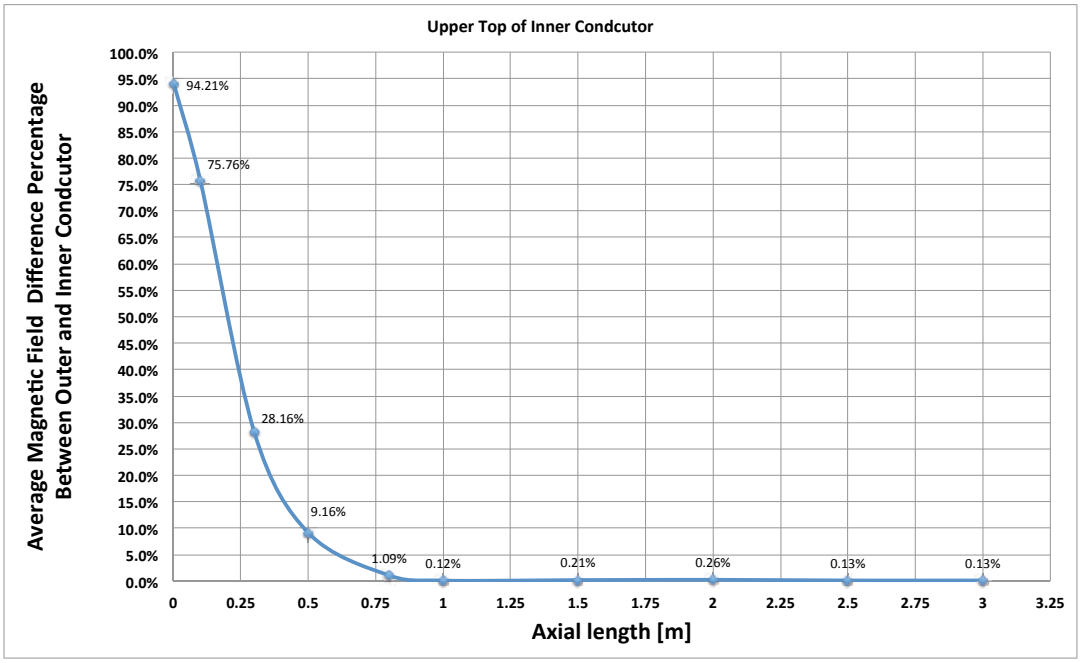

Figure F.44 The average magnetic field difference percentage along the current equalization section of LBNF Horn B

The LBNF Horn B with attached optimal length current equalization section is shown in Figure F.45.

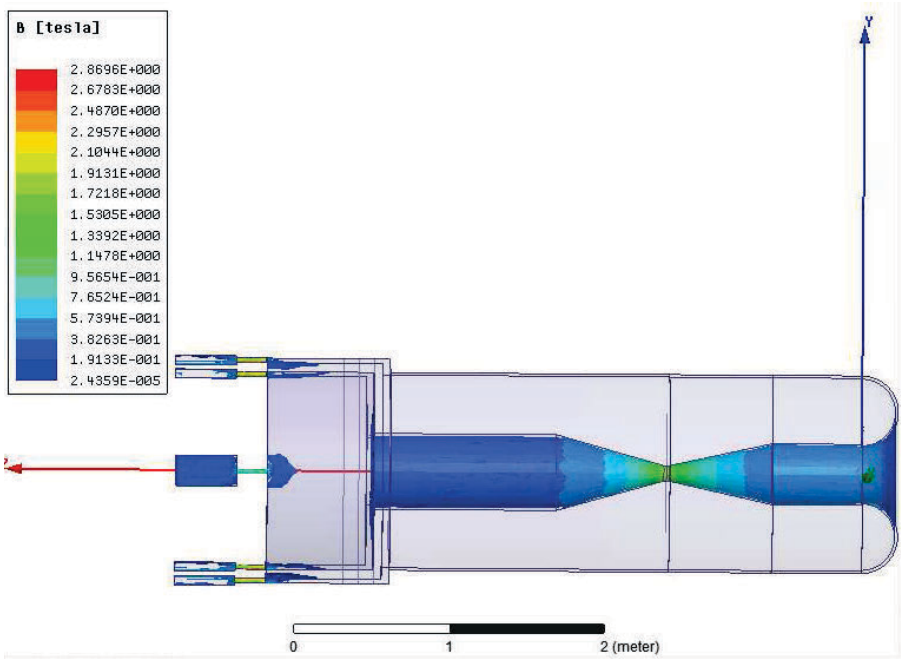

Figure F.45 LBNF Horn B with attached optimal length equalization section fed by 300 kA DC

An alternative design that has the same path length in total but also has a torus at the stripline end of the inner conductor provides the same results. This is shown in Figure F.46.

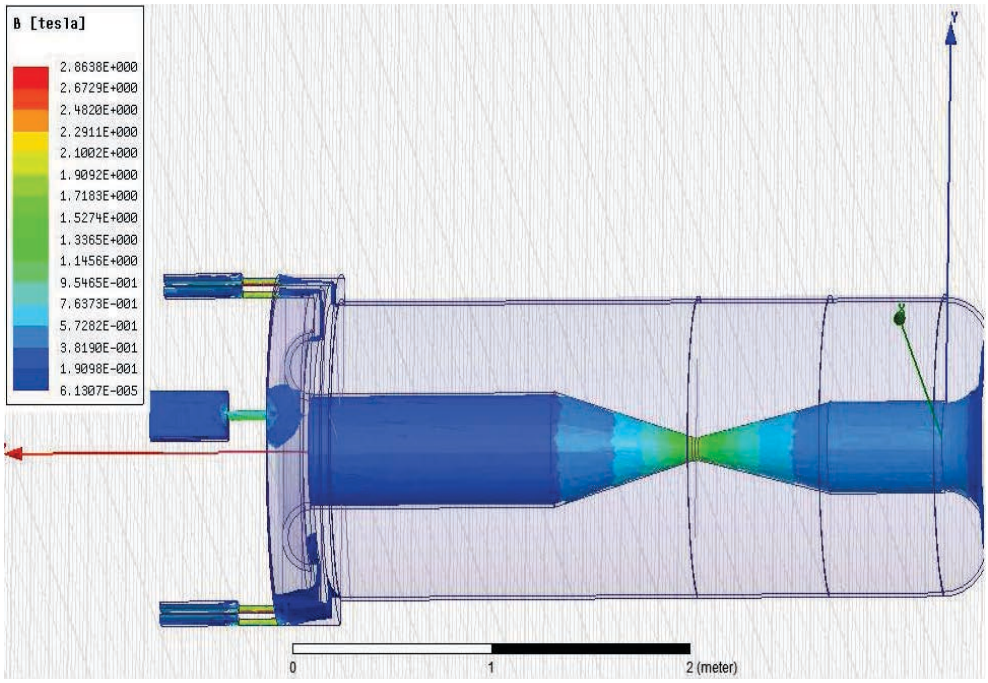

Figure F.46 An alternative LBNF Horn B design with torus end cap attached to inner conductor